

ALBERT-LUDWIGS-UNIVERSITY  
FREIBURG IM BREISGAU

Faculty of Mathematics and Physics

---

MODELING AND SIMULATION  
OF ATMOSPHERIC CLOUD DROPLETS

---

by  
Jan Kai Bohrer

A thesis submitted to the Institute of Physics  
in partial fulfillment of the requirements  
for the degree of *Master of Science Physics*

Supervisors:  
Prof. Dr. Ina Tegen, Leibniz Institute for Tropospheric Research  
Dr. Oswald Knoth, Leibniz Institute for Tropospheric Research  
Prof. Dr. Tanja Schilling, Institute of Physics, University Freiburg

Freiburg im Breisgau, October 2019



## ZUSAMMENFASSUNG

### **Modellierung und Simulation atmosphärischer Wolkentröpfchen**

Die vorliegende Arbeit präsentiert die Entwicklung, numerische Implementation und Validierung eines partikelbasierten (Lagrange-artigen) Mikrophysikmodels für warme (eisfreie) Wolken. Hierbei wird das Wolkentropfenensemble durch eine rechnerisch realisierbare Anzahl von diskreten Simulationsteilchen (ebenfalls bezeichnet als Super-Tröpfchen) beschrieben, die jeweils eine Multiplizität von realen Tröpfchen mit den selben physikalischen Eigenschaften, wie Ort, Geschwindigkeit, Masse und chemischer Zusammensetzung, darstellen. Im Unterschied zu rein hydrodynamischen Modellen, ermöglicht dieser Ansatz eine detaillierte Beschreibung physikalischer Prozesse auf individueller Teilchenebene und gleichzeitig die Beobachtung einzelner Tröpfchen während eines Lebenszyklus'. Das entwickelte Modell beinhaltet den Transport von Feuchte und Energie in der Atmosphäre, dynamische Beschleunigung von Tröpfchen durch Luftwiderstand und Gravitation, Austausch von Masse und Wärme während Kondensation und Verdunstung, sowie Wachstum durch Kollisionen mit anschließender Koaleszenz. Im Zuge eines Ausblicks, der mögliche Erweiterungen für das vorgestellte Programm präsentiert, werden bedeutende Vorteile von Algorithmen mit diskreten Partikeln gegenüber traditionellen Bulk- und Bin-Modellen dargestellt. Anwendungsmöglichkeiten schließen die detaillierte Beschreibung von lokaler Turbulenz, mehrkomponentiger Chemie der flüssigen und festen Phase und individueller Morphologie von Eis-Partikeln ein. Letztere hat erheblichen Einfluss auf Sedimentation, Bildung von Raueis und Aggregationsprozesse.

Eine Auswertung durchgeföhrter Simulationen zeigt, dass der implementierte stochastische Kollektionsalgorithmus eine praktikable Alternative zu neuesten Bin-Modellen darstellt. Die Analyse beinhaltet eine Untersuchung des Konvergenzverhaltens mit steigender Zahl von Super-Tröpfchen für einen additiven, massenbasierten Kollisions-Kernel und für zwei Parametrisierungen des hydrodynamischen Kernels. Im Weiteren findet eine Validierung des kompletten Models durch die Simulation einer nieselnden Stratocumulus-Wolke statt. Dabei wird ein zweidimensionales, kinematisches Framework mit stationären Feldern für Massendichte und Geschwindigkeit der Trockenluft verwendet, welches eine geschlossene Zirkulationszelle repräsentiert, mit der die Prozessierung von Wolken-Kondensationskeimen untersucht werden kann. Das Programm läuft numerisch stabil und liefert plausible Simulationsergebnisse bei Variation der physikalischen Umgebungsbedingungen in Form von Konzentration und Material der Kondensationskeime. Es werden sowohl Ammoniumsulfat und Natriumchlorid verglichen, als auch saubere und verschmutzte Luftbedingungen. Durch weitere Auswertungen wird deutlich, dass die anfängliche Anzahl von Simulationsteilchen pro Zelle signifikanten Einfluss auf die Verteilungsfunktion der Tröpfchengrößen hat. Dieses Verhalten tritt verstärkt in sensitiven Bereichen der Wolkenuntergrenze und der atmosphärischen Fallwindzone auf.



## ABSTRACT

### **Modeling and simulation of atmospheric cloud droplets**

This thesis presents the development, numerical implementation and validation of a particle based (Lagrangian) microphysics model for warm (ice-free) clouds. Here, the cloud droplet ensemble is described by a computational feasible number of discrete simulation particles (also called super-droplets), each of which represents a multiplicity of real droplets with exactly the same physical properties, like position, velocity, mass and chemical composition. In contrast to purely Eulerian models, this approach enables a detailed description of physical processes on the individual particle level and the observation of distinct droplets during their life cycle. The developed model includes transport of atmospheric moisture and energy, dynamic droplet acceleration due to drag force and gravity, mass and heat exchange during condensation/evaporation and growth by collision-coalescence. In connection to an outlook, featuring possible extensions for the presented program, significant advantages of discrete particle schemes over traditional bulk and bin models are summarized, including the detailed treatment of local turbulence, multi-component liquid/solid phase chemistry and individual morphology of ice particles, which has considerable influence on sedimentation velocities, riming and aggregation.

Evaluation of performed collision box model simulations reveals that the implemented stochastic collection scheme is a viable alternative to state-of-the-art bin models. Convergence behavior with increasing number of super-droplets is investigated for the sum-of-mass collision kernel and two parametrizations of the hydrodynamic kernel. Furthermore, the complete model is validated by simulating a drizzling stratocumulus cloud in a two-dimensional kinematic framework with stationary velocity field and dry air density, featuring a closed circulation cell for the processing of cloud condensation nuclei. The program exhibits stable performance and the simulation results show plausible behavior, when varying the physical conditions of cloud condensation nuclei material and concentration (comparing ammonium sulfate to sodium chloride and pristine to polluted scenarios). By analyzing additional simulations, significant dependence of the droplet size distribution on the initial number of simulation particles per cell is observed, which is most distinct in sensitive areas at the cloud base and the atmospheric downdraft regions.



# CONTENTS

DECLARATION	<b>xi</b>
ACKNOWLEDGMENTS	<b>xiii</b>
LIST OF SYMBOLS	<b>xv</b>
<b>1 INTRODUCTION</b>	<b>1</b>
<b>2 ATMOSPHERIC PHYSICS</b>	<b>7</b>
2.1 The earth's atmosphere . . . . .	7
2.2 Atmospheric model: Cloud particles in a continuous air field . . . . .	8
2.3 Atmospheric fluid dynamics . . . . .	9
2.3.1 Fluid field time evolution . . . . .	10
2.3.2 Conservation of mass . . . . .	11
2.3.3 Conservation of energy . . . . .	12
2.4 Kinematic framework . . . . .	14
2.4.1 Initial atmospheric configuration . . . . .	15
2.4.2 Transport equations for energy and water vapor in the kinematic framework	16
2.5 Transport equations for the atmosphere . . . . .	17
<b>3 MODELING DISCRETE CLOUD DROPLETS</b>	<b>19</b>
3.1 Saturation pressure at the droplet surface . . . . .	19
3.1.1 Surface tension effect (Kelvin equation) . . . . .	20
3.1.2 Solute effect (Raoult relation) . . . . .	21
3.1.3 Köhler equation . . . . .	22
3.2 Mass diffusion and heat conduction . . . . .	22
3.2.1 Condensation rate . . . . .	24
3.3 Particle dynamics . . . . .	24
3.3.1 Drag force $F_d$ . . . . .	24
3.3.2 Pressure gradient force $F_{pr}$ and gravitational force $F_g$ . . . . .	25
3.3.3 Basset force, Saffman and Magnus lift forces . . . . .	26
3.3.4 Dynamics summary . . . . .	26
3.4 Equations of motion . . . . .	26
3.5 Particle collisions . . . . .	27
3.5.1 Stochastic coalescence equation . . . . .	27
<b>4 DISCRETIZATION</b>	<b>31</b>
4.1 Transport of energy and water vapor . . . . .	31
4.1.1 Spatial grid . . . . .	31

---

4.1.2	Discretized divergence . . . . .	32
4.1.3	Time integration . . . . .	33
4.2	Simulation particles (super-droplets) . . . . .	34
4.2.1	Generation of SIP ensembles . . . . .	34
4.2.2	Reconstruction of the distribution function from a SIP ensemble . . . . .	36
4.3	Particle propagation . . . . .	37
4.4	Particle collisions . . . . .	39
4.4.1	Collection algorithm using SIPs . . . . .	40
4.4.2	Collision kernels . . . . .	41
4.5	Update scheme . . . . .	42
4.6	Implementation . . . . .	44
4.6.1	Procedure . . . . .	44
5	<b>COLLISION BOX MODEL</b> . . . . .	<b>45</b>
5.1	Description . . . . .	45
5.2	Results . . . . .	46
5.2.1	Golvin kernel . . . . .	46
5.2.2	Long Kernel . . . . .	47
5.2.3	Hall Kernel . . . . .	50
5.3	Conclusions . . . . .	50
6	<b>TEST CASE: DRIZZLING STRATOCUMULUS</b> . . . . .	<b>53</b>
6.1	Initial atmospheric setup and saturation adjustment . . . . .	53
6.1.1	Particle dry size distribution . . . . .	53
6.1.2	Layering of the atmosphere . . . . .	53
6.1.3	Spin-up . . . . .	54
6.2	Simulation results . . . . .	56
6.2.1	Time evolution of coarse grained fields . . . . .	56
6.2.2	Particle size spectra . . . . .	61
6.2.3	Droplet growth cycle . . . . .	63
6.3	Comparison to external sources . . . . .	65
6.4	Finite size analysis . . . . .	68
6.4.1	Influence of the collision time step . . . . .	68
6.4.2	Influence of the number of SIPs per cell . . . . .	70
6.4.3	Influence of the spatial grid step size . . . . .	77
6.5	Influence of the collision kernel . . . . .	77
6.6	Variation of physical conditions . . . . .	79
6.6.1	Influence of the solute type . . . . .	79
6.6.2	Influence of the CCN number concentration . . . . .	79
7	<b>CONCLUSIONS AND OUTLOOK</b> . . . . .	<b>83</b>
A	<b>APPENDIX</b> . . . . .	<b>89</b>
A	Material properties . . . . .	89
B	Advection test by solid body rotation . . . . .	92
C	Derivations . . . . .	94
C.1	Integration of the hydrostatic equation for linear temperature profiles . .	94
C.2	Lognormal distribution . . . . .	94

D	Collision box model . . . . .	96
D.1	Comparison to reference data . . . . .	96
D.2	Convergence behavior when increasing the number of simulation particles	99
E	Test case . . . . .	100
E.1	Simulation without collisions . . . . .	100
E.2	Simulation of the default case . . . . .	101
E.3	Simulation with constant collision efficiency . . . . .	102
E.4	Variation of the collision time step . . . . .	104
	<b>BIBLIOGRAPHY</b>	<b>107</b>



## DECLARATION

I, Jan Kai Bohrer, declare that I have composed the presented thesis independently on my own and without any other resources than the ones indicated. All thoughts taken directly or indirectly from external sources are properly denoted as such. The thesis has neither been previously submitted to another authority in this or a similar form nor has it yet been published.

Freiburg im Breisgau, October 29, 2019

## EIDESSTATTLICHE ERKLÄRUNG

Ich, Jan Kai Bohrer, erkläre an Eides statt durch meine Unterschrift, dass ich die vorliegende Masterarbeit selbständig verfasst und alle Stellen, die ich wörtlich oder annähernd wörtlich aus Veröffentlichungen entnommen habe, als solche kenntlich gemacht habe und mich auch keiner anderen als der angegebenen Literatur, Quellen oder sonstiger Hilfsmittel bedient habe. Die Arbeit hat in dieser oder ähnlicher Form noch keiner anderen Prüfungsbehörde vorgelegen und wurde bisher nicht veröffentlicht.

Freiburg im Breisgau, 29. Oktober 2019



## ACKNOWLEDGMENTS

At this point, I would like to express my gratitude to a number of people who supported me during my research in preparation of the presented thesis. My thanks go to

Prof. Dr. Ina Tegen for providing the opportunity for me to work on the fascinating topic of cloud modeling in her department at the Leibniz Institute for Tropospheric Research (TROPOS),

Prof. Dr. Tanja Schilling for her advice and support and for enabling the cooperation between the University Freiburg and TROPOS, thus making it possible for me to do research in my favored subject area,

Dr. Oswald Knoth for his supervision, plenty scientific discussions and for opening several possibilities to deepen my knowledge and obtain valuable insights into the scientific world,

Dr. Dennis Niedermeier for a hands-on introduction in experimental measuring methods at the Turbulent Leipzig Aerosol Cloud Interaction Simulator,

the whole TROPOS modeling department for a pleasant working atmosphere,

my family for their steady and unconditional support in many different ways.



## LIST OF SYMBOLS

$\Delta t$	Time step, page 33
$\Delta t_{\text{adv}}$	Advection time step, page 33
$\Delta t_{\text{col}}$	Collision time step, page 39
$\Delta x, \Delta z$	Horizontal/vertical grid spacing, page 31
$\Phi_{\text{con}}$	Condensation mass rate, page 11
$\Theta$	Dry potential temperature, page 16
$\Theta_l$	Liquid water potential temperature, page 15
$\Theta_m$	Moist potential temperature, page 13
$\epsilon_v = \tilde{R}_{\text{dry}}/\tilde{R}_v$	Ratio of specific gas constants, page 12
$\gamma$	Particle mass rate (condensation/evaporation), page 26
$\kappa_{\text{dry}} = \tilde{R}_{\text{dry}}/c_{\text{dry}}$	Ratio of specific gas constant and heat capacity for dry air, page 12
$\kappa_m = \tilde{R}_m/c_m$	Ratio of specific gas constant and heat capacity for moist air, page 12
$\kappa_t = \kappa_m(r_{\text{tot}})$	Ratio $\kappa_m$ for $r_l = 0$ , page 15
$\lambda_{m,k}$	$k$ -th moment of the mass distribution $f_m$ , page 27
$\mu_f$	Dynamic shear viscosity, page 10
$\phi_s$	Osmotic coefficient, page 21
$\phi_{\text{con}}$	Condensation density rate, page 11
$\rho$	Mass density, see Table 2.2 for subscripts, page 9
$\rho_p$	Particle mass density, page 8
$\sigma_{\text{cs}}$	Collision cross section, page 28
$\sigma_p$	Particle (droplet) surface tension, page 20
$\xi$	Simulation particle multiplicity, page 34
$\mathbf{a}$	Particle acceleration, page 26
$\mathbf{a}_d$	Particle acceleration due to drag, page 25
$a_K$	Factor in the Kelvin equation, page 20
$a_w$	Water activity, page 21
CCN	Cloud condensation nucleus, page 7
$c_{\text{dry}}$	Specific isobaric heat capacity of dry air, page 12
$c_m$	Specific isobaric heat capacity of moist air, page 12
$\text{div}_{\text{eff}}$	Discretized divergence, page 32
$D_v$	Diffusion coefficient of water vapor in air, page 22
DNC	Droplet number concentration, page 27
$e$	Water vapor pressure, page 7
$e_s$	Saturation pressure of water (vapor-liquid), page 7
$E_{\text{coal}}$	Coalescence efficiency, page 28
$E_c$	Collection efficiency, page 28
$E_{\text{cls}}$	Collision efficiency, page 28
$\mathbf{F}$	Force, page 24
$\mathbf{F}_d$	Drag force, page 25
$\mathbf{F}_g$	Gravitational force, page 19

---

$f_m$	Droplet mass distribution (not normalized), page 27
$f_R$	Droplet radius distribution (not normalized), page 27
$\tilde{f}_m$	Droplet mass probability density function, page 27
$G = (\Theta, r_v)$	Thermodynamic state variables, page 33
$g_{\ln(R)}$	Logarithmic radius distribution function, page 46
$h$	Refined particle interaction time step, page 33
$h_e$	Specific enthalpy, page 12
$i_s$	van't Hoff factor, page 21
$j_{\text{dry}}$	Dry air mass flux density, page 14
$j_Q$	Heat flux density, page 10
$j_v$	Water vapor mass flux density, page 11
$K(m, m')$	Collection kernel for masses $m, m'$ , page 28
$K(R, R')$	Collection kernel for radii $R, R'$ , page 29
$K_Q$	Thermal conductivity of moist air, page 22
$k_d$	Drag force factor, page 25
$L_v$	Specific heat of vaporization, page 12
LMC	Liquid mass content, page 27
$l_\alpha, l_\beta$	Accommodation ( $\alpha$ ) and condensation ( $\beta$ ) length corrections, page 23
$m$	Mass, see Table 2.2 for subscripts, page 10
$m_p$	Particle mass, page 8
$M_s$	Molar mass of the solute, page 22
$M_w$	Molar mass of water, page 22
$p$	Pressure, page 9
$p_*$	Reference pressure (1000 hPa), page 13
$q$	Specific heat, page 12
$\text{Re}_p$	Particle Reynolds number, page 25
$R_{\text{act}}$	Droplet activation radius, page 8
$R_p$	Particle radius, page 7
$r$	Position vector originating at the particle center, page 22
$\tilde{R}_{\text{dry}}$	Specific gas constant of dry air, page 12
$\tilde{R}_m$	Specific gas constant of moist air, page 12
$\tilde{R}_v$	Specific gas constant of water vapor, page 12
$r_k = \rho_k / \rho_{\text{dry}}$	Mixing ratio of species $k$ , see Table 2.2 for subscripts, page 11
$S = e/e_s$	Saturation, here equal to relative humidity, page 7
$S_{\text{act}}$	Saturation required for droplet activation, page 8
$S_{\text{crit}}$	Critical saturation, page 8
$S_{\text{del}}$	Deliquescence saturation, page 7
$S_{\text{effl}}$	Efflorescence saturation, page 8
SD	Standard deviation (estimation), page 36
SIP	Simulation particle (super-droplet), page 34
$s$	Specific entropy, page 10
$T$	Temperature, page 9
$t$	Time, page 9
$\mathbf{u}$	Air velocity field, page 9
$\mathbf{v}$	Particle velocity, page 26
$w_s = m_s/m_p$	Solute mass fraction, page 22
$\mathbf{x}$	Position vector, page 9

# 1 INTRODUCTION

Clouds are visible, air-suspended aggregates of aqueous droplets and/or ice crystals. In the earth's atmosphere, they appear in various shapes, compositions, spatial extents and heights above the surface and are of vital importance for both, the global energy budget and hydrological cycle. Evaporated water is transported over distances of various length scales and subsequently redistributed by precipitation, thereby additionally transferring latent heat from the earth's surface to higher atmospheric layers. Moreover, clouds interact with terrestrial (thermal) as well as solar (shortwave) radiation, the latter of which can be appreciated on satellite images, where the cloud albedo is visible as, partially impressive, white to gray structures. It is evident that clouds have major impact on the earth's weather and climate.

The evolution of a cloud is influenced by numerous physical processes on a variety of length scales, ranging from large scale atmospheric motion (up to thousands of kilometers) to mass and heat exchange between the smallest particulate constituents and the local, surrounding gaseous air molecules. Additionally, relevant atmospheric regions contain a multitude of different chemical species, coming in various phases, shapes and sizes. To describe a cloud in all its detail, it is thus necessary to consider a variety of chemical multi-component reaction systems, including molecular and particulate cloud condensation nuclei, aqueous solution droplets and ice crystals.

In meteorology, the individual physical description of cloud particles is referred to as *microphysics*. Since growth by condensation of water vapor and particle-particle coalescence are crucial for the cloud evolution, it is important to find appropriately detailed descriptions for these microscale processes. On the other hand, it is desirable to include sufficiently large atmospheric regions to capture the determining dynamics, generally described by the Navier-Stokes equations (NSE). For any chosen open domain, the right formulation of the boundary conditions is moreover of major importance for a consistent physical representation. The stated requirements lead to challenging tasks in modeling and vast computational demands for numerical simulations.

*Direct numerical simulation* (DNS) aims to solve the NSE directly by numerical discretization and considers mass, momentum and heat exchange involving the fluid phase by molecular transport coefficients. This method enables the physical treatment of each individual particle. Nevertheless, it requires spatial discretization steps in the order of millimeters, limiting the computationally feasible domain extent to the order of cubic centimeters. While DNS proved useful for investigations of small scale turbulence effects [Grabowski13], it is evidently not applicable for weather and climate applications. Models including larger atmospheric domains require a coarser grid and thereby additional methods to consider sub grid processes, such as turbulence, chemical reactions and phase transitions. Moreover, observations show that the number of cloud droplets in one cubic meter is typically in the order of 100 million [Allen11]. This prohibits the numerical treatment of distinct particles in clouds, which may stretch over several kilometers and more.

*Large-eddy simulations* (LES) are sophisticated tools to numerically investigate clouds or relevant cloud regions in considerably large domains, see e.g. [Grabowski93, Carpenter98, Bryan03, Stevens05, Lebo15]. Here, the smallest spatial units are "large eddies" with edge lengths of tens to hundreds of meters, which capture the dominant motion. Dynamical processes on smaller scales, including diffusion and turbulence, are treated by sub-grid parametrization, trying to average unresolved flow effects by appropriate methods. To describe the vast amount of cloud

particles with varying number concentration, mass, phase and chemical composition still remains a challenge. As common for complex systems, some kind of coarse graining may be applied, leading to a continuous, position-dependent mass or size distribution, which, via its unnormalized zeroth moment, additionally provides information about the number concentration. The objective is then to find a formulation for the evolution of this distribution function. As will be elucidated below, it is not necessary to use a continuum mechanics description. Formally, it would even be possible to represent point particles by using delta functions, both, in mass or spatial space.

However, the traditional method for cloud modeling is to apply an Euler-Euler approach, where both, the ambient air and the cloud particles are considered as continuous fluids. This is currently state-of-the-art in numerical weather and climate simulations [Grabowski19]. Aqueous components in liquid or solid state are typically classified into a limited number of type categories, like cloud water, rain water, ice, snow or graupel, each of which is described by a separate distribution function. Since ice systems occur in a variety of shapes, densities and compositions, they are generally much more versatile and complex than liquid droplets. The processes of formation, growth, coagulation/sticking, melting and sublimation require sophisticated numerical methods, often including a higher number of prognostic variables.

In pioneering work, a single-moment bulk scheme was formulated, where each particle type is exclusively represented by the first moment of the mass distribution, i.e. its mass density, which is often normalized to the density of dry air [Kessler69, Liu69, Klemp78, Lin83, Rutledge83]. A consequent progression was the development of multi-moment bulk schemes, including now variables for the concentration and possibly larger moments [Ziegler85, Schoenberg Ferrier94, Milbrandt05]. With increasing computational resources, significant progress was made in the demanding simulation of ice containing systems [Chen94, Morrison08, Harrington13, Jensen17]. Current weather prediction models on regional and global scale continue to use this kind of bulk formulation [Grabowski19].

Another, more sophisticated Eulerian approach is to discretize the mass distribution, with a number of mass bins (*bin model*) [Berry67, Bleck70, Clark79, Berry74a,b,c]. In combination with LES, each spatial grid cell now contains one discretized spectrum per type category (like cloud water, rain water, etc.). This is computationally much more demanding than the previously introduced bulk schemes and implementation in three-dimensional dynamic models became feasible only in the last thirty years [Kogan91, Stevens98]. In course of steady development, they have been applied to numerous use cases (cf. an extensive review in [Khain15]) and currently provide state-of-the-art validation references for both, bulk parametrization and new approaches, like Lagrangian particle methods, introduced below. In bin models, the classified mass distributions are propagated in time, enabling interactions between particles of different size categories and providing detailed information about the cloud characteristics. Nevertheless, there remain significant numerical and conceptual issues, which shall be addressed in the following.

First, the computation of mass transfer between discrete bins is unavoidably accompanied by numerical diffusion, which leads to an unphysical broadening of the mass distribution during condensation and coalescence [Grabowski19]. Even when minimizing these artifacts by refining the mass grid and using more sophisticated methods [Tzivion87, Stevens96], there remains an erroneous broadening due to the spatial advection of particles from one grid cell to another [Morrison18]. Furthermore, it is challenging to account for spatial, turbulence-induced velocity fluctuations, which, in nature, may have large influence on the trajectory of distinct particles.

A second crucial limitation is the "curse of dimensionality", as formulated in [Grabowski19]. Bin models typically utilize a number of discretized distributions, each depending on the particle mass or size. For example, this could be a function of the cloud droplet mass. Particle growth is performed by calculating stepwise shifts of mass weight between different bins. Physically, growth by condensation does however not only depend on the droplet radius, but also on the

---

chemical composition and weight fraction of the occurring species, which evidently differs between droplets. Therefore, recent approaches introduce two-dimensional distributions, now depending on the solute mass and the water mass, i.e., provide a droplet mass spectrum for each solute mass category. This assumes that all particles contain the same chemical species. For a more realistic description, including liquid phase chemistry, it would be necessary to extend the distribution function such that its dimensions (number of arguments) include all relevant chemical components. In discretized form, this leads naively to an exponential increase ( $N_{\text{bin},1} \times N_{\text{bin},2} \times \dots$ ) in numerical operations and storage capacity. Currently, extensive simulations with more than two dimensions are computationally not feasible [Grabowski19]. For ice containing systems, condensation, freezing and aggregation/sticking additionally depends on the crystal morphology, which can be described by additional parameters for each particle. Accordingly, the required number of dimensions is even larger than for liquid droplets.

Third, turbulence effects on the particle movement need to be considered. Subgrid fluctuations in velocity lead to modifications of the trajectories, such that particles from different spatial origins occasionally end up in the same vicinity, thereby altering the local size distribution. This leads to a broadening of the spectra and to more variability by the introduction of additional modes [Cooper89]. Purely Eulerian schemes are not able to represent the trajectories of individual particles and experience major limitations, when modeling the introduced kind of turbulence effects [Grabowski13].

Fourth, the traditional approach experiences limitations in the formulation of collision-coalescence. As complex, thermodynamic systems, clouds can effectively be described by stochastic processes. This includes collision interactions between particles in the same vicinity. In Eulerian models, coagulation is typically described by a deterministic kind of the population balance equation, which can be obtained by averaging over the underlying stochastic description [Gillespie72]. Nevertheless, the hydrodynamic interaction kernel is still derived under the assumption of a well mixed cloud, i.e., that particles have equal probability to be anywhere in a well defined volume, thereby showing characteristics of a stochastic system. The deterministic description does not capture the effects of rare events, e.g., where so called "lucky droplets" undergo a series of unlikely collisions and consequently grow exceptionally fast, which might further initiate additional acceleration of the coagulation process. Considering the whole cloud, this might lead to earlier rain formation and precipitation [Kostinski05, Wilkinson16], which is not sufficiently represented in models applying the deterministic balance equation [Bayewitz74].

In consideration of the listed shortcomings coming with bulk and bin schemes, particle based, so called *Lagrangian*, models have received growing attention in the last decade after pioneering work [Andrejczuk08, Shima09, Andrejczuk10, Sölch10]. The approach is to describe the physical ensemble of cloud droplets and/or ice crystals by a number of discrete point particles, called *super-droplets* [Shima09] or *simulation particles* (SIPs) [Unterstrasser17]. Each SIP represents a multiplicity of real particles of similar kind, which, in the numerical model, are assumed to have exactly the same physical properties, including mass, position, velocity and chemical composition. When regarding the multi-dimensional distribution function, depending on position, water mass, solute masses and additional size parameters, every super-droplet is characterized by values for all arguments and should therefore cover a volume in discretized argument space, weighted by its multiplicity. During initialization, it is possible to adjust the refinement in different regions of the spectrum, enabling higher representation of sensitive areas, which turns out to be of major importance for the convergence behavior [Unterstrasser17].

Using the discrete particle approach, it is possible to avoid numerical diffusion for both of the previously described cases, i.e., during collision-coalescence and due to the transport of particle ensembles from one grid cell to another. The origin of this improvement is that particle movement and growth are no longer described by partial, but rather by ordinary differential equations

[Grabowski19]. The "curse of dimensionality" is lifted as well, because each SIP is able to contain values for all necessary parameters, enabling furthermore the modeling of chemical reactions in individual droplets, as recently presented in [Jaruga18]. Evidently, the precision of simulation results will still depend on the number of super-droplets in the domain. Opposed to the bin model, it is nevertheless not necessary to discretize the whole argument space of the distribution function, which contains negligible weight in considerably large regions. It is thus applicable to include more information about the particle characteristics and model the interactions accordingly.

Turbulence effects on individual particles can be formulated as stochastic fluctuations of the local velocity [Sölch10] and saturation [Grabowski17, Abade18]. A way to implement this in a Lagrangian cloud model is by assigning stochastic variables to each particle, which fluctuate according to generated pseudo-random numbers. Thereby, it is possible to account for the variations of size spectra due to turbulence induced irregularities in the droplet trajectories [Dziekan19]. Finally, coalescence can now be modeled as stochastic process, including all particles in a certain vicinity, which removes the limitations of a purely deterministic description. Several collision schemes have been proposed, of which the all-or-nothing method by Shima *et al.* currently shows the most promising results [Shima09, Unterstrasser17]. While the algorithm was originally proposed in linearized form to reduce computational effort, it has been shown that the full number of pair interactions can be applied, when using appropriate initialization methods [Unterstrasser17]. The preceding history, introduction and comparison of state-of-the-art bulk, bin and particle based schemes for cloud simulations are based on a concise review in [Grabowski19].

Although promising results have been achieved, Lagrangian cloud models as well as their application and validation in use cases are currently object of ongoing research and development [Arabas13, Grabowski17, Hoffmann17, Schwenkel18, Hoffmann19, Maronga19]. Especially the simulation of ice containing systems remains a major challenge due to the variety of required parameters and the complexity of involved physical processes, many of which are not entirely understood [Sölch10, Unterstrasser14, Brdar18]. Experimental observations, (semi)-analytical box model solutions and numerical bin models serve as reference, when assessing the results.

This work focuses on the numerical implementation of a particle based (Lagrangian) micro-physics model, applying the concept of simulation particles (super droplets). The scheme includes individual particle dynamics by one-way force interaction with the ambient air, according to [Crowe11]. Condensation and evaporation are realized by two-way coupled mass and heat exchange with the surrounding atmosphere, applying formulae derived in [Fukuta70]. Particle coagulations are implemented using a non-linearized form of the all-or-nothing algorithm proposed in [Shima09], as presented in [Unterstrasser17]. The current version of the developed microphysics scheme is only applicable in combination with a two-dimensional kinematic atmospheric framework. Moreover, all cloud condensation nuclei in the simulated domain are made of the same material, either ammonium sulfate or sodium chloride, and chemical reactions other than condensation and evaporation of water vapor, are not considered. Furthermore, the formation and evolution of ice crystals is not yet implemented and it is thus only possible to simulate warm (ice-free) clouds.

Nevertheless, a solid framework was developed, which can be extended with reasonably small effort to enable dynamic large-eddy simulations in three dimensions by coupling an existing fluid dynamics solver. Due to the particle based implementation structure, it is furthermore straightforward to add the treatment of multi-component aqueous chemistry, ice formation and local turbulence, as mentioned previously.

Chapter 2 provides an introduction to atmospheric physics, featuring the relevant fluid dynamical processes and transport equations for the applied model as well as the kinematic framework. Next, the discrete cloud particle model is described in Ch. 3, including dynamics, thermodynamics and collisions. Numerical discretization of configuration space, time and the concept

of super-droplets as well as the program implementation are presented in the following Ch. 4. The coagulation algorithm is evaluated in a collision box model (Ch. 5) and simulation results of the full microphysics scheme for a two-dimensional, kinematic drizzling stratocumulus test case are shown and discussed in Ch. 6. Here, the reader can furthermore find a finite size analysis regarding time steps, grid steps and number of simulation particles as well as an investigation of the influence of physical parameters, including cloud condensation nuclei material and number concentration. The thesis concludes with a summary and discussion of the results, followed by an outlook, concerning sensible improvements and extensions of the implemented program and successive research possibilities in Ch. 7.



# 2 ATMOSPHERIC PHYSICS

## 2.1 The earth's atmosphere

The earth's atmosphere is composed of a mixture of molecular gases and other particles (like airborne particulates, cloud droplets and ice crystals), which consist of multiple components (water and soluble or insoluble species) and can be in a solid, liquid or liquid-solid multi phase. Depending on the particle size, regions of the atmosphere can be regarded as a colloidal systems (called *aerosols*) with dispersed particles of dimensions up to about 1  $\mu\text{m}$  (like cloud condensation nuclei (CCNs) and artificial smokes) or as suspension with particles much larger than 1  $\mu\text{m}$  (like rain drops or dust). The size categorization is by no means strictly predefined and shall only serve as rough estimate. In the following, liquid water and all dissolved, suspended or dispersed particulates, which can effectively act as cloud condensation nuclei, will not be included in the term *air*, but considered as constituents of separately described *cloud particles*.

While the content and composition of air might vary, depending on the local atmospheric conditions, it consists always of N<sub>2</sub> (about 78 %), O<sub>2</sub> (about 21 %) and Ar (about 1 %) and might contain molecular H<sub>2</sub>O, CO<sub>2</sub> and other trace gases. The composition of the *international (dry) standard atmosphere* (ISA) defined by the international organization for standardization (ISO) is given in Table 2.1.

**Table 2.1:** ISO standard dry atmosphere composition [ISO75].

Gas	Volume fraction (%)	Molar mass (g/mol)
Nitrogen (N <sub>2</sub> )	78.084	28.013
Oxygen (O <sub>2</sub> )	20.947	31.999
Argon (Ar)	0.934	39.948
Carbon dioxide (CO <sub>2</sub> )	0.0314	44.010
Dry Air	100	28.964

Aerosol particles play a huge role in the formation of clouds, because, in nature, the majority of water droplet nucleations begins with a soluble particulate (like sodium chloride [NaCl] or ammonium sulfate [(NH<sub>4</sub>)<sub>2</sub>SO<sub>4</sub>]), which acts as CCN [Lohmann16]. The air's water vapor content can be expressed by the *saturation*  $S = e/e_s$  (here equal to the *relative humidity*), which is the ratio of the actual ambient water vapor pressure  $e$  and the *saturation pressure*  $e_s$  for a vapor-liquid phase transition. We represent the size of a particle with a certain volume by the radius  $R_p$  of an equivalent sphere.

Placing a dry CCN of a certain radius in a dry atmosphere and slowly increasing the ambient water vapor content with time, the particle's size will basically remain constant until it abruptly absorbs water vapor from the air and transforms into an aqueous solution droplet at a certain *deliquescence saturation*  $S_{\text{del}} \sim 0.8$ , as illustrated in Fig. 2.1. The phase transition is accompanied by a sudden size increase. From here on, the droplet is mainly liquid and takes up water continuously, when the ambient saturation increases. In this growth regime, each saturation level is associated

with an equilibrium radius. Keeping the saturation constant, the droplet size will stop to increase after converging to its equilibrium radius. Should the ambient saturation reach an *activation level*  $S_{act} \gtrapprox 1$  and the particle the corresponding radius  $R_{act}$ , there won't exist an equilibrium radius anymore and the droplet will keep growing, when the saturation is kept constant and even when it resides in a range  $S_{crit} < S < S_{act}$ , where  $S_{crit} \gtrapprox 1.0$ . For radii smaller than  $R_{act}$ , the particle shrinks in any case with declining saturation. In this decreasing case, the particle remains in solution, even when  $S_{del}$  is passed from above (see Fig. 2.1). Only at a lower *efflorescence saturation*  $S_{effl} \sim 0.4$ , the particle suddenly releases most of its water and crystallizes, leading to a hysteresis curve for the particle radius with ambient saturation.

For our purposes, the water uptake in the range  $S < S_{del}$  is insignificant. Therefore we will make the assumption that the cloud particles are never completely dry, but always contain at least enough water to be in (potentially highly supersaturated) aqueous solution. This is realized by setting a lower threshold for the fraction of water relative to the total particle mass. Consequently, we consider only the deliquescent case, i.e., the upper branch of the previously described hysteresis curve. Details are provided in Sec. 3.1.3.

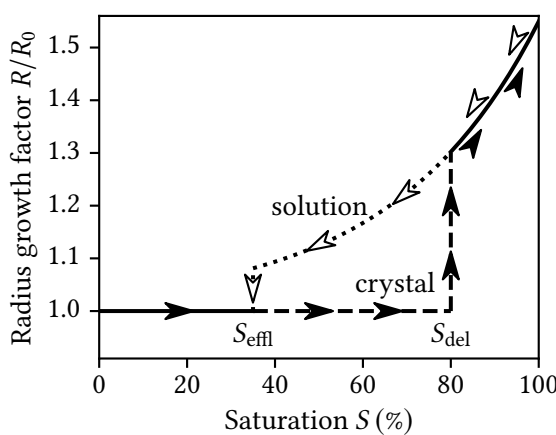


**Figure 2.1:** Idealized hygroscopic hysteresis curve of an ammonium sulfate particle with dry radius  $R_0 = 5 \mu\text{m}$ . Experimental data taken from [Biskos06] and [Haemeri00].

## 2.2 Atmospheric model: Cloud particles in a continuous air field

Figure 2.2 illustrates the size scales of relevant atmospheric components. Since the considered droplet systems are much larger than both, the air molecules and the average intermolecular distances, we choose a coupled computational fluid dynamics (CFD) - discrete particle (DPM) approach (which is traditionally called *Euler-Lagrangian* model). The surrounding air (as defined in Sec. 2.1) is treated as continuous fluid, while all particles are modeled as discrete spheres with radius  $R_p$  and mass  $m_p = 4\pi\rho_p R_p^3/3$ , where  $\rho_p$  is the particle density. In general, particles and ambient fluid interact via mass, momentum and heat exchange. As presented in Sec. 2.3, heat of condensation is distributed in the fluid system only and mass is exchanged in both directions (two-way coupling), thereby remaining conserved. On the other hand, particles gain or lose momentum due to a drag force without altering the surroundings (one-way-coupling, see Sec. 3.3). This limitation is accepted because of the used kinematic model, described in Sec. 2.4, and due to significant increase of complexity and computation time, when including the influence of the cloud droplets on the surrounding fluid field. We are however confident that the induced errors are acceptable compared to otherwise applied simplifications and approximations, as discussed in [Crowe11] and [Sommerfeld08].

In this work, the ambient thermodynamic conditions are chosen such that no ice crystallization occurs. Ice-liquid multi-phase systems are neither considered in the theory nor implemented in

the program. We are thus only able to study so called “warm” (ice-free) clouds. Summarizing, we investigate discrete aqueous solution droplets interacting with moist air as gaseous carrier fluid. Subscripts used throughout the text are given in Table 2.2. Vectors are denoted in bold, like the position vector  $\mathbf{x}$ , and the time derivative might be indicated by a dot above the corresponding variable, like the mass rate  $\dot{m}$ .

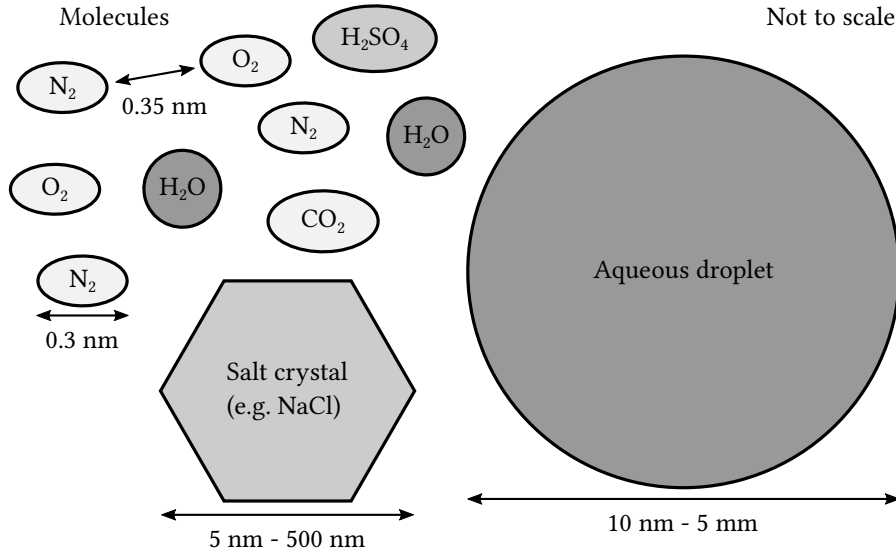


**Figure 2.2:** Size scales of the atmospheric constituents.

**Table 2.2:** Subscripts used.

Subscript	Description for	Subscript	Description for
<i>a</i>	ambience	<i>r</i>	rain (precipitating)
<i>c</i>	cloud water (not precipitating)	<i>s</i>	solute
<i>d</i>	drag	<i>sln</i>	solution
<i>f</i>	carrier fluid (air)	<i>svt</i>	solvent
<i>l</i>	liquid water	<i>v</i>	water vapor
<i>m</i>	moist	<i>w</i>	water
<i>p</i>	particle ( $\hat{=}$ aqueous droplet)		

## 2.3 Atmospheric fluid dynamics

As introduced, air is modeled as continuous fluid with density  $\rho$ , velocity  $\mathbf{u}$ , pressure  $p$  and temperature  $T$ , all of which are time dependent fields at position  $\mathbf{x}$  and time  $t$ . For a non-reactive single-phase system, the conserving dynamics of mass, momentum and energy are given by the Navier-Stokes equations (e.g. [Aris62, Ch. 6]):

$$\partial_t \rho + \nabla \cdot (\rho \mathbf{u}) = 0 \quad (2.1)$$

$$\partial_t (\rho \mathbf{u}) + \nabla \cdot (\mathbf{u} \rho \mathbf{u}^\top) = -\nabla p + \nabla \cdot \boldsymbol{\sigma}' + \rho \mathbf{f}_{\text{ext}} \quad (2.2)$$

$$T\partial_t(\rho s) + T\nabla \cdot (\mathbf{u}\rho s) = -\nabla \cdot \mathbf{j}_Q + \rho\varepsilon_E + \rho q_s. \quad (2.3)$$

The fluid may be accelerated by pressure gradients, external specific forces  $\mathbf{f}_{\text{ext}}$  (like gravity) and divergences in the friction tensor

$$\boldsymbol{\sigma}'_{ij}(\mathbf{u}) = \mu_f \left( \frac{\partial u_i}{\partial x_j} + \frac{\partial u_j}{\partial x_i} \right) + \delta_{ij} \left( \zeta_f - \frac{2}{3} \mu_f \right) \nabla \cdot \mathbf{u}, \quad (2.4)$$

which depends on the material properties *dynamic (shear) viscosity*  $\mu_f$  and *dynamic compression viscosity*  $\zeta_f$ . Here,  $\delta_{ij}$  represents the Kronecker-delta. Changes in specific entropy  $s$  arise due to divergence of the heat flux density  $\mathbf{j}_Q$ , internal or external specific heat sources  $q_s$  and energy dissipation with a specific rate of

$$\varepsilon_E = \frac{1}{\rho} \boldsymbol{\sigma}'_{ij} \frac{\partial u_j}{\partial x_i}, \quad (2.5)$$

using Einstein's sum convention.

For multi-phase/multi-component reactive species, the equations get far more complicated, depending on the level of detail and chosen assumptions. For example, the different species can be treated as interpenetrating continua [Hoffmann12, Aris62, Ch. 11] or different phases can be separated by a number of (time and space dependent) arbitrarily shaped interfaces [Zein10, Thein18]. The focus of this work shall however not lie on the treatment of continuum mechanics or thermodynamics of the fluid phase, but rather on the implementation of a model for discrete cloud particles. We will therefore focus on the relevant processes for moist air containing aqueous solution droplets and, in the following, develop the necessary theory.

### 2.3.1 Fluid field time evolution

Let  $b(\mathbf{x}, t)$  be a scalar field quantity of the fluid, belonging to a fluid parcel with mass  $dm_f$  at position  $\mathbf{x}$  at time  $t$ . A fluid parcel starting at  $(\mathbf{x}_0, t_0)$  will follow the velocity field  $\mathbf{u}(\mathbf{x}, t)$  and describe a trajectory  $\mathbf{x}(t; \mathbf{x}_0, t_0)$ . In the Lagrangian frame, we follow a specific fluid parcel and the field quantity along its trajectory is given by

$$b_{\text{Lag}}(t; \mathbf{x}_0, t_0) = b(\mathbf{x}(t; \mathbf{x}_0, t_0), t). \quad (2.6)$$

While the local (Euler) time derivative  $\partial_t b$  states the change with time when remaining at a fixed point  $\mathbf{x}$ , the Lagrangian time derivative,

$$D_t b = \lim_{\Delta t \rightarrow 0} \frac{b(\mathbf{x} + \Delta \mathbf{x}, t + \Delta t) - b(\mathbf{x}, t)}{\Delta t} = \partial_t b + \mathbf{u} \cdot \nabla b \quad (\text{with } \Delta \mathbf{x} \rightarrow \mathbf{u} \Delta t), \quad (2.7)$$

represents the change with time that our tracked fluid parcel will notice.

Consider now a continuous volume  $V(t_0)$  given at time  $t_0$ . The volume includes fluid mass  $m_f$ , liquid water mass  $m_l$  and solute mass  $m_s$ , where  $m_f = m_{\text{dry}} + m_v$  consists of dry air mass  $m_{\text{dry}}$  and water vapor mass  $m_v$ . The gaseous (fluid) components will follow the flow field  $\mathbf{u}(\mathbf{x}, t)$  directly and are considered to be well mixed in  $V$ , meaning that we find the homogeneous composition of constituents. Following the volume  $V(t)$  taken by the gaseous mass  $m_f(t, t_0)$ , which was initially included in the volume  $V(t_0)$ , the number of dry air molecules inside the volume will not change. On the other hand, the number of water vapor molecules might change due to evaporation and condensation. We define a system  $\Sigma$  by the gaseous mass  $m_f(t)$  that is included in the described volume  $V(t)$  at any time  $t$ . Note that we consider an open system with respect to  $m_v$ , but a closed (not isolated) system with respect to  $m_{\text{dry}}$ . It is therefore useful to define the *mixing ratios*  $r_k$  of

water vapor, liquid water and total water by

$$r_v := \frac{\rho_v}{\rho_{\text{dry}}}, \quad r_l := \frac{\rho_l}{\rho_{\text{dry}}} \quad \text{and} \quad r_{\text{tot}} := r_v + r_l, \quad (2.8)$$

where  $\rho_k := dm_k/dV$  is the mass density of species  $k$ . All properties without particular labeling refer to the defined system  $\Sigma$ .

Let  $B$  be an extensive fluid property. We shall differentiate between volumetric densities  $b_V = dB/dV$  and specific (*mass based*) quantities  $b = dB/dm_f$  with the conversion  $b_V = \rho_f b$ . Our system volume  $V(t)$  contains

$$B(t) = \int_{V(t)} dV \rho_f(\mathbf{x}, t) b(\mathbf{x}, t) \quad (2.9)$$

of quantity  $B$  at time  $t$ . Since the volume surfaces will move according to  $\mathbf{u}(\mathbf{x}, t)$ , one needs to consider the expansion and deformation of the volume itself, when regarding the change of  $B(t)$  with time:

$$\frac{d}{dt} B(t) = \frac{d}{dt} \int_{V(t)} dV \rho_f(\mathbf{x}, t) b(\mathbf{x}, t) = \int_{V(t)} dV [\partial_t(\rho_f b) + \nabla \cdot (\rho_f b \mathbf{u})]. \quad (2.10)$$

In the following, expressions are derived for the dynamics of mass and energy. Fluid momentum is not treated at this point, because we use a kinematic framework for the velocity field, presented in Sec. 2.4.

### 2.3.2 Conservation of mass

When  $B$  is the dry mass  $m_{\text{dry}}$ , the intensive property is  $b = \rho_{\text{dry}}/\rho_f$  and

$$\frac{d}{dt} m_{\text{dry}} = \int_{V(t)} dV [\partial_t(\rho_{\text{dry}}) + \nabla \cdot (\rho_{\text{dry}} \mathbf{u})] = 0, \quad (2.11)$$

which must hold for arbitrary volumes  $V(t)$  and is thus equivalent to (2.1), because we constructed the system by definition such that the dry air mass in the volume  $V(t)$  will not change.

The only way water vapor mass in the volume can change is by condensation and evaporation. Denoting the total condensed mass per time in  $V$  as *condensation mass rate*  $\Phi_{\text{con}}$  and the condensed mass per volume and time as *condensation (density) rate*  $\phi_{\text{con}}$ , we can write

$$\frac{d}{dt} m_v = \frac{d}{dt} m_{v,\text{con}} =: -\Phi_{\text{con}} = - \int_{V(t)} dV \phi_{\text{con}}. \quad (2.12)$$

The condensation rate will be calculated from the local saturation and properties of the cloud droplets in the considered volume (see Sec. 3.2). Combining the previous equations leads to

$$\frac{d}{dt} m_f = \frac{d}{dt} (m_{\text{dry}} + m_v) = \frac{d}{dt} m_v = \int_{V(t)} dV [\partial_t(\rho_v) + \nabla \cdot (\rho_v \mathbf{u})] = - \int_{V(t)} dV \phi_{\text{con}}. \quad (2.13)$$

By comparison of the integrands and combination of  $\rho_v = \rho_{\text{dry}} r_v$ , (2.7) and (2.11), we obtain the continuity equation for water vapor density,

$$\partial_t \rho_v + \nabla \cdot (\rho_v \mathbf{u}) = \rho_{\text{dry}} D_t r_v = -\phi_{\text{con}}, \quad (2.14)$$

with mass flux density  $\mathbf{j}_v := \rho_v \mathbf{u}$ .

### 2.3.3 Conservation of energy

We will make three major assumptions in the description of exchange and advective distribution of heat. First, we neglect heat exchange by radiation and by dissipation due to friction (ideal flow). Furthermore, heat conduction is only considered for the transport of latent heat from a droplet surface into the environment. The heat entry into the System  $m_f(t)$  is described exclusively by the latent enthalpy change  $\delta\mathcal{H}_{\text{con}} := \delta\mathcal{U}_{\text{con}} + p\delta V_{\text{con}} = L_v\delta m_{\text{con}} = -L_v\delta m_v$  during condensation of mass ( $-\delta m_v$ ) in  $V(t)$ , where  $\mathcal{U}$  is the internal energy and  $L_v$  is called the (*specific*) *heat of vaporization*. The associated heat is converted to internal energy of the fluid mass and expansion work, as given by (2.22). The approach (according to Sec. 3.2) is that all the heat released at the droplet surface is transported away into the environment, while the droplet surface immediately approaches a steady state temperature  $T_{ps}$  at the current location (see (3.15)). Further, evaporating particles do not remove any internal energy from the fluid phase and, other than its surface, the droplet “bulk” is assumed to always be in thermal equilibrium with the ambient fluid.<sup>1</sup>

Second, the condensation process is considered to be reversible, leading to  $\delta q = T \, ds$  for the relation of specific heat and total change in specific fluid entropy. Third, we will assume moist air to behave like an ideal gas, for which the specific enthalpy  $h_e$  depends only on temperature [Sonntag03],

$$dh_e = c_m \, dT, \quad (2.15)$$

where the specific isobaric heat capacity of moist air is given by

$$c_m = \frac{\rho_{\text{dry}} c_{\text{dry}} + \rho_v c_v}{\rho_{\text{dry}} + \rho_v} = c_{\text{dry}} \frac{1 + r_v c_v / c_{\text{dry}}}{1 + r_v} \approx c_{\text{dry}} \left[ 1 + (c_v / c_{\text{dry}} - 1) r_v \right], \quad (2.16)$$

with the heat capacity ratio of water vapor and dry air,  $c_v / c_{\text{dry}} \approx 1.897$ . Furthermore, we apply the ideal gas equation of state,

$$p = p_{\text{dry}} + e = \rho_{\text{dry}} \tilde{R}_{\text{dry}} T + \rho_v \tilde{R}_v T = \rho_{\text{dry}} \tilde{R}_{\text{dry}} (1 + r_v / \epsilon_v) T = \rho_m \tilde{R}_m T, \quad (2.17)$$

where in our case  $\rho_m = \rho_f$  and the specific gas constant of moist air  $\tilde{R}_m$  can be approximated for small  $r_v$  as

$$\tilde{R}_m = \frac{\rho_{\text{dry}} \tilde{R}_{\text{dry}} + \rho_v \tilde{R}_v}{\rho_{\text{dry}} + \rho_v} = \tilde{R}_{\text{dry}} \frac{1 + r_v / \epsilon_v}{1 + r_v} \approx \tilde{R}_{\text{dry}} (1 + \epsilon'_v r_v), \quad (2.18)$$

with the specific gas constant ratio of dry air and water vapor

$$\epsilon_v := \tilde{R}_{\text{dry}} / \tilde{R}_v \approx 0.622 \quad \text{and} \quad \epsilon'_v = \epsilon_v^{-1} - 1 \approx 0.608. \quad (2.19)$$

We further define

$$\kappa_{\text{dry}} := \tilde{R}_{\text{dry}} / c_{\text{dry}} \approx 0.286 \quad (2.20)$$

and, approximated for small  $r_v$ ,

$$\kappa_m = \frac{\tilde{R}_m}{c_m} = \frac{\tilde{R}_{\text{dry}}}{c_{\text{dry}}} \frac{1 + r_v \tilde{R}_v / \tilde{R}_{\text{dry}}}{1 + r_v c_v / c_{\text{dry}}} \approx \frac{\tilde{R}_{\text{dry}}}{c_{\text{dry}}} \left[ 1 + r_v \left( \frac{\tilde{R}_v}{\tilde{R}_{\text{dry}}} - \frac{c_v}{c_{\text{dry}}} \right) \right] \approx \kappa_{\text{dry}} (1 - 0.289 r_v). \quad (2.21)$$

---

<sup>1</sup>See footnote 2 on page 13 for a discussion.

Combining (2.15), (2.17) and the first law of thermodynamics,<sup>2</sup>

$$dh_e = \delta q + \mathcal{V} dp = T ds + \frac{1}{\rho_f} dp, \quad (2.22)$$

with specific volume  $\mathcal{V} = dV/dm_f$  and solving for  $ds$  leads to

$$ds = \frac{\delta q}{T} = c_m \frac{dT}{T} - \tilde{R}_m \frac{dp}{p} = c_m d(\ln T) - \tilde{R}_m d(\ln p) = c_m d(\ln \Theta_m), \quad (2.23)$$

where

$$\Theta_m := T \left( \frac{p_*}{p} \right)^{\kappa_m} \quad (2.24)$$

is the moist potential temperature and we define the reference pressure at  $p_* := 1000$  hPa. For an adiabatic process,  $\Theta_m$  is constant and we obtain the relation

$$\frac{T}{\Theta_m} = \left( \frac{p}{p_*} \right)^{\kappa_m}. \quad (2.25)$$

Under the given assumptions, the heat entry in (2.22) is given by

$$\delta q = \frac{d\mathcal{H}_{\text{con}}}{m_f} = -\frac{VL_v d\rho_v}{V\rho_f} = -\frac{L_v}{1+r_v} dr_v, \quad (2.26)$$

which, with (2.14), yields the heat rate per time and fluid mass

$$D_t q = -\frac{L_v}{1+r_v} D_t r_v = \frac{L_v}{\rho_{\text{dry}} (1+r_v)} \phi_{\text{con}}, \quad (2.27)$$

where  $r_v < 1\%$  is often neglected in the denominator (see e.g. [Curry99]). Considering (2.23), the reversible entropy rate of a moving air parcel is given by  $D_t s = (D_t q) / T = c_m D_t (\ln \Theta_m)$ . Substituting the heat rate from (2.27) leads to the transport equation for potential temperature,

$$\frac{1}{\Theta_m} D_t \Theta_m = \frac{1}{\Theta_m} [\partial_t \Theta_m + \mathbf{u} \cdot \nabla \Theta_m] = \frac{\dot{q}}{c_m T} = \frac{L_v \phi_{\text{con}}}{c_m \rho_{\text{dry}} (1+r_v) T}. \quad (2.28)$$

---

<sup>2</sup> The applied model is commonly used for atmospheric simulations with discrete particles [Shima09, Arabas15], but has some inaccuracies. Since we consider a closed system for  $m_{\text{dry}}$ , but an open system for  $m_v$ , a more complete formulation of the first law is  $dh = \delta q + \mathcal{V} dp + \mu_c d(n_v)/\rho_f$ , where  $n_v$  and  $\mu_c$  are the number density of water vapor molecules and the chemical potential of the mixture, respectively. Furthermore, only part of the heat of vaporization would remain in the fluid part (concerning the formulation of  $\delta q$  in this case), while another part is distributed onto the liquid particles. The simplification made here has its origins in the traditional Euler-Euler continuum approach, where the liquid part is described as part of the fluid and states that all of the enthalpy stays in the considered fluid system, when water molecules condense. This would mean that liquid particles also follow the velocity field, which is not the case when heavier particles leave the field trajectories, e.g., due to inertia effects. In sophisticated Eulerian cloud models, the sedimentation of liquid water is considered, e.g., by parametrization of the additional falling velocity and there are approaches to account for the corresponding energy transport. It shall be emphasized that the energy balance of the whole system is not violated by the used model. It is only the distribution of energy, which suffers due to the assumption that the internal energy of the liquid particles remains in the fluid and is not transported along their trajectories. This effect should be acceptable due to the small portion of liquid water mass compared to the total mass ( $r_l \sim 1 \times 10^{-3}$ ). See also, e.g., [Bryan08] for a discussion of thermodynamic variables.

## 2.4 Kinematic framework

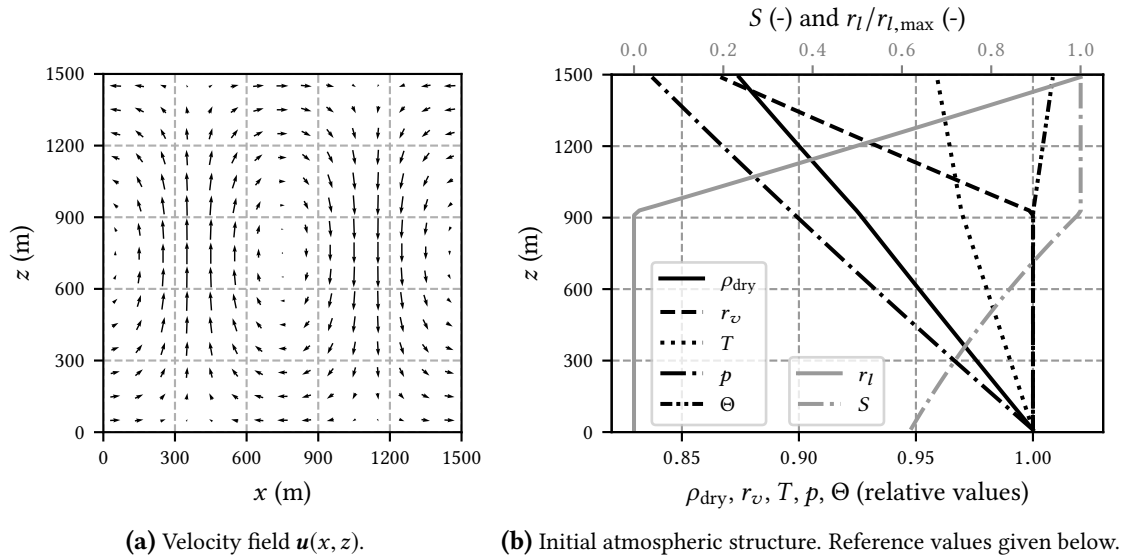


**Figure 2.3:** Kinematic framework motivated by the ICMW 2012 test case 1. (a) The velocity field is prescribed, stationary and periodic in  $x$ . (b) The initial configuration is set up by saturation adjustment under homogeneous total water content and liquid potential temperature. The initial atmospheric state variables  $\rho_{\text{dry}}(z)$ ,  $T(z)$  and  $p(z)$  decrease monotonically with height, while dry potential temperature  $\Theta$  and vapor mixing ratio  $r_v$  are nearly constant below 900 m, when  $S$  reaches unity and significant condensation begins, leading subsequently to monotonic increase in  $r_l$  and  $\Theta$  with height. The reference values at  $z = 10$  m are  $\rho_{\text{dry},10} = 1.2 \text{ kg/m}^3$ ,  $r_{v,10} = 7.5 \text{ g/kg}$ ,  $T_{10} = 290 \text{ K}$ ,  $p_{10} = 1014 \text{ hPa}$  and  $\Theta_{10} = 290 \text{ K}$  and the maximum liquid mixing ratio amounts to  $r_{l,\max} = 1 \text{ g/kg}$ .

Since the focus of this work lies on the implementation of a discrete cloud particle model, we utilize a two-dimensional *kinematic framework* for the ambient air, presented in Fig. 2.3a. The time dependence of the fluid velocity field is not calculated by solving the dynamic equations, but directly prescribed by a function  $\mathbf{u}(x, t)$ . Three-dimensional space is defined by the orthonormal basis  $\{\hat{\mathbf{e}}_x, \hat{\mathbf{e}}_y, \hat{\mathbf{e}}_z\}$  and the position vector is  $\mathbf{x} = x \hat{\mathbf{e}}_x + y \hat{\mathbf{e}}_y + z \hat{\mathbf{e}}_z$ . Following convention, two-dimensional description means here that all fields are translation-invariant in  $y$  and it is thus sufficient to consider the subspace spanned by  $\{\hat{\mathbf{e}}_x, \hat{\mathbf{e}}_z\}$ .

In the present study, we use test case 1 of the 8<sup>th</sup> international cloud modeling workshop (ICMW) 2012 [Muhlbauer13], where the dry air mass flux density

$$\mathbf{j}_{\text{dry}}(x, z) = \rho_{\text{dry}} \mathbf{u} = \nabla \times (\psi(x, z) \hat{\mathbf{e}}_y) \quad (2.29)$$

is stationary and defined by the stream function

$$\psi(x, z) = -j_{\max} \frac{X}{\pi} \sin\left(\pi \frac{z}{Z}\right) \cos\left(2\pi \frac{x}{X}\right), \quad (2.30)$$

with equal domain width and height  $X = Z = 1500$  m and maximum flux  $j_{\max} = 0.6 \text{ kg}/(\text{m}^2 \text{ s})$ . The system has periodic boundaries in the horizontal direction ( $x$ ) and open boundaries in the vertical direction ( $z$ ). Particles are allowed to leave the domain by sedimentation, when hitting the earth surface ( $z = 0$ ).

Since the flux field is divergence free,  $\nabla \cdot \mathbf{j}_{\text{dry}} = 0$ , we conclude from (2.11) that velocity field

and dry air density, shown in Fig. 2.3b, are stationary as well:

$$\partial_t \rho_{\text{dry}}(x, z) = 0 \quad \text{and} \quad \mathbf{u}(x, z) = \mathbf{j}_{\text{dry}} / \rho_{\text{dry}}. \quad (2.31)$$

### 2.4.1 Initial atmospheric configuration

The initial atmosphere is constructed under horizontally uniform, hydrostatic conditions,

$$\frac{dp}{dz} = -\rho_{\text{tot}} g = -(\rho_{\text{dry}} + \rho_v + \rho_l + \rho_s) g \approx -(\rho_{\text{dry}} + \rho_v + \rho_l) g = -\rho_{\text{dry}} (1 + r_v + r_l) g, \quad (2.32)$$

where  $g$  is the earth's gravitational constant. For the chosen test case, the task at hand is to integrate (2.32) with initial conditions

$$z_0 = 0 \text{ m}, \quad p_0 = p(z_0) = 1015 \text{ hPa}, \quad (2.33)$$

and under the restrictions

$$r_{\text{tot}}(x, z) = r_v + r_l = 7.5 \text{ g/kg} = \text{const.} \quad \text{and} \quad \Theta_l(x, z) = 289 \text{ K} = \text{const.}, \quad (2.34)$$

where the liquid water potential temperature  $\Theta_l$  is defined as *the moist potential temperature that an air parcel attains, when all of its liquid water evaporates due to reversible moist decent*. An approximate formulation was given in [Betts73]:

$$\Theta_l \approx \Theta_m \exp \left( -\frac{L_v r_l}{c_m T} \right). \quad (2.35)$$

However, we won't use this approximation, but start with a moist atmosphere without any liquid water and thereafter let all of the excess water vapor condense in an isobaric process until saturation is reached everywhere, leading to the configuration shown in Fig. 2.3b. The corresponding algorithm is presented in Sec. 6.1.

#### INITIAL ATMOSPHERE WITHOUT LIQUID WATER

Setting up an atmosphere with the given initial conditions  $r_{\text{tot}} = \text{const}$ ,  $\Theta_l = \text{const}$ , but without any liquid water, we obtain  $r_{\text{tot}} = r_v$  and  $\Theta_l = \Theta_m$  everywhere. Combining  $T = \Theta_m (p/p_*)^{\kappa_m(r_v)}$ ,  $\kappa_m(r_v) = \kappa_m(r_{\text{tot}}) =: \kappa_t$ , (2.17) and (2.32) leads to

$$1. \quad \frac{dp}{dz} = -\rho_{\text{dry}} (1 + r_{\text{tot}}) g \quad (2.36)$$

$$2. \quad p = \rho_{\text{dry}} \tilde{R}_{\text{dry}} \Theta_l \left( \frac{p}{p_*} \right)^{\kappa_t} \left( 1 + \frac{r_{\text{tot}}}{\epsilon_v} \right). \quad (2.37)$$

After eliminating  $\rho_{\text{dry}}$  and defining

$$\beta_t := \frac{\kappa_t g (1 + r_{\text{tot}})}{\tilde{R}_{\text{dry}} \Theta_l (1 + r_{\text{tot}}/\epsilon_v)}, \quad (2.38)$$

we obtain the differential equation

$$\frac{dp}{dz} = -\frac{(p_*)^{\kappa_t} \beta_t}{p^{\kappa_t-1} \kappa_t}, \quad (2.39)$$

which can be integrated to yield

$$\frac{\kappa_t}{(p_*)^{\kappa_t}} \int_{p_0}^p dp' (p')^{\kappa_t-1} = \left( \frac{p}{p_*} \right)^{\kappa_t} - \left( \frac{p_0}{p_*} \right)^{\kappa_t} = -\beta_t(z - z_0). \quad (2.40)$$

Using this result, we can formulate liquid-free initial profiles of environmental pressure, temperature and density, which will be used when constructing the initial atmospheric configuration in Sec. 6.1:

$$\begin{aligned} 1. \quad \left( \frac{p}{p_*} \right) &= \left[ \left( \frac{p_0}{p_*} \right)^{\kappa_t} - \beta_t(z - z_0) \right]^{1/\kappa_t} \\ 2. \quad \left( \frac{T}{\Theta_l} \right) &= \left( \frac{p_0}{p_*} \right)^{\kappa_t} - \beta_t(z - z_0) \\ 3. \quad \rho_{\text{dry}} = \frac{\left( \frac{p}{p_*} \right) p_* \beta_t}{\left( \frac{T}{\Theta_l} \right) g \kappa_t} &= \frac{p_* \beta_t}{g \kappa_t} \left[ \left( \frac{p_0}{p_*} \right)^{\kappa_t} - \beta_t(z - z_0) \right]^{1/\kappa_t-1} \\ 4. \quad \Theta_m = \Theta_l &= 289.0 \text{ K} \\ 5. \quad r_v = r_{\text{tot}} &= 7.5 \text{ g/kg} \\ 6. \quad r_l &= 0. \end{aligned} \quad (2.41)$$

#### 2.4.2 Transport equations for energy and water vapor in the kinematic framework

Since  $D_t \rho_{\text{dry}} = 0 = \partial_t \rho_{\text{dry}}$ , it is convenient to define the dry potential temperature

$$\Theta := T \left( \frac{p_*}{p_{\text{dry}}} \right)^{\kappa_{\text{dry}}} \quad (2.42)$$

as state variable with

$$d(\ln \Theta) = c_{\text{dry}} d(\ln T) - \tilde{R}_{\text{dry}} d(\ln p_{\text{dry}}) = \frac{dT}{T} (1 - \kappa_{\text{dry}}), \quad (2.43)$$

where we made use of  $d\rho_{\text{dry}} = 0$  and thus

$$\frac{dp_{\text{dry}}}{p_{\text{dry}}} = \frac{d(\rho_{\text{dry}} \tilde{R}_{\text{dry}} T)}{\rho_{\text{dry}} \tilde{R}_{\text{dry}} T} = \frac{dT}{T}. \quad (2.44)$$

Considering further  $d\rho_m = d\rho_v = \rho_{\text{dry}} dr_v$ , we derive

$$\frac{dp}{\rho_m} = \frac{1}{\rho_m} \left( \tilde{R}_m T d\rho_m + \rho_m \tilde{R}_m dT \right) = \frac{\tilde{R}_m T}{1 + r_v} dr_v + \tilde{R}_m dT, \quad (2.45)$$

which leads with (2.22) and (2.26) to

$$(c_m - \tilde{R}_m) dT = \frac{L_v - \tilde{R}_m T}{1 + r_v} d(-r_v). \quad (2.46)$$

Substituting in (2.43) yields

$$d(\ln \Theta) = \frac{1}{c_{\text{dry}}} \left[ \frac{1}{1 + \frac{c_v - \tilde{R}_v}{c_d - \tilde{R}_{\text{dry}}} r_v} \right] \left[ \frac{L_v}{T} \left( 1 - \frac{\tilde{R}_m}{L_v/T} \right) \right] d(-r_v). \quad (2.47)$$

Regarding that  $\tilde{R}_m/(L_v/T) \approx 3\%$ , we neglect the corresponding term to arrive at

$$\frac{1}{\Theta} D_t \Theta = \frac{1}{\Theta} [\partial_t \Theta + \mathbf{u} \cdot \nabla \Theta] = -\frac{L_v}{c_{\text{dry}} \rho_{\text{dry}} (1 + \alpha_v r_v) T} D_t r_v = \frac{L_v \phi_{\text{con}}}{c_{\text{dry}} \rho_{\text{dry}} (1 + \alpha_v r_v) T}, \quad (2.48)$$

which (for  $(1 + \alpha_v r_v) \approx 1$ ) is also used in [Grabowski96] and [Arabas15] and differs from (2.28) by the definition of  $\Theta$ , using dry versions of pressure and adiabatic coefficient  $\kappa_{\text{dry}}$ , and by replacing  $c_m (1 + r_v)$  with  $c_{\text{dry}} (1 + \alpha_v r_v)$ , where  $\alpha_v := (c_v - \tilde{R}_v)/(c_d - \tilde{R}_{\text{dry}}) \approx 2$ .

## 2.5 Transport equations for the atmosphere

Finally, we multiply (2.48) by  $\rho_{\text{dry}} \Theta$  and make use of  $\nabla \cdot \mathbf{j}_{\text{dry}} = 0$  to write (2.48) in the convenient form,

$$\partial_t (\rho_{\text{dry}} \Theta) + \nabla \cdot (\mathbf{j}_{\text{dry}} \Theta) = \frac{L_v}{c_{\text{dry}} (1 + \alpha_v r_v)} \frac{\Theta}{T} \phi_{\text{con}}, \quad (2.49)$$

which has the same structure as (2.14) formulated for  $r_v$ ,

$$\partial_t (\rho_{\text{dry}} r_v) + \nabla \cdot (\mathbf{j}_{\text{dry}} r_v) = -\phi_{\text{con}}. \quad (2.50)$$

The condensation rate  $\phi$  depends on the presence of cloud droplets and is given in Sec. 3.2.1. In the following, we use the state variables  $G := (\Theta, r_v)$  and the corresponding transport equations (2.49) and (2.50) to describe the evolution of the atmosphere. All remaining thermodynamic properties can always be calculated from the chosen state variables, e.g. by

$$\frac{p_{\text{dry}}}{p_*} = \left[ \frac{\rho_{\text{dry}} R_{\text{dry}} \Theta}{p_*} \right]^{(1/(1-\kappa_{\text{dry}}))}, \quad p = p_{\text{dry}} \left( 1 + \frac{r_v}{\epsilon_v} \right), \quad T = \Theta \left( \frac{p_{\text{dry}}}{p_*} \right)^{\kappa_{\text{dry}}}. \quad (2.51)$$



# 3 MODELING DISCRETE CLOUD DROPLETS

As introduced, cloud particles are modeled as spheres of radius  $R_p$ , interacting with the surrounding continuous air field by forces, mass condensation/evaporation and heat distribution. Furthermore, a droplet of mass  $m_p$  is accelerated by gravity  $F_g = m_p \mathbf{g}$ , with constant  $\mathbf{g} = -g \hat{\mathbf{e}}_z$ . In the present model, a particle consists of water with mass  $m_w$  and one solute (either ammonium sulfate or sodium chloride) with mass  $m_s$ . Multi-component species and chemistry are not considered. The total particle mass is thus given by  $m_p = m_w + m_s$ . The approach is to describe each particle as an open thermodynamic system with a control volume, the surface of which is given by the phase separation of liquid and gas phase (i.e. the droplet surface).

Considering a typical sodium chloride CCN with dry radius  $R_{\text{dry}} = 10 \text{ nm}$ , the number of molecules amounts to  $1 \times 10^5$  for the dry particle and exceeds  $1 \times 10^6$  for the activation radius  $R_{\text{act}} > 21 \text{ nm}$ . The droplet can thus appropriately be considered as an thermodynamic ensemble. Additionally, the solute mass fraction of the whole droplet is  $m_s/m_p < 3 \times 10^{-4}$  for  $R_p > 200 \text{ nm}$  and will therefore be neglected, when calculating the particle mass, volume and number of molecules for sufficiently large particle radii. However, it should be noted that the number of solute molecules plays a huge role for the saturation pressure at the particle surface and can not be neglected, when considering mass exchange.

As an open thermodynamic system, the droplet exchanges water molecules with the surrounding air. Since the solute is strongly bound in the solution and its isolated state of aggregation would be the solid phase, no solute molecules join or leave the cloud particles by condensation or evaporation. The particles' mass evolution due to phase transitions is thus exclusively given by the change in the amount of water ( $\dot{m}_p = \dot{m}_w$ ). The amount of solute in any droplet may only change, when coagulating with other particles.

In equilibrium, the uptake and release of water molecules balance on average and the macroscopic total number of particles remains the same (when averaging the thermodynamic fluctuations), as shown in Fig. 3.2a (top). In the atmosphere however, we most often find non-equilibrium conditions due to transport of particles to different regions and explicitly time dependent changes in the environment. The equilibrium state is described by Köhler-theory and mass transport is modeled by a diffusion approach with molecular kinetics corrections at the droplet surface. Again, we take water vapor to be an ideal gas with partial pressure

$$e = \rho_v \tilde{R}_v T . \quad (3.1)$$

## 3.1 Saturation pressure at the droplet surface

While it is not the purpose of this work to develop a detailed theory of phase transitions, the underlying physical concepts and assumptions shall nevertheless be presented at this point, mostly following [Lohmann16]. The gas-liquid saturation pressure  $e_s$  for a phase transition of water vapor over an infinite flat water surface is illustrated in the phase diagram (Fig. 3.1) and can be described by the Clausius-Clapeyron equation,

$$\frac{de_s}{dT} = \frac{L_v e_s}{\tilde{R}_v T^2} , \quad (3.2)$$

which was used by [Rogers89] to approximate the saturation pressure for our temperature range,

$$e_s(T) = A_w \exp(-B_w/T), \quad (3.3)$$

with empirical constants  $A_w = 2.53 \times 10^{11}$  Pa and  $B_w = 5420$  K.

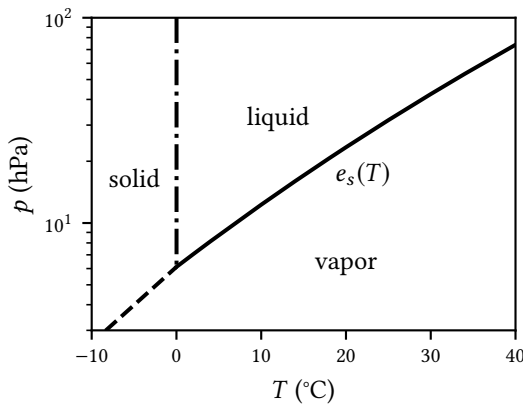


**Figure 3.1:** Phase diagram of water in the relevant temperature range. The saturation pressure  $e_s(T)$  of water vapor over an infinite flat liquid water surface separates liquid and vapor phases. Values taken from [Lohmann16].

### 3.1.1 Surface tension effect (Kelvin equation)

The systems' probability  $P_{\text{sys}}(\Sigma') \propto \exp[-\mathcal{G}(\Sigma')/(k_B T)]$  to be in a state  $\Sigma'$  is proportional to the exponential of negative Gibbs free energy  $\mathcal{G} = \mathcal{H} - T \mathcal{S}$ , where  $\mathcal{H}$  and  $\mathcal{S}$  are the total enthalpy and entropy, respectively (not to be confused with the saturation  $S$ ). The system is thus driven to stable minima of  $\mathcal{G}$  while reaching equilibrium. When liquid and vapor phase are separated by a flat extended interface, the change in Gibbs free energy can be shown to be  $\Delta\mathcal{G} = \Delta N_l (\mu_{c,l} - \mu_{c,v}) = -\Delta N_l k_B T \ln(e/e_s(T))$  during transition of  $\Delta N_l$  molecules from vapor to liquid, where  $\mu_{c,k}$  is the chemical potential of phase  $k$  [Pruppacher97]. Equilibrium is reached, when the rate of water molecules leaving and entering the liquid phase is equal, as depicted in Fig. 3.2a (top).

Considering now a pure gas phase at some pressure and temperature, liquid clusters with  $N_l$  molecules might form due to thermodynamic fluctuations (Fig. 3.2a (bottom)). The question is, if these spontaneously formed clusters remain stable, grow in size or dissolve again into vapor. Additionally to a change in chemical potential, the formation of the finite droplet surface  $A_s$  requires energy  $\Delta\mathcal{G}_s = A_s \sigma_p$  with *surface tension*  $\sigma_p$ , illustrated in Fig. 3.2b. Rearranging terms for the droplet radius  $R_p$  leads to [Lohmann16]

$$\Delta\mathcal{G} = -\frac{4\pi}{3} \rho_l \tilde{R}_v T \ln(S) R_p^3 + 4\pi \sigma_p R_p^2. \quad (3.4)$$

For a given saturation  $S > 1$ , the function  $\Delta\mathcal{G}(R_p)$  shows a maximum at the *critical radius*  $R_{\text{cr}}$ . Without surface tension effect, the global maximum would be at  $R_{\text{cr}} = 0$ . Considering the finite size, the critical radius is shifted to  $R_{\text{cr}} = 2\sigma_p/(\tilde{R}_v T \rho_p \ln(S)) > 0$ . Clusters with  $R_p < R_{\text{cr}}$  are not stable and will most likely dissolve into vapor. The saturation vapor pressure over a droplet with radius  $R_p$  surrounded by air is thus larger than over a flat surface, which is expressed by the Kelvin-equation

$$\frac{e_s(T, R_p)}{e_s(T, R_p = \infty)} = \exp\left(\frac{a_K}{R_p}\right), \quad \text{where} \quad a_K = \frac{2\sigma_p}{\rho_p \tilde{R}_v T}. \quad (3.5)$$

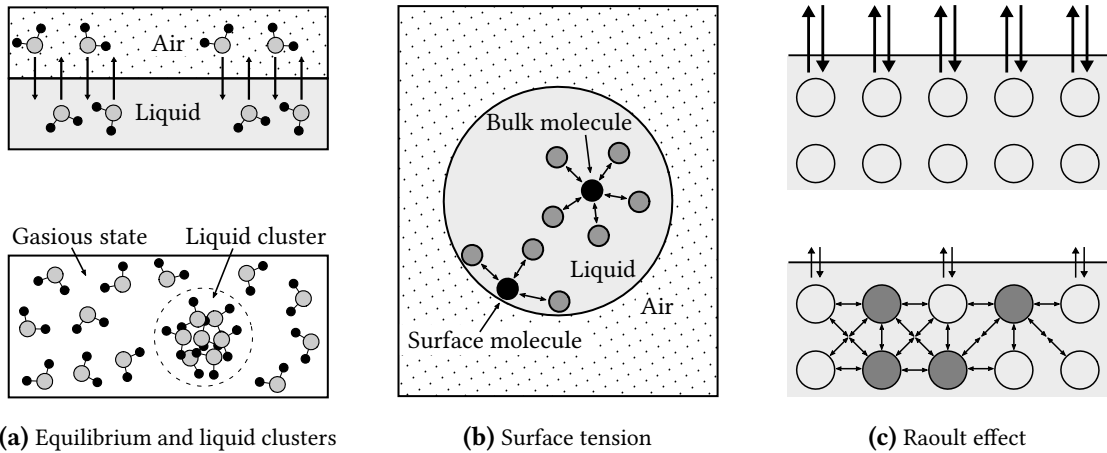


**Figure 3.2:** (a) Phase transition of water for an existing flat surface and cluster formation in surrounding vapor phase. (b) Surface tension effect: While a bulk molecule on average experiences the same attractive forces from all directions, a surface molecule misses attractive forces in direction of the water surface. This leads to a contraction and increase of the pressure inside of the droplet. Moreover, additional energy must be provided during the formation of the surface. (c) For pure water, the gain and loss rates are equal and indicated by the arrows (top). On average, we find a homogeneous density of water molecules at the surface. For a solution, the exchange rates are reduced (smaller arrows) by two factors. First, part of the surface is occupied by molecules of other species. Here, no water molecules can evaporate. Second, the other substance might introduce additional attractive interactions, which increase the required energy to leave the liquid state (bottom). Overall, the effect is a decreased saturation vapor pressure over the solution surface.

### 3.1.2 Solute effect (Raoult relation)

In contrast to the Kelvin effect, the presence of solute molecules may hinder the evaporation process and thus decrease the saturation pressure of an aqueous solution, as illustrated in Fig. 3.2c. This is expressed by the *water activity*,

$$a_w = \frac{e_s(T, R_p = \infty, N_s)}{e_s(T, R_p = \infty, N_s = 0)}, \quad (3.6)$$

for  $N_s$  effectively dissolved ions. Among several approaches for the water activity of solution droplets, we use Raoult's law,

$$a_w = \frac{N_w}{N_s + N_w}, \quad (3.7)$$

where  $N_w$  is the number of water molecules.

The degree of ionic dissociation states how many ions are dissolved on average for each dry molecule of the solute and is given by the van't Hoff factor  $i_s = \phi_s v_{ion,s}$ , where the *osmotic coefficient*  $\phi_s$  describes the deviation from ideal solvent behavior and  $v_{ion,s}$  is the *stoichiometric ionization coefficient* (e.g.  $v_{ion,s} = 2$  for  $\text{NaCl} \rightarrow \text{Na}^+ + \text{Cl}^-$ ). While we find  $N_w = N_A m_w / M_w$  molecules in water with mass  $m_w$ , a given solute mass  $m_s$  contains  $N_{s,dry} = N_A m_s / M_s$  molecules in dry state and

$$N_s = \frac{i_s N_A m_s}{M_s} \quad (3.8)$$

effectively dissolved ions, where  $M_w$  and  $M_s$  are the molar masses of water and solute and  $N_A$  is

Avogadro's number. After substituting in Eq. (3.7), the water activity is given by

$$a_w = \frac{m_w}{m_w + m_s i_s M_w / M_s} . \quad (3.9)$$

For a dilute bulk solution, where the solute mass fraction  $w_s := m_s/m_p$  is much smaller than one, NaCl dissolves completely in water and thus  $\phi_s = 1$  and  $i_{\text{NaCl}} = 2$ . In droplets of finite size and for large solute concentrations  $w_s \gtrapprox 0.1$ , the osmotic coefficient may differ from the ideal value, which is shown in the appendix (Fig. A.1). To include this effect, we approximate the van't Hoff factor  $i_s(w_s)$  for NaCl with a linear fit to data given by [Archer92]. For  $(\text{NH}_4)_2\text{SO}_4$  we use a 4<sup>th</sup> order polynomial parametrization  $a_w(w_s)$  by [Tang97].

### 3.1.3 Köhler equation

We finally arrive at the Kelvin-Raoult relation (also known as Köhler-equation) for the saturation pressure over a solution droplet with finite radius  $R_p$ :

$$\frac{e_s(T, R_p, N_s)}{e_s(T, R_p = \infty, N_s = 0)} = a_w(w_s) \exp\left(\frac{a_K}{R_p}\right) = \frac{m_w}{m_w + m_s i_s(w_s) M_w / M_s} \exp\left(\frac{2 \sigma_p}{\rho_p \tilde{R}_v T R_p}\right) . \quad (3.10)$$

## 3.2 Mass diffusion and heat conduction

From here on, we follow the derivation by [Fukuta70] for mass and heat exchange, trying to state applied assumptions and simplifications. Starting point are the equations for diffusion and heat conduction in the region  $r := |\mathbf{r}| > R_p$ ,

$$\frac{\partial \rho_v}{\partial t} + \nabla \cdot \mathbf{j}_v = \frac{\partial \rho_v}{\partial t} + \nabla \cdot (-D_v \nabla \rho_v) = 0 , \quad (3.11)$$

$$\rho_f c_m \frac{\partial T}{\partial t} + \nabla \cdot \mathbf{j}_Q = \rho_f c_m \frac{\partial T}{\partial t} + \nabla \cdot (-K_Q \nabla T) = 0 , \quad (3.12)$$

where  $D_v$  is the *diffusion coefficient* of water vapor in air,  $K_Q$  the *thermal conductivity* of moist air and  $\mathbf{r}$  the position vector originating at the particle center (Fig. 3.3). Both are solved for radial symmetry and stationary conditions, i.e., we assume that the water vapor number concentration field  $n_v$  depends on the radial distance only and does not change with time,  $n_v(\mathbf{r}, t) = n_v(r)$ , and the particle temperature at the surface is stationary,  $dT_{ps}/dt = 0$ .

It shall be emphasized that the assumed stationary conditions are strictly local. The idea is that the particle moves to a new location and instantly reaches a stationary state within the environment at that specific location, assuming exactly such a temperature that the heat by condensation/evaporation is balanced by heat conduction. Furthermore, the water vapor pressure at the droplet surface instantly assumes the saturation pressure for a curved surface (Köhler Eq. (3.10)) and the local water vapor concentration field in the air adopts a stationary form. While moving through the carrier fluid, the particle will thus continuously change its surface temperature and saturation pressure to the equilibrium values referring to the ambient conditions.

Combining the solutions of the diffusion and heat conduction equations for  $r > R_p$ , with the boundary conditions of mass and heat rates at the droplet surface,

$$\frac{dm_p}{dt} = \frac{dm_w}{dt} = \int_{V_p} dA \cdot j_v = 4\pi R_p D_v (\rho_v(\infty) - \rho_v(R_p)) , \quad (3.13)$$

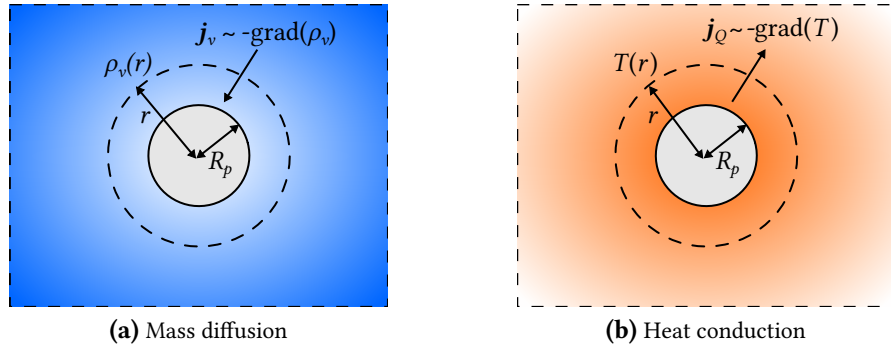


**Figure 3.3:** Mass diffusion and heat conduction for the condensation case (evaporation is exactly reverse).  
(a) The vapor density at the droplet surface is smaller than in the vicinity inducing a diffusion flux  $j_v$  in direction of the droplet center. (b) During condensation, the surface temperature increases by latent heat release, leading to a heat flux  $j_Q$  by thermal conduction.

$$\dot{Q} = \int_{V_p} dA \cdot j_Q = 4\pi R_p K_Q (T(\infty) - T(R_p)), \quad (3.14)$$

and  $-L_v m_w = \dot{Q}$ , leads to two coupled rate equations for mass and heat exchange, depending on particle mass and temperature and the ambient conditions. By making the assumption of instantaneous temperature adjustment at the droplet surface,

$$T_{ps} = T_a + \frac{L_v dm_p/dt}{4\pi R_p K_Q}, \quad (3.15)$$

we can eliminate the temperature and end up with a rate equation for the particle mass [Fukuta70],

$$\dot{m}_p = \frac{dm_p}{dt} = 4\pi R_p^2 (S - S_{eq}) \left[ \frac{L_v^2 S_{eq} (R_p + l_\alpha)}{K_Q \tilde{R}_v T_a^2} + \frac{\tilde{R}_v T_a (R_p + l_\beta)}{D_v e_s(T_a)} \right]^{-1}. \quad (3.16)$$

The equilibrium saturation

$$S_{eq} = \frac{e_{eq}}{e_s(T)} = \frac{m_w}{m_w + m_s i_s M_w / M_s} \exp \left( \frac{2 \sigma_p}{\tilde{R}_v T_a \rho_p R_p} \right) \quad (3.17)$$

describes the case, where the ambient vapor pressure is equal to the saturation pressure of the solution droplet,  $e_{eq} = e_s(T, R_p, N_s)$ , as given by Eq. (3.10). The length corrections  $l_\alpha$  and  $l_\beta$  consider deviations from the diffusion equation due to high water molecule density gradients at the droplet surface. These regions are treated as Knudsen flow and the length corrections are given by

$$l_\alpha = \frac{K_Q}{\alpha_{acc} p_a} \frac{\sqrt{2\pi \tilde{R}_m T_a}}{c_m - \tilde{R}_m/2}, \quad l_\beta = \left( \frac{2\pi M_w}{R^* T_a} \right)^{\frac{1}{2}} \frac{D_v}{\beta_{con}}, \quad (3.18)$$

where we use  $\alpha_{acc} = 1.0$  and  $\beta_{con} = 0.0415$  for the *accommodation coefficient* and the *condensation coefficient*, respectively, after recommendations in [Fukuta70] and [Pruppacher97]. To provide an overview of the behavior with droplet size,  $S_{eq}(R_p)$  is illustrated for different dry radii and solute materials in Fig. 3.4. We identify the required activation saturations at the maxima of  $S_{eq}$ , which must be reached for particles to attain their activation radii and subsequently grow to larger cloud and rain droplets. Due to higher water activities, equilibrium saturations of ammonium sulfate are constantly larger than for sodium chloride.

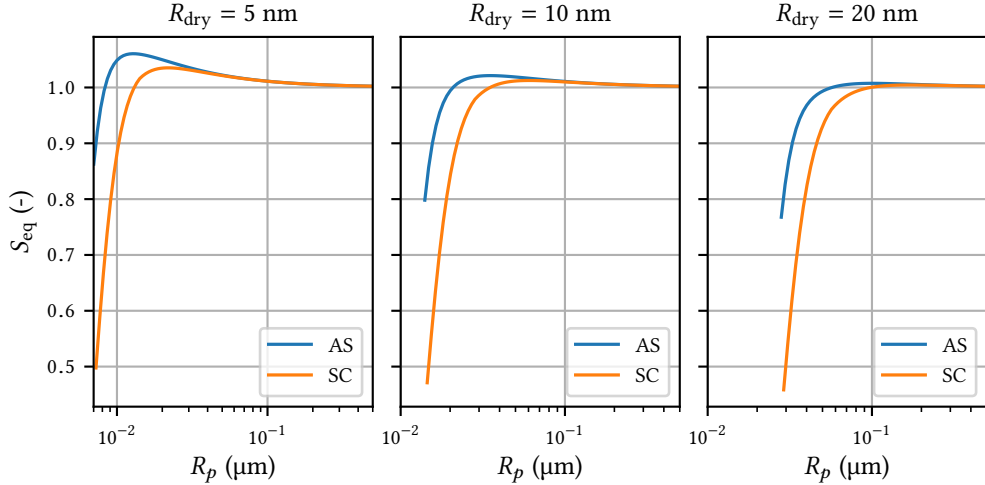


**Figure 3.4:** Dependence of the equilibrium saturation  $S_{\text{eq}}$  on the particle radius  $R_p$  for three different CCN dry sizes. In all cases, ammonium sulfate (AS) shows larger values than sodium chloride (SC) due to higher water activities.

### 3.2.1 Condensation rate

After deriving the particle mass equation, we can now give an expression for the condensation rate in a volume  $\Delta V$  by coarse graining the contributions of all present particles:

$$\phi_{\text{con}} = \frac{1}{\Delta V} \sum_{\{k : \mathbf{x}_k \in \Delta V\}} \dot{m}_{p,k}. \quad (3.19)$$

## 3.3 Particle dynamics

When described as a rigid sphere, each droplet has three translational and three rotational degrees of freedom. In the present model however, we neglect rotational movement of the particle entirely to reduce computational effort, as is common practice for particle based cloud models [Shima09, Sölch10, Arabas15]. The effects of droplet rotation on larger atmospheric scales are considered too small to justify the additional computational cost. Particle-particle interactions are not formulated by an interaction potential, but exclusively described using a stochastic collision approach in Sec. 3.5. Translational dynamics follow Newton's second law. Zhu *et al.* summarize relevant forces acting on a particle with position  $\mathbf{x}$  and velocity  $\mathbf{v}$  [Zhu07]:

$$m_p \ddot{\mathbf{x}} = \mathbf{F}(\mathbf{x}, \mathbf{v}, t) = \sum_k \mathbf{F}_k = \mathbf{F}_g + \mathbf{F}_d + \mathbf{F}_{\text{pr}} + \mathbf{F}_{\text{Basset}} + \mathbf{F}_{\text{Saffman}} + \mathbf{F}_{\text{Magnus}}. \quad (3.20)$$

A brief discussion of the forces is given in the following.

### 3.3.1 Drag force $F_d$

The main contribution to the total force (cf. [Sommerfeld08, Crowe11]) under the present conditions is due to the drag force exerted onto a rigid sphere by a fluid with local velocity  $\mathbf{u}$ ,

$$\mathbf{F}_d = - \int_{\partial V_p} dA p(\mathbf{x}) + \int_{\partial V_p} dA \cdot \boldsymbol{\sigma}'(\mathbf{x}, \tilde{\mathbf{u}}), \quad (3.21)$$

where  $\tilde{\mathbf{u}} = \mathbf{u} - \mathbf{v}$  is the relative velocity and  $\sigma'$  is the friction tensor defined in (2.4). An evaluation of the drag force for the present conditions yields [Crowe11]

$$\mathbf{a}_d := \frac{\mathbf{F}_d}{m_p} = k_d (\mathbf{u}(\mathbf{x}, t) - \mathbf{v}), \quad (3.22)$$

where the drag parameter  $k_d$  is approximated by

$$k_d = \begin{cases} k_d^0, & \text{Re}_p < 0.5 \\ k_d^0 \times \left(1 + 0.15 \text{Re}_p^{0.687}\right), & 0.5 \leq \text{Re}_p < 1000 \\ k_d^0 \times \frac{0.44}{24} \text{Re}_p, & \text{Re}_p \geq 1000, \end{cases} \quad (3.23)$$

with

$$k_d^0 = \frac{9}{2} \frac{\mu_f}{\rho_p R_p^2}. \quad (3.24)$$

The particle Reynolds number

$$\text{Re}_p := \frac{2 \rho_f R_p |\mathbf{u} - \mathbf{v}|}{\mu_f} \approx 0.11 \times R_p^* \tilde{u}^* \quad (3.25)$$

describes different flow regimes illustrated in Fig. 3.5. The approximated formula with values for the particle radius  $R_p^*$  (in  $\mu\text{m}$ ) and for the relative velocity  $\tilde{u}^*$  (in m/s) is only reported to enable an estimation of the expected scales of  $\text{Re}_p$ . In the simulation program,  $\text{Re}_p$  is always computed using the complete formula. It should be noted that, compared to [Crowe11], we use a different, but equivalent formulation of the drag force, which is more convenient during numerical implementation. For low Reynolds numbers the drag force is given by Stokes drag

$$\mathbf{a}_d = m_p (\mathbf{u} - \mathbf{v}) / \tau_p, \quad (3.26)$$

with particle momentum response time  $\tau_p = 2 \rho_p R_p^2 / (9 \mu_f)$ .

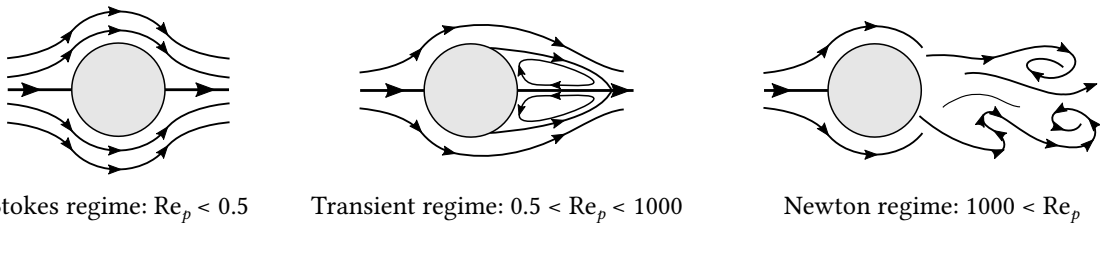


**Figure 3.5:** Flow regimes around a rigid sphere represented by the particle Reynolds number  $\text{Re}_p$ . In the Stokes regime, the relative fluid velocity is small enough to form a creeping flow. With increasing particle Reynolds number, stationary vortices begin to form, which finally detach irregularly in the Newton regime.

### 3.3.2 Pressure gradient force $F_{\text{pr}}$ and gravitational force $F_g$

The forces of gravity and pressure gradient are given by

$$\mathbf{F}_g = V_p \rho_p \mathbf{g} \quad (3.27)$$

and

$$\mathbf{F}_{\text{pr}} = -V_p \nabla p. \quad (3.28)$$

Under non-static compressible conditions, we get

$$\partial_t \mathbf{u} + \mathbf{u} \cdot \nabla \mathbf{u} = \frac{1}{\rho_f} (-\nabla p + \nabla \cdot \boldsymbol{\sigma}') + \mathbf{f}_{\text{ext}} \quad (3.29)$$

with the mass specific external forces  $\mathbf{f}_{\text{ext}} = \mathbf{g} + \dots$ .

Following [Zhu07] and our kinematic framework, we use the approximation of a static fluid, negligible dissipative forces and  $|\mathbf{u} \cdot \nabla \mathbf{u}| \ll |\mathbf{g}|$ , which leads to the hydrostatic buoyancy force ( $\nabla p = \rho_f \mathbf{g}$ ) and thus

$$\mathbf{F}_g + \mathbf{F}_{\text{pr}} = V_p (\rho_p - \rho_f) \mathbf{g}. \quad (3.30)$$

Noting that  $\rho_f / \rho_p \approx 1/1000$ , we will further neglect the pressure force entirely.

### 3.3.3 Basset force, Saffman and Magnus lift forces

The Basset force takes the history of the particle  $\leftrightarrow$  fluid interaction along the particle trajectory into account. It is neglected, because the effect is typically small compared to the drag force, while the computational time increases by a factor of about 10 [Sommerfeld08]. Saffmann and Magnus lift forces are only present under rotational movement, which is not considered in this model.

### 3.3.4 Dynamics summary

Under the presented approximations, the only two contributions to the acceleration of particles are drag force and gravity, as illustrated in Fig. 3.6:

$$\mathbf{a} = \ddot{\mathbf{x}} = \mathbf{a}_d + \mathbf{g} = k_d (\mathbf{u}(\mathbf{x}, t) - \mathbf{v}) + \mathbf{g}. \quad (3.31)$$

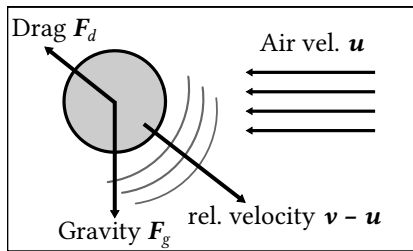


**Figure 3.6:** Considered forces acting on a cloud particle.

## 3.4 Equations of motion

Conclusively, we are left with three coupled equations of motion for each individual particle:

$$\begin{aligned} \frac{d\mathbf{x}}{dt} &= \mathbf{v} \\ \frac{d\mathbf{v}}{dt} &= \mathbf{a}(\mathbf{x}, \mathbf{v}, m_p, t) := k_d (\mathbf{u}(\mathbf{x}, t) - \mathbf{v}) + \mathbf{g} \\ \frac{dm_p}{dt} &= \gamma(\mathbf{x}, m_p, t) := 4\pi R_p^2 (S - S_{\text{eq}}) \left[ \frac{(R_p + l_\alpha) L_v^2 S_{\text{eq}}}{K_Q R_v T_a^2} + \frac{(R_p + l_\beta) R_v T_a}{D_v e_s(T_a)} \right]^{-1}. \end{aligned} \quad (3.32)$$

The drag parameter  $k_d$ , equilibrium saturation  $S_{\text{eq}}$  and size corrections ( $l_\alpha, l_\beta$ ) are given in Eqs. (3.23), (3.17) and (3.18). It shall be noted that nearly all of the appearing quantities depend either

on the particle properties or on the local ambient temperature and pressure. In particular, we find

$$\begin{aligned} w_s &= w_s(m_p), \quad L_v = L_v(T), \quad K_Q = K_Q(T), \quad D_v = D_v(p, T), \quad e_s = e_s(T), \\ k_d &= k_d\left(R_p, \rho_p(w_s, T), \mu_f, \text{Re}_p\left(R_p, \rho_f(T, r_v), |\mathbf{u}(\mathbf{x}, t) - \mathbf{v}|\right)\right), \\ S_{\text{eq}} &= S_{\text{eq}}\left(w_s, \sigma_p(w_s, T), \rho_p(w_s, T), T, R_p\right), \quad l_\alpha = l_\alpha(p, T), \quad l_\beta = l_\beta(p, T). \end{aligned}$$

Applied relations for the material properties and corresponding data sources are summarized in the appendix (Table A.1).

## 3.5 Particle collisions

After reaching a certain size by hygroscopic growth, coagulation becomes the significant factor for the growth of cloud particles [Lohmann16]. Immediately after two liquid droplets collide, their masses can either remain together to form one larger particle (*coalescence*) or they might disband into two or more smaller elements (*break-up*). The successful formation of a larger droplet by collision-coalescence is summarized by the term *collection*.

An ensemble of a sufficiently large number of particles can be characterized by a so called *mass distribution*  $f_m$  with dimensions  $(\text{volume} \times \text{mass})^{-1}$ , where  $f_m(m, \mathbf{x}, t) dm$  is the number of particles per volume with masses in the interval  $[m, m + dm]$ , such that  $\text{DNC}(\mathbf{x}, t) = \int dm f_m(m, \mathbf{x}, t)$  is the *droplet number concentration*, which changes with time due to collisions and sedimentation. We obtain the normalized probability density function by  $\tilde{f}_m = f_m / \text{DNC}$ , where  $\tilde{f}_m dm$  expresses the probability that the mass of any arbitrarily chosen particle is contained in  $[m, m + dm]$ .

Further, the  $k$ -th moment of the mass distribution is defined by

$$\lambda_{m,k} := \int_0^\infty dm f_m(m) m^k, \quad (3.33)$$

with  $\text{DNC} = \lambda_{m,0}$ , *liquid mass content*  $\text{LMC} := \lambda_{m,1}$  and average particle mass  $m_{\text{avg}} = \text{LMC}/\text{DNC}$ . Analogously to  $f_m$ , we define the size distribution  $f_R = f_m dm/dR = 3m(R) f_m/R$  with corresponding moments  $\lambda_{R,k}$ , where  $\lambda_{R,0} = \text{DNC}$  and the average radius is given by  $R_{\text{avg}} = \lambda_{R,1}/\text{DNC}$ .

### 3.5.1 Stochastic coalescence equation

In bulk or bin cloud models, the growth by collection of a particle ensemble is typically described by a deterministic equation, which is inconsistently denoted as *stochastic coalescence equation* (SCE), because it can be derived by averaging over underlying stochastic processes [Gillespie72]. In the SCE (also known as *Smoluchowski equation* or *population balance equation*), the time evolution of the mass distribution function  $f_m(m)$  consists of a gain term, where two lighter particles with masses  $m_1 = m'$  and  $m_2 = m - m'$  coagulate and a loss term, where a particle of mass  $m$  is collected by any other mass:

$$\begin{aligned} \frac{\partial f_m(m, t)}{\partial t} &= \frac{1}{2} \int_0^m dm' f_m(m', t) f_m(m - m', t) K(m', m - m') \\ &\quad - \int_0^\infty dm' f_m(m, t) f_m(m', t) K(m, m'). \end{aligned} \quad (3.34)$$

The *collection kernel*  $K(m, m')$  expresses the rate of coagulations of droplets with masses  $m$  and  $m'$  and can be defined in our stochastic discrete particle approach as

$$K(m, m') := \lim_{\delta t \rightarrow 0} \frac{P_{\delta t}(m, m') \Delta V}{\delta t}, \quad (3.35)$$

where  $P_{\delta t}(m, m')$  is the probability that two arbitrary particles in volume  $\Delta V$  with masses  $m$  and  $m'$  collide and coalesce in a time interval  $\delta t$ . The volume  $\Delta V$  has to be chosen such that the particles can be considered to be well-mixed, i.e., have spatially uniform probability to be anywhere inside this volume.

The SCE has been solved analytically for a limited number of initial distributions and kernel functions [Golovin63, Scott68]. Golovin showed that a solution exists for an initial exponential distribution and the kernel

$$K(m, m') = b_G(m + m'), \quad (3.36)$$

with constant  $b_G$ . Although the Golovin kernel is artificial, it presents nonetheless a useful case for testing simulations against an analytic reference, as shown for a box model in Sec. 5.2.1.

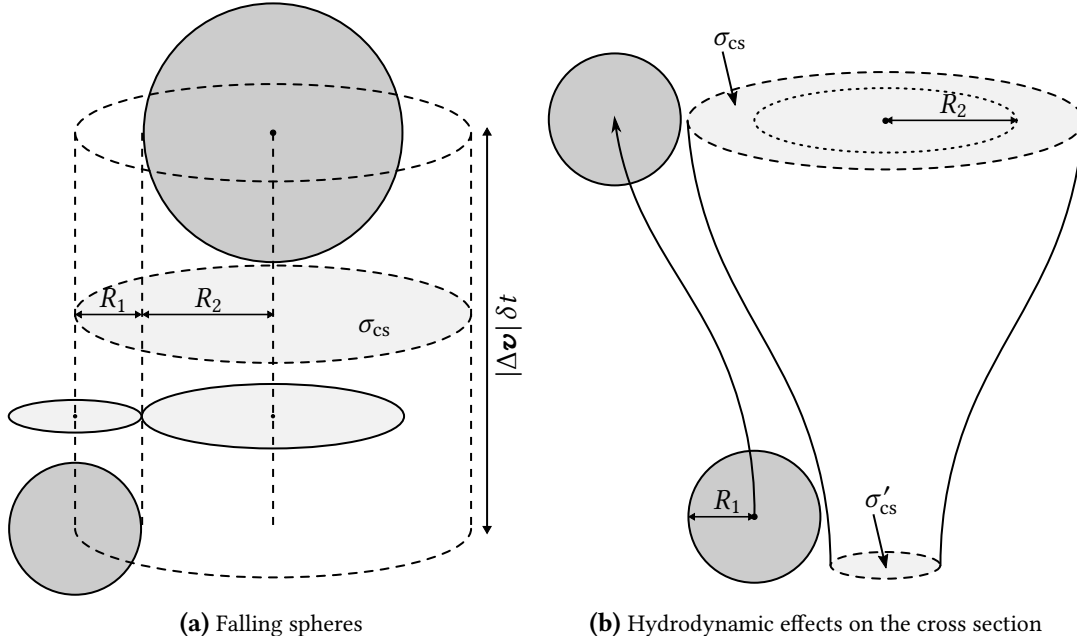


**Figure 3.7:** (a) Two spherical particles with relative velocity  $|\mathbf{v}|$  collide during  $\delta t$ , when they reside in a volume of  $\sigma_{\text{cs}} |\mathbf{v}| \delta t$ , where  $\sigma_{\text{cs}} = \pi (R_1 + R_2)^2$ . (b) The particle movement induces alterations in the surrounding fluid field, which effectively changes the cross section to  $\sigma'_{\text{cs}} = E_{\text{cls}} \sigma_{\text{cs}}$ . In the illustration, sphere 1 is pushed aside by moving according to the induced velocity field of sphere 2, which is taken as reference frame for the coordinate system.

A more realistic approach for spherical droplets with radius  $R$ , mass  $m = \rho_p R^3 4\pi/3$  and velocity  $\mathbf{v}$  is based on the model of falling spheres, illustrated in Fig. 3.7. The size of the volume in which two particles must reside to collide during time step  $\delta t$  is  $\delta V = \sigma'_{\text{cs}} |\Delta \mathbf{v}| \delta t$ , where the collision cross section  $\sigma'_{\text{cs}} = E_{\text{cls}} \sigma_{\text{cs}}$  is equal to the product of geometric cross section  $\sigma_{\text{cs}} = \pi (R_1 + R_2)^2$  and *collision efficiency*  $E_{\text{cls}}$ . This latter factor represents hydrodynamic effects due to the local modification of the fluid field by the moving droplets and is strongly dependent on the particle radii  $R_1$  and  $R_2$ . When both droplets are small, the efficiency is mostly much smaller than one, because the induced creeping flow tends to push the particles away from each other (cf. Figs. 3.5

and 3.7b). For size combinations including larger particles,  $E_{\text{cls}}$  increases and might even exceed one, when considering wake capture effects [Lin75, Hall80].

After colliding, the particles merge and actually remain together only with *coalescence efficiency*  $E_{\text{coal}}$ . The total collection efficiency is thus given by the product  $E_c = E_{\text{cls}} \times E_{\text{coal}}$ . Since both particles are equally likely to be anywhere inside  $\Delta V$ , the probability for a collection event during  $\delta t$  is

$$P_{\delta t} = E_{\text{coal}} \frac{\delta V}{\Delta V} = \frac{E_{\text{coal}} \sigma'_{\text{cs}} |\Delta \mathbf{v}| \delta t}{\Delta V}, \quad (3.37)$$

and, using (3.35), we can derive an equation for the *hydrodynamic kernel*

$$K(R_1(m_1), R_2(m_2)) = \lim_{\delta t \rightarrow 0} E_{\text{coal}} \sigma'_{\text{cs}} |\Delta \mathbf{v}| \frac{\delta t}{\Delta V} \frac{\Delta V}{\delta t} = E_c(R_1, R_2) \pi (R_1 + R_2)^2 |\mathbf{v}_2 - \mathbf{v}_1|. \quad (3.38)$$

For cloud and drizzle drops with radius  $R < 100 \mu\text{m}$ , the case of immediate break-up is however insignificant and we will assume  $E_{\text{coal}} = 1$  and consequently  $E_c = E_{\text{cls}}$  [Croft09, Lohmann16]. There exist several approaches for the collection efficiency  $E_c(R_1, R_2)$  based on theoretical work and experimental data for a variety of ambient conditions. In this work, we use modifications of the kernels from [Long74] and [Hall80], further described in Sec. 4.4.2.

The question, how to connect the deterministic evolution of a continuous mass distribution to our finite number of discrete droplets by the application of stochastic methods, will be addressed when presenting the collision algorithm in Sec. 4.4.



# 4 DISCRETIZATION

In discretized form, multi particle collision dynamics aims to predict the evolution of a number of particle ensembles assigned to a multitude of connected cells with volumes  $\Delta V$ . The particles can change their masses by condensation and collision as well as their positions by moving to an adjacent cell, thereby leaving one local ensemble and joining another one. Especially the collision process depends on the current mass (or size) distribution of the ensemble in a certain cell. The challenge is to describe the ensemble by a number of discrete variables, which is numerically manageable but still allows to reproduce the main characteristics of the distribution over time.

In the following, we will first describe the spatial discretization of atmospheric fields using a rectangular grid and the applied integration schemes for the evolution of thermodynamic state variables on a discrete time axis. Afterwards, we introduce the concept of super-droplets for the representation of particle ensembles and the method for discrete time propagation of particle position, velocity and mass coupled to the evolution of the ambient fields.

## 4.1 Transport of energy and water vapor

### 4.1.1 Spatial grid

To describe the fluid field variables, we discretize configuration space using a two-dimensional  $\{\hat{e}_x, \hat{e}_z\}$  rectangular C-staggered Arakawa grid with cells  $[i, j]$ , illustrated in Fig. 4.1. The cell corner positions are given by  $\hat{x}_i = i \Delta x$  and  $\hat{z}_j = j \Delta z$  with homogeneous grid spacings  $\{\Delta x, \Delta z\}$ . Any scalar field  $b(\mathbf{x})$  is given at the cell centers,  $b[i, j]$ , and assumed to be constant in each cell. The components of the fluid velocity field  $\mathbf{u} = (u, w)^\top$  are described by the normal flow between adjacent cells, such that  $u[i, j]$  states the  $u$ -component at position  $\mathbf{x}_u[i, j] = (i \Delta x, (j + 1/2) \Delta z)^\top$ . When calculating the particle drag forces, the fluid velocities  $\mathbf{u}$  at the particle positions  $\mathbf{x}$  are calculated by bilinear interpolation.

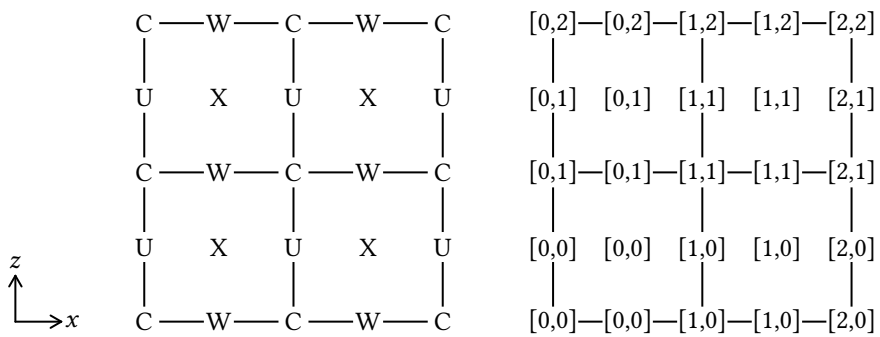


**Figure 4.1:** Spatial two-dimensional rectangular C-staggered Arakawa grid. The cells are denoted by  $[i, j]$  and their positions are defined by the corners (C). Scalar fields are given at the centers (X) and assumed to be constant in each cell. The vector components of the velocity field  $\mathbf{u} = (u, w)^\top$  describe the normal flow at the cell surfaces, indicated by U and W. When calculating the forces, the velocity is interpolated at the particle positions in a bilinear manner.

### 4.1.2 Discretized divergence

Disregarding the source terms, our atmospheric transport equations (2.49) and (2.50) are given in the form

$$\partial_t (\rho_{\text{dry}} b) + \nabla \cdot (\mathbf{j}_{\text{dry}} b) = \partial_t (\rho_{\text{dry}} b) + \sum_l \partial_l (j_l b) = 0, \quad (4.1)$$

where  $b$  is one of the state variables ( $\Theta, r_v$ ) and  $\rho_{\text{dry}}$  and  $\mathbf{j} = \mathbf{j}_{\text{dry}}$  are the density and mass flux density of dry air, respectively. To solve this kind of equation numerically, Hundsorfer *et al.* proposed upwind schemes for the spatially discretized form [Hundsorfer95]

$$\frac{d(\rho_{\text{dry}} b)_{i,j}}{dt} + \frac{J_{i+\frac{1}{2},j} - J_{i-\frac{1}{2},j}}{\Delta x} + \frac{J_{i,j+\frac{1}{2}} - J_{i,j-\frac{1}{2}}}{\Delta z} = 0, \quad (4.2)$$

where  $(i, j)$  indicates the center of cell  $[i, j]$  and  $(i + 1/2)$  describes the border dividing cell  $[i, j]$  from cell  $[i + 1, j]$ . Because of the linearity, it suffices to consider the one-dimensional case  $\mathbf{j} = j \hat{\mathbf{e}}_x$ :

$$\frac{d(\rho_{\text{dry}} b)_{i,j}}{dt} + \frac{J_{i+\frac{1}{2}} - J_{i-\frac{1}{2}}}{\Delta x} = 0. \quad (4.3)$$

The third order upwind scheme provides fluxes  $J_{i+\frac{1}{2}}$  such that continuity and positivity is conserved during time integration and is given by Eqs. (40) and (43) in [Hundsorfer95]:

$$J_{i+\frac{1}{2}}^+ = j_{i+\frac{1}{2}} \left( b_i + \frac{1}{2} \psi(\eta_i) (b_i - b_{i-1}) \right) \quad (4.4)$$

$$J_{i+\frac{1}{2}}^- = j_{i+\frac{1}{2}} \left( b_{i+1} + \frac{1}{2} \psi \left( \frac{1}{\eta_{i+1}} \right) (b_{i+1} - b_{i+2}) \right), \quad (4.5)$$

where

$$\psi(\eta) = \max \left\{ 0, \min \left[ 2\eta, \min \left( \delta, \tilde{K}(\eta) \right) \right] \right\} \quad (4.6)$$

is the limiter function with  $\eta_i = (b_{i+1} - b_i) / (b_i - b_{i-1})$  and  $\tilde{K}(\eta) = (1 + 2\eta) / 3$ .

The effective flux at the right surface of box  $i$  is then given by

$$J_{i+\frac{1}{2}} = \begin{cases} J_{i+\frac{1}{2}}^+, & u_{i+\frac{1}{2}} \geq 0 \\ J_{i+\frac{1}{2}}^-, & u_{i+\frac{1}{2}} < 0 \end{cases}. \quad (4.7)$$

In two dimensions, the second component is constructed analogously. We denote the discretized divergence in Eq. (4.2) as

$$\text{div}_{\text{eff}}(\mathbf{j} b)_{i,j} := \frac{J_{i+\frac{1}{2},j} - J_{i-\frac{1}{2},j}}{\Delta x} + \frac{J_{i,j+\frac{1}{2}} - J_{i,j-\frac{1}{2}}}{\Delta z}, \quad (4.8)$$

such that numerically

$$\partial_t (\rho_{\text{dry}} b) + \nabla \cdot (\mathbf{j}_{\text{dry}} b) \rightarrow \left( \rho_{\text{dry}} \right)_{i,j} \frac{db_{i,j}}{dt} + \text{div}_{\text{eff}} (\mathbf{j}_{\text{dry}} b)_{i,j}, \quad (4.9)$$

where we considered  $\partial_t \rho_{\text{dry}} = 0$ .

The advection algorithm with the presented upwind scheme was tested by simulating the

transport of a solid cylinder in a circular velocity field. The results, presented in the Appendix (Sec. B), indicate sufficiently low numerical diffusion.

### 4.1.3 Time integration

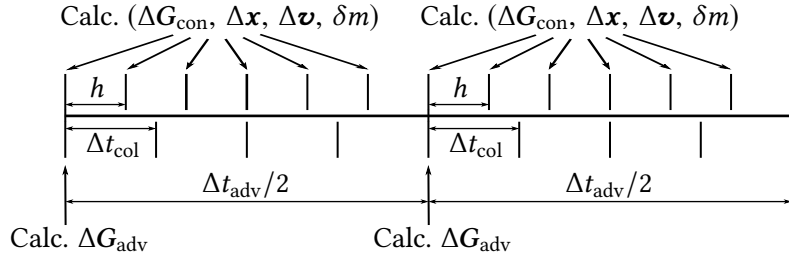


**Figure 4.2:** The advection time step  $\Delta t_{\text{adv}}$  is divided in  $N_h$  condensation steps  $h$  and  $N_{\text{col}}$  collision steps  $\Delta t_{\text{col}}$ . The change of atmospheric state variables  $G = (\Theta, r_v)$  due to advection  $\Delta G_{\text{adv}}$  is calculated twice during one advection step, using different formulae for the first and second half, as given in (4.14).

The time evolution of the thermodynamic state variables  $G = (\Theta, r_v)$  can be separated in an advection part  $\dot{G}_{\text{adv}}$  and a condensation part  $\dot{G}_{\text{con}}$ , which describes the interaction with the particles,

$$\dot{G} = \dot{G}_{\text{adv}} + \dot{G}_{\text{con}} = f_{\text{adv}}(G) + f_{\text{con}}(G, \phi_{\text{con}}). \quad (4.10)$$

In a given cell, the change of  $r_v$  and  $\Theta$  due to advection is given by (cf. (4.9))

$$\begin{aligned} \frac{d\Theta}{dt} \Big|_{\text{adv}} &= f_{\text{adv}}^\Theta(\Theta) = -\frac{1}{\rho_{\text{dry}}} \text{div}_{\text{eff}} \left( j_{\text{dry}} \Theta \right), \\ \frac{dr_v}{dt} \Big|_{\text{adv}} &= f_{\text{adv}}^{r_v}(r_v) = -\frac{1}{\rho_{\text{dry}}} \text{div}_{\text{eff}} \left( j_{\text{dry}} r_v \right), \end{aligned} \quad (4.11)$$

while the condensation of water contributes with (cf. (2.49) and (2.50))

$$\begin{aligned} \frac{d\Theta}{dt} \Big|_{\text{con}} &= f_{\text{con}}^\Theta(G, \phi_{\text{con}}) = \frac{L_v}{c_{\text{dry}} \rho_{\text{dry}} (1 + \alpha_v r_v)} \frac{\Theta}{T} \phi_{\text{con}}, \\ \frac{dr_v}{dt} \Big|_{\text{con}} &= f_{\text{con}}^{r_v}(\phi_{\text{con}}) = \frac{1}{\rho_{\text{dry}}} \phi_{\text{con}}. \end{aligned} \quad (4.12)$$

For the discretized time integration ( $t^{n+1} := t^n + h$ ) we use a coupled scheme with time step  $\Delta t_{\text{adv}}$  for the “slow” changing advection part and refined time step  $h = \Delta t_{\text{adv}}/N_h$ , for the “fast” interaction with the particles, as illustrated in Fig. 4.2. To evaluate the change during time step  $h$ , we apply a scheme based on implicit-explicit Runge-Kutta methods, proposed in [Knoth98]:

$$G^{n+1} = G^n + \Delta G_{\text{adv}}^n + h f_{\text{con}}(G^n, \phi_{\text{con}}^n). \quad (4.13)$$

In the interval of any advection step ( $t^0 \rightarrow t^{N_h} = t^0 + \Delta t_{\text{adv}}$ ), the change  $\Delta G_{\text{adv}}^n$  is reevaluated only twice, i.e., after each period of  $\Delta t_{\text{adv}}/2$ :

$$\Delta G_{\text{adv}}^n = \begin{cases} h f_{\text{adv}}(G^0), & 0 \leq n < N_h/2 \\ 2h f_{\text{adv}}(G^{N_h/2}) - h f_{\text{adv}}(G^0), & N_h/2 \leq n < N_h. \end{cases} \quad (4.14)$$

During the advection interval, the particle equations are solved in a subloop, where the atmospheric conditions change according to (4.13). The condensation rate  $\phi_{\text{con}}^n$  in a given cell is then

approximated by calculating the total condensed water mass  $\Delta m_l$  and dividing by cell volume  $\Delta V$  and time step  $h$ :  $\phi_{\text{con}}^n \approx \Delta m_l / (\Delta V h)$ . The particle algorithms and the complete update scheme are presented in Sec. 4.3 and Sec. 4.5, respectively.

## 4.2 Simulation particles (super-droplets)

Considering a regime of  $1500 \times 1500 \times 1 \text{ m}^3$ , the total number of aerosol particles in the simulation box is in the order of  $2 \times 10^{14}$ . To keep the particle number computational feasible, we divide the box into grid cells of volume  $\Delta V$ , and describe the ensemble of real (physical) particles in cell  $n$  by a number  $N_{\text{SIP},n}$  of *simulation particles* (SIPs, following the notation used in [Unterstrasser17]), also called *super-droplets*, *super-particles* or *computational particles*, as introduced by Shima *et al.* [Shima09]. Each simulation particle represents a *multiplicity* or *stochastic weight*  $\xi$  of real particles and is numerically simulated as one entity with defined physical properties, like mass, composition, position and velocity. It is important to note that one SIP actually covers a certain interval of the mass distribution as well as a certain volume in configuration space. Therefore, it should be considered as an abstract numerical tool used to model a stochastic system. In fact, the multiplicity  $\xi$  does not have to be an integer and may be smaller than one.

We again use the common assumption that the configuration is well mixed in the current grid cell  $\Delta V$ , i. e., that all real particles in a cell (and thereby also all particles which are represented by a certain SIP) have the same probability to be at any spatial position in this cell. Regardless, the SIPs are propagated spatially with defined position and velocity, which definitely leads to a conflict with the well mixed assumption, because the position of the SIP is obviously not regarded as spatial center of mass of the represented particles. The propagation scheme can be justified as a method, which reduces the numerical diffusion of the whole system [Morrison18, Grabowski19], while the well mixed assumption reduces the complexity to a computationally manageable state.

Regarding the particle time evolution (Sec. 3.4), the equations (3.32) for position, velocity and mass are directly applied to the super-droplets with masses  $\mu_{p,i}$ . The only change occurs for the condensation rate (3.19), where each SIP is weighted by its multiplicity,

$$\phi_{\text{con}} = \frac{1}{\Delta V} \sum_{\{i : \mathbf{x}_i \in \Delta V\}} \xi_i \dot{\mu}_{p,i}. \quad (4.15)$$

After these initial considerations, we will now further elaborate the connection of a SIP-ensemble to the real-particle ensemble and introduce a technique to generate SIP ensembles from a given distribution function. Furthermore, we will discuss the challenges of reproducing a distribution from a given SIP-ensemble.

### 4.2.1 Generation of SIP ensembles

Consider a volume  $\Delta V$  containing a number of  $\mathcal{N}$  physical (*real*) cloud particles of different masses  $\{m_{\text{real},i}\}$ . The total particle mass  $\mathcal{M}$  in  $\Delta V$  is given by

$$\mathcal{M} = \sum_{i=1}^{\mathcal{N}} m_{\text{real},i} = \Delta V \int_0^{\infty} dm f_m(m) m = \Delta V \times \text{LMC}, \quad (4.16)$$

where  $f_m$  is the corresponding mass distribution (cf. Sec. 3.5). The task at hand is to generate a set of  $N_{\text{SIP}}$  simulation particles, which represent the stochastic properties of  $f_m$  and, when undergoing collision events, allow to reproduce the time evolution of  $f_m$  up to acceptable errors. For the SIP ensemble initialization, we will present the "probabilistic SingleSIP" method proposed in [Unterstrasser17].

At first, the mass space is divided into bins  $\{\hat{m}_i\}$ , where  $\hat{m}_i$  describes the left border of bin  $i$ . The bin widths  $\Delta\hat{m}_i = \hat{m}_{i+1} - \hat{m}_i$  do not have to be of equal size, but should be adjusted according to the underlying distribution  $f_m$ . In this work, we use an exponential distribution for the collision box model (Sec. 5.1) and a log-normal distribution for the kinematic test case (Sec. 6.1.1). A sensible binning choice for our purposes turns out to be a constant spread on the logarithmic axis,  $\hat{m}_{i+1} = \hat{m}_i 10^{1/s_b}$ , with spreading parameter  $s_b$ , lower boundary  $\hat{m}_{\text{low}} = \hat{m}_0$  and upper boundary  $\hat{m}_{\text{high}}$ . Particles with masses less than  $\hat{m}_{\text{low}}$  and greater than  $\hat{m}_{\text{high}}$  are not considered initially.

In the SingleSIP method, one simulation particle with mass  $\mu_i$  and multiplicity  $\xi_i$  is generated for each bin  $i$ . The mass is chosen by drawing a uniformly distributed random number from each bin, i.e. the PDF of mass  $\mu_i$  is

$$\tilde{f}_{\mu,i} = \begin{cases} \frac{1}{\Delta\hat{m}_i}, & \mu_i \in [\hat{m}_i, \hat{m}_{i+1}) \\ 0, & \text{else} \end{cases}, \quad (4.17)$$

and the multiplicity is then set to

$$\xi_i = f_m(\mu_i) \Delta\hat{m}_i \Delta V. \quad (4.18)$$

To avoid SIPs with ineffectively small multiplicities, a lower threshold  $\xi_{\text{low}} = \eta_b \xi_{\text{high}}$  with parameter  $\eta_b$  is set, where  $\xi_{\text{high}} = \max\{\xi_i\}$  is the largest multiplicity in the ensemble. It is now possible either to use a *fixed threshold*, removing all SIPs with  $\xi_i < \xi_{\text{low}}$  or to apply a *weak threshold*. In the latter case, a uniform random number  $\alpha \in [0, 1)$  is drawn for each SIP with  $\xi_i < \xi_{\text{low}}$  and the multiplicity is set to

$$\xi_i = \begin{cases} \xi_{\text{low}}, & \alpha < P_{\mu,i} \\ 0, & \alpha \geq P_{\mu,i} \end{cases}, \quad (4.19)$$

where  $P_{\mu,i} = \xi_i / \xi_{\text{low}}$  is the probability for a simulation particle to remain in the ensemble.

We will now analyze the statistical properties of the generated SIPs, when creating a large number of different ensembles. The number and mass of real particles in bin  $i$  are given by

$$\mathcal{N}_i = \Delta V \int_{\hat{m}_i}^{\hat{m}_{i+1}} dm f_m(m) \quad \text{and} \quad \mathcal{M}_i = \Delta V \int_{\hat{m}_i}^{\hat{m}_{i+1}} dm f_m(m) m. \quad (4.20)$$

For a single generated SIP ensemble we find  $N_i = \xi_i$  real particles and a particle mass of  $M_i = \xi_i \mu_i$  in bin  $i$ , where  $\mu_i$  and  $\xi_i$  are stochastic variables defined in Eqs. (4.17) and (4.18). We will first consider bins with  $\xi_i \geq \xi_{\text{min}}$  for all possible values of  $\mu_i$ . When generating an infinite number of ensembles, the expectation values in these bins are

$$\begin{aligned} \langle \mu_i \rangle &= \frac{1}{2} (\hat{m}_i + \hat{m}_{i+1}), \\ \langle N_i \rangle &= \langle \xi_i \rangle = \langle f_m(\mu_i) \Delta\hat{m}_i \Delta V \rangle = \Delta V \int_{\hat{m}_i}^{\hat{m}_{i+1}} dm \tilde{f}_{\mu,i}(m) f_m(m) \Delta\hat{m}_i \\ &= \Delta V \int_{\hat{m}_i}^{\hat{m}_{i+1}} dm \frac{\Delta\hat{m}_i}{\Delta\hat{m}_i} f_m(m) = \mathcal{N}_i, \\ \langle M_i \rangle &= \langle \xi_i \mu_i \rangle = \langle f_m(\mu_i) \Delta\hat{m}_i \mu_i \rangle = \mathcal{M}_i. \end{aligned} \quad (4.21)$$

The zeroth and first moment of the distribution  $f_m$  in each bin is thus conserved on average.

When applying a weak threshold, we can analyze bins with  $\xi_i < \xi_{\text{min}}$  (for all possible values of

$\mu_i$ ) to find

$$\langle \xi_i \rangle = \langle \xi_{\min} P_{\mu,i} \rangle + \langle 0 \times (1 - P_{\mu,i}) \rangle = \frac{\xi_{\min}}{\xi_{\min}} \langle f_m(\mu_i) \Delta m_i \Delta V \rangle = \mathcal{N}_i, \quad (4.22)$$

with  $P_{\mu,i}$  from Eq. (4.19) and analogously  $\langle \xi_i \mu_i \rangle = \mathcal{M}_i$ . From here, one can further conclude average moment conservation for those bins, where  $\xi_i < \xi_{\min}$  and  $\xi_i > \xi_{\min}$  are both possible.

Using the fixed threshold method will introduce errors in bins with small  $\xi_i$ . However, results presented in [Unterstrasser17] as well as our box model simulations (described in Sec. 5.2) indicate no significant difference between weak and fixed threshold generation methods, when analyzing the time evolution of the distribution function, as long as the parameter  $\eta_b$  is chosen small enough. We will therefore apply the fixed threshold method to have more control over the number of SIPs in each cell, which shall be explained in the following.

Due to the probabilistic mass assignment, it is not certain, if a SIP is created in mass bins where  $f_m(m)$  is relatively small. Consequently, there is a variation in the number of SIPs  $\{N_{\text{SIP},n}\}$ , when generating separate ensembles in several simulation cells  $\{n\}$ . In further course, whenever the number of SIPs per cell is stated, this actually describes the average number over all cells. When choosing a fixed threshold, the variation in  $N_{\text{SIP}}$  is still present, but can be reduced to a maximum difference of about two simulation particles, when the average number of SIPs per cell is in the order of 50.

#### 4.2.2 Reconstruction of the distribution function from a SIP ensemble

When the form of the underlying distribution is known, it can be parametrized by its moments and some typical distributions are fully determined by the zeroth, first and second moment. It is then sufficient to determine an accurate estimate of these moments with time to get all necessary information of the system. Assuming first a case where all stochastic weights are unity ( $\xi_l = 1 \forall l$ ), a simulation ensemble is given by a set of  $N_{\text{SIP}}(t)$  masses  $\{\mu_l\}$  at any time  $t$ . The moments can then be estimated by

$$\hat{\lambda}_k = \frac{1}{\Delta V} \sum_{l=1}^{N_{\text{SIP}}} \mu_l^k. \quad (4.23)$$

Using SIPs with different stochastic weights will generate a set of  $N_{\text{SIP}}$  value pairs  $\{(\xi_l, \mu_l)\}$ , where each particle represents  $\xi_l$  real particles. Consequently, the moments are now estimated by

$$\hat{\lambda}_k = \sum_{l=1}^{N_{\text{SIP}}} \xi_l \mu_l^k. \quad (4.24)$$

Conducting  $N_{\text{sim}}$  independent simulations with different initialization leads to  $N_{\text{sim}}$  ensembles, thus to a set of estimators  $\{\hat{\lambda}_k^0, \hat{\lambda}_k^1, \dots, \hat{\lambda}_k^J, \dots, \hat{\lambda}_k^{N_{\text{sim}}}\}$  for each moment  $k$ , where  $J$  denotes the simulation number. From these sets, the average of a moment  $\bar{\lambda}_k$  as well as the standard deviation of this average,

$$\text{SD}(\bar{\lambda}_k) = \sqrt{\frac{1}{N_{\text{sim}}(N_{\text{sim}}-1)} \sum_{J=1}^{N_{\text{sim}}} (\hat{\lambda}_k^J - \bar{\lambda}_k)^2}, \quad (4.25)$$

can be estimated.

When the type of the underlying distribution is not known, it is desirable not only to evaluate the moments, but also the shape of the distribution function  $f_m(m; t)$  with time. We will now address the task of reconstructing the distribution function from a given particle ensemble, i.e., of generating a continuous density function from a set of discrete data points, in this case  $\{(\xi_l, \mu_l)\}$ . It is important to note that we initially constructed a maximum of one SIP per bin. Evolving with

time, the SIPs change in mass and might leave their initial bins. Therefore, it might be sensible to choose another binning for each considered point in time. For now, we will just assume that we are presented with a given ensemble and a set of bins  $\{\hat{m}_i\}$ , which does not have to be equal to the initial set. For a given bin, the true number of particles is

$$\mathcal{N}_i = \Delta V \int_{\hat{m}_i}^{\hat{m}_{i+1}} dm f_m(m) = \Delta \hat{m}_i \bar{f}_{m,i} \Delta V, \quad (4.26)$$

where  $\bar{f}_{m,i} = \Delta \hat{m}_i^{-1} \int_{\hat{m}_i}^{\hat{m}_{i+1}} dm f_m(m)$  is the *average* value of the distribution in bin  $i$ . When simulating a given ensemble of SIPs  $\{\xi_l, \mu_l\}$  marked by  $J$ , one gets an estimate  $N_i^J$  of  $\mathcal{N}_i$  by counting the number of particles in bin  $i$ ,

$$N_i^J = \sum_{k \in \Gamma_i} \xi_k, \quad (4.27)$$

where  $\Gamma_i = \{k \mid \mu_k \in [\hat{m}_i; \hat{m}_{i+1}]\}$ . We can then estimate  $\bar{f}_{m,i} \approx \hat{f}_{m,i} = N_i^J / \Delta \hat{m}_i$  for ensemble  $J$ . Simulating a number of ensembles  $N_{\text{sim}}$  and choosing the same binning for each ensemble, improves the estimation by applying

$$\hat{f}_{m,i} = \frac{1}{N_{\text{sim}} \Delta \hat{m}_i} \sum_{J=1}^{N_{\text{sim}}} N_i^J, \quad (4.28)$$

and we can again state the standard deviation of this average  $\text{SD}(\hat{f}_{m,i})$  analogously to (4.25).

Assuming that the function  $f_m(m)$  has linear behavior in each bin, one can assign the average values to the bin centers  $\hat{m}'_i := (\hat{m}_i + \hat{m}_{i+1})/2$  to get a discrete representation  $f_m(\hat{m}'_i) \approx \hat{f}_{m,i}$ . While the results of the box model simulations in Sec. 5.2 are presented with single data points obtained in the described way, we use piecewise constant  $f_{m,i} = \hat{f}_{m,i}$  in each bin to illustrate the size spectra in Sec. 6.2.2 to obtain better comparability with [Arabas15]. At this point, we want to note that the method of bin centers is quite reasonable for small bin width, because well behaving functions  $f_m(m)$  can in this case be approximated linearly in each bin. When it is however not possible to work with small bin widths due to regions with sparse data density, one might induce errors in the function  $f_m(m)$  by assuming that the bin represents a mass located in the bin center. Some authors choose to assign the values of  $\hat{f}_{m,i}$  to the bin centers referring to a logarithmic mass axis [Wang07]. For a more meaningful selection of connected data pairs  $(m_i, \hat{f}_{m,i})$ , some properties of the function  $f_m(m)$  must be either known or estimated.

## 4.3 Particle propagation

For convenience, we will denote the SIP mass by  $m$ , i.e.,  $m := \mu_p = m_p = m_s + m_w$ . The particle equations of motion are given as a reformulation of (3.32),

$$\dot{\mathbf{x}} = \mathbf{v}, \quad \dot{\mathbf{v}} = \mathbf{a}(\mathbf{x}, \mathbf{v}, m, G), \quad \dot{m} = \gamma(\mathbf{x}, m, G), \quad (4.29)$$

depending on the ambient conditions  $G = (\Theta, r_v)$ . We apply a discretized integration scheme, consisting of a Velocity-Verlet propagation of the particle position coupled to implicit equations

for mass and velocity:

$$\begin{aligned}\mathbf{x}^{n+\frac{1}{2}} &= \mathbf{x}^n + \frac{h}{2} \mathbf{v}^n \\ m^{n+1} &= m^n + h \gamma\left(\mathbf{x}^{n+\frac{1}{2}}, m^{n+1}, \mathbf{G}^{n+1}\right) \\ \mathbf{v}^{n+1} &= \mathbf{v}^n + h \mathbf{a}\left(\mathbf{x}^{n+\frac{1}{2}}, \mathbf{v}^{n+1}, m^{n+1}, \mathbf{G}^{n+1}\right) \\ \mathbf{x}^{n+1} &= \mathbf{x}^{n+\frac{1}{2}} + \frac{h}{2} \mathbf{v}^{n+1}.\end{aligned}$$

**The implicit mass equation** is approximately solved using a Newton algorithm. With fixed  $\mathbf{x} = \mathbf{x}^{n+\frac{1}{2}}$  and  $\mathbf{G}^{n+1} \approx \mathbf{G}^n$ , we begin with

$$\frac{m^{n+1} - m^n}{h} \approx \gamma\left(m^{n+1}\right), \quad (4.30)$$

and define

$$F(m) := \frac{m - m^n}{h} - \gamma(m) \stackrel{!}{=} 0. \quad (4.31)$$

The Newton iterations  $l = 0, \dots, l_{\max}$  are calculated by

$$m_{l+1}^* = m_l^* - \left[ F'\left(m_l^*\right) \right]^{-1} F\left(m_l^*\right) = m_l^* + \frac{h \gamma\left(m_l^*\right) - (m_l^* - m^n)}{1 - h \gamma'\left(m_l^*\right)}, \quad (4.32)$$

where  $m_0^* = m^n$ . We summarize the application of Newton's method with the placeholder  $g_{\text{impl}}$ :

$$m^{n+1} = m^n + \Delta m^n \quad (4.33)$$

$$\Delta m^n =: g_{\text{impl}}\left(\mathbf{x}^{n+\frac{1}{2}}, m^n, \mathbf{G}^n\right) \quad (4.34)$$

**The velocity derivative** is given by (3.23),

$$\dot{\mathbf{v}} = \mathbf{a} = -k_d(\mathbf{v} - \mathbf{u}(\mathbf{x})) + \mathbf{g}, \quad (4.35)$$

where  $k_d = k_d(|\mathbf{u}(\mathbf{x}) - \mathbf{v}|, m, T, r_v)$ . To solve the implicit formulation, we make the approximation

$$k_d\left(\mathbf{x}^{n+\frac{1}{2}}, \mathbf{v}^{n+1}, m^{n+1}, \mathbf{G}^{n+1}\right) \approx k_d\left(\mathbf{x}^{n+\frac{1}{2}}, \mathbf{v}^n, m^{n+1}, \mathbf{G}^n\right) =: k_d^{n+1}, \quad (4.36)$$

and thus

$$\mathbf{v}^{n+1} \approx \mathbf{v}^n - h k_d^{n+1} \left( \mathbf{v}^{n+1} - \mathbf{u}\left(\mathbf{x}^{n+\frac{1}{2}}\right) \right) + h \mathbf{g}, \quad (4.37)$$

which finally leads to

$$\mathbf{v}^{n+1} = \frac{\mathbf{v}^n + h k_d^{n+1} \mathbf{u}\left(\mathbf{x}^{n+\frac{1}{2}}\right) + h \mathbf{g}}{1 + h k_d^{n+1}}. \quad (4.38)$$

Noteworthy, this is an approximation of a semi-analytical scheme, where the position  $\mathbf{x}(t)$  is set to  $\mathbf{x}^* := \mathbf{x}(h/2) \approx \mathbf{x}(0) + \mathbf{v}(0) h/2$  and thus  $k_d = k_d(|\mathbf{u}(\mathbf{x}^*) - \mathbf{v}(0)|, m(0), T(\mathbf{x}^*, t = 0))$ . We are then able to integrate (4.35),

$$\frac{d\mathbf{v}}{dt} = -k_d(\mathbf{v} - \mathbf{u}(\mathbf{x})) + \mathbf{g} = -k_d(\mathbf{v} - \mathbf{u}(\mathbf{x}^*)) + \mathbf{g},$$

from  $t = 0$  to  $t = h$ . The solution

$$\mathbf{v}(h) = \mathbf{v}_{\text{eq}} + (\mathbf{v}(0) - \mathbf{v}_{\text{eq}}) e^{-k_d h}, \quad (4.39)$$

approaches the stationary velocity

$$\mathbf{v}_{\text{eq}} = \mathbf{u}(\mathbf{x}^*) + \frac{\mathbf{g}}{k_d} \quad (4.40)$$

and we note that  $k_d \Delta t \gg 1 \Rightarrow \mathbf{v} \approx \mathbf{v}_{\text{eq}}$  and  $k_d \gg |\mathbf{g}| \Rightarrow \mathbf{v}_{\text{eq}} \approx \mathbf{u}(\mathbf{x}^*)$ . The approximated form of the exponential function yields Eq. (4.38):

$$e^{-k_d h} = \frac{1}{e^{k_d h}} \approx \frac{1}{1 + k_d h}. \quad (4.41)$$

Using these results, the discretized particle scheme can finally be written in approximated form as

$$\begin{aligned} \mathbf{x}^{n+\frac{1}{2}} &= \mathbf{x}^n + \frac{h}{2} \mathbf{v}^n \\ m^{n+1} &= m^n + g_{\text{impl}}\left(\mathbf{x}^{n+\frac{1}{2}}, m^n, G^n\right) \\ \mathbf{v}^{n+1} &= \frac{\mathbf{v}^n + h k_d^{n+1} \mathbf{u}\left(\mathbf{x}^{n+\frac{1}{2}}\right) + h \mathbf{g}}{1 + h k_d^{n+1}} \\ \mathbf{x}^{n+1} &= \mathbf{x}^{n+\frac{1}{2}} + \frac{h}{2} \mathbf{v}^{n+1}, \end{aligned} \quad (4.42)$$

where  $g_{\text{impl}}$  is described by (4.30) to (4.34) and  $k_d^{n+1} = k_d\left(\mathbf{x}^{n+\frac{1}{2}}, \mathbf{v}^n, m^{n+1}, G^n\right)$ .

## 4.4 Particle collisions

In the following, we will present a scheme, which describes collision-coalescence of a particle ensemble during time step  $t \rightarrow t + \Delta t_{\text{col}}$ , motivated by the formulation in [Unterstrasser17]. As mentioned previously, the droplets have uniform probability to be anywhere in their respective grid cells and are grouped into ensembles accordingly. Particles are only allowed to collide, when they reside in the same cell of volume  $\Delta V$  at time  $t$ . Following (3.35), we approximate the probability for a collection event of two arbitrary particles in this volume during  $\Delta t_{\text{col}}$  by

$$P_{\Delta t_{\text{col}}}(R_1, R_2) \approx K(R_1, R_2) \frac{\Delta t_{\text{col}}}{\Delta V} \quad (4.43)$$

applying the hydrodynamic kernel  $K(R_1, R_2)$ . For other kernels, it might be more convenient to give an equivalent formulation using the particle masses  $K(m_1, m_2)$ .

Considering the real particle ensemble with radii  $\{R_{\text{real},n}\}$ , one could now draw a random number for all possible particle pairs  $(R_i, R_j)$  and use the respective probability to decide, if a collection happens. This is certainly not feasible for large ensembles and we will reformulate the algorithm for simulation particles to reduce computation time.

Beforehand, we want to emphasize a general difficulty of this specific probabilistic approach, when using finite collision time steps. Regarding the iteration over the droplet pairs, it is by no means certain, in which order the pairs should be evaluated. Particles might change their size or vanish entirely during successful collections, thereby continuously varying the number of pairs and the kernel function value. An approach, which we will also use for the SIP description, is to define an order of pairs before each collection time step and update the particle properties on the

fly, i.e. after each successful event. Collections listed "earlier" in the iteration chain have thus the possibility to effect "following" collision events. Notably, we prescribe some kind of time order in which collections are possible, which is not justified physically, but just a numerical artifact. Nevertheless, this approach is commonly used in particle based cloud simulations. It is argued that the collision time step can be chosen sufficiently small, such that a successful collection is a rare event. The fewer collections happen in  $\Delta t_{\text{col}}$ , the smaller is the influence of the introduced error. During initialization, an unique ID is assigned to each particle. In the collision step, particles of a given cell are always ordered by their ID and the list of pairs is generated accordingly (cf. Algo. 1). Thereby, a preferred order is generated, where particles with smaller ID generally have the chance to collide earlier. Nevertheless, Unterstrasser *et al.* showed that for the chosen algorithm and time step, collisions are a rare event and the ordering method has no significant influence on the collection process [Unterstrasser17].

At this point, we want to mention a more sophisticated method proposed in [Gillespie72, 75, 76]. Here, a waiting time distribution is utilized, which depends on the kernel function. At time  $t$ , a waiting time  $\tau$  is drawn for each droplet pair. Only the pair with the smallest waiting time  $\tau_{\min}$  conducts a collision and the time is propagated to  $t + \tau_{\min}$ . Consequently, the time step is not fixed but varies with each collision event. However, when tested in our box model, the average waiting times were so small, that the required number of executions per time step  $\Delta t_{\text{col}}$  increased significantly, even when using SIPs. Although this approach conserves the time order, we were not able to make it applicable in our case. It shall be mentioned that there are several works using and improving the efficiency of Gillespie's original algorithm, mostly for the coagulation of smaller elements, like during soot formation [Patterson11, 12][Lee15]. The improved algorithms increase complexity and were not tested in this work.

#### 4.4.1 Collection algorithm using SIPs

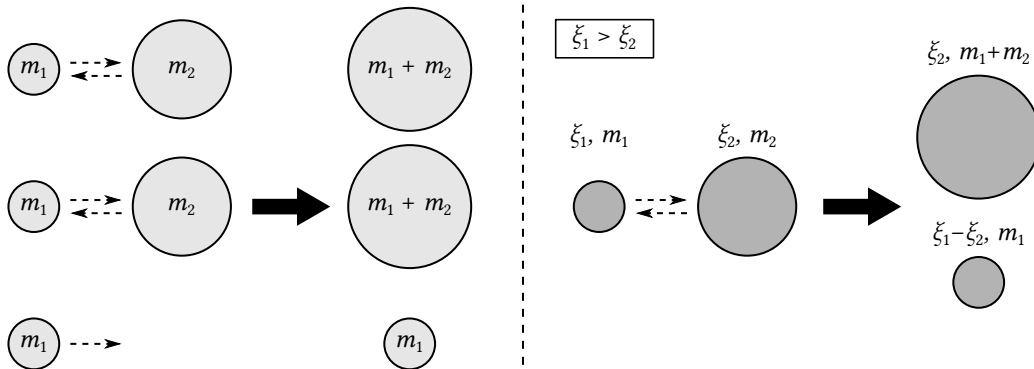


**Figure 4.3:** Two simulation particles with multiplicities  $\xi_k$  and masses  $m_k$  collide and coalesce. In this all-or-nothing scenario, proposed in [Shima09], a number of  $\xi_{\min}$  "real" collisions happen (left side), where  $\xi_{\min}$  is the smaller number of  $\xi_1$  and  $\xi_2$ . In this illustration  $\xi_1 = 3 > \xi_2 = 2$  and SIP 1 loses  $\xi_2$  droplets, while the mass of SIP 2 increases by  $m_1$  (right side).

When representing an ensembles of real particles by a number of SIPs, we need to modify the probability from (4.43) and state what a collision of two super-droplets actually implies. Disregarding minor modifications, we follow the all-or-nothing (AON) method, proposed in [Unterstrasser17], which is based on the algorithm of Shima *et al.* [Shima09] and used in similar form for cloud simulations in [Arabas13, 15].

Let  $N_{\text{sim}}$  be the number of SIPs in a grid cell with volume  $\Delta V$ . For the collection algorithm, the particles are well mixed and each SIP  $n$  is described by its multiplicity, mass and velocity

$(\xi_n, m_n, \mathbf{v}_n)$  and derived radius  $R_n(m_n)$ . The probability for a coagulation of an arbitrary pair of real particles of radii  $R_1$  and  $R_2$  is formulated by (4.43). Considering two SIPs, we now find  $\xi_n$  real particles of radius  $R_n$  ( $n \in \{1, 2\}$ ) and a number of  $\xi_1 \times \xi_2$  represented pairs, each having the same probability. Disregarding the time order, as discussed in Sec. 4.4, we thus find a binomial distribution for the number of collection events during  $\Delta t_{\text{col}}$  with an average of  $P_{\Delta t_{\text{col}}} \xi_1 \xi_2$ .

One could now draw a random number  $\alpha$  from the binomial distribution for each pair of SIPs, reduce the multiplicities by this amount and form a new super-droplet with  $\xi = \alpha$  and  $m = m_1 + m_2$ . Consequently, multiplicities decrease and the number of SIPs increases with time, leading to growing computational effort, thus counteracting the advantages of using super-droplets in the first place. To control the number of SIPs, we apply an algorithm illustrated in Fig. 4.3, abiding the average probability of the binomial distribution:

For each pair of super-droplets with  $(m_1, \xi_1)$  and  $(m_2, \xi_2)$ , define  $\xi_{\min} = \min \{\xi_1, \xi_2\}$  and  $\xi_{\max} = \max \{\xi_1, \xi_2\}$ . The probability for a SIP collection is

$$P_{\Delta t_{\text{col}}}^S = \xi_{\max} P_{\Delta t_{\text{col}}} = \xi_{\max} K(R_1, R_2) \frac{\Delta t_{\text{col}}}{\Delta V}. \quad (4.44)$$

In case of a collection, a number of  $\xi_{\min}$  real particles coagulate, such that the average number of real collections is  $P_{\Delta t_{\text{col}}} \xi_1 \xi_2$ . Assuming  $\xi_1 \geq \xi_2$  without loss of generality, the successful coagulation is described by

$$\xi'_1 = \xi_1 - \xi_2, \quad m'_1 = m_1, \quad \xi'_2 = \xi_2, \quad m'_2 = m_1 + m_2, \quad (4.45)$$

where the primed variables indicate the state after the event. Because the multiplicities are real numbers (contrary to the integer approach in [Shima09]), it is very unlikely that  $\xi_1 = \xi_2$  exactly. Nevertheless, when this case occurs, one of the SIPs is left with  $\xi'_1 = 0$  and could thus be removed from the ensemble, loosing resolution of the mass distribution. To avoid this behavior, we replace the former SIPs with two super-droplets of the same mass  $m' = m_1 + m_2$  and  $\xi'_1 = \chi_S (\xi_1/2)$ ,  $\xi'_2 = (1 - \chi_S) (\xi_1/2)$ . The splitting factor  $\chi_S \in (0, 1)$  prevents SIPs with the same multiplicity and thereby a chain reaction of this special collision case, as proposed in [Unterstrasser17].

In addition to the scheme of Unterstrasser *et al.*, we treat the case when two multiplicities are close,  $(\xi_{\max} - \xi_{\min})/\xi_{\max} < \epsilon_S \ll 1$ . Here, we are left with a marginal number  $\xi'_1$  connected to the smaller mass  $m'_1 < m'_2$ , i.e., with a SIP carrying little additional information at the same computational cost. In this case, we define  $\xi_{\text{ges}} = \xi_1 + \xi_2$  and  $m_{\text{ges}} = \xi_1 m_1 + \xi_2 m_2$  and redistribute the masses and multiplicities by

$$\xi'_1 = \chi_S (\xi_{\text{ges}}/2), \quad \xi'_2 = (1 - \chi_S) (\xi_{\text{ges}}/2), \quad m'_1 = m'_2 = 2 m_{\text{ges}}/\xi_{\text{ges}}, \quad (4.46)$$

which conserves the accumulated mass. In the presented simulations, we use  $\chi_S = 0.7$  and  $\epsilon_S = 1 \times 10^{-5}$ .

When there are large differences in masses and multiplicities, it might also occur that  $P_{\Delta t_{\text{col}}}^S > 1$ . This case is treated as multiple collections, i.e., the SIP with  $\xi_{\min}$  collects  $\xi_{\text{col}} = P_{\Delta t_{\text{col}}}^S \xi_{\min}$  real particles, leading to  $\xi'_1 = \xi_1 - \xi_{\text{col}}$  and  $m'_2 = (\xi_2 m_2 + \xi_{\text{col}} m_1)/\xi_2$ . The whole algorithm during one collision step  $\Delta t_{\text{col}}$  is presented in Algo. 1. Notably, we neglect self collections, i.e., between particles of the same SIP, because the hydrodynamic kernel vanishes for equal velocities.

#### 4.4.2 Collision kernels

In the collision box model, we will compare three different kernels. The first is the sum-of-mass (Golovin) kernel, described in Sec. 3.5.1. The other two are versions of the hydrodynamic kernel with different approaches for the collection efficiency  $E_c$ , explicated in the following. Both

---

**Algorithm 1** Collection algorithm for simulation particles during time step  $\Delta t_{\text{col}}$ 

---

```

1: for  $i = 1 \dots (N_{\text{SIP}} - 1)$  do
2:   for  $j = (i + 1) \dots N_{\text{SIP}}$  do
3:     if  $\xi_i \leq \xi_j$  then
4:        $\min \leftarrow i$ ;  $\max \leftarrow j$ 
5:     else
6:        $\min \leftarrow j$ ;  $\max \leftarrow i$ 
7:     end if
8:      $P_{\text{crit}} \leftarrow \xi_{\max} K(m_i, m_j) \Delta t_{\text{col}} / \Delta V$ 
9:     if  $P_{\text{crit}} > 1$  then
10:       $\xi_{\text{col}} \leftarrow P_{\text{crit}} \xi_{\min}$ 
11:       $m_{\min} \leftarrow (\xi_{\min} m_{\min} + \xi_{\text{col}} m_{\max}) / \xi_{\min}$ 
12:       $\xi_{\max} \leftarrow \xi_{\max} - \xi_{\text{col}}$ 
13:    else if  $\text{rand}(0, 1) < P_{\text{crit}}$  then
14:      if  $(\xi_{\max} - \xi_{\min}) / \xi_{\max} < \varepsilon_S$  then
15:         $\xi_{\text{ges}} \leftarrow \xi_{\min} + \xi_{\max}$ 
16:         $m_{\text{ges}} \leftarrow \xi_{\min} m_{\min} + \xi_{\max} m_{\max}$ 
17:         $m_{\min} \leftarrow 2 m_{\text{ges}} / \xi_{\text{ges}}$ 
18:         $m_{\max} \leftarrow m_{\min}$ 
19:         $\xi_{\max} \leftarrow \chi_S \xi_{\text{ges}} / 2$ 
20:         $\xi_{\min} \leftarrow (1 - \chi_S) \xi_{\text{ges}} / 2$ 
21:      else
22:         $m_{\min} \leftarrow m_{\min} + m_{\max}$ 
23:         $\xi_{\max} \leftarrow \xi_{\max} - \xi_{\min}$ 
24:      end if
25:    end if
26:  end for
27: end for

```

---

hydrodynamic kernels are used in several numerical cloud studies, e.g. [Seeßelberg96, Bott98, Wang07, Unterstrasser17].

#### LONG KERNEL

Long fitted values for the collision efficiencies of cloud droplet pairs with radii  $R_1 > R_2$  from [Shafrir71] and [Klett73] to parametrize the function  $E_c = k_1 R_1^2 (1 - k_2/R_2)$  in the range  $R_1 \leq 50 \mu\text{m}$  and  $E_c = 1$  for  $R_1 > 50 \mu\text{m}$  [Long74]. We will use a version, which was slightly modified in [Bott98] to be numerically stable for small  $R_1$ , but still refer to it as the *Long* kernel.

#### HALL KERNEL

Seeßelberg combined results from [Davis72] and [Jonas72] for droplets with  $\min \{R_1, R_2\} \leq 30 \mu\text{m}$  and tabulated values from [Hall80] for larger radii with wake capture effects presented in [Lin75] to build a table for the collection efficiency  $E_c(R_1, R_2)$ , referred to as *Hall* kernel [Seeßelberg96].

## 4.5 Update scheme

We are now able to present the complete update scheme for particles and atmospheric variables during one advection time step  $\Delta t_{\text{adv}}$  with refined steps  $h = \Delta t_{\text{adv}} / N_h \leq \Delta t_{\text{col}} = \Delta t_{\text{adv}} / N_{\text{col}} \leq \Delta t_{\text{adv}}$

and running time  $\tau$ . Applied values are  $\Delta t_{\text{adv}} = 1 \text{ s}$ ,  $N_h = 10$ ,  $N_{\text{col}} \in \{2, 10\}$ . The default number of Newton iterations during the implicit mass calculation is set to three.

- 
- A)  $h \leftarrow \Delta t_{\text{adv}}/N_h$ ,  $\Delta t_{\text{col}} \leftarrow \Delta t_{\text{adv}}/N_{\text{col}}$
  - B) **For all** particles:  $\mathbf{x} \leftarrow \mathbf{x} + \mathbf{v} h/2$
  - C)  $\Delta G_{\text{adv}} \leftarrow h f_{\text{adv}}(G)$
  - D) **If** ( $N_{\text{col}} == 2$ ): **Collision step** (time step  $\Delta t_{\text{col}}$ ) in all cells
  - E) SUBLOOP 1: **For**  $n_h = 0 .. (N_h/2) - 1$  ( $\Rightarrow \tau = 0, h, \dots, \Delta t_{\text{adv}}/2$ ):
    - i) **For all** cells  $[i, j]$ :  $\Delta m_l[i, j] \leftarrow 0$
    - ii) **For all** particles  $p$ :
      - 1. **If** ( $N_{\text{col}} == N_h$ ): **Collision step** (time step  $\Delta t_{\text{col}}$ ) in all cells
      - 2.  $T_p \leftarrow T[i, j]_p$
      - 3.  $(\Delta m_p, \gamma) \leftarrow g_{\text{impl}}(\mathbf{x}, m_p, T_p)$
      - 4.  $m_p \leftarrow m_p + \Delta m$
      - 5.  $\Delta m_l[i, j]_p \leftarrow \Delta m_l[i, j]_p + \Delta m_p$
      - 6.  $\mathbf{v} \leftarrow [\mathbf{v} + (\mathbf{u}(\mathbf{x}) k_d + \mathbf{g}) h] / (1 + k_d h)$ , where  $k_d = k_d(|\mathbf{u}(\mathbf{x}) - \mathbf{v}|, m_p, T_p, r_v[i, j]_p)$
      - 7.  $\mathbf{x} \leftarrow \mathbf{x} + \mathbf{v} h$
      - 8.  $[i, j]_p \leftarrow [i, j](\mathbf{x})$
- 

**Array operations** iii) to vii) (affecting all cells):

- iii)  $G \leftarrow G + \Delta G_{\text{adv}}$
- iv)  $r_v \leftarrow r_v - \Delta m_l / (\Delta V \rho_{\text{dry}})$
- v)  $\frac{\Theta}{T} \leftarrow \frac{\Theta}{T}(\Theta, r_v)$
- vi)  $\Theta \leftarrow \Theta + \frac{L_v \Delta m_l}{\Delta V c_{\text{dry}} \rho_{\text{dry}} (1 + \alpha_v r_v)} \frac{\Theta}{T}$
- vii) Update  $(p, T, e_s, S)$  and  $(L_v(T), K_Q(T), D_v(T, p_f), c_{p,f}(r_v), \sigma_p(w_s, T), \mu_f(T))$

SUBLOOP 1 END

- F)  $\Delta G_{\text{adv}} \leftarrow 2h f_{\text{adv}}(G) - \Delta G_{\text{adv}}$
- G) **If** ( $N_{\text{col}} \in \{1, 2\}$ ): **Collision step** (time step  $\Delta t_{\text{col}}$ ) in all cells
- H) SUBLOOP 2: **For**  $n_h = 0 .. (N_h/2) - 2$  ( $\Rightarrow \tau = \Delta t_{\text{adv}}/2, \Delta t_{\text{adv}}/2 + h, \dots, \Delta t_{\text{adv}} - h$ ):
  - i) **For all** cells  $[i, j]$ :  $\Delta m_l[i, j] \leftarrow 0$
  - ii) **For all** particles  $p$ :

→ 1. to 8.

→ iii) to vii)

SUBLOOP 2 END (The time is  $\tau = \Delta t_{\text{adv}} - h$ : Propagate  $\mathbf{v}$  and  $m$  by  $h$  and  $\mathbf{x}$  by  $h/2$ )

- I) **For all** cells  $[i, j]$ :  $\Delta m_l[i, j] \leftarrow 0$
- J) **For all** particles  $p$ :
  - 1. to 6.
  - 7b.  $\mathbf{x} \leftarrow \mathbf{x} + \mathbf{v} h/2$
  - 8.  $[i, j]_p \leftarrow [i, j](\mathbf{x})$

K) → iii) to vii)

L) **end:**  $t \leftarrow t + \Delta t_{\text{adv}}$

---

## 4.6 Implementation

The simulation code was written in Python (V. 3.7), utilizing the NumPy and SciPy packages for numeric and scientific programming with multi-dimensional arrays.<sup>1</sup> As dynamic, high level language with efficient syntax, Python allows high productivity during the coding process and provides versatile environments for data analysis and visualization. On the other hand, being an interpreted language, it generally performs significantly worse than compiled alternatives like C++ and Fortran. There are numerous use cases, where the differences in computation speed are most distinct. One of these bottlenecks, also when using NumPy, is the processing of loop-iterations, which are however inevitable in most physical applications. To increase performance, we apply the just-in-time (JIT) compiler Numba<sup>2</sup> (V. 0.46) [Lam15]. This package translates decorated Python functions to machine code at run time. The possible acceleration depends strongly on the algorithm in question. For basic applications, the speedup compared to pure Python is in the order of 10 to 1000 and computation speeds of C or Fortran can be reached [Lam15, Marowka18]. Parallelization for CPUs and GPUs is possible in Python, using Numba or other packages, but was beyond the scope of this work and thus not implemented in our code. However, this was not a major constraint for the overall computation output, because, for statistical analysis, we required at least 50 independent simulations for each set of chosen parameters, which could be performed simultaneously on a cluster of multiple cores.

The simulation program is freely available under an open GitHub repository.<sup>3</sup> All non-official modules and packages provided therein, including the main Python scripts `run_box_model` and `cloudMP` as well as codes for data analysis and visualization, were written from scratch by the thesis' author in course of this work. The repository represents the program state at the date of submission and will not be changed afterwards in any way.

### 4.6.1 Procedure

First, spatial grid and particles are initialized and stored to files by running `generate_grid_and_particles.py`. Several instances can be started at once using the bash script `run_gen_grid.sh`. Therein, the parameters  $N_{\text{SIP}}$  (for both spectral modes),  $\Delta x$ ,  $\Delta z$ , the solute type (NaCl for sodium chloride or AS for ammonium sulfate) and the random seed for the particle generation must be set. The function creates an object of the `Grid` class, which holds the basic parameters as well as several arrays for the fluid velocity field and thermodynamic properties. These fields and arrays for particle masses, positions and velocities are initialized according to the layering process described in Sec. 6.1.2. Finally, the function `save_grid_and_particles_full` is called, which, at any time, is able to store a complete, reconstructable image of the system state on the hard disc, using the efficient binary data format `.npy` for NumPy arrays.

Subsequently, a number of instances of the main script `cloudMP.py` can be started simultaneously using the executable `run_cloudMP.sh`. It loads a previously stored system state and simulates for a time interval defined by  $t_{\text{start}}$  and  $t_{\text{end}}$ . The parameter  $N_{\text{col}}$  as well as the kernel type (Long, Hall or Golovin), kernel method (tabular or analytic), simulation type (spin up, with or without collisions) and random seed for the particle collision algorithm must be set. The program stores scalar fields and droplet properties after chosen intervals. It is also possible to select a number of tracer particles, for which the trajectories are written out more often. Each storage interval consists of a serial loop over a number of advection steps, which are the main units of the program. The processing during one advection step is given by the update scheme in Sec. 4.5.

---

<sup>1</sup><https://www.python.org/>    <https://numpy.org/>    <https://www.scipy.org/>

<sup>2</sup><https://numba.pydata.org/>

<sup>3</sup><https://github.com/JanKBohrer/ProgramMasterthesis>

# 5 COLLISION BOX MODEL

## 5.1 Description

The coalescence algorithm is tested in a box model motivated by Wang *et al.* and Unterstrasser *et al.* [Wang07, Unterstrasser17]: At time  $t = 0$  a number of  $N_0 = \Delta V \text{DNC}_0$  water droplets, represented by  $N_{\text{SIP}}$  simulation particles are located in a fixed volume  $\Delta V$ . Over time, the particles collide and coalesce as described by the Kernel-formulation in Sec. 4.4. Besides the collisions, all interactions and external forces are switched off. Consequently, the particles are constrained to remain in the given volume and there is no mass exchange by condensation or evaporation. As before, we assume the particles to be well mixed in  $\Delta V$ , i.e., each particle has the same probability to be anywhere in this volume. The super-droplet ensemble is initialized with an exponential mass distribution (cf. Sec. 3.5),

$$f_m(m, 0) = \frac{\text{DNC}_0}{\bar{m}_0} \exp\left(-\frac{m}{\bar{m}_0}\right), \quad (5.1)$$

where  $\bar{m} := \int dm \tilde{f}_m(m) m = \text{LMC}/\text{DNC}$  is the average droplet mass, calculated using the PDF  $\tilde{f}_m = f_m/\text{DNC}$ . The SIP generation method is described in Sec. 4.2.1. We use the same initial values as in [Unterstrasser17],  $\text{DNC}_0 = 2.968 \times 10^8 \text{ m}^{-3}$ ,  $\text{LMC}_0 = 1 \text{ g/m}^3$  and thus  $\bar{m}_0 = 3.4 \times 10^{-12} \text{ kg}$ , corresponding to  $R(\bar{m}_0) = 9.3 \mu\text{m}$ . Over time, the particles coagulate and  $f_m$  decreases in regions with smaller  $m$  and increases in regions with larger  $m$ , while the concentration (DNC) decreases and the overall mass (represented by LMC) is conserved.

The applied algorithm is an attempt to compute the evolution of an ensemble of colliding droplets, using stochastic, discrete particle methods. We will present results for the introduced kernels of Golovin, Long and Hall (Sec. 4.4.2). The set-up and algorithms are essentially the same as in the box model of Unterstrasser *et al.* [Unterstrasser17] (see Sec. 4.4.1 for a description of minor differences). Since droplet dynamics are not considered, we can not propagate the velocity as in the full simulations. For the required values in the hydrodynamic kernel, we use semi-empirical formulas  $v_{\text{sed}}(R)$  from [Beard76], based on experimental measurements of the size-dependent sedimentation velocity of cloud droplets.

In case of the Golovin kernel, a reference is given by the analytic solution of the stochastic coalescence equation [Golovin63],

$$f_m(m, t) = \frac{\text{DNC}_0}{\bar{m}_0} (1 - \chi_G(t)) \exp\left[-\frac{m}{\bar{m}_0}(1 + \chi_G(t))\right] \frac{I_1\left(2\frac{m}{\bar{m}_0}\sqrt{\chi_G(t)}\right)}{\frac{m}{\bar{m}_0}\sqrt{\chi_G(t)}}, \quad (5.2)$$

where  $\chi_G(t) = 1 - \exp(-b_G \text{DNC}_0 \bar{m}_0 t)$  and  $I_1$  is the modified Bessel function of first kind and order. In case of the other two kernels, we choose fine resolved bin model simulations presented in [Wang07] as reference, according to the procedure in [Unterstrasser17].

## 5.2 Results

Corresponding to [Unterstrasser17], we performed one hour simulations with collision time step  $\Delta t_{\text{col}} = 1$  s for the Golovin kernel and  $\Delta t_{\text{col}} = 10$  s for the hydrodynamic kernels to compute the time evolution of particle ensembles, represented by  $\{\{\xi_n(t), m_n(t)\}\}$ . In the following, the behavior of the particle size spectrum with time is presented. To reduce uncertainties,  $N_{\text{sim}} = 500$  independent simulations were performed for every parameter setup, each initialized with another random number seed. Distribution functions, moments and their estimated standard deviation are evaluated with  $N_{\text{bin}} = 50$  bins as described in Sec. 4.2.2. For better visualization of the size spectra, we will use the logarithmic radius distribution function  $g_{\ln(R)} := 3m^2 f_m = mR f_R$  with

$$\int d(\ln R) g_{\ln(R)}(R) = \text{LMC}. \quad (5.3)$$

### 5.2.1 Golovin kernel

Figure 5.1 shows simulation results for the Golovin kernel compared to the analytic reference solution. The droplet number concentration  $\lambda_0$  decreases, while the second and third moments increase with time ( $\lambda_0$  and  $\lambda_2$  show and  $\lambda_3$  approaches linear behavior on a logarithmic axis). Consequently, the size spectrum gets flatter and broader, allowing larger maximum radii. As expected, the liquid mass content  $\lambda_1$  is conserved during all simulations.

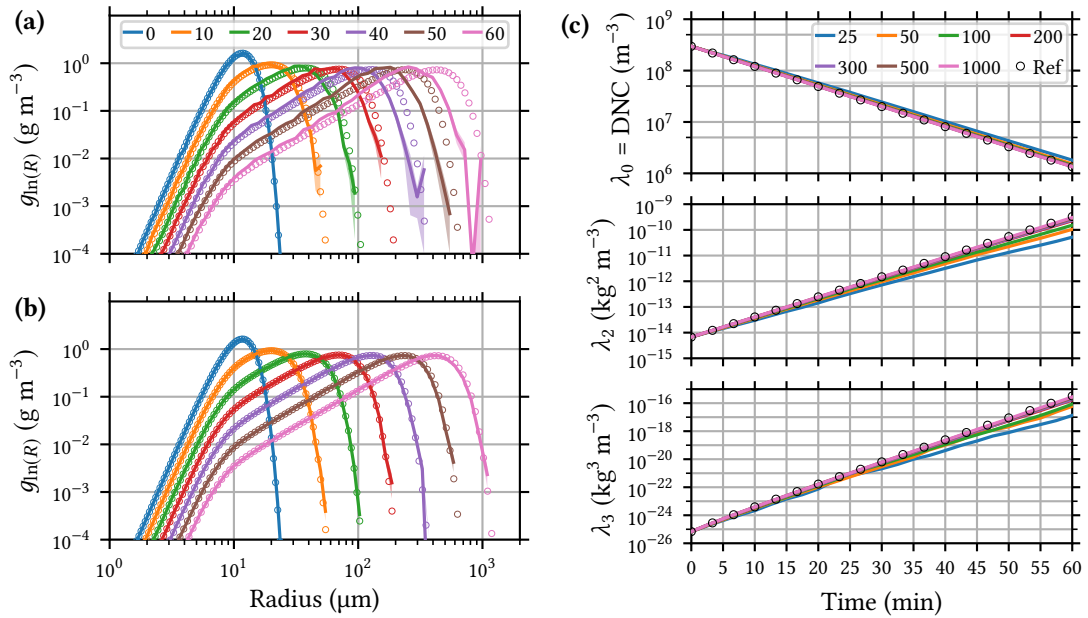


**Figure 5.1:** Simulation results (solid lines) and analytic reference (Ref.) solution (circles) for the Golovin kernel. The time evolution of the distributions is shown for  $N_{\text{SIP}} = 50$  (a) and  $N_{\text{SIP}} = 1000$  (b), where error bars are indicated by shaded areas of the same color. Times are given in the legend (in minutes). Influence of  $N_{\text{SIP}}$  on the time evolution of the moments  $\lambda_k$  is presented in (c).

The number of simulation particles per box has large influence on the time evolution of the size spectra and their fluctuations. In Fig. 5.1(a,b), we compare two setups with  $N_{\text{SIP}} = 50$  and  $N_{\text{SIP}} = 1000$ . For the smaller SIP numbers, decisive deviations from the reference are visible for  $t > 20$  min, which can not be explained by the error bars and thus indicate systematic behavior.

The deviations can be reduced significantly, when using a larger number of particles. This is also evident, when analyzing the evolution of moments in Fig. 5.1c. With increasing  $N_{\text{SIP}}$ , we note a continuous converging behavior for all three moments towards the reference. The illustration gives an overview of the general trend, but, even on a logarithmic scale, shows insufficient resolution to make precise statements. A detailed presentation of the relative deviations  $|\lambda_k - \lambda_{\text{ref}}| / \lambda_{\text{ref}}$  and relative errors  $\text{SD}(\lambda_k) / \lambda_{\text{ref}}$  is given in the Appendix (Fig. D.1) and enables some relevant conclusions.

Relative deviations are larger for moments 2 and 3 than for the zeroth moment. They increase with time and show maxima of 30 % ( $\lambda_0$ ) and 100 % ( $\lambda_{2,3}$ ) for  $N_{\text{SIP}} = 25$ , which can be reduced to 0.2 % and 10 %, respectively, for  $N_{\text{SIP}} = 1000$ . Notably, there still is significant improvement, when going from 500 to 1000 SIPs (cf. Fig. D.4). The convergence is thus not yet reached. Nevertheless, we decided to invest no more simulation time at this point, because the zeroth moment reached a level of accuracy, which is covered by its estimated standard deviation. Relative errors are in the order of (3, 1, 1) % ( $\lambda_{0,2,3}$ ) for the smallest number of SIPs and (0.2, 1, 3) % for  $N_{\text{SIP}} = 1000$ .

### 5.2.2 Long Kernel

In case of the Long Kernel, we use a fine resolved state-of-the-art bin model by Wang, Xue and Grabowski as reference for our particle based scheme [Wang07]. In contrast to the Golovin kernel, we find a splitting of the size spectrum, where a second maximum at  $R > 1000 \mu\text{m}$  is forming at cost of the decreasing initial maximum at around  $10 \mu\text{m}$  (cf. Fig. 5.2). Again, the moments show converging behavior and again, the reference solution is not reached entirely. Relative deviations are reduced from  $(1000 \pm 200, 100 \pm 1, 100 \pm 2) \%$  ( $\lambda_{0,2,3}$ ) for  $N_{\text{SIP}} = 25$  to  $(20 \pm 1, 2 \pm 0.9, 2 \pm 1) \%$  for  $N_{\text{SIP}} = 15\,000$  (cf. Appendix, Fig. D.2).

To analyze the convergence behavior after one hour simulation time, we illustrate relative deviations  $\text{RD}_k := |\lambda_k - \lambda_{\text{maxSIP}}| / \lambda_{\text{maxSIP}}$  between moments  $\lambda_k$  of several  $N_{\text{SIP}}$  and values  $\lambda_{\text{maxSIP}}$  for the largest SIP number  $N_{\text{SIP}} = 15\,000$  in Fig. 5.3. Considering the zeroth moment, we determine a power law of the kind

$$\text{RD}_0(N_{\text{SIP}}) = c N_{\text{SIP}}^{-a}, \quad (5.4)$$

with exponent  $a = 1.17 \pm 0.04$  by fitting linearly on a log-log scale. In the cases of moments  $\lambda_{2,3}$ , the trend is not as evident. We approximate the characteristics of the curves in Fig. 5.3 by logarithmic functions of the kind

$$\text{RD}_k(N_{\text{SIP}}) = c - a \ln(N_{\text{SIP}}). \quad (5.5)$$

For  $\lambda_2$ , the slope changes significantly at higher SIP numbers and we divide the range into two intervals for  $N_{\text{SIP}} \leq 1000$  and  $N_{\text{SIP}} \geq 2000$ . This provides a piecewise approximation to the actual, more complex function. Fitting parameters are shown in Table 5.1. After a time of one hour, the moments of our simulations with 10 000 and 15 000 SIPs agree up to a relative deviation of 1 %, indicating that convergence is nearly reached (cf. Figs. 5.3 (below) and D.5 (Appendix) for more detail). It is thus questionable, if the remaining 20 % difference to the reference solution can be removed by using even more particles.

Our box model simulations and illustrations are motivated by the work in [Unterstrasser17]. In the original paper, Unterstrasser *et al.* presented corresponding plots for  $N_{\text{SIP}} = 25$  to 2000, showing values of the zeroth moment for 2000 SIPs, which are well below our values (by a factor of 4) and even below the reference bin model (by a factor of 2). After personal communication with the first author and comparison of the codes, the most recent repetition of their simulations now provides results, which coincide with the ones presented in this thesis.

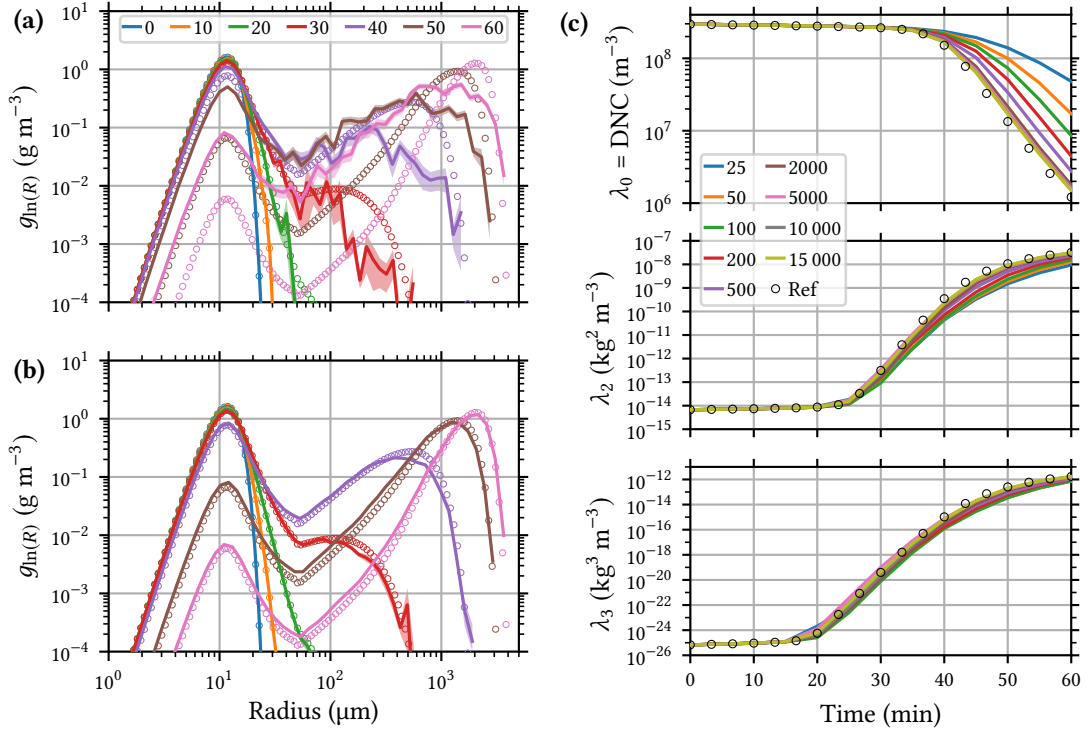


**Figure 5.2:** Simulation results (solid lines) and bin model reference (Ref.) solution (circles) from [Wang07] for the Long kernel. The time evolution of the distributions is shown for  $N_{\text{SIP}} = 50$  (a) and  $N_{\text{SIP}} = 15\,000$  (b), where error bars are indicated by shaded areas of the same color. Times are given in the legend (in minutes). Influence of  $N_{\text{SIP}}$  on the time evolution of the moments  $\lambda_k$  is presented in (c).

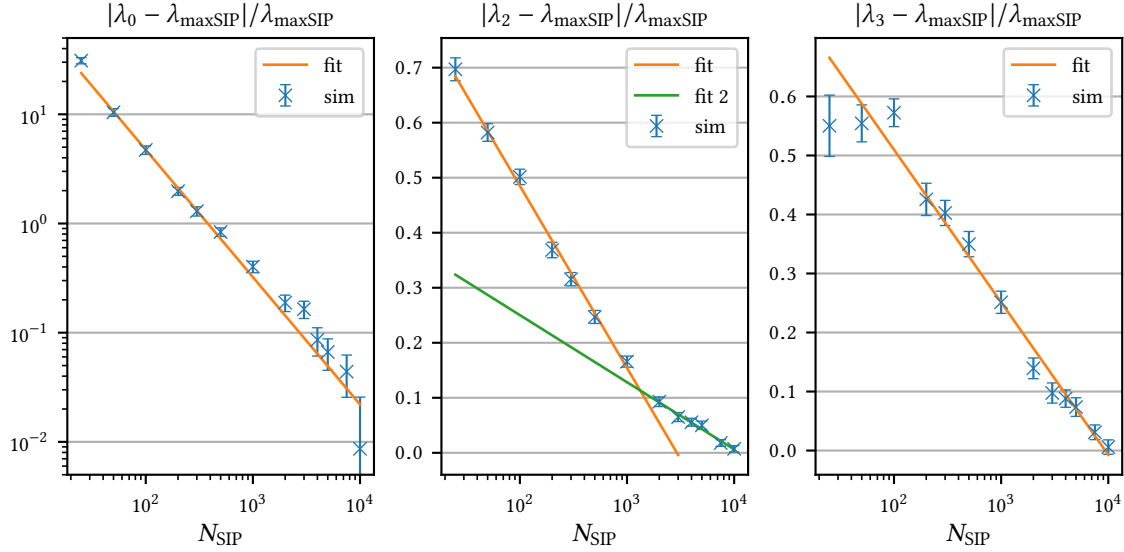


**Figure 5.3:** Convergence behavior for the Long kernel. The plots show relative deviations to the moments  $\lambda_{\text{maxSIP}}$  of the largest SIP number  $N_{\text{SIP}} = 15\,000$  after a simulation time of one hour. Fitting functions and parameters are given by (5.4) for  $\lambda_0$ , (5.5) for  $\lambda_{2,3}$  and in Table 5.1.

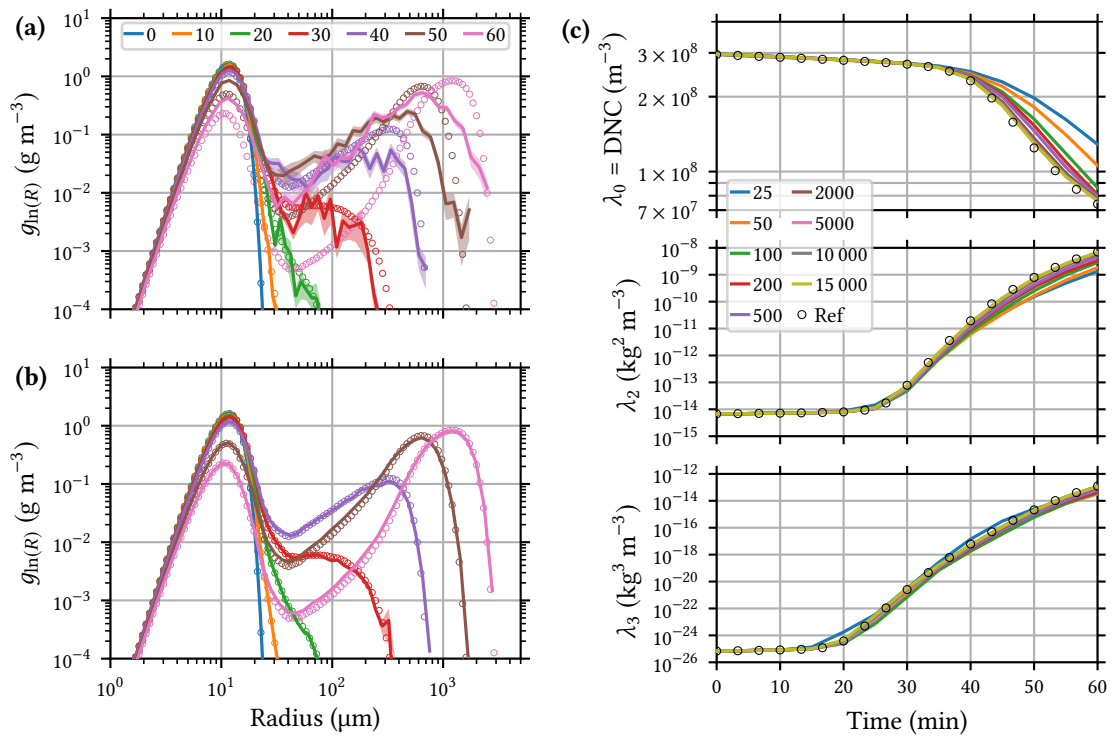


**Figure 5.4:** Simulation results (solid lines) and bin model reference (Ref.) solution (circles) from [Wang07] for the Hall kernel. The time evolution of the distributions is shown for  $N_{\text{SIP}} = 50$  (a) and  $N_{\text{SIP}} = 15\,000$  (b), where error bars are indicated by shaded areas of the same color. Times are given in the legend (in minutes). Influence of  $N_{\text{SIP}}$  on the time evolution of the moments  $\lambda_k$  is presented in (c).

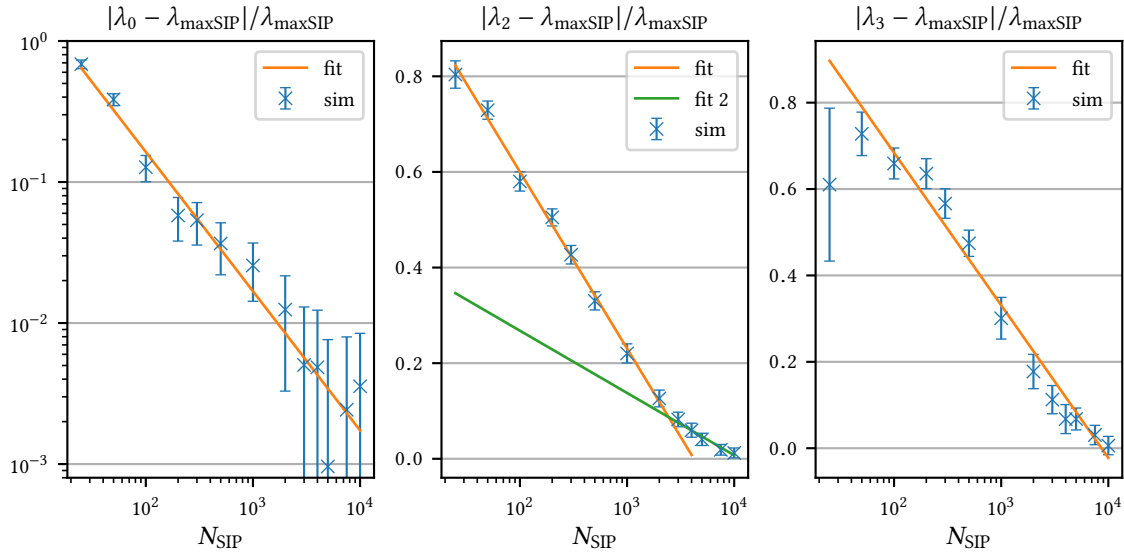


**Figure 5.5:** Convergence behavior for the Hall kernel. The plots show relative deviations to the moments  $\lambda_{\text{maxSIP}}$  of the largest SIP number  $N_{\text{SIP}} = 15\,000$  after a simulation time of one hour. Fitting functions and parameters are given by (5.4) for  $\lambda_0$ , (5.5) for  $\lambda_{2,3}$  and in Table 5.1.

**Table 5.1:** Fitted parameters for the functions (5.4) ( $\lambda_0$ ) and (5.5) ( $\lambda_{2,3}$ ). For  $\lambda_2$ , the  $N_{\text{SIP}}$  range is divided into two intervals (1, 2), and the function is approximated piecewise. Interval 1 includes  $N_{\text{SIP}} \leq 1000$  and  $N_{\text{SIP}} \leq 2000$  for the Long and Hall kernel, respectively.

Moment	Long kernel		Hall kernel	
	$a$	$c$	$a$	$c$
$\lambda_0$	$1.17 \pm 0.04$	$1020 \pm 170$	$0.99 \pm 0.06$	$15.4 \pm 5.8$
$\lambda_2$ (1)	$0.14 \pm 0.005$	$1.15 \pm 0.03$	$0.161 \pm 0.004$	$1.33 \pm 0.02$
$\lambda_2$ (2)	$0.053 \pm 0.004$	$0.49 \pm 0.03$	$0.057 \pm 0.006$	$0.53 \pm 0.05$
$\lambda_3$	$0.11 \pm 0.005$	$1.03 \pm 0.04$	$0.153 \pm 0.007$	$1.39 \pm 0.06$

### 5.2.3 Hall Kernel

For the Hall kernel, we again use the bin model reference from [Wang07]. As for Longs' Kernel, we find a splitting of the size spectrum, but with less pronounced minimum between the two maxima, as can be seen in Fig. 5.4. Furthermore, the initial maximum at  $R = 10 \mu\text{m}$  is not degraded as quickly, which leads to a smaller reduction of the droplet number concentration ( $\lambda_0$ ) with time. Zeroth and second moment again show continuous converging behavior, while the third moment fluctuates about the reference. Nevertheless, the result of the simulation with the most SIPs is still closest to the reference. Relative deviations of the three moments after one hour show quite similar values in this case and can be reduced from  $(100 \pm 10)\%$  for  $N_{\text{SIP}} = 25$  to  $(3 \pm 1)\%$  for  $N_{\text{SIP}} = 15\,000$  (cf. Fig. D.3 in the Appendix). The droplet number concentration is thus much closer to the reference as for the Long kernel, which is also detectable in the spectra in Fig. 5.4b, which cover the first maximum more accurately.

A convergence analysis for the relative deviations after one hour is illustrated in Fig. 5.5 and shows similar behavior as for the Long kernel, i.e., a negative power law (5.4) with slightly smaller exponent  $a = 0.99 \pm 0.06$  for  $\lambda_0$  and logarithmic functions (5.5) for  $\lambda_{2,3}$ . In case of  $\lambda_2$ , the range of  $N_{\text{SIP}}$  is now divided into the intervals  $N_{\text{SIP}} \leq 2000$  and  $N_{\text{SIP}} \geq 5000$ . The fitting parameters are listed in 5.1. Furthermore, our results imply that convergence is almost reached, because after one hour the change when increasing from 10 000 to 15 000 SIPs is below 0.8 % for moments  $\lambda_{0,3}$  and below 2 % for  $\lambda_2$  (cf. Figs. 5.5 (below) and D.6 (Appendix) for more detail).

## 5.3 Conclusions

Our results for all kernels coincide with the most recent discrete particle simulations of the authors of [Unterstrasser17], who use an equivalent algorithm and can be brought within 3 % of the reference values for kernels from Golovin (analytic) and Hall (bin model), when using 1000 and 15 000 SIPs, respectively. In case of the Long kernel, the deviation of  $\lambda_0$  still lies at 20 %, while the other two moments are sufficiently close to the reference. We conclude that the main features of the size spectrum shape agree reasonably well, while the overall particle concentration is depleted somewhat slower in our algorithm, indicating a reduced rate of successful collections. It shall be emphasized that both methods, the bin model and the particle based scheme, are numerical techniques to solve the same physical problem and each is prone to finite size errors. It is not evident, which one provides a more precise approximation of the physical process in question.

Concerning the following simulations, we want to make some statements about the effects of the applied particle number per cell. Our results indicate that convergence is reached up to about 1 %, when  $N_{\text{SIP}}$  is in the range of 15 000. The grid of the stratocumulus test case (Sec. 6.1) will be constructed of  $75 \times 75 = 5625$  cells, which would imply about  $100 \times 10^6$  particles in total to reach

convergence. Since this number is not manageable with the available resources, we will choose a default of 64 SIPs per cell, in accordance with simulations presented in [Arabas15]. In the box model, the difference between  $N_{\text{SIP}} = 50$  and  $N_{\text{SIP}} = 15\,000$  is in the order of (1000, 70, 70) % ( $\lambda_{0,2,3}$ ) for the Long kernel and (40, 70, 70) % for the Hall kernel. This also confirms previous findings that more numerical effort is necessary to handle the Long kernel compared to the Hall kernel [Unterstrasser17].

Due to these major deviations, we would expect significant reduction of the collision process efficiency. We propose that this reduction arises partly due to coarser coverage of the particle size spectrum, when using less SIPs. In the consequence, the internal interactions of some underrepresented ranges of the distribution function are omitted, while the interaction of other ranges is overrepresented. Regarding this, we want to make the important point, that in the full cloud model, we consider not only one, but several grid cells, which are not isolated from each other. Particles can rather move to other boxes and thereby change their ensemble. The movement speed and thus the rate of change will depend on the particle weight. Consequently, ensembles do not remain together, but will change their composition continuously.

Since each cell is initialized with another particle ensemble realization, the coverage of the size spectrum is increased, when considering not only one, but a number of adjacent cells. In spite of the fact that a collision step only includes particles from one ensemble, we expect significant improvement, when ensembles are allowed to mix and thereby exchange information about the local size spectrum. This proposition is supported by recent, unpublished box model simulations with connected cells by the authors of [Unterstrasser17] (acquired in personal communication). We will in any case conduct a finite size analysis of the test case within the range of our possibilities, by comparing simulations with 32, 64 and 128 initial particles per cell (Sec. 6.4) and attempt to make some statements about convergence behavior. To study the stability of our program, we will further use the numerically more challenging Long kernel as default and include a comparison to results for the Hall kernel.



# 6

## TEST CASE: DRIZZLING STRATOCUMULUS

The previously mentioned test case was designed by Grabowski, Lebo and Xue for the 8<sup>th</sup> international cloud modeling workshop 2012 [Muhlbauer13]. It is based on observations of drizzling stratocumulus clouds over subtropical easter Pacific and focuses on microphysical processes inside closed circulation cells. Setups of the idealized kinematic velocity field, total water mixing ratio and liquid potential temperature as well as the shape of the initial dry particle number concentration are based on VOCALS campaign measurements from October 2008 [Allen11]. The design enables detailed investigation of cloud concentration nuclei processing inside marine stratocumulus and should lead to progressive formation of drizzle drops, i.e., rain droplets with considerable sedimentation velocities, which are nevertheless mostly too small to reach the earth surface before evaporating below the cloud base.

### 6.1 Initial atmospheric setup and saturation adjustment

#### 6.1.1 Particle dry size distribution

For a given simulation setup, we assume that all CCNs and droplets contain the same type of solute material. As default, we choose ammonium sulfate and, in due course, compare to additional simulations with sodium chloride. The number density of particles with dry radius  $R_s$  ( $s$  for solute) is given by a bimodal log-normal size distribution,

$$f_{R,s}(R_s) = \sum_k \frac{\text{DNC}_k}{\sqrt{2\pi} \ln(\sigma_{R,k}^*) R_s} \exp \left[ - \left( \frac{\ln(R_s/\mu_{R,k}^*)}{\sqrt{2} \ln(\sigma_{R,k}^*)} \right)^2 \right], \quad (6.1)$$

where  $k \in \{1, 2\}$  and

$$\begin{aligned} \sigma_{R,1}^* &= 1.4, & \mu_{R,1}^* &= 0.02 \mu\text{m}, & \text{DNC}_1 &= 60 \text{ cm}^{-3}, \\ \sigma_{R,2}^* &= 1.6, & \mu_{R,2}^* &= 0.075 \mu\text{m}, & \text{DNC}_2 &= 40 \text{ cm}^{-3}, \end{aligned} \quad (6.2)$$

as used in [Arabas15], based on [Allen11, Table 4]. Here,  $\mu_{R,k}^*$  and  $\sigma_{R,k}^*$  are the geometric expectation value and standard deviation, respectively. It turns out that the corresponding mass distribution  $f_{m,\text{dry}}$  is also of log-normal type with parameters  $\mu_{m,k}^* = 4\pi \rho_s \mu_{R,k}^*/3$  and  $\sigma_{m,k}^* = (\sigma_{R,k}^*)^3$ , where  $\rho_s$  is the solute dry density. We can thus directly apply the SIP generation method described in Sec. 4.2.1. The connection of log-normal and normal distribution and between arithmetic and geometric moments is elaborated in the Appendix, Sec. C.2.

#### 6.1.2 Layering of the atmosphere

The atmosphere is set up under hydrostatic conditions and the restrictions of constant  $r_{\text{tot}}$  and  $\Theta_I$  listed in Eqs. (2.34) by the following procedure: Let  $z_j = z_0 + j \Delta z$  and  $b(z_j) = b_j$  for any scalar quantity  $b$ , where  $z_j$  are the vertical positions of the cell corners, i.e., cell  $[i, j]$  lies between  $z_j$  and  $z_{j+1}$ . We set the grid cell sizes  $\Delta x = X/N_x$ ,  $\Delta z = Z/N_z$  with default values  $N_x = N_z = 75$  and a

small slice  $\Delta y = 1$  m and start an iterative layering from the ground,  $z_0 = 0$ , with  $p_0 = 1015$  hPa. For the condensation of water vapor during initialization, we use the implicit scheme from Eq. (4.42) with time step  $\Delta t_{\text{init}}$  and artificially fixed particle positions. **For each** level  $j$ , the bottom pressure  $p_j$  is already given by the previous step and we can describe the applied algorithm as:

1. Use the SinSIP method described in Sec. 4.2.1 with the dry size distribution (6.1) to generate an ensemble of dry masses with an average number of  $N_{\text{SIP}}$  super-particles in each cell  $[i, j]$  of layer  $j$ , i.e., for  $i = 0, \dots, N_x - 1$ . Let the dry particles take up a small fraction of liquid water from the air, such that they can be considered as solution droplets, corresponding to Sec. 2.1. The particle positions are initialized randomly in each cell by drawing numbers from a uniform distribution.
2. Use (2.41) to calculate estimates of  $p(z_{j+1})$ ,  $T_{\text{avg}} = (T(z_j) + T(z_{j+1}))/2$ ,  $\rho_{\text{dry,avg}} = (\rho_{\text{dry}}(z_j) + \rho_{\text{dry}}(z_{j+1}))/2$ , assuming an atmosphere with  $r_v = r_{\text{tot}}$ .
3. Let water vapor condense on the particles in a loop using time step  $\Delta t_{\text{init}}$ . The positions of all particles are artificially fixed. In this saturation adjustment loop
  - a) Calculate and apply the change in liquid water mass  $\Delta m_l^k$  for each particle  $k$  in the layer during  $\Delta t_{\text{init}}$  and thereby the total change in each cell  $\Delta m_l[i, j]$  and the accumulated change in the layer  $\Delta m_l = \sum_i \Delta m_l[i, j]$ . Update the liquid water mass  $m_l[i, j]$  and the water vapor mass  $m_v[i, j]$ . Stop the loop, when the relative change of liquid water mass in layer  $j$  is smaller than a defined threshold:  $|\Delta m_l/m_l| < \epsilon_{\text{lim}} = 1 \times 10^{-5}$ . The moist air and the droplets in level  $j$  should then be in equilibrium.
  - b) Calculate the total latent heat  $\Delta Q = L_v \Delta m_l$  released in the  $z$ -level between  $z_j$  and  $z_{j+1}$  and assume an isobaric heating of the matter in this level. The average temperature will change by  $\Delta T = \Delta Q/C_p$ , where  $C_p = m_{\text{dry}} c_{p,\text{dry}} + m_v c_{p,v} + m_{p,\text{tot}} c_{p,p}$  with accumulated particle mass  $m_{p,\text{tot}}$ . Add  $\Delta T$  to both,  $T(z_j)$  and  $T(z_{j+1})$ .
  - c) The heating led to an expansion of the air in the  $z$ -level. Assume a linear  $T$ -profile between  $z_j$  and  $z_{j+1}$  to update the pressure at  $z_{j+1}$  to

$$p_{j+1} = p_j (T_{j+1}/T_j)^{[(1+r_t)g\Delta z]/[(1+r_{v,\text{avg}}/\epsilon_v)\tilde{R}_{\text{dry}}(T_j-T_{j+1})]} ,$$

which follows from the integration of the hydrostatic equation (2.32) for linear  $T$ , as derived in the Appendix, Sec. C.1

- d) Update  $\rho_{d,\text{avg}} = (p_{j+1} - p_j)/(\Delta z (1 + r_{\text{tot}}) g)$ , again using the hydrostatic equation.
- e) Update  $r_{l,\text{avg}}[i, j] = m_l[i, j]/(\rho_{d,\text{avg}} V_0)$ , where  $V_0 = \Delta x \Delta y \Delta z$ .
- f) Update  $r_{v,\text{avg}}[i, j] = r_{\text{tot}} - r_{l,\text{avg}}[i, j]$  to fulfill the restriction.

Particles are initialized with ambient temperature and fluid field velocity at their respective positions, illustrated in Fig. 6.1a. The algorithm yields an atmosphere with initial  $p(z)$ ,  $T(z)$ ,  $\rho_{\text{dry}}(z)$ ,  $S(x, z)$ ,  $r_v(x, z)$  and  $r_l(x, z)$ , as shown in Fig. 6.1b and previously in Fig. 2.3b. A continuously layered cloud has formed above a height of approximately 900 m, indicated by sufficiently large values of the liquid water content  $r_l$ . After initialization, the particles are however too small to reach significant sedimentation velocities and thus considered to be cloud droplets rather than rain droplets. The corresponding droplet size classification is defined and illustrated in Sec. 6.2.1.

### 6.1.3 Spin-up

Each simulation begins with a two hour spin-up phase, in which gravity and collisions are switched off and the majority of particles describes at least one full growth cycle. The droplets

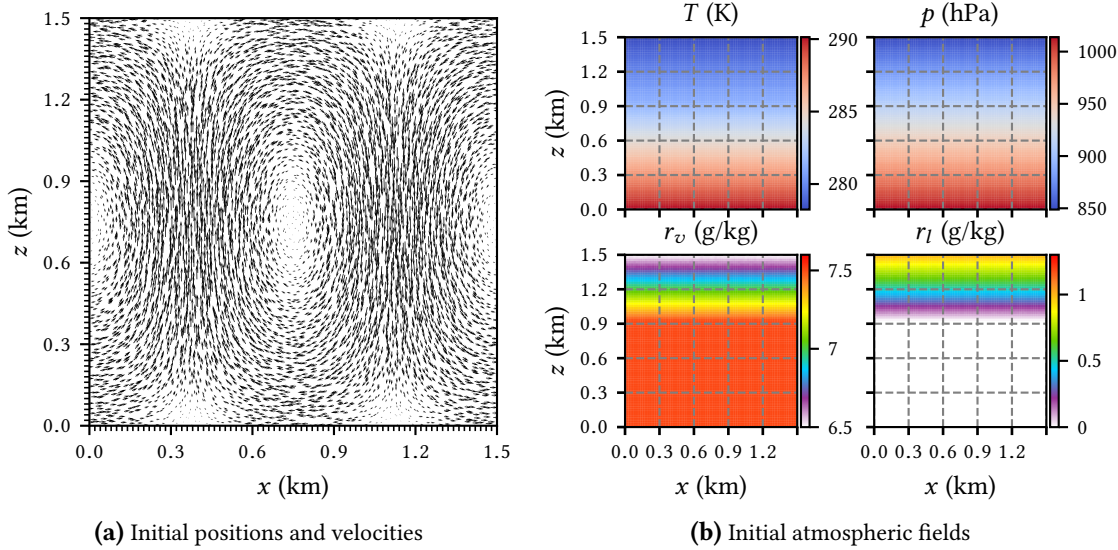


**Figure 6.1:** (a) Particles are initialized at random positions in each cell. Their velocities are set by bilinear interpolation of the discretized fluid velocity field at the respective particle positions. To get a comprehensible illustration, only one particle per grid cell is shown. Even though it might seem that some regions with small velocity arrows are more depleted than others, the number concentration of SIPs is uniform over the whole domain. (b) Atmospheric fields right after the initialization algorithm. Another representation including additional quantities is shown in Fig. 2.3b.

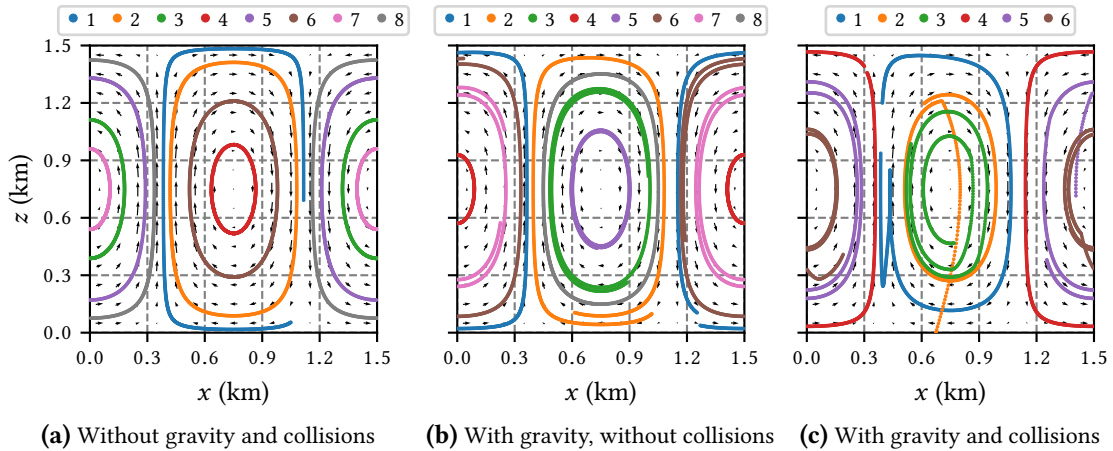


**Figure 6.2:** Trajectories of a particle selection during a simulation time of two hours. Note that the particle numbering and coloration in (a) to (c) is created separately for each plot and not connected in any way. When gravity and collisions are both switched off, the droplets remain very light and follow the periodic fluid field closely (a). With gravity, heavier particles will leave the fluid trajectories (b). When additionally allowing collisions, some particles will get large in size and thus experience strong accelerations due to gravity (c). Single droplets may attain high enough sedimentation velocities to reach the ground (see “orange” particle 2 in (c)). In some special cases, we recognize transitory floating effects, where the gravitational force and the drag force balance each other for short intervals of time (see “blue” particle 1 in (c)).

are light enough to follow the fluid velocity field closely, as indicated by a selection of trajectories in Fig. 6.2a. During spin-up, droplets go through the phases of condensational growth in higher regions and evaporation below the cloud base, continuously competing for water vapor with other droplets in their vicinity. By going through one growth cycle, numerical artifacts of the initialization are smoothed out and we expect to reach a state, where particles are in balance with each other and the environment. This might be regarded similar to a relaxation process in molecular dynamics. As expected, the cloud water content develops notable spatial fluctuations, while cloud base and layering become less defined (cf. Fig. 6.3). Still, all atmospheric fields show steady behavior during the initial two hours, describing a distinct, rain free cloud above 900 m.

## 6.2 Simulation results

After spin-up, gravity and collisions are switched on and the relevant part of the simulation begins. We also conducted simulations with gravity, but without collisions and compare the resulting particle trajectories in Fig. 6.2. Due to gravity, heavier droplets will leave the fluid parcel paths and move closer to the orbit centers, thereby depleting the updraft and downdraft regions around  $x = 375$  m and  $x = 1125$  m (Fig. 6.2b). When additionally allowing collisions, some particles get heavy enough to attain considerable sedimentation velocities and might even reach the ground as precipitation (Fig. 6.2c). This is however a rare case in the given drizzling cloud set-up.

For any simulation, we need to declare a set of parameters, including solute type ( $(\text{NH}_4)_2\text{SO}_4$ ), number of SIPs per cell  $N_{\text{SIP}}$  (64), time steps of advection  $\Delta t_{\text{adv}}$  (1 s) and condensation  $h$  (0.1 s), collision kernel (Long) and time step  $\Delta t_{\text{col}}$  (0.5 s), grid step sizes  $\Delta x$ ,  $\Delta z$  (20 m) and mode dependent, initial dry number concentrations  $\text{DNC}_k$  (Eq. (6.2)), where the default settings are given in parenthesis. The chosen advection time step leads to a maximal fluid field Courant–Friedrichs–Lewy number of  $\text{CFL}_{\max} = \Delta t_{\text{adv}} \max(|u/\Delta x| + |w/\Delta z|) < 0.06$ . For each fixed parameter set, we conducted a number of  $N_{\text{sim}} = 50$  simulations with different random seeds used during initialization and stochastic collisions. We are thus able to apply a statistical analysis of these  $N_{\text{sim}}$  runs and state the average values and estimated standard deviations, as described in Sec. 4.2.2.

### 6.2.1 Time evolution of coarse grained fields

In Figures 6.3 and 6.4, we present results for the time evolution of atmospheric fields and particle properties during simulations of 60 minutes under default settings. The state variables  $\Theta$  and  $r_v$  remain mostly stable, but for the development of updraft and, most distinctly, downdraft tunnels after 30 minutes, in accordance to gravity effects. Particles get heavier in high layers of the cloud and begin to descent before reaching the downdraft center. Thereby, droplets move closer to the orbit centers and the tunnels are left with diminished droplet density. The particles transport water from the depleted regions, which leads to the gap in liquid water mixing ratio  $r_l$ . Concerning  $\Theta$  and  $r_v$ , there are just not enough droplets with considerable dry masses left in the downdraft tunnel to balance the advection from upper cloud layers with small vapor concentration.

When collisions are switched on, the overall liquid water content in the cloud increases initially up to 30 minutes, when considerable rain formation begins. At 60 minutes, we detect measurable liquid water in the region below the cloud base at cost of a decrease in the cloud water content. This indicates that rain droplets have formed and could reach the regions below the cloud in the form of drizzle. For a detailed analysis, we will further classify all droplets into three size categories, according to [Arabas15]: Small particles with  $R_p < 0.5 \mu\text{m}$  will be called *aerosols* with number concentration  $n_{\text{aero}}$ . Droplets in the ranges  $0.5 \leq R_p < 25 \mu\text{m}$  and  $R_p \geq 25 \mu\text{m}$  are considered to be *cloud droplets* and *rain droplets*, respectively. Results for the mixing ratios  $r_c$  and  $r_r$ , as well as the rain droplet number concentration  $n_r$  are shown in Fig. 6.4.

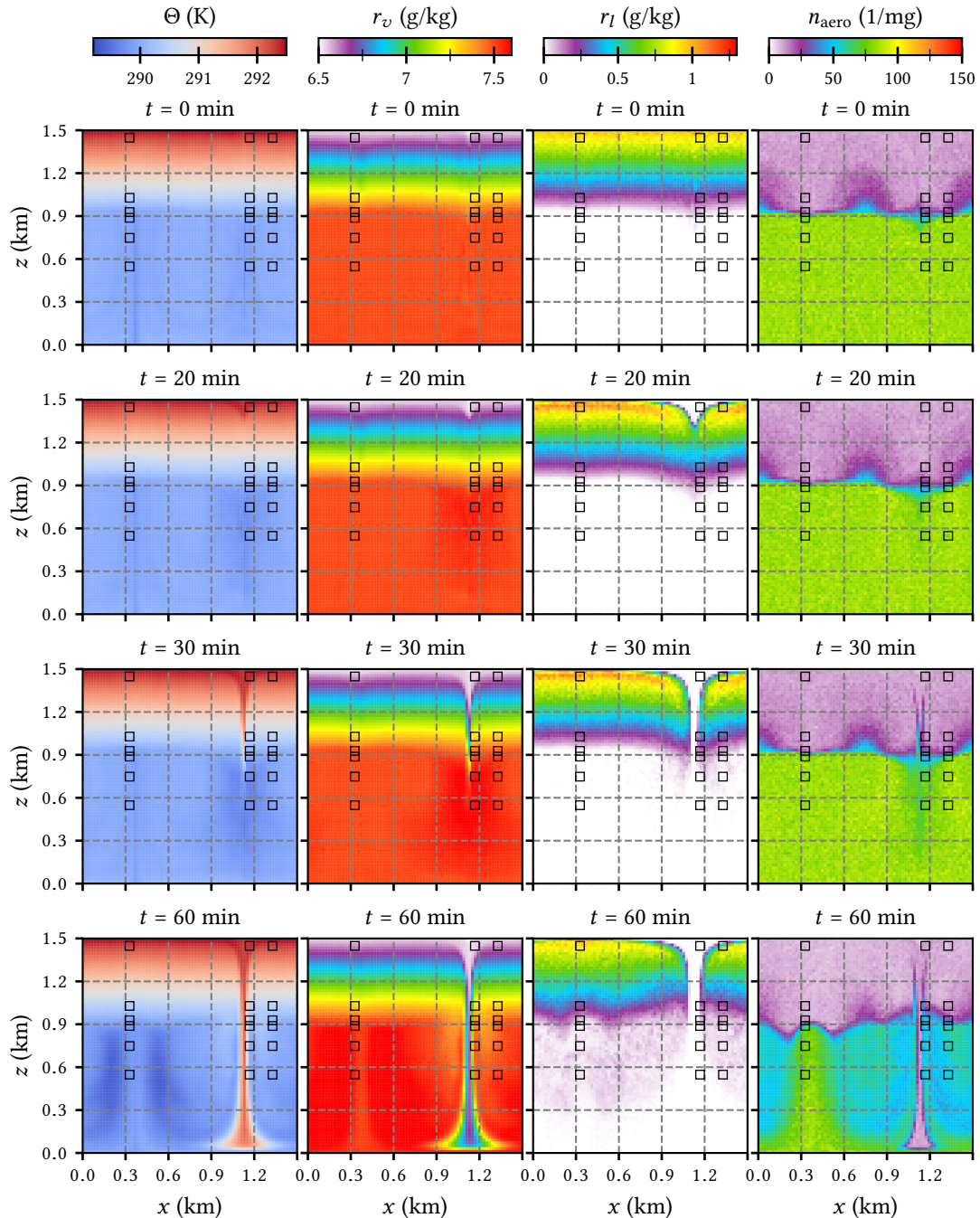


**Figure 6.3:** Simulation results for the time evolution of moist potential temperature, water vapor and liquid water mixing ratios and aerosol number concentration (per dry air mass) using the Long collision kernel with  $N_{\text{SIP}} = 64$  and ammonium sulfate as solute material (**default case**). Presented values are averages over 50 independent simulations. The initial two hour spin-up period is not shown. Black boxes indicate regions where the particle size distribution is calculated in detail.

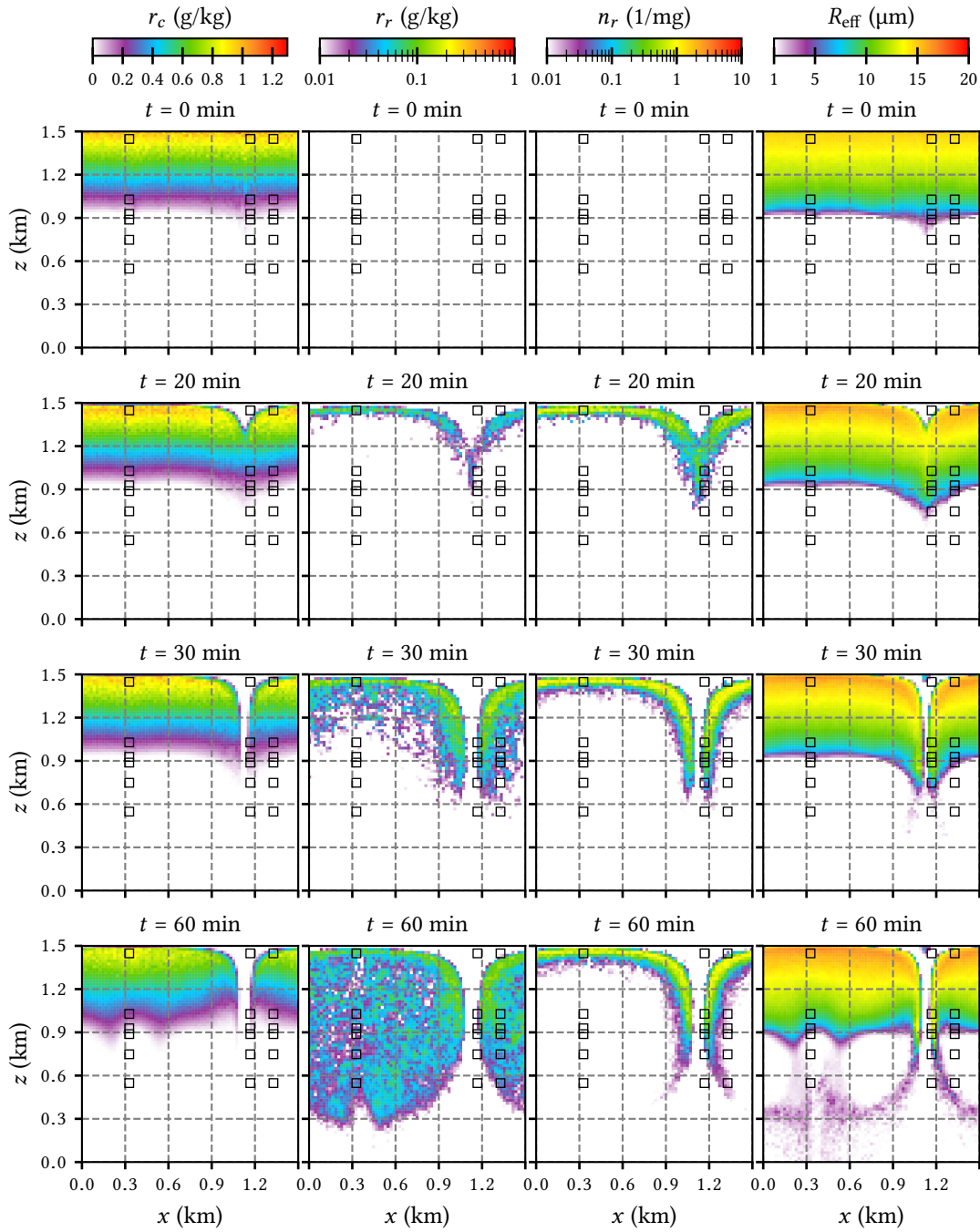


**Figure 6.4:** Simulation results for the time evolution of cloud water and rain water mixing ratios, rain droplet number concentration (per dry air mass) and effective cloud droplet radius, using the Long collision kernel with  $N_{\text{SIP}} = 64$  and ammonium sulfate as solute material (**default case**). Presented values are averages over 50 independent simulations. The initial two hour spin-up period is not shown. Black boxes indicate regions where the particle size distribution is calculated in detail.

Investigating the classified fields, we can now confirm that our simulations start with a rain free cloud. Due to collisions, heavier cloud droplets are formed, which then additionally bind more water vapor, because larger particles need less ambient saturation for condensational growth. The cloud is subsequently depleted by rain drop formation, which begins after about 20 minutes, but takes another 10 minutes until considerably large droplets have formed and begin to leave the cloud region (minding the logarithmic scale in the illustration of  $r_r$  and  $n_r$ ). The concentration of rain water content around the downdraft tunnel edges emerges due to high droplet densities in these regions as a result of the tunnel formation, described previously. Increased particle density leads to frequent and effective collection events and thereby to significant rain drop growth. As expected for a drizzling cloud, the vast majority of rain droplets does not reach the ground before shrinking by evaporation, but describes orbits of some (possibly irregular) kind and ascend again towards the cloud base.

Another parameter used in cloud physics, is the ratio of third to second moment of the cloud droplet size distribution, called *effective radius*,

$$R_{\text{eff}} = \int_{R_{c,0}}^{R_{r,0}} dR R f_R(R) \pi R^2 / \int_{R_{c,0}}^{R_{r,0}} dR f_R(R) \pi R^2, \quad (6.3)$$

where the borders  $R_{c,0} = 0.5 \mu\text{m}$  and  $R_{r,0} = 25 \mu\text{m}$  select only cloud droplets from the spectrum. This quantity weights each radius with the product of its concentration and cross section and thus characterizes the local light scattering behavior [Hansen74]. For the effective radius we observe continuous temporal growth and a smooth layering, which shows increasing cloud thickness with height.

To get an estimation of the fluctuations between independent simulation runs, the relative uncertainties of water vapor mixing ratio and variables describing the three size categories are presented in Fig. 6.5. Complementary absolute errors are shown in the Appendix (Fig. E.2). The results for  $r_v$  are congruent up to 0.2 %, indicating that the kinematic framework acts as stable environment for the atmospheric variables. The aerosol concentration has highest uncertainties of 10 % to 20 % in cloud regions, where  $n_{\text{aero}}$  itself shows small values. In well covered areas, the error reaches about 3 %. For the cloud and rain parameters  $r_c$  and  $r_r$ , we find high uncertainties of up to 100 % in regions, were one of the following factors is present: First, the concentration of particles in the respective size category itself is low. Second, the region is characterized by spatial fluctuations or a sharp gradient, i.e., at a border separating continuous from depleted zones. It is reasonable that the described cases are sensitive to relative deviations between different realizations. For example, a large error will be induced, when we find one specific simulation, where a large particle reaches a grid cell outside of the cloud, which usually (in all other simulations) contains no rain particles. Since there can always be one of the 50 simulations, where such an exception might happen, we can explain the large *relative* errors in Fig. 6.5. These estimated uncertainties of the mean can be reduced by conducting a larger number of independent simulations. Outside the sensitive areas, errors are reduced to an order of 10 %, which we consider acceptable, regarding the complexity of the system.

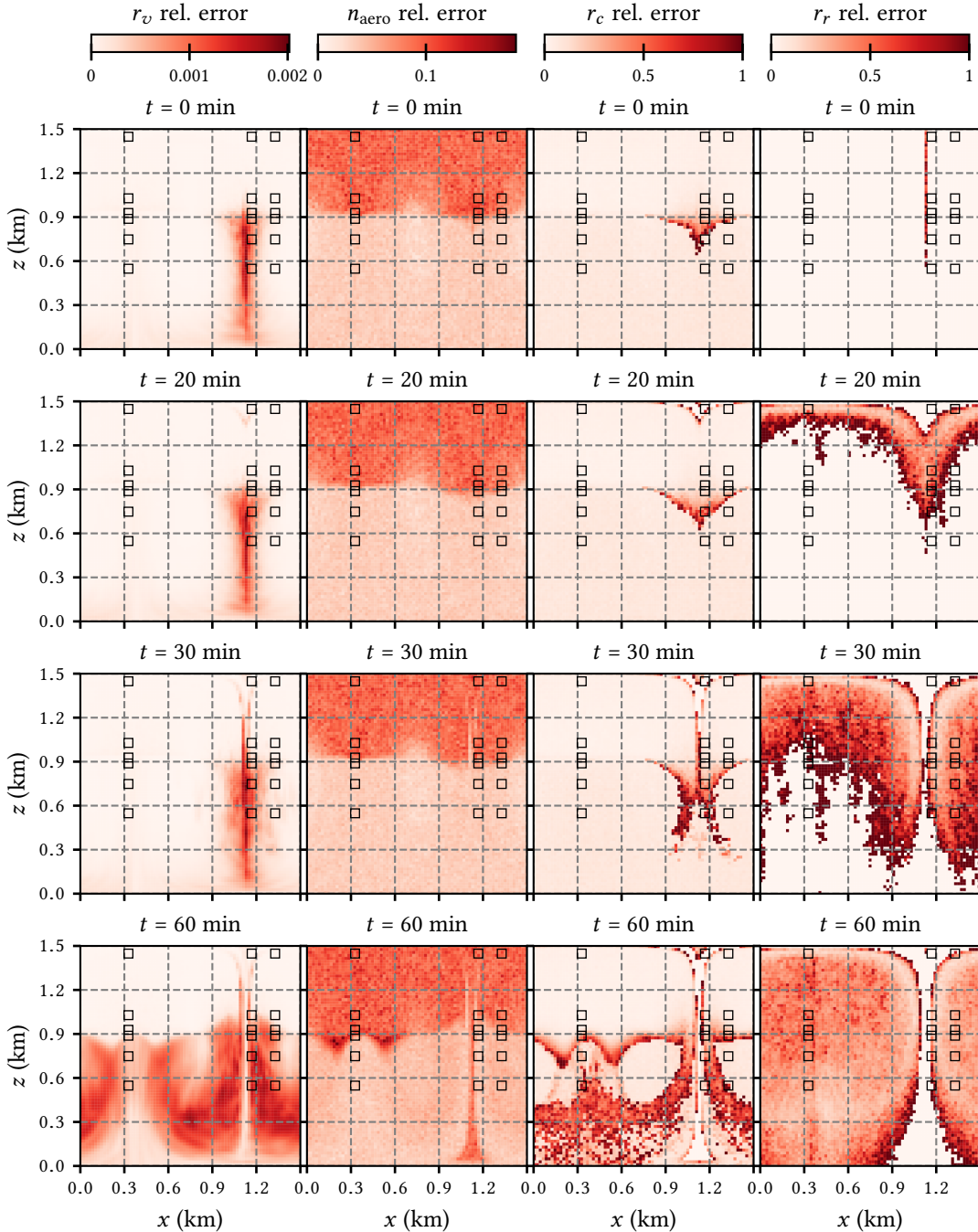


**Figure 6.5:** Relative errors for the aerosol number concentration (per dry air mass) and the mixing ratios of water vapor, cloud water and rain water, using the Long collision kernel with  $N_{\text{SIP}} = 64$  and ammonium sulfate as solute material (**default case**). The relative error of variable  $b$  is defined as fraction of estimated standard deviation and average value,  $\text{SD}(b_{\text{avg}}) / b_{\text{avg}}$ , obtained by analyzing 50 independent simulations. The initial two hour spin-up period is not shown. Black boxes indicate regions where the particle size distribution is calculated in detail.

### 6.2.2 Particle size spectra

The shape of the droplet size distribution is of great importance for the characterization and evolution of a cloud. We will analyze the spectra presented in Fig. 6.7 after a simulation time of 30 minutes, when considerable rain formation begins. Figure 6.6a indicates the positions at which the size distributions are calculated by sampling all particles contained in volumes of  $3 \times 3$  grid cells. The evaluated boxes are taken from three vertical columns, each characterizing a different zone of the domain. Boxes A-F and G-L cover the edges of updraft and downdraft tunnels, respectively. Results for these regions are also presented in [Arabas15] for the case of a hydrodynamic collision kernel with constant collection efficiency  $E_c = 0.5$ . A comparison is provided in Sec. 6.3. Boxes M-R are located between the vortex center and the downdraft tunnel and should cover more stable conditions. The distributions shown in Fig. 6.7 are calculated by sampling the droplet radii in 30 logarithmic bins. The wet spectra include the full solution droplet sizes, while the dry spectra assume that all liquid water is evaporated before sampling the radii.

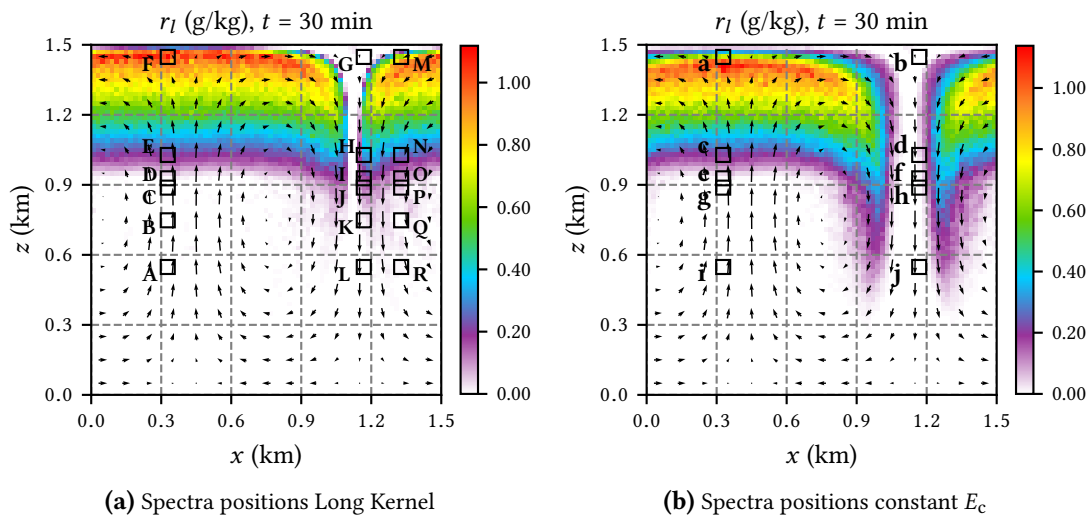


**Figure 6.6:** Positions of the selected volumes of  $3 \times 3$  grid cells each, where the droplet size spectra are analyzed for the Long kernel in Fig. 6.7 and for the hydrodynamic kernel with constant  $E_c = 0.5$  in Fig. 6.9 (Appendix).

We start by describing the updraft tunnel from bottom to top (A-F). Up to 750 meters height, the atmosphere is undersaturated and the droplets essentially remain in dry state (A, B). When approaching the cloud base, the size spectrum broadens by condensation (C) and considerable cloud water content has formed at 930 m (D). At a height of 1000 m, we find a split in the droplet spectrum, typical for bimodal dry size distributions (E). When the saturation exceeds the equilibrium value  $S_{eq}$  of a droplet, it will grow and thus withdraw water from the atmosphere, thereby in turn decreasing the ambient saturation. Analogously, the droplet will shrink, if  $S < S_{eq}$ . Since  $S_{eq}$  decreases with particle radius, there is a competition for the present water vapor. Droplets, which are already large (*activated*), will grow in size, while small (*not activated*) droplets tend to evaporate, when the saturation remains in a certain range. This leads to the gap in the spectrum (E), where particles are now either “small” or “large”. At the cloud top, droplets have already experienced collection events and the distribution covers cloud and rain water (F). By comparing to simulations without any collisions (Appendix, Fig. E.1), we can be certain that coagulations are actually necessary, i.e., condensation alone is not sufficient, to form rain droplets.

Next, we investigate the edge of the downdraft tunnel from top to bottom (G-L), following the fluid field. At  $t = 30$  min there are only few considerably large droplets left at the cloud top,

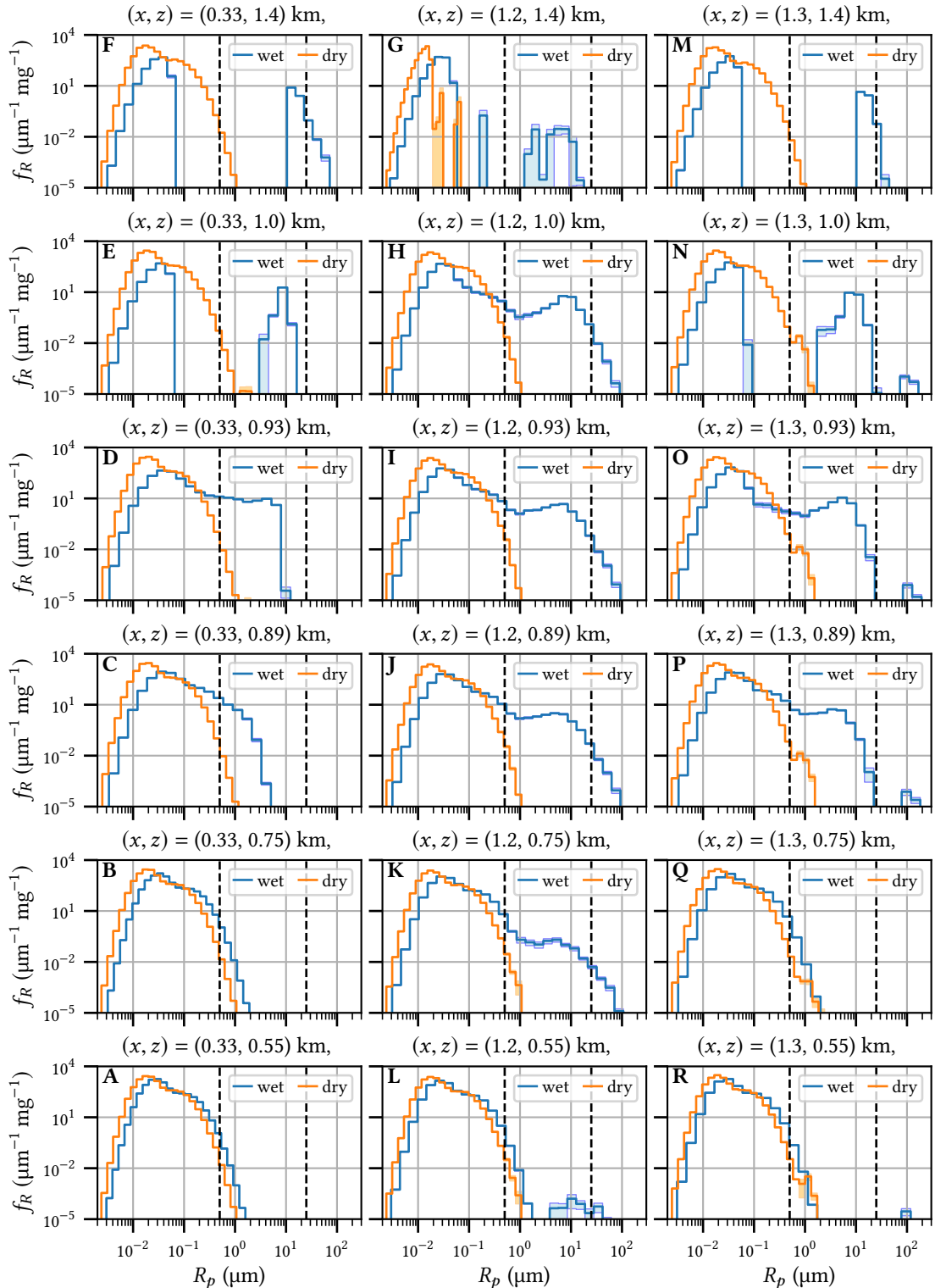


**Figure 6.7:** Droplet size spectra (number density per radius and mass of dry air) for the Long kernel with  $N_{\text{SIP}} = 64$  after 30 minutes simulation time at selected volumes of  $3 \times 3$  grid cells in three vertical columns, shown in Fig. 6.6a. Wet distributions include the full droplet sizes, while dry spectra are calculated by assuming that all liquid water is evaporated from each particle. The spectra values are averages over 50 independent simulations. Estimated errors are illustrated as shaded areas of the same color.

indicated as well by the gaps in cloud and rain water mixing ratio (Fig. 6.4). All contributions to the spectrum for  $R > 0.1 \mu\text{m}$  have minor weights (regarding the logarithmic scale), which are mostly covered by their error bars (G). The dry size distribution is cut at  $R \approx 0.02 \mu\text{m}$ , again considering the estimated uncertainties. This means that particles with larger dry radii were activated previously and never reached this region due to gravitational descent. At a height of 1000 m, the bimodal wet spectrum extends continuously over a large size range, including aerosols as well as cloud and rain droplets, and still contains radii up to 100  $\mu\text{m}$  (H). We find two maxima, but without the sharp gap dividing “small” from “large” droplets, as for the updraft region (E). This is likely due to the fact that trajectories of particles from a large cloud region are moving closer together, leading to a sharp gradient of both, cloud water and rain water mixing ratio (cf. Figs 6.4 and 6.6a). Sampling over this gradient results in the broad droplet size spectrum. Following the fluid field downwards to the cloud base, the spectrum essentially conserves its shape, but the second peak at 5  $\mu\text{m}$  is depleted by two effects: The first maximum increases due to evaporation, while only the largest droplets gain weight by collection (I, J). After leaving the cloud, low saturations lead to fast evaporation. Nevertheless, the particle density is large enough for heavy droplets to partially balance their shrinking by efficient collection of lighter particles. Thus, rain droplets still remain in the highly undersaturated region at 750 m and precipitate as drizzle (K). As mentioned previously, the system is constructed such that the rainfall is too weak to effectively reach the ground. At a height of 550 m, the spectrum almost returned to its dry state with some rare and scattered droplets left, indicated by large uncertainties for  $R > 4 \mu\text{m}$  (L).

At last, we compare the former results with the behavior in the third column between downdraft and vortex center (M-R). At the cloud top, we find larger resemblance to the updraft tunnel with the typical split in the size distribution (M). In contrast, we now observe fewer rain droplets, because heavier particles already left their trajectories due to gravitational acceleration. At  $z = 1000 \text{ m}$ , the split is still present and collection events additionally led to the formation of some large rain droplets up to 150  $\mu\text{m}$  (N). At the cloud base, we again sample over a distinct gradient in water mixing ratio and the distribution becomes broader and continuous (O, P). At this height, the previously developed rain droplets remain by balancing evaporation and collection. In contrast to the downdraft tunnel, the region below the cloud does not yet contain enough cloud droplets for efficient collisions and, similar to the updraft case, the whole spectrum approaches its dry state below 750 m, when considering the error bars (Q, R).

### 6.2.3 Droplet growth cycle

An advantage of the applied discrete particle method is, that we can track the evolution of any individual droplet and investigate the conditions experienced on its way. To analyze the plausibility of our simulations, the growth cycle of a typical SIP is illustrated in Fig. 6.8. The particle starts in the bottom area of the vortex and describes a clockwise inward spiral trajectory, which is shown in Fig. 6.8b together with a snapshot of the liquid water mixing ratio  $r_l$ , indicating the cloud structure at  $t = 30 \text{ min}$ . We present the evolution of droplet radius as well as the atmospheric conditions  $r_v$ ,  $r_l$ ,  $p$ ,  $T$  and  $S$  experienced by the particle in Fig. 6.8a. Size spectra are shown in Fig. 6.8c at 6 characteristic positions A-F along the trajectory, indicated by the boxes in Fig. 6.8b.

At the initial height of 120 m, pressure and temperature are still close to their maximum surface values. The atmosphere is thus undersaturated ( $S < 0.7$ ) and the particle, like all other droplets in its vicinity, contains almost no water (dry state). When rising up,  $T$  and  $p$  decrease, while  $S$  increases until saturated conditions  $S \approx 1$  are reached after 30 minutes, when the particle crosses the cloud base at 920 m. From here on, the size spectrum broadens (B) and our tracked droplet grows by condensation, while the saturation remains at about 100 % and the cloud water mixing ratio decreases. Somewhat higher, at  $z = 1200 \text{ m}$ , the particle has reached a radius of

$R_p = 12 \mu\text{m}$  and we detect the typical split in the wet size spectrum (C). Rare collection events lead to formation of the first rain droplets (D). However, our particle remains yet unaffected by collisions and its radius attains the first maximum after 48 minutes at its highest position, in accordance with a minimum in ambient temperature.

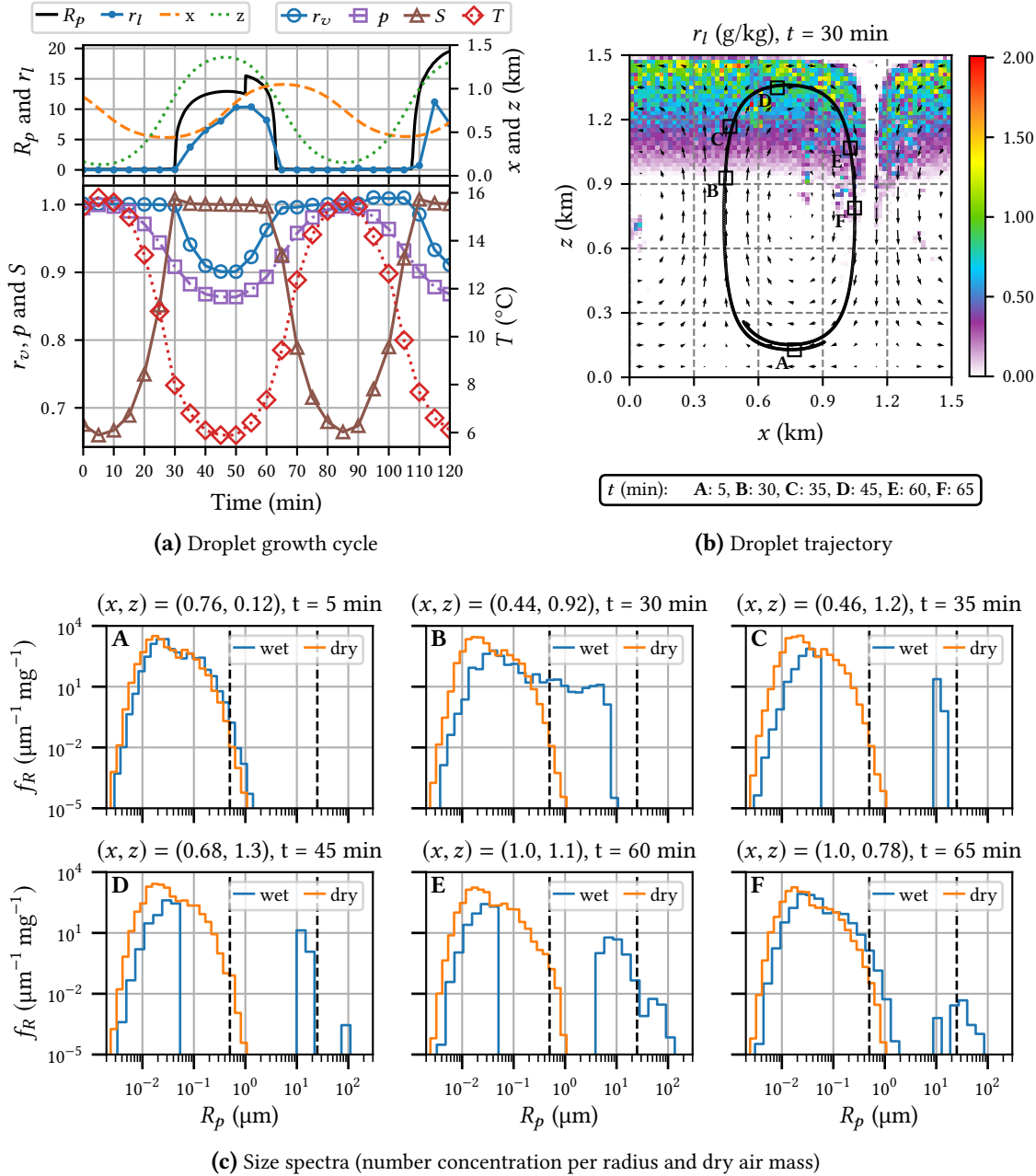


**Figure 6.8:** (a) Evolution of the droplet radius and the experienced ambient conditions during the growth cycle of one selected particle. The units are:  $R_p$  in  $\mu\text{m}$ ,  $r_l$  in  $0.1 \text{ g/kg}$ ,  $p$  in bar,  $r_v$  relative to  $r_{v,\text{max}} = 7.5 \text{ g/kg}$ . (b) Trajectory during 95 minutes after spin-up. The labeled boxes indicate the positions of the volumes, where size spectra are presented in (c). The respective times are given in the legend of (b) and help to connect the box positions specified in the plot headings of (c) to the results shown in (a).

After passing the highest point, heavy droplets obtain significant sedimentation velocities and the major collection process begins. In Figure 6.8a we detect the effect of a collection event on the droplet size by the jump in radius  $R_p$  at about 53 min. The maximum average radius and rain

water mixing ratio is reached after approximately 60 minutes at a height of 1100 m, which can be seen in the spectrum (E). Below the cloud, saturation decreases and our particle shrinks by evaporation. There is now a competition between evaporation and collection events, leading to some heavy rain drops, which can maintain their size, while the cloud water mixing ratio is depleted and most particles (including the tracked one) attain effectively dry states after 65 minutes (F). From here on, the particle follows the fluid field closely, but now on a trajectory, which is somewhat closer to the vortex center and crosses initial box A at 85 minutes.

### 6.3 Comparison to external sources

Discrete particle simulations for the same kinematic test case were performed by Arabas *et al.* [Arabas15]. The numeric models are similar in kind, but show some distinct differences, as listed below.

1. In this work, multiplicities  $\xi$  are continuous real numbers and might attain values  $< 1$ , as proposed in [Unterstrasser17]. In contrast, Arabas *et al.* use the super-droplet approach of Shima *et al.*, where  $\xi$  takes only integer values  $\geq 1$  [Shima09].
2. In the collision step, we iterate over all droplet pairs contained in a grid cell, leading to an order of  $N_{\text{SIP}}^2$ . The model of Arabas *et al.* applies a linearized form of the algorithm, where the possible number of collision pairs is restricted to order  $N_{\text{SIP}}$ . As a consequence, the algorithm is numerically less demanding and they are able to reduce the collision time step to  $\Delta t_{\text{col}} = 0.1$  s, while our default time step is  $\Delta t_{\text{col}} = 0.5$  s. We however conclude from the analysis in Sec. 6.4.1 that, in our case, a smaller collision time step has no significant influence.
3. While we use the SingleSIP initialization process to generate SIP ensembles, Arabas *et al.* draw logarithmic radii from a uniform distribution and then assign the corresponding stochastic weights. It has been shown that the initialization method has major influence on the number of SIPs per cell required to reach convergence [Unterstrasser17].
4. We use a dynamic approach, which calculates particle accelerations from drag force and gravity and then propagates velocity and position. Thereby, we directly attain the droplet velocities used in the hydrodynamic kernel to calculate the collection probabilities. In contrast, Arabas *et al.* propagate particles with the fluid field and additionally add a sedimentation velocity, which is calculated using an empirical formula, depending on droplet size and the ambient conditions.
5. Opposed to our model, Arabas *et al.* compute the growth by condensation based on the droplet radius, using an effective diffusion coefficient and a different parametrization of the water activity. While we include the effect of temperature and solute concentration on the droplet density, they consider ventilation effects by modification of the vapor and heat diffusion coefficients.
6. Concerning the atmospheric variables of the kinematic model, Arabas *et al.* use additional relaxation terms in the transport equations for  $r_v$  and  $\Theta$ , which shift the horizontal mean towards initial values. The relaxation time scale depends on height and ranges exponentially from 5 min at the surface to 150 h at the cloud top. This artificial source term shall compensate for latent heating of the cloud layer and water loss by precipitation and stabilize the ambient atmosphere.

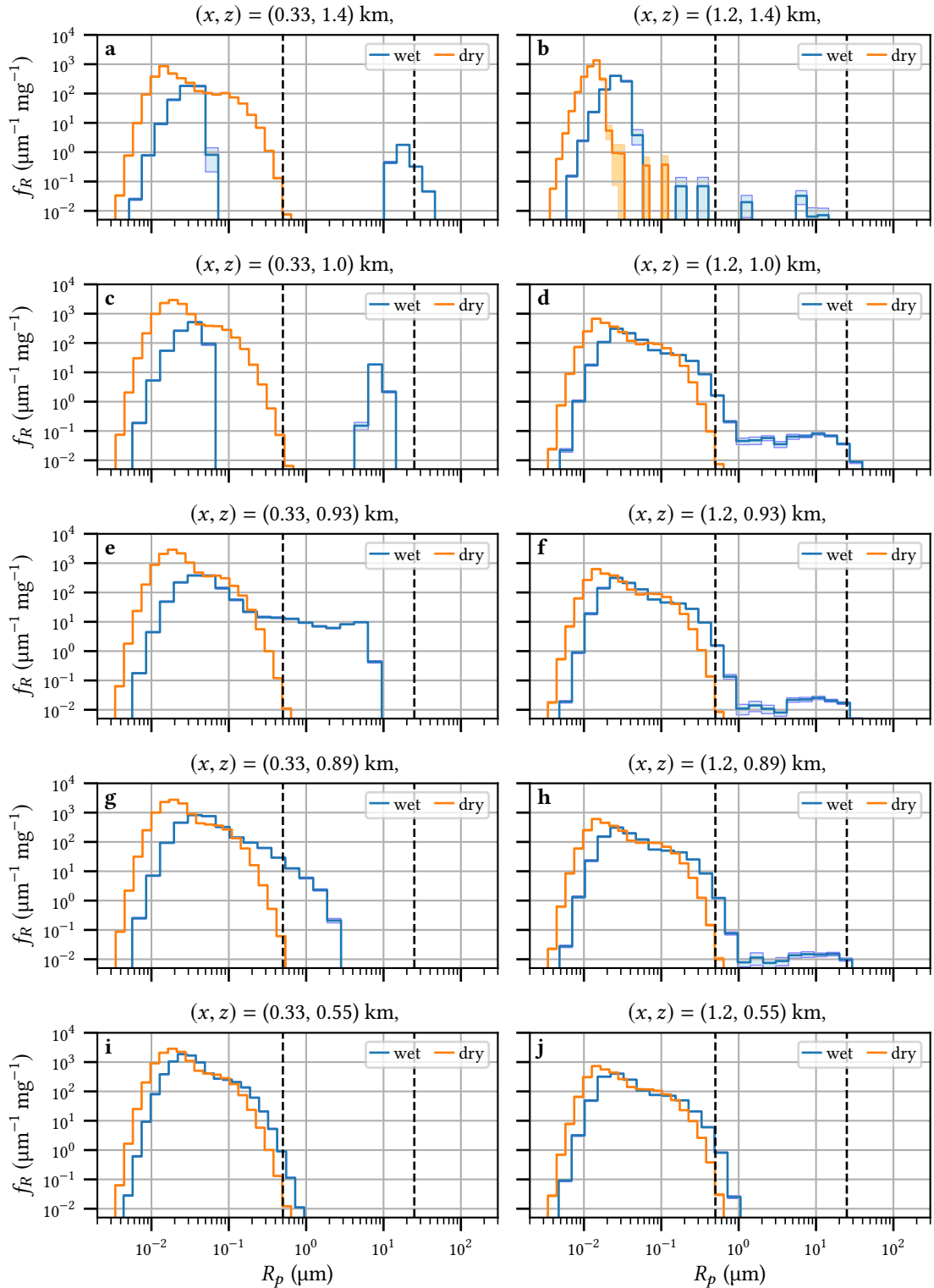


**Figure 6.9:** Droplet size spectra (number density per radius and mass of dry air) after a 30 minute simulation at selected volumes of  $3 \times 3$  grid cells in two vertical columns, shown in Fig. 6.6b. The same spectra positions are used in [Arabas15]. Results are presented for the hydrodynamic kernel with **constant collision efficiency**  $E_c = 0.5$ . The spectra values are averages over 50 independent simulations. Estimated errors are illustrated as shaded areas of the same color.

Arabas *et al.* present snapshots of the mixing ratios  $r_c$  and  $r_r$ , the number concentrations  $n_{\text{aero}}$  and  $n_r$ , the effective radius  $R_{\text{eff}}$  as well as cloud spectra at 10 selected positions after 30 minutes simulation time, excluding spin-up [Arabas15, pp. 1697]. They apply the hydrodynamic kernel, but with constant collection efficiency  $E_c = 0.5$ . For direct comparison, results of our model with corresponding set-up are shown in the Appendix (Figs. E.3 and E.4). Here, we utilize the exact same size and color scales for illustration. Noteworthy, we average over 50 independent runs as before, while Arabas *et al.* present results for one single simulation. This explains why our plots show much less spatial fluctuations and a smoother layering. Further differences are discussed in the following.

For the cloud water mixing ratio  $r_c$ , we observe the same general cloud shape and stratification with slightly broader downdraft tunnel. Furthermore, the tunnel edges and the whole cloud in general show smoother gradients and less spatial fluctuations, which can be explained by the averaging procedure. Concerning  $n_r$  and  $r_r$ , the overall shape and order of magnitude is similar, as well. In our case, the rain water is spatially continuous and extends to a larger region. Considering the logarithmic scales, the main contribution, where the values exceed 10 % of their maximum, coincides with the areas of Arabas *et al.*, but shows approximately 30 % larger values. This will be discussed, when analyzing the spectra below. Spatially separated clusters in their illustrations are smoothed out by our averaging. However, we detect a somewhat broader downdraft tunnel, for which we offer an explanation considering the different approaches for droplet dynamics and the additional relaxation term. Our applied force model might lead to larger velocities of heavy particles, which deviate more from the fluid parcel trajectories and move closer to the orbit centers, thereby depleting the downdraft region. This would also lead to higher particle densities and thus more effective collection, which might explain the spatial extend of the rain water below 600 m height, which is not present in the results shown in [Arabas15]. Furthermore, the previously described artificial relaxation term will transport water vapor towards and thermal energy from the downdraft tunnel. Thereby, condensation is increased in the depleted region, leading to a shift in the concentration of cloud and rain droplets and finally to a smaller gap.

For the aerosol number concentration  $n_{\text{aero}}$ , we observe the same separation between depleted cloud regions with  $n_{\text{aero}} \approx 20 \text{ mg}^{-1}$  and lower areas with  $n_{\text{aero}} \approx 90 \text{ mg}^{-1}$ . The effect of the downdraft tunnel is also indicated in [Arabas15], but less pronounced than in our illustration, where the depleted region stretches well below 300 m. This is in accordance to the broadening of the rain water gap, described above. In similar manner, we explain the differences in the effective cloud droplet radius  $R_{\text{eff}}$ . While the general shapes agree well, in our model the horizontal gap is more pronounced and the values extend below 600 m height. Additionally, our values are higher at the cloud top, which will be addressed, when analyzing the spectra.

Figure 6.6b indicates the volumes of  $3 \times 3$  grid boxes, where the size distributions are calculated. The spatial positions, simulation time, units, scales and numeration of the plotted spectra in Fig. 6.9 are the same as for the ones presented in [Arabas15, p. 1698]. We will first compare the results for the updraft column from bottom to top (i-a). Up to 930 meters (i, g, e), our spectra are quite similar, but for a broader wet distribution in our case, which indicates stronger droplet mass growth, partly as a result of differing condensation equations, as described previously. Above the cloud base (c, a), we observe the same split in the size distribution. In our case, the propagation of the mentioned broadening leads however to a weight shift to larger cloud and rain droplets. At the cloud top, the second maximum of the spectra lies at  $R = 10 \mu\text{m}$  in [Arabas15] and at  $R = 20 \mu\text{m}$  for our model. Furthermore, we find higher contribution of rain droplets. The spectra agree with higher values of  $r_r$ ,  $n_r$  and  $R_{\text{eff}}$ , mentioned previously. An explanation is the broader size distribution at the cloud base, which leads subsequently to more efficient collection. For sure, the different approaches for particle initialization and collisions will additionally alter the coagulation process.

For the downdraft tunnel, we begin at the cloud top (b), where Arabas *et al.* report a strict cut of the dry and wet size spectra at  $R \approx 20$  nm and  $R \approx 60$  nm, respectively. We can confirm this behavior, when considering the large errorbars of some scattered contributions of larger radii. Further down, at  $z = 1000$  m, we observe the same bimodal wet distribution but with less pronounced second maximum at a larger radius (d). In our case, there are just less cloud droplets present, which coincides with the larger downdraft tunnel of  $r_c$ , discussed previously. At the cloud base (f, h), the second maximum is split and reduced and our spectra agree well with the ones illustrated in [Arabas15]. This is also the case for the dry state at 550 m height (j).

Conclusively, the main features of the atmospheric fields and particles size distributions are comparable to the results in [Arabas15]. Main differences are higher values of  $r_c$ ,  $r_r$  and  $R_{\text{eff}}$  at the cloud top, larger vertical extend of rain drops below 600 m height, more pronounced gaps in the downdraft region and a broader size spectrum in the updraft tunnel with larger cloud and rain droplets, which indicates stronger contributions from either the condensation or collision terms due to different modeling approaches. The discrepancies in the downdraft tunnel can be explained by the atmospheric relaxation term and larger deviations from the fluid parcel trajectories, when using dynamic velocity calculation. Regarding the highlighted distinctions in the underlying algorithms, we conclude that our models agree well enough to at least yield plausible results.

## 6.4 Finite size analysis

Next, we will present an analysis of finite size effects and the convergence behavior by varying the collision time step, the initial number of SIPs per cell and the spatial grid cell size. The evaluation will include illustrations of the deviations  $\Delta b = b_* - b_{\text{def}}$  between scalar fields of the default case ( $b_{\text{def}}$ ) and simulations with varied parameters ( $b_*$ ). An assessment of these differences  $\Delta b$  is only meaningful, when considering the uncertainties. Within the given limitations, we will estimate the standard deviation of the average difference  $\Delta \bar{b}$  by

$$\text{SD}(\Delta \bar{b}) = \sqrt{\text{SD}^2(\bar{b}_*) + \text{SD}^2(\bar{b}_{\text{def}})}, \quad (6.4)$$

assuming stochastically independent variables.<sup>1</sup>

### 6.4.1 Influence of the collision time step

To investigate the influence of the collision time step  $\Delta t_{\text{col}}$ , 50 independent simulations were performed with  $\Delta t_{\text{col}} = 0.1$  s and compared to the default case with five times larger step  $\Delta t_{\text{col}} = 0.5$  s. Figure 6.10 illustrates the deviations  $\Delta b = b_* - b_{\text{def}}$  of refined ( $b_*$ ) and default case ( $b_{\text{def}}$ ), where  $b$  represents the coarse grained particle properties aerosol number concentration, cloud

---

<sup>1</sup> For the difference of two stochastic variables  $Z = X - Y$ , which can be described by a common PDF  $f_2(x, y)$ , an unbiased estimation of the standard deviation of the average  $\bar{z} = \bar{x} - \bar{y}$  is given by  $\text{SD}^2(\bar{z}) = \sum_i^N (z_i - \bar{z})^2 / (N(N - 1)) = \text{SD}^2(\bar{x}) + \text{SD}^2(\bar{y}) - 2 \sum_i^N (x_i - \bar{x})(y_i - \bar{y}) / (N(N - 1))$ . In our case, the summation is performed over independent simulation runs with different random seeds and  $N = N_{\text{sim}}$ . In the estimation of the covariance,  $\sum_i^N (x_i - \bar{x})(y_i - \bar{y}) / (N - 1)$ , the values  $x_i$  and  $y_i$  must respectively be measured in the same system, indicated by index  $i$ , to be able to make statements about the correlations. This requirement is not applicable, when comparing results from simulations running over longer periods of time with different basic parameters like the number of SIPs or the collision time step. When we, for example, consider the case, where 50 simulations are conducted, both for  $N_{\text{SIP}} = 64$  and  $N_{\text{SIP}} = 128$ , it is not evident, which variables  $x_i$  and  $y_i$  from the respective sets of simulations to compare in the covariance calculation, because there is no reason to connect specific pairs of  $x$  and  $y$ . Therefore, we propose the assumption that  $X$  and  $Y$  are independent, when calculating the standard deviation  $\text{SD}^2(\bar{z}) = \text{SD}^2(\bar{x}) + \text{SD}^2(\bar{y})$ . Another approach could be to use maximum error propagation with  $\text{SD}(\bar{z}) = \text{SD}(\bar{x}) + \text{SD}(\bar{y})$ , which would however imply a correlation coefficient of  $-1$ .

water mixing ratio, rain water mixing ratio and effective cloud droplet radius. Absolute values of the default case are discussed previously (Figs. 6.3 and 6.4), while errors of the deviations  $\text{SD}(\Delta b)$  are shown in Fig. E.5 (Appendix).

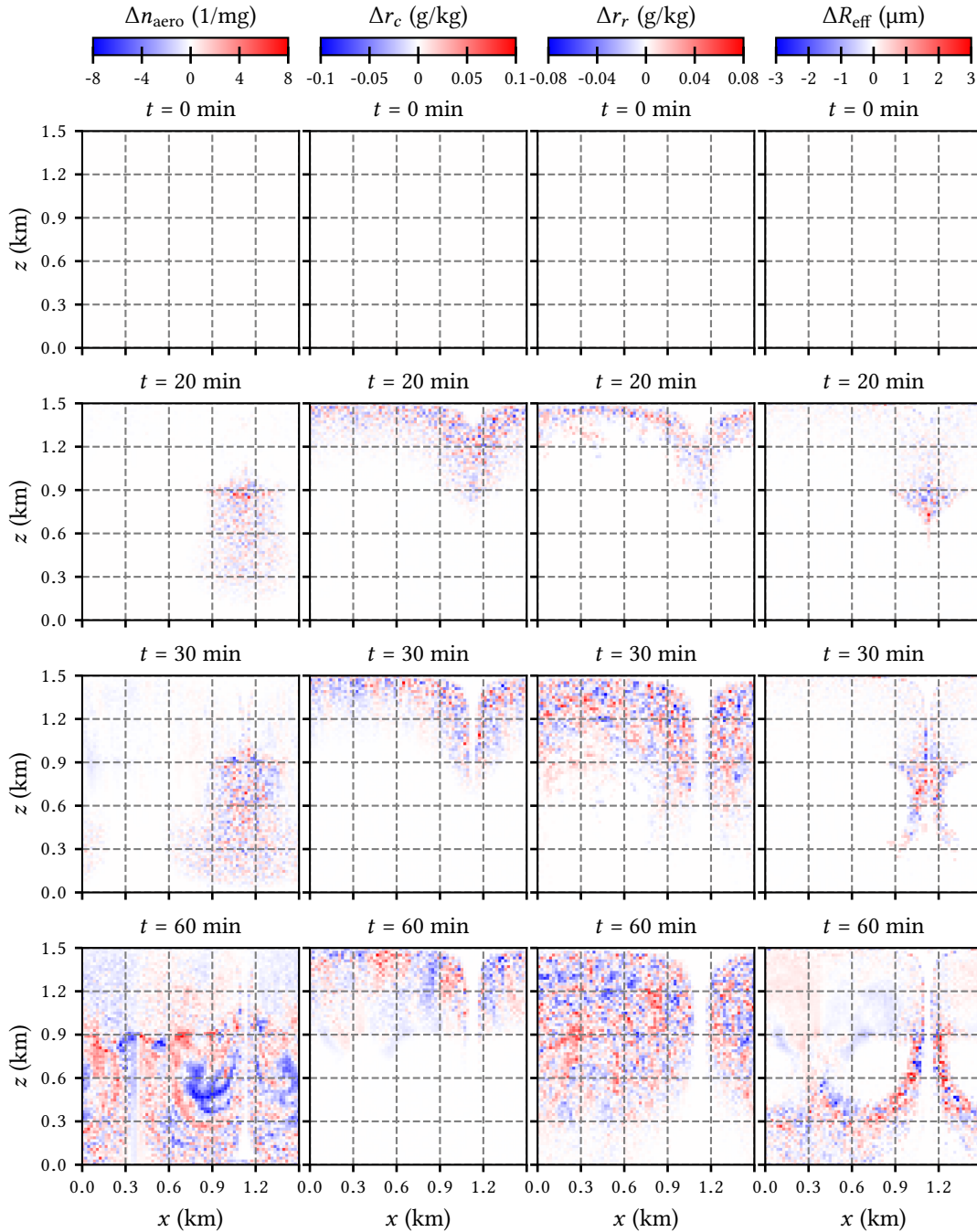


**Figure 6.10:** Deviations  $\Delta b = b_* - b_{\text{def}}$  between results of simulations with **collision time step**  $\Delta t_{\text{col}} = 0.1 \text{ s}$  ( $b_*$ ) and  $\Delta t_{\text{col}} = 0.5 \text{ s}$  ( $b_{\text{def}}$ ), where  $b_k$  is either the aerosol number concentration (per dry air mass), cloud water mixing ratio, rain water mixing ratio or effective cloud droplet radius. In both cases, the Long kernel is used with  $N_{\text{SIP}} = 64$  and the results are averages over 50 independent simulation runs.

Considering the aerosol density  $n_{\text{aero}}$ , we detect discrepancies only in the downdraft region for  $t \leq 30 \text{ min}$ , which spread to the whole area below the cloud after 60 min. Deviations range from  $-8$  to  $8 \text{ mg}^{-1}$ , and are thus in the order of 13 %, regarding absolute values of the default case. In

the corresponding regions, absolute errors amount to approximately  $5 \text{ mg}^{-1}$ , implying that all deviations are covered by a  $2\sigma$  interval. For the cloud and rain water mixing ratios  $r_c$  and  $r_r$ , the spatial structure of the deviations resembles the absolute fields, forming in the cloud region and extending below the cloud for  $t \geq 30 \text{ min}$ . Differences range from  $-0.1$  to  $0.1 \text{ g/kg}$  and  $-0.08$  to  $0.08 \text{ g/kg}$ , respectively, corresponding to relative values of approximately 10 %, which is again covered by an interval of two estimated standard deviations. For the effective radius  $R_{\text{eff}}$ , the effect of the downdraft tunnel and its tails is again visible in the spatial structure of  $\Delta R_{\text{eff}}$ . Discrepancies between the systems are highest in the sensitive regions, where the relative fluctuations are high. Values range from  $-3$  to  $3 \mu\text{m}$ , indicating relative values up to 100 %. However, absolute errors are also largest in the corresponding areas, amounting to approximately  $1.5 \mu\text{m}$ .

Common features of all presented variables are that the differences are largest, where the fields themselves show high uncertainties. Furthermore, the magnitude increases with time, which is expected for numeric simulations. Most importantly, the deviations do in no case show visible, distinct, systematic patterns. The values fluctuate spatially between positive and negative entries of similar magnitude and, in all cases, are covered by an interval of two times the estimated standard deviations. Noteworthy, simulations with smaller time step additionally do not lead to reduced absolute errors (not shown). We conclude that a reduction of the collision time step from  $\Delta t_{\text{col}} = 0.5 \text{ s}$  to  $\Delta t_{\text{col}} = 0.1 \text{ s}$  does not have significant influence, when all other parameters are chosen as in our default case.

#### 6.4.2 Influence of the number of SIPs per cell

The variation of the number of SIPs per cell  $N_{\text{SIP}}$  showed major influence on conducted box model simulations, presented in Sec. 5.2. Furthermore, the analysis indicated that convergence is by far not reached for  $N_{\text{SIP}} = 64$ . To investigate the impact for the kinematic test case, we additionally performed 50 independent simulations with  $N_{\text{SIP}} = 32$  and  $N_{\text{SIP}} = 128$ , respectively.

First, the deviations  $\Delta b = b_* - b_{\text{def}}$  between  $N_{\text{SIP}} = 128$  ( $b_*$ ) and  $N_{\text{SIP}} = 64$  ( $b_{\text{def}}$ ) are presented in Fig. 6.11. Considering  $r_c$  and  $r_r$ , we are not able to detect systematic patterns, because, as for the time step variation, values fluctuate spatially and the magnitudes are covered by  $2\sigma$  intervals of the estimated uncertainties, shown in Fig. E.6 (Appendix). For  $n_{\text{aero}}$  deviations are likewise insignificant for  $t \leq 30 \text{ min}$ . After one hour, we observe a field between updraft and downdraft tunnel, were the case with more SIPs shows a reduction in concentration of about 30 %. Analyzing the effective radius  $R_{\text{eff}}$  reveals the largest and most distinct discrepancies. Simulations with higher  $N_{\text{SIP}}$  lead to an increase of  $R_{\text{eff}}$  along the edges of the downdraft tunnel up to  $5 \mu\text{m}$ , while the uncertainties reside below  $1.5 \mu\text{m}$ . Since  $R_{\text{eff}}$  represents the ratio of third to second moment of the cloud droplet distributions, this indicates systematic deviation in the size spectra. Therefore, we analyze the moments  $\lambda_k$  at  $t = 30 \text{ min}$  in three vertical columns, which are indicated in Fig. 6.11 and coincide with the positions of the particle spectra presented in Fig. 6.7.

At each of the three horizontal coordinates, moments  $\lambda_0$  to  $\lambda_3$  are investigated as a function of height  $z$  for the three cases of  $N_{\text{SIP}} = 32, 64$  and  $128$ , as shown in Fig. 6.12. As for the distributions, values are respectively averaged over boxes of  $3 \times 3$  grid cells. Each order is displayed with the same axis scale in all columns. Starting with the zeroth moment (droplet number concentration), we observe a linear decrease with height in all columns from about  $1.02 \times 10^8 \text{ m}^{-3}$  to  $0.88 \times 10^8 \text{ m}^{-3}$ . The case with largest  $N_{\text{SIP}}$  shows the smoothest curve and smallest error bars. Uncertainties and fluctuations increase with decreasing number of SIPs. Nevertheless, the general trend remains the same and deviations are mostly covered within two error bars. We can not detect systematic deviations as for the box model.

Considering higher moments  $\lambda_{1,2,3}$ , the first and third columns show similar behavior. Here, we find a clear separation at the cloud base at approximately  $900 \text{ m}$ . Beginning from the earth surface, all three moments increase nearly exponentially with height (following the temperature

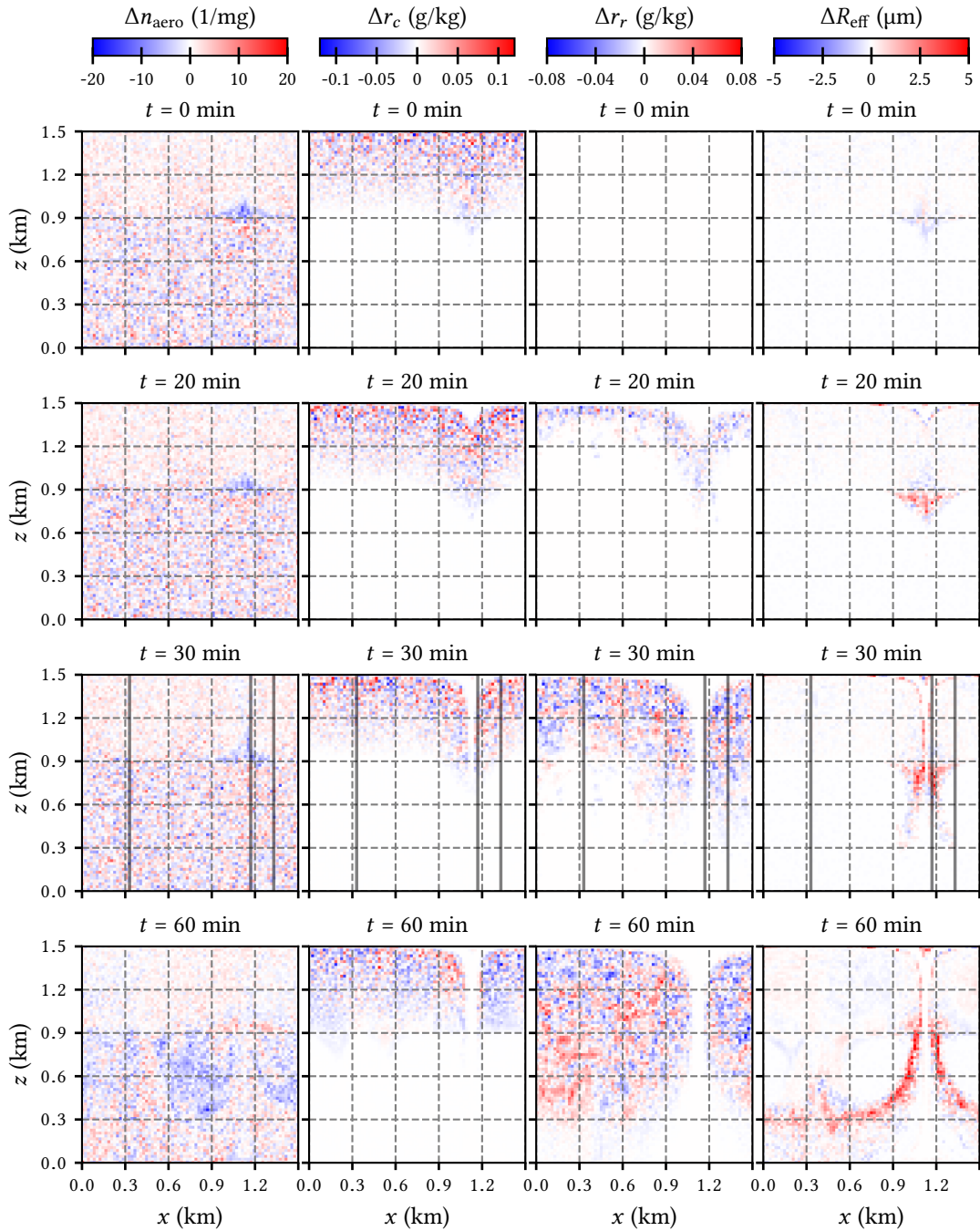


**Figure 6.11:** Deviations  $\Delta b = b_* - b_{\text{def}}$  between results of simulations with **numbers of simulation particles per cell**  $N_{\text{SIP}} = 128$  ( $b_*$ ) and  $N_{\text{SIP}} = 64$  ( $b_{\text{def}}$ ), where  $b_k$  is either the aerosol number concentration (per dry air mass), cloud water mixing ratio, rain water mixing ratio or effective cloud droplet radius. The vertical gray lines in the plots for  $t = 30 \text{ min}$  indicate the columns, where the size distribution is analyzed in more detail in Figs. 6.12 and 6.13.

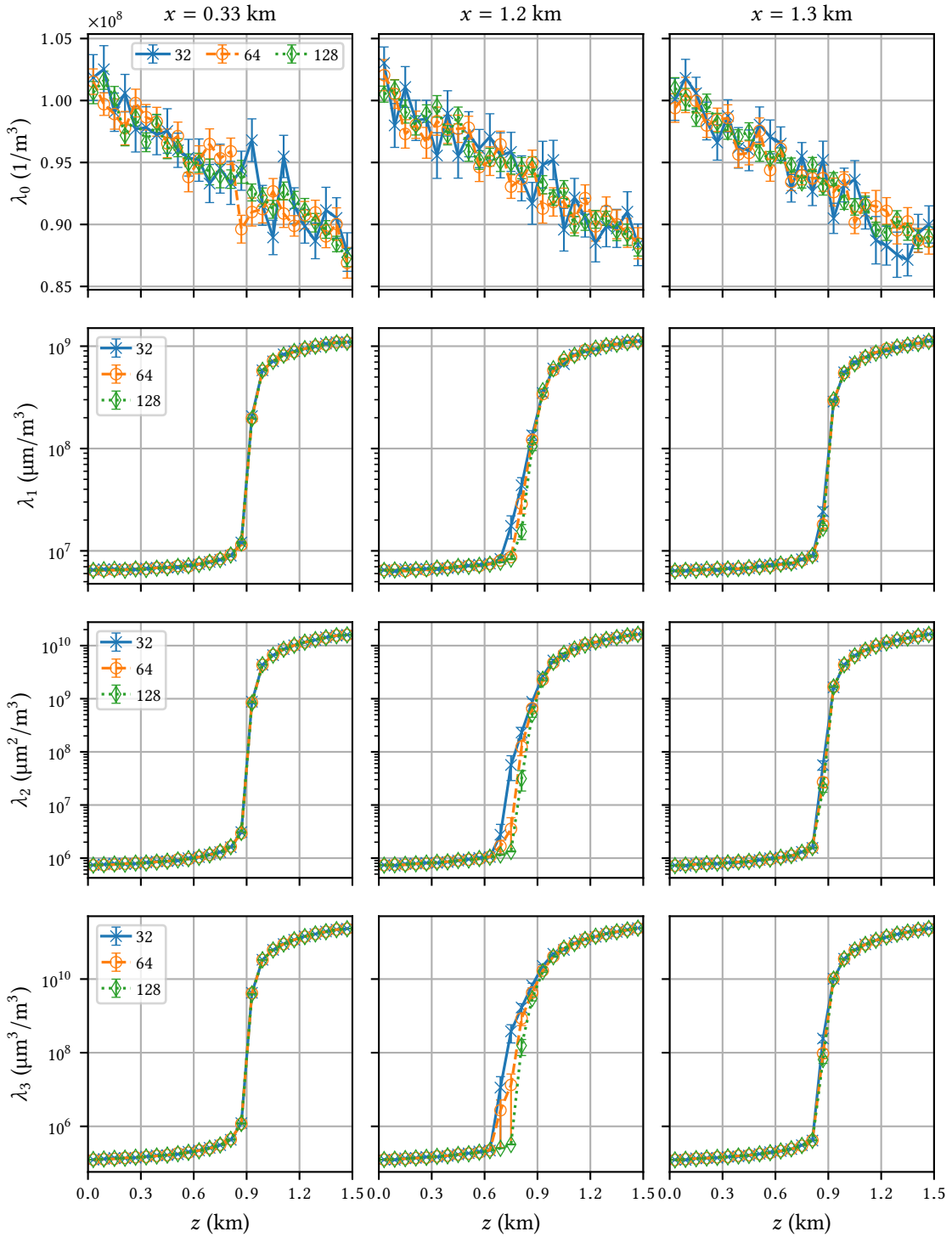


**Figure 6.12:** Effect of varying the **particle number per cell**  $N_{\text{SIP}}$  on the first four moments of the size distribution, when using the Long collision kernel. The plots show the behavior after 30 minutes simulation time in vertical columns (depending on  $z$ ) at three different horizontal positions  $x$ , which are indicated in Fig. 6.11 and coincide with the columns for the size spectra in Fig. 6.7. As for the distributions, moments are calculated using all radii in boxes of  $3 \times 3$  grid cells each.

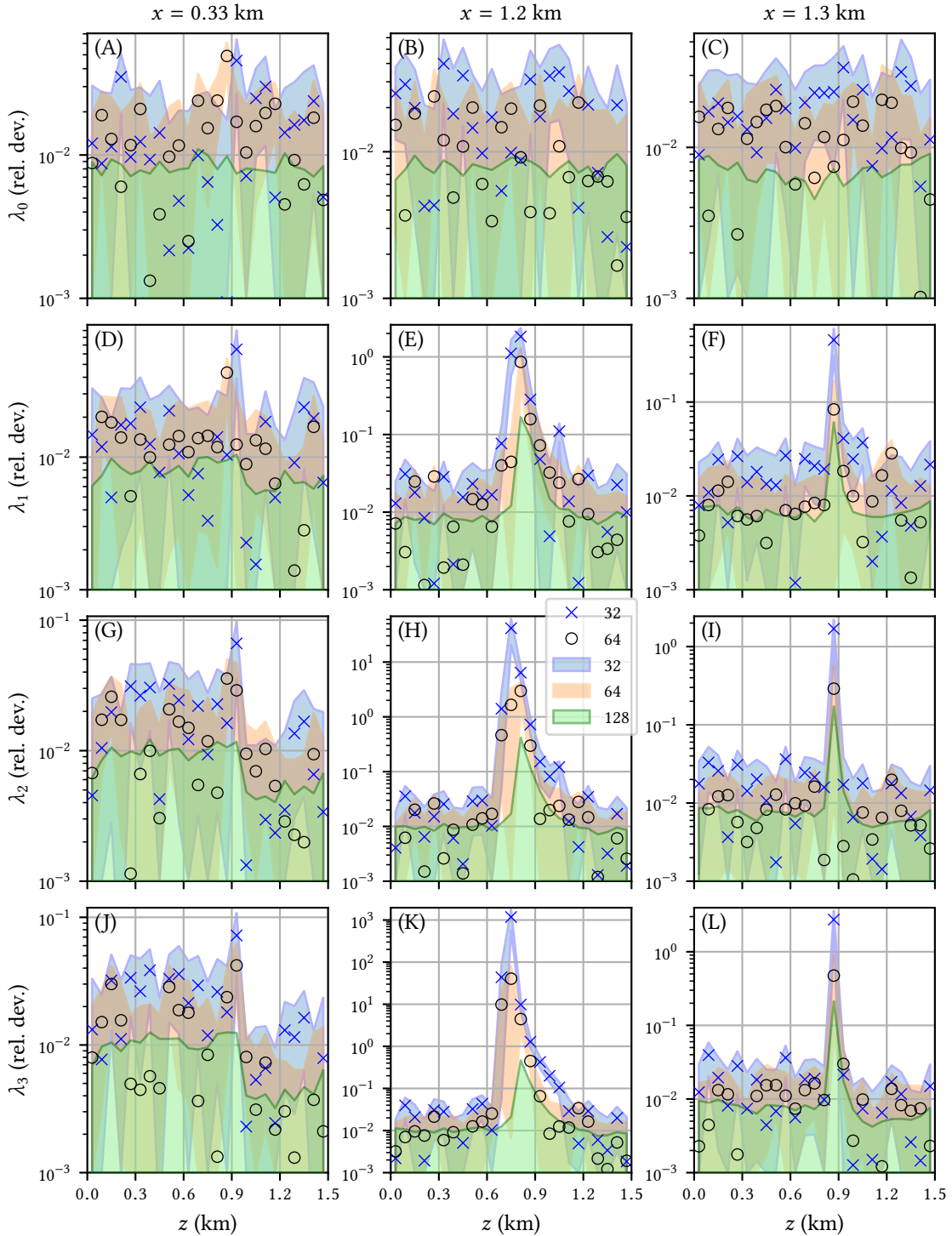


**Figure 6.13:** Relative deviations  $|\lambda_k - \lambda_{\text{ref}}| / \lambda_{\text{ref}}$  for the moments of the size distribution, when varying the **particle number per cell**  $N_{\text{SIP}}$  in case of the Long kernel. The “reference” is set to the simulation with the most SIPs ( $N_{\text{SIP}} = 128$ ). Blue crosses and black circles indicate relative deviations for 32 and 64 SIPs, respectively, as shown in the legend. The shaded areas illustrate relative errors  $\text{SD}(\lambda_k)/\lambda_{\text{ref}}$  for 32 (blue), 64 (orange) and 128 (green) SIPs. The plots show the behavior after 30 minutes simulation time in vertical columns (depending on  $z$ ) at three different horizontal positions  $x$ , which are indicated in Fig. 6.11 and coincide with the columns for the size spectra in Fig. 6.7. As for the distributions, moments are calculated using all radii in boxes of  $3 \times 3$  grid cells each.

and thus the saturation behavior) until a distinct junction is notable between 800 and 1000 m, followed again by a smooth increase. Values for simulations with different number of SIPs are quite close in this illustration. Significant deviations are only detectable for single data points in the third column at  $z = 870$  m. Close to the downdraft tunnel (column 2), we observe similar shape, but for a less steep transition at the cloud border. The junction now extends down to 750 m. Moreover, major deviations are visible in this region, when comparing runs with different  $N_{\text{SIP}}$ . The values increase unambiguously with decreasing number of SIPs. Nevertheless, it shall be emphasized that the deviation is only observable in the transition region. Close to the earth's surface and inside the cloud, there is no significant difference detectable on the chosen scales.

To obtain more conclusive statements, we present a detailed analysis of the relative deviations  $|\lambda_k - \lambda_{\text{ref}}| / \lambda_{\text{ref}}$  in Fig. 6.13, where the “reference” is set to the simulations with largest  $N_{\text{SIP}} = 128$ . We will first analyze the behavior of  $\lambda_0$ , which is similar in all three columns. All calculated deviations for both,  $N_{\text{SIP}} = 32$  and  $N_{\text{SIP}} = 64$ , reside below 5 %. For the last two columns, we can confirm that discrepancies and uncertainties increase for smaller SIP numbers. In the case of  $N_{\text{SIP}} = 128$  we observe relative errors below 1 percent. The deviations for smaller  $N_{\text{SIP}}$  are not covered by the estimated uncertainties. For moments 1 to 3, we will investigate each vertical column separately. At the updraft tunnel ( $x = 330$  m), all deviations reside below 4 %, when excluding the cloud base region, where maxima of 8 % are reached. At the downdraft tunnel, we observe major peaks in the transition region, where relative differences amount to  $(2 \pm 0.5, 50 \pm 25, 1000 \pm 400)$  ( $\lambda_{1,2,3}$ ) for  $N_{\text{SIP}} = 32$  and  $(0.8 \pm 0.3, 3 \pm 1, 40 \pm 35)$  ( $\lambda_{1,2,3}$ ) for  $N_{\text{SIP}} = 64$  (note that these values are not given in percent). Noteworthy, the described regions coincide with the crossing of the vertical column and areas, where  $\Delta R_{\text{eff}}$  assumes largest values, indicated by red color in Fig. 6.11. On average, simulations with the smaller SIP number lead to larger discrepancies to the reference case. Previously noted maximum deviations are significantly reduced by duplicating the number of SIPs. Nevertheless, they still can not be justified by the error bars. The third column shows similar behavior, but with narrower and less pronounced peaks at  $z = 900$  m, where relative deviations reach up to  $(300 \pm 100)$  % and  $(50 \pm 45)$  % for  $N_{\text{SIP}} = 32$  and 64, respectively. When disregarding the irregularities near the cloud junction, relative differences remain below 10 % and 5 % for columns 2 and 3, respectively.

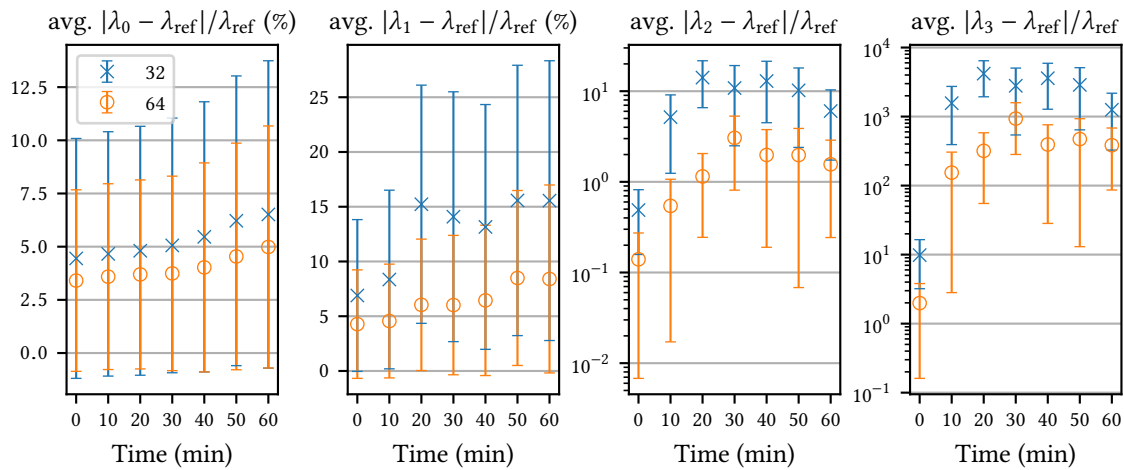


**Figure 6.14:** Moment deviations  $|\lambda_k - \lambda_{\text{ref}}| / \lambda_{\text{ref}}$  relative to the “reference” of  $N_{\text{SIP}} = 128$  are calculated for each grid cell and subsequently averaged over the whole grid.

Finally, we shall attempt to draw some conclusions regarding the influence of the average number of SIPs per cell. Consistent with the error analysis in Fig. 6.5, we observe sensitive regions at the edges of downdraft tunnel and cloud base, where relative deviations and errors increase by orders

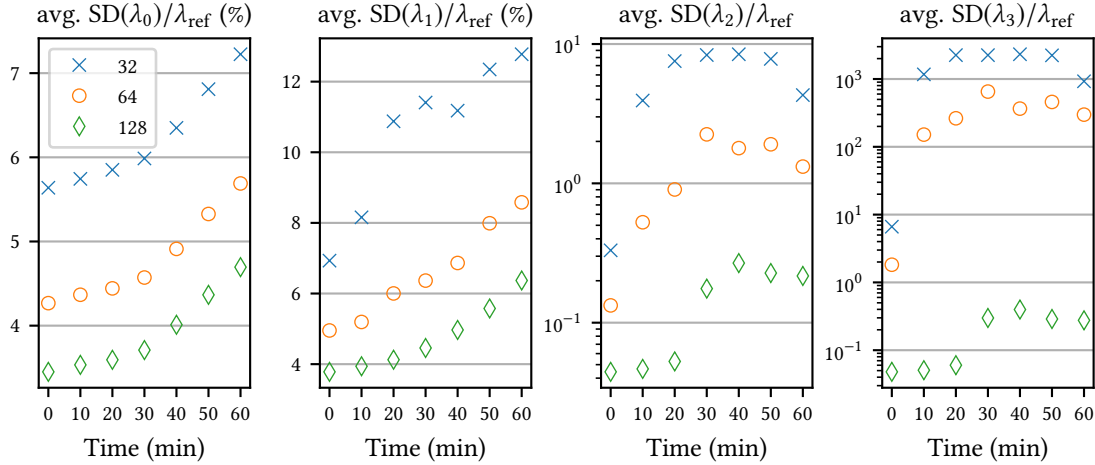


**Figure 6.15:** Estimated uncertainties  $\text{SD}(\lambda_k) / \lambda_{\text{ref}}$  relative to the “reference” of  $N_{\text{SIP}} = 128$  are calculated for each grid cell and subsequently averaged over the whole grid.

of magnitude. Since the results are presented on a high resolution level and additionally fluctuate strongly, we will make some generalizations to detect significant trends. Therefore, deviations  $|\lambda_k - \lambda_{\text{ref}}| / \lambda_{\text{ref}}$  and estimated uncertainties  $\text{SD}(\lambda_k) / \lambda_{\text{ref}}$  relative to the “reference” of  $N_{\text{SIP}} = 128$  were calculated for each grid cell and subsequently averaged over the whole grid. We thus obtain spatially averaged parameters for each moment and SIP number. The time evolution for one hour is shown in Figs. 6.14 and 6.15. In contrast to Figs. 6.12 and 6.13, moments are initially not calculated in boxes of  $3 \times 3$  cells, but separately for all single cells, leading to larger spatial averages of the deviation. We emphasize that all implications should be handled cautiously due to major spatial fluctuations, large error bars and the limited amount of parameter variations. Simulations with  $N_{\text{SIP}} = 32$  and  $N_{\text{SIP}} = 64$  will be denoted as case 1 and 2, respectively.

Regarding the major trends, relative deviations increase with moment order, time and, more relevantly, with decreasing SIP number (Fig. 6.14). When additionally averaging over time, results of the reference are closer to case 2 than to case 1 by factors of 1.3, 2, 6 and 7 ( $\lambda_{0,1,2,3}$ ), which indicates some kind of convergence with SIP number. We point out that this behavior is not continuous over all positions ( $x, z$ ), but prone to significant fluctuations, as discussed previously. Due to missing data for larger  $N_{\text{SIP}}$  and the system complexity with  $75 \times 75$  grid cells, describing spatially inhomogeneous fields, we are not able to provide more precise statements. For the grid average of  $\lambda_0$ , cases 1 and 2 are both accurate within error bars. This can even be stated for  $\lambda_1$  and  $N_{\text{SIP}} = 64$ . Higher moments show an increase in the deviations by orders of magnitudes. We conclude that a significantly larger number of super-droplets per cell is necessary to reach convergence in all aspects of the size distribution. Considering the spatial averages of estimated uncertainties, we observe similar behavior: Relative errors increase with moment order, time and decreasing  $N_{\text{SIP}}$  (Fig. 6.15). Most remarkably, uncertainties can be reduced by 1 and even 3 orders of magnitude for  $\lambda_2$  and  $\lambda_3$ , respectively, when duplicating the SIP number from 64 to 128.

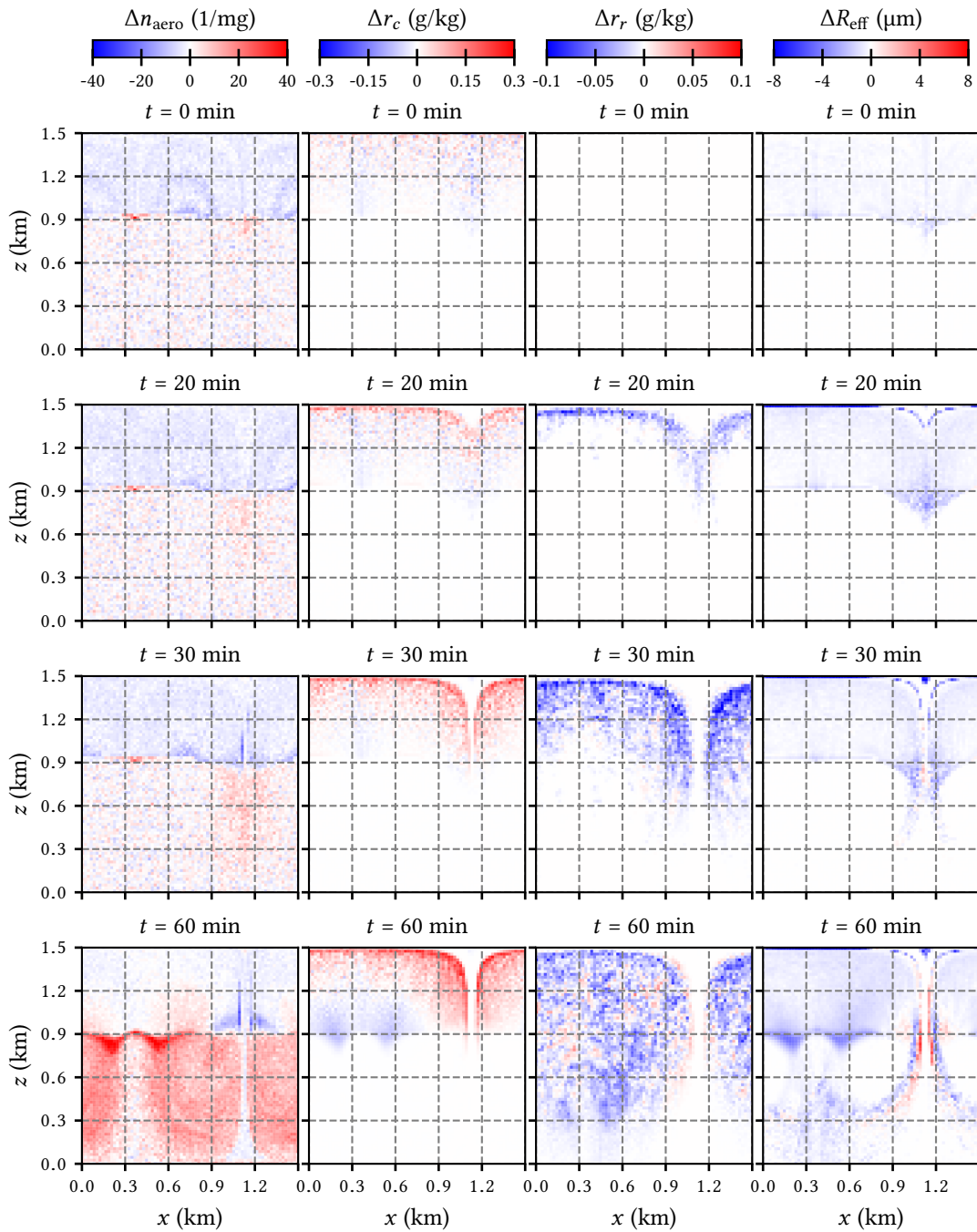


**Figure 6.16:** Deviations  $\Delta b = b_* - b_{\text{def}}$  between results of simulations with **grid cell size**  $\Delta x = 10 \text{ m}$  ( $b_*$ ) and  $\Delta x = 20 \text{ m}$  ( $b_{\text{def}}$ ), where  $b_k$  is either the aerosol number concentration (per dry air mass), cloud water mixing ratio, rain water mixing ratio or effective cloud droplet radius. In both cases, the Long kernel was used with  $N_{\text{SIP}} = 64$ , implying that the finer grid also contains four times more simulation particles.

### 6.4.3 Influence of the spatial grid step size

To analyze the influence of the grid cell size, we performed 50 simulations with refined grid steps  $\Delta x = \Delta z = 10$  m and  $N_{\text{SIP}} = 64$ , thereby quadrupling both, the number of grid cells and total number of SIPs. We choose the same advection time step of  $\Delta t_{\text{adv}} = 1$  s, because the maximum CFL number of the fluid flow is still  $\text{CFL}_{\max} = \Delta t_{\text{adv}} \max(|u/\Delta x| + |w/\Delta z|) < 0.12$ . Even though the volumetric density of super-droplets increases, the same initial amount of particles remains in every ensemble, when applying the collision algorithm. To enable direct comparison, the results of the finer grid were averaged over  $2 \times 2$  grid cells, leading to the same resolution of  $75 \times 75$  data points. Figure 6.16 illustrates the deviations  $\Delta b = b_* - b_{\text{def}}$  between the cases  $\Delta x = 10$  m ( $b_*$ ) and  $\Delta x = 20$  m ( $b_{\text{def}}$ ), where  $b_k$  represents the particle field properties aerosol number concentration, cloud water mixing ratio, rain water mixing ratio and effective radius. Other than for the collision time step, we identify distinct, systematic patterns in the scalar fields.

For the finer grid, the aerosol number concentration  $n_{\text{aero}}$  is smaller inside the cloud and, more distinctly, larger below the cloud by an order of 40 %. Moreover, we unambiguously observe more cloud water  $r_c$  in the cloud and less rain water  $r_r$  in the whole domain. Deviations are in the order of 30 %. The effective radius  $R_{\text{eff}}$  is mostly decreased, indicating a shift of the distribution to smaller cloud droplets. Only for  $t = 60$  min, small slices at the edges of the downdraft tunnel show increased values of  $R_{\text{eff}}$ . Noteworthy, the effective radius is now reduced in exactly the same regions, where an increase was indicated for higher  $N_{\text{SIP}}$  in Fig. 6.11. We attempt to investigate this apparent contradiction: An increased SIP density due to a larger amount of grid cells leads to a reduction, while a higher number of SIPs per cell leads to an increase of  $R_{\text{eff}}$ .

We offer the explanation that not only the collision, but also the condensation process is influenced by a finer grid resolution. In each cell, all super-droplets compete for the water vapor during the condensation step. We propose that this process is realized with higher precision, when the cell volumes are smaller, which might lead to a shift of the size distribution to a larger number of small particles. This behavior is ultimately amplified, because now there are fewer large rain droplets, which can effectively collect aerosols on their descending path. As a consequence, we observe much larger aerosol concentrations in the regions below the cloud at  $t = 60$  min. Unfortunately, the scope of this work did not allow to investigate the condensation process in more detail for the finer grid resolution. The presented 50 simulations took three weeks of computation time.

In any case, we observe significant systematic deviations and must conclude that convergence is not reached at a grid cell size of  $20 \times 20$  m. Remarkably, refining the grid, when using the same SIP number per cell leads to larger differences of the scalar particle fields than increasing  $N_{\text{SIP}}$  in each cell (cf. Figs. 6.11 and 6.16).

## 6.5 Influence of the collision kernel

As for the box model, we analyze the influence of the applied collision kernel. Results for simulations, where the collisions are switched off entirely and where the hydrodynamic kernel is applied with constant collection efficiency (cf. Sec. 6.3) are shown in the Appendix (Figs. E.1 and E.4). A comparison between the kernels of Hall and Long (default) is presented in Fig. 6.17.

Quite similar to the refined grid case, the Hall kernel leads to a reduction in rain water and to an increase in cloud water content. This behavior develops after 20 minutes and intensifies after 30 minutes simulation time. As a consequence, there are less large collector droplets in the region below the cloud, leading to a considerable increase in small aerosol particles below the cloud at  $t = 60$  min. Moreover, the effective radius shows reduced values, indicating a shift of the distribution to smaller cloud droplets, as well. The observed behavior coincides with the

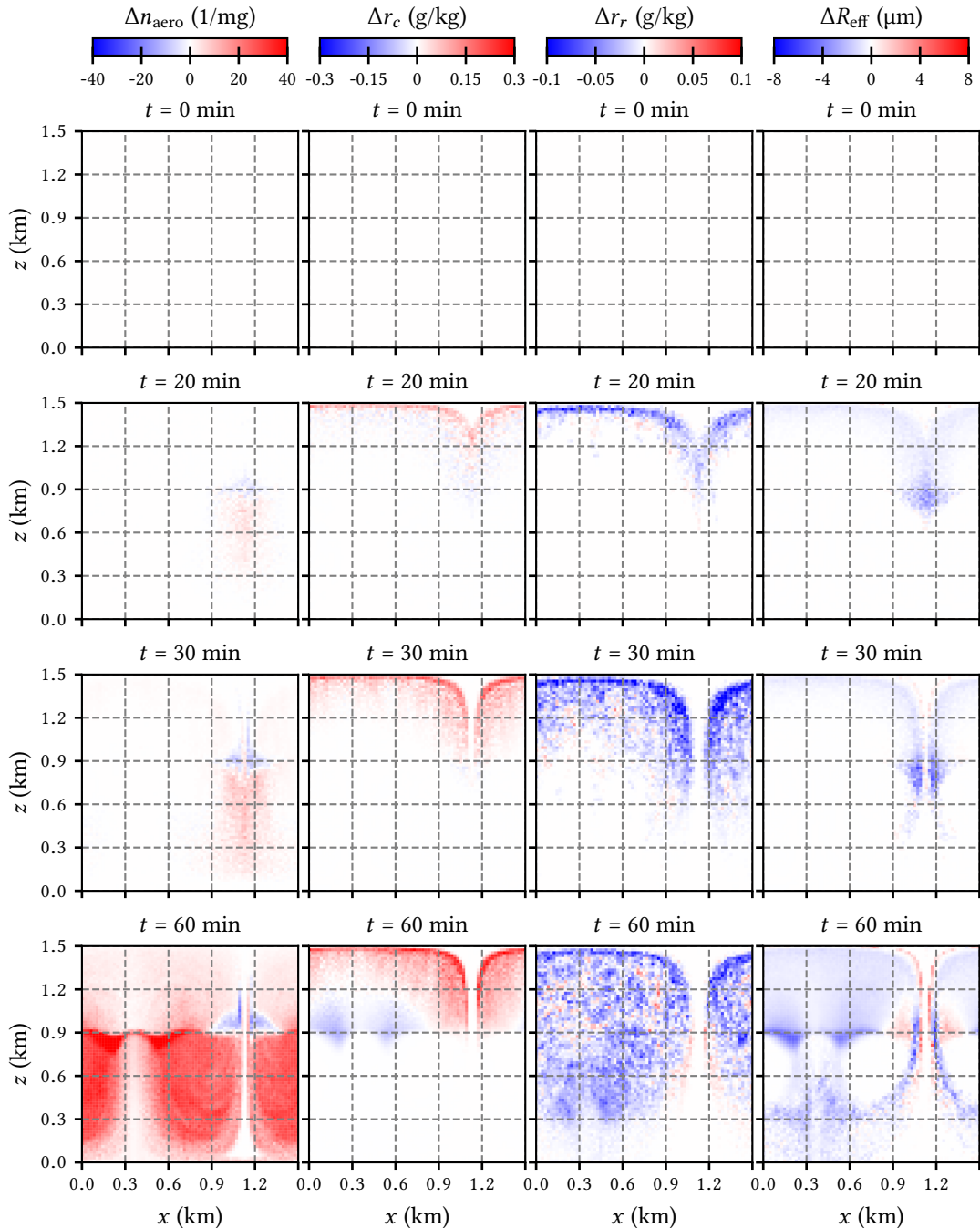


**Figure 6.17:** Deviations  $\Delta b = b_* - b_{\text{def}}$  between results of simulations using the **Hall kernel** ( $b_*$ ) and the **Long kernel** ( $b_{\text{def}}$ ), where  $b_k$  is either the aerosol number concentration (per dry air mass), cloud water mixing ratio, rain water mixing ratio or effective cloud droplet radius. In both cases,  $N_{\text{SIP}} = 64$  is used.

results of the collision box model (Sec. 5.2.3): Considering simulations with  $N_{\text{SIP}} = 50$ , the droplet concentration here decreases by 8.7 % (64 %) for the Hall kernel and by 9.9 % (94 %) for the Long kernel after 30 (60) minutes. This indicates that the overall efficiency of collections is significantly reduced, when using the Hall kernel and explains the observed differences in Fig. 6.17.

## 6.6 Variation of physical conditions

In the following, we will assess the plausibility of results from simulations with different physical parameter settings, including solute type and initial CCN number concentration. We will restrict the following analyses to a qualitative level.

### 6.6.1 Influence of the solute type

Due to larger water activities, the equilibrium saturation  $S_{\text{eq}}(R_p)$  of ammonium sulfate is higher than for sodium chloride at any given radius (cf. Fig. 3.4). This must have significant effects on the condensation process within a particle ensemble. To check the response of our model, 50 additional simulations were performed, using NaCl as solute material for all CCNs. The resulting differences to the default case  $((\text{NH}_4)_2\text{SO}_4)$  are presented in Fig. 6.18.

From the beginning (i.e. after spin-up), we observe less aerosol particles and more cloud water content inside the cloud. Additionally, less rain water forms in the cloud region, when considerable collection starts after 20 minutes. The effective radius shows reduced values inside the cloud (neglecting minor tendencies at the downdraft tunnel edges), which indicates a shift of the size distribution to smaller droplets. Below the cloud, we find a larger number of aerosol particles after 60 minutes simulation time. Considering that sodium chloride is characterized by smaller water activity, we conclude that our model provides plausible results: Because the activation level is lower, more droplets with smaller dry radius will be activated at a given saturation  $S > 1$ . Consequently, the water vapor is distributed to a larger number of particles and large rain droplets will not be able to grow as much by condensation. This leads to a reduced number of particles with  $R_p < 0.5 \mu\text{m}$  (aerosols) and at the same time to a reduction of the average rain droplet size. Hence, aerosols are less efficiently collected below the cloud.

### 6.6.2 Influence of the CCN number concentration

The CCN number concentration is of major importance for the cloud evolution. As customary in meteorological context, we differentiate between *pristine* environments with low concentrations and *polluted* environments with high concentrations. Precise definitions vary and always depend on a variety of conditions for the described system [Hamilton14]. To investigate the response of our model, we performed additional simulations with half and twice the number concentration of default case, which we will denote by “pristine” and “polluted”, respectively. For an qualitative analysis, results for both additional scenarios are illustrated in Figs. 6.19 and 6.20, using the same size scales for the color bars.

As expected, the aerosol and cloud droplet number concentration is much higher for the polluted scenario (by a factor of approximately 4). Noteworthy, at the beginning, there are less droplets in the pristine cloud, but the cloud water content has the same shape and magnitude as in the polluted case. This means that the same amount of water vapor has condensed on a smaller number of particles. At  $t = 0$ , the average cloud droplet mass must thus be about four times higher in the pristine scenario. Consequently, the size dependent collection process is more efficient and rain droplet formation is accelerated. Already after 20 minutes, we observe a considerable amount of rain water content. Subsequently, the cloud droplets and aerosols are depleted due to collections by the growing rain drops, which finally leads to a cloud consisting of few, but large

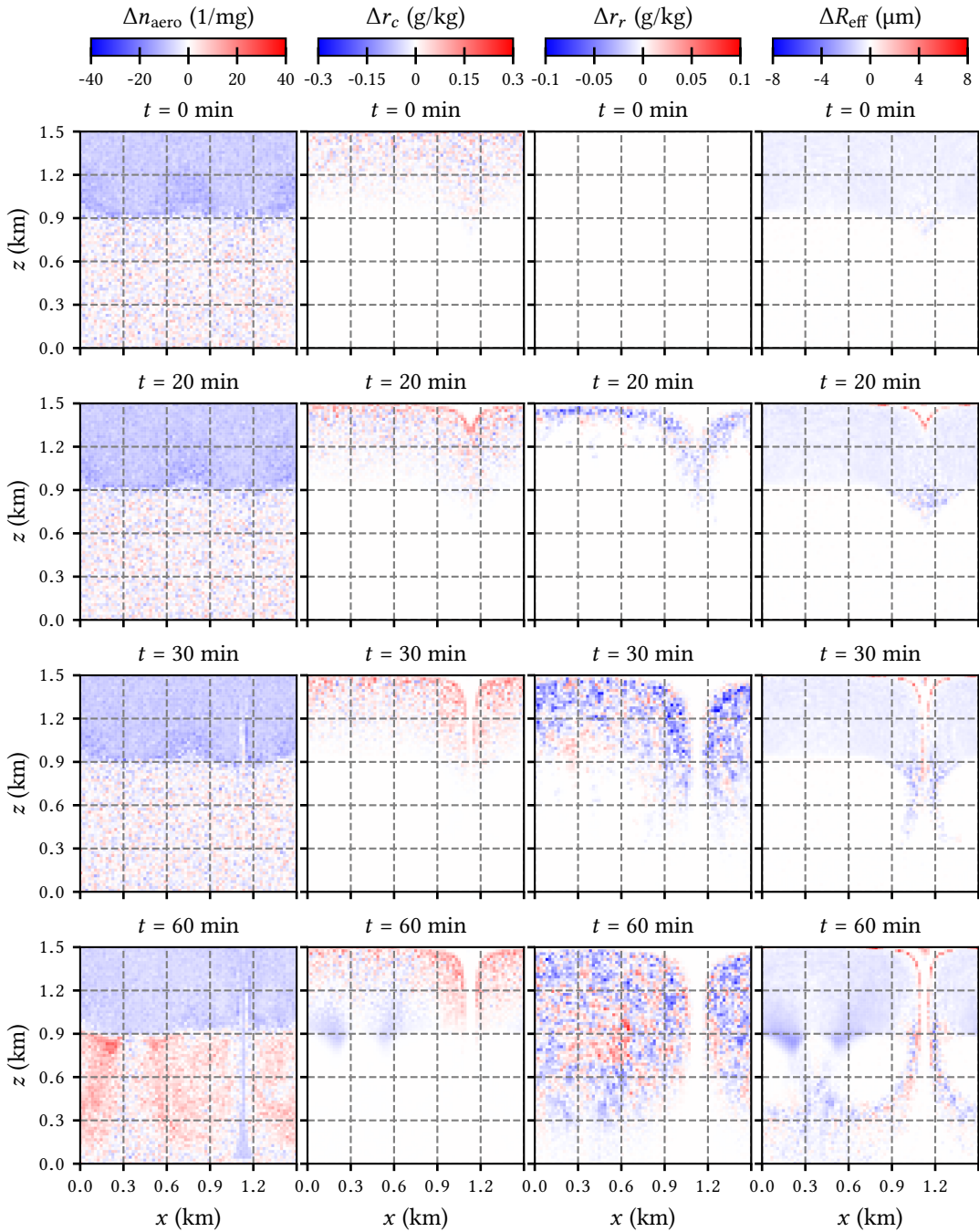


**Figure 6.18:** Deviations  $\Delta b = b_* - b_{\text{def}}$  between results of simulations, where sodium chloride ( $b_*$ ) and ammonium sulfate ( $b_{\text{def}}$ ) are used as CCN **solute material**. The field  $b_k$  is either the aerosol number concentration (per dry air mass), cloud water mixing ratio, rain water mixing ratio or effective cloud droplet radius. In both cases, the number of super-droplets per cell is  $N_{\text{SIP}} = 64$ . The initial two hour spin-up period is not shown.

particles after 60 minutes simulation time. Additionally, the downdraft tunnel broadens, because heavier particles deviate stronger from the cyclic fluid trajectories and accumulate closer to the vortex centers.

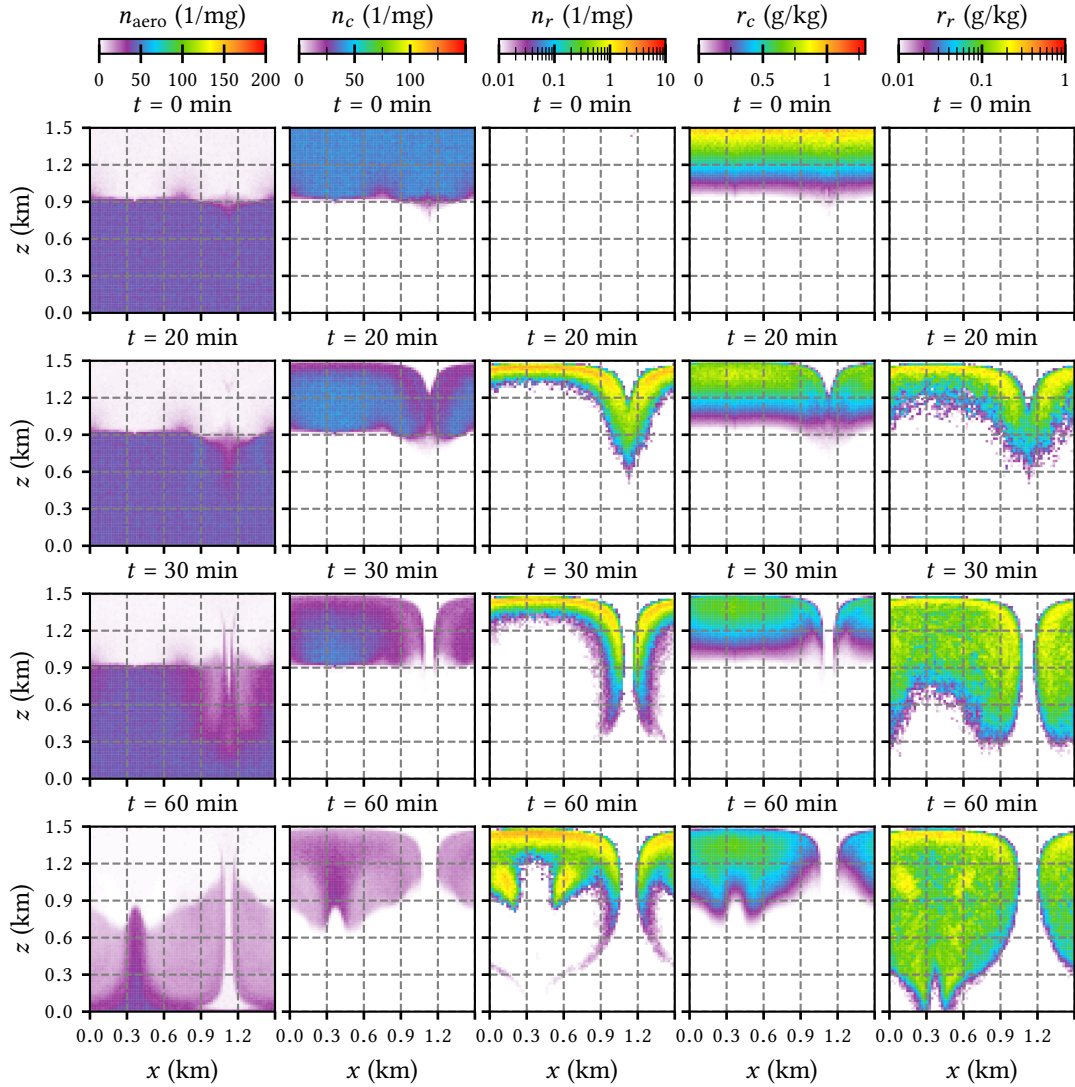


**Figure 6.19:** Simulation results for the time evolution of aerosol, cloud droplet and rain droplet number concentrations (per dry air mass) and cloud water and rain water mixing ratios, using the Long collision kernel with  $N_{\text{SIP}} = 64$  in a **more pristine environment** with half the CCN number concentration, i.e.,  $\text{DNC}_1 = 30 \text{ cm}^{-3}$ ,  $\text{DNC}_2 = 20 \text{ cm}^{-3}$ . The presented values are averages over 50 independent simulations. The initial two hour spin-up period is not shown.

In the polluted environment we observe opposing behavior. Droplets have smaller average radii, which leads to less effective collection and thus considerable limitation of rain formation. Even after one hour, the rain water content is nearly negligible, considering the logarithmic scale. On the other hand, the cloud water increases, while  $n_{\text{aero}}$  decreases below the cloud. This indicates that aerosols are primarily collected by cloud droplets rather than rain drops. Consequently, the cloud consists of many, but smaller particles and the downdraft tunnel is narrower than in the pristine case. Since the main features of the well known pristine and polluted scenarios are reproduced, we conclude that, on a qualitative level, the model generates plausible results, when varying the CCN number concentration.

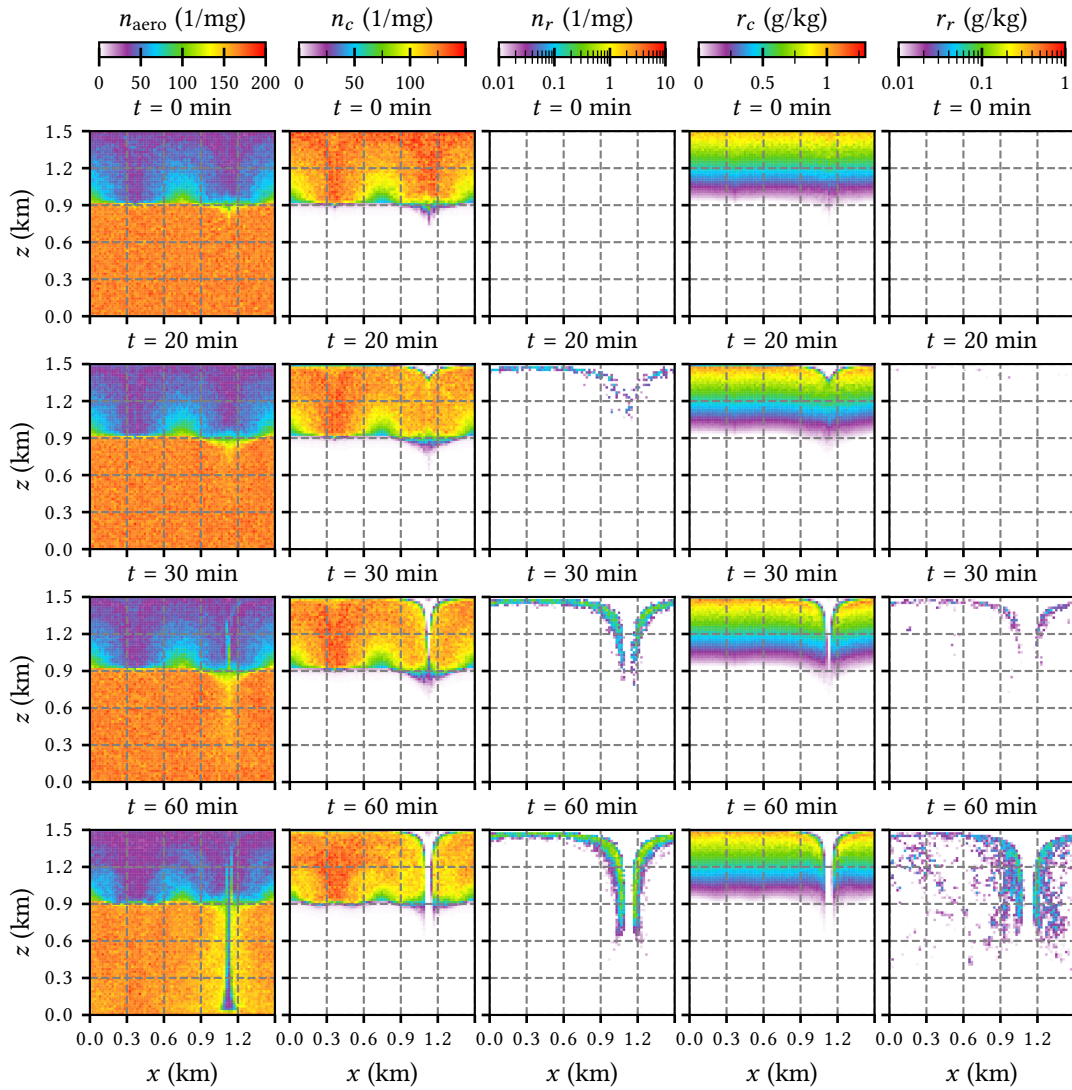


**Figure 6.20:** Simulation results for the time evolution of aerosol, cloud droplet and rain droplet number concentrations (per dry air mass) and cloud water and rain water mixing ratios, using the Long collision kernel with  $N_{\text{SIP}} = 64$  in a **more polluted environment** with doubled CCN number concentration, i.e.,  $\text{DNC}_1 = 120 \text{ cm}^{-3}$ ,  $\text{DNC}_2 = 80 \text{ cm}^{-3}$ . The presented values are averages over 50 independent simulations. The initial two hour spin-up period is not shown.

# 7

## CONCLUSIONS AND OUTLOOK

Due to significant advantages of particle based schemes over state-of-the-art bulk and bin models, the description of associated physical phenomena and development of appropriate numerical techniques are subject to intensive and ongoing research in the cloud modeling community (cf. Ch. 1 and [Grabowski19]). The presented work's objective was to develop and numerically implement a solid Lagrangian particle model for cloud microphysics. Related to fully dynamic atmospheric simulations, as utilized in weather predictions and climate research, the featured formulation of individual cloud particle behavior constitutes one important part in a larger framework. Since the variety and complexity of underlying atmospheric processes leads to considerable demands during modeling and coding, the created program's scope is currently restricted to the specific case of ice-free cloud simulations in two-dimensional atmospheric kinematic frameworks with one type of CCN material (either ammonium sulfate or sodium chloride). However, the program is designed to be efficiently extendable by its modular structure. Without unreasonable additional effort, three-dimensional, fully dynamic simulations can be enabled by coupling to existing CFD solvers. Furthermore, the applied super-droplet method allows sophisticated implementation of liquid and ice phase multi-component chemistry and treatment of local turbulence, which will be elucidated below (pp. 86-87). Main features of the developed algorithm, including schemes for the advection of atmospheric fields and particle collisions, were tested in isolated environments (see Sec. B and 5.2, respectively), while the complete program was validated by simulating a kinematic drizzling stratocumulus test case (Ch. 6). This chapter will proceed with a summary and discussion of the presented results and concludes with an overview of reasonable extensions and improvements as well as future research possibilities.

As introduced in Sec. 3.5, the applied Lagrangian model enables a stochastic description of the droplet coagulation process, thus requiring less assumptions than Eulerian schemes, which typically depend on deterministic types of the collection equation. We analyzed the implemented algorithm in a collision box model, neglecting particle dynamics and mass exchange by condensation/evaporation (Ch. 5). Since the coverage of sensitive regions of the particle mass distribution has significant effects on the convergence behavior, we applied the SingleSIP method introduced by Unterstrasser, Hoffmann and Lerch during ensemble initialization [Unterstrasser17]. As expected, both, the result quality and the computational effort increased with number of simulated SIPs per cell. It is thus of great interest to assess if the advantages of a larger SIP count justify the quadratic growth of required numerical operations. In all box model cases, we performed 500 independent one hour simulations to enable statistical analysis.

For the artificial Golovin (sum-of-mass) kernel, it is possible to compare the time evolution of the droplet size spectrum to an analytic solution of the stochastic coalescence equation. All analyzed moments ( $\lambda_{0,2,3}$ ) show converging behavior towards the reference with increasing SIP count (the box model conserves the first moment, equal to the liquid mass content). For the largest simulated number  $N_{\text{SIP}} = 1000$ , the distributions match well enough to state that the implemented algorithm is able to generate reasonable results, when additionally considering the convergence trend (Sec. 5.2.1). In case of the hydrodynamic kernel, there is no analytic solution and we compare to a state-of-the-art bin model [Wang07]. For both investigated parametrizations of the collection efficiency (modified versions of the ones presented in [Long74] and [Hall80], see

Sec. 4.4.2), the zeroth moment's convergence shows a negative power law ( $\propto N_{\text{SIP}}^{-a}$  with  $a \approx 1$ ), while the behavior of higher moments can be approximated by logarithmic functions ( $c - a \ln(N_{\text{SIP}})$  with  $a > 0$ , see Table 5.1). We observe that convergence is reached within  $2\sigma$  intervals of the estimated uncertainties for  $N_{\text{SIP}} = 15\,000$ . Furthermore, the general shape and features of the reference bin model spectra can be reproduced. For the tabulated Hall kernel, maximum deviations of all investigated moments can be reduced to  $(3 \pm 1)\%$ , when using 15 000 SIPs. In case of the Long kernel, similar coincidence is possible for  $\lambda_{2,3}$ , while  $\lambda_0$  shows deviations up to  $(20 \pm 1)\%$  after a simulation time of one hour, which implies that our discrete particle method leads to slightly reduced average collection rates. It is known that the Long kernel generates spectra with more distinct extrema and is thus more difficult to handle numerically, which corresponds with our observations [Unterstrasser17]. We emphasize that both, the bin model and the Lagrangian scheme, are numeric tools to solve the same physical problem, namely the collision interactions of a complex droplet ensemble. For the two compared implementations, it is not evident, which method yields a representation closer to the exact solution. In conclusion of our analysis, we are however confident that our algorithm generates reasonable results and is a feasible alternative to the state-of-the-art bin model.

To validate the developed microphysics scheme, including droplet dynamics, thermodynamics, condensation/evaporation and collisions, a drizzling stratocumulus cloud was simulated in a two-dimensional kinematic framework with stationary dry air density and velocity field (test case 1 of the 8<sup>th</sup> international cloud modeling workshop 2012, see Sec. 2.4, Ch. 6 and [Muhlbauer13]). The setup features a closed circulation cell and provides the possibility to investigate the processing of cloud condensation nuclei during complete growth cycles in minute detail. For each set of chosen parameters, we performed 50 independent one-hour simulation runs (following a two hour spin-up phase) with different random number seeds to enable statistical analysis. The default case uses the Long kernel with 64 SIPs per cell and ammonium sulfate as CCN material. Our evaluation addresses two major tasks: Firstly, assessment of the result's plausibility, including a comparison to Lagrangian simulations of the same test case by Arabas *et al.* and the variation of physical conditions and secondly, investigation of numerical stability and finite size effects [Arabas15].

An atmospheric cloud domain can be characterized by numerous different properties. To cover the ambient air, we provide results for the chosen state variables dry potential temperature  $\Theta$  and water vapor mixing ratio  $r_v$  (Sec. 6.2.1). The cloud is represented by the effective radius and a particle classification in *aerosols* (almost dry), *cloud droplets* (radius  $R_p < 25\,\mu\text{m}$ ) and larger *rain drops*, leading to respective mixing ratios  $r_k$  and number concentrations  $n_k$ . Additionally, we analyze the particle size spectra of selected regions in more detail.

As expected for this kinetic setup, the atmospheric fields  $\Theta$  and  $r_v$  show steady behavior and negligible uncertainties, except for evolving updraft and downdraft tunnels (Fig. 6.3) at the edges of the flow field circulation cells, which can be explained due to inertia and gravity effects (Sec. 6.2.1). Our simulations generate the intended evolution of a well layered cloud above approximately 900 meters with considerable rain water formation starting after 20 minutes, followed by drizzling rain onset at  $t \approx 30$  min. Due to the Lagrangian formulation, we are able to track the evolution of individual cloud particles. Our presentation of one chosen droplet trajectory shows all important stages of the complete growth cycle and indicates allover explainable and plausible behavior (Sec. 6.2.2). Variation of the initial CCN number concentration leads to the expected behavior of increasing rain water content with larger drops in the more pristine environment and negligible drizzle formation in the more polluted case (Figs. 6.19 and 6.20). Comparing simulations with CCNs consisting of sodium chloride instead of ammonium sulfate, we can confirm the expected increase in cloud water at the cost of aerosols and rain water content due to reduced water activity (see Sec. 6.6.1 and Figs. 3.4, 6.18).

Arabas *et al.* provide simulation results for the same setup, but with constant collection efficiency  $E_c = 0.5$  and further differences in the implementation of the particle based scheme [Arabas15], which are listed and discussed in Sec. 6.3. Our results for the corresponding kernel formulation generally show similar features in cloud structure and stratification and for the droplet size distributions (Figs. E.3 and E.4). In Section 6.3 we offer reasonable explanations for the most distinct differences in rain water amount (maximum deviations of 30 %) and broadening of the downdraft tunnel, regarding alternative approaches for droplet dynamics and collision algorithm as well as additional relaxation terms in the formulation applied in [Arabas15]. In consideration of the presented response to physical parameter variations and the agreeable coincidence with other particle based simulations, we conclude that the developed model behaves reasonable and provides plausible results for the cloud evolution. Since the utilized test case constitutes an artificially idealized environment, direct comparison to experimental data is not possible. Our assessment regarding the expected behavior of the simulated cloud relies on the collected, modeling and observation based experiences presented in studies of several author's, who investigated kinematic frameworks of similar kind [Szumowski98, Grabowski98, Grabowski99, Morrison07, Rasinski11, Arabas15, Jaruga18].

In course of a finite size analysis, we observe no significant systematic effect, when reducing the collision time step from 0.5 s to 0.1 s and thus conclude that the default time step provides sufficient resolution for the given setup (Sec. 6.4.1). Refinement of the grid spacing from 20 to 10 meters on the other hand leads to significant deviations in the structure and magnitude of aerosol concentration as well as cloud and rain water content, indicating that convergence is not yet reached for the coarser grid resolution (Sec. 6.4.3). Since the computation time increases by a factor of approximately 11, it was however not manageable to choose the refined setup as default for all simulations. We further present an extensive comparison of three simulation cases with 32, 64 and 128 SIPs per cell, including the behavior of size distribution moments  $\lambda_{0,1,2,3}$  (Sec. 6.4.2). Our findings implicate three major points:

First, the estimated uncertainties (i.e. deviations between independent runs with same parameters and different random seed) decrease significantly with SIP number (Fig. 6.15). Second, results of the case using the largest  $N_{\text{SIP}} = 128$  are closer to the ones generated with  $N_{\text{SIP}} = 64$  than with  $N_{\text{SIP}} = 32$  (Fig. 6.14). This indicates some kind of convergence behavior, which we were not able to classify further (see discussion in Sec. 6.4.2, p. 74). Deviations between  $N_{\text{SIP}} = 128$  and  $N_{\text{SIP}} = 64$  are in the order of 5 % and 10 % for  $\lambda_0$  and  $\lambda_1$ , respectively. Higher moments show much less coincidence, indicating large influence of undersampled regions in the size distribution. Third, position dependent analysis reveals that in most of the domain, differences between the three cases are acceptably small (order of 1 to 3 %), while there are distinct regions close to the downdraft tunnel and cloud base, where deviations for all moments are exceptionally high (Figs. 6.11 and 6.13). These sensitive areas are also characterized by the largest estimated uncertainties, spatial fluctuations and field gradients and deteriorate the domain-averaged deviations by orders of magnitude. We conclude that convergence is not yet reached for  $N_{\text{SIP}} = 64$ , but the effect of smaller SIP numbers is less pronounced than expected from the collision box model simulations (see also discussion in Sec. 5.3). Characteristics of the droplet number concentration ( $\lambda_0$ ) and average radius ( $\propto \lambda_1$ ) are well represented, while higher moments show considerable sensitivity, especially in distinct regions. Regarding the possible reduction in estimated error bars, our observations suggest significant improvements, when using at least 128 SIPs per cell for the given setup. Since the larger SIP number requires approximately twice as much computation time, it was however out of scope to choose  $N_{\text{SIP}} = 128$  as default parameter.

Following the preceding assessment, we want to present some suggestions how to extend the program's capabilities and improve its performance. Due to the fact that there is no interaction between particles of different grid cells, the algorithm is perfectly suitable for parallelization. It

is expected that parallel computing on CPUs or GPUs would significantly reduce the required computation time and allow for refinement of the grid spacing and setups with more simulation particles. Although the implementation was out of scope for this thesis, it would certainly be one of the next logical steps.

When using kinematic frameworks, it can be sensible to add source terms for the atmospheric state variables  $\Theta$  and  $r_v$ , which relax the horizontal mean towards the initial profiles, as proposed in the original formulation of the test case and applied in [Arabas15]. This accounts for progressing latent heating of the cloud layer and water loss due to precipitation and leads to steady profiles of the mean moisture and temperature. We expect higher stability of the ambient air and less pronounced downdraft tunnels in the fields of  $r_v$  and  $T$ , which may have positive effects, when investigating certain cloud aspects. The proposed relaxation terms were not implemented in the present model, because they constitute another artificial restriction, which would be realized by choosing quite arbitrary relaxation times without evident physical background.

A major capability-improvement would certainly be an extension to three spatial dimensions and the implementation of a CFD solver to enable fully dynamic large eddy simulations. For a quick realization, it would, for example, be possible to utilize CFD algorithms of the Python based atmospheric LES-code PyCLES<sup>1</sup>, developed by Pressel *et al.* in the Caltech Climate Dynamics Group [Pressel15]. Regarding the modeling of microphysical processes, notable advantages of particle based methods are already summarized in Ch. 1. Next, we will specify further, how certain aspects can be implemented numerically and add some approaches for general enhancements of the microphysics scheme.

Over the years, numerous formulations of cloud particle condensational mass growth were developed on varying levels of detail, assumptions and numerical performance, e.g. [Fukuta70, Sedunov74, Pruppacher97, Vaillancourt02, Petters07]. It was found that, among others, ventilation and turbulence effects have significant influence on the heat and mass transport. In course of experimental investigations, Smolík *et al.* proposed that the heat conduction and vapor diffusion coefficients around ventilated droplets can be parametrized by the Sherwood and Nusselt number formulations of Clift *et al.* [Clift78, Smolík01]. This additional consideration, as used in the model applied in [Arabas15], could lead to a more precise representation of the condensation process. Nevertheless, it depends on a parametrization under certain conditions, which might not be fulfilled in all use cases.

Following Crowe *et al.*, we propose to include a fourth particle equation for the droplet temperature in (3.32), thereby modeling the heat generation by condensation/evaporation and the heat conduction explicitly and obtaining a more precise value of the surface temperature [Crowe11]. Consequently, the assumption of instantaneous equilibrium between latent heat production and heat conduction would no longer be necessary. Furthermore, the mass rate equation could be considered on a level closer to the diffusion equation, i.e., with less approximations. It should be examined, whether the advantages justify to invest more computational time by propagating another variable. If the equilibrium temperature turns out to be very close to the ambient temperature at any time, the effects of more detailed heat conduction modeling should be negligible.

The Lagrangian model allows for a stochastic treatment of turbulence effects, novel for cloud applications. Generally, it is possible to develop a description of the particle behavior, completely based on stochastic differential equations. The impact on the velocity evolution was formulated by Söhlch and Kärcher, adding a term  $\mathbf{v}'$  for stochastic fluctuations [Söhlch10]:

$$\dot{\mathbf{x}} = \mathbf{v} + \mathbf{v}' \quad \text{with} \quad \mathbf{v}'(t) = \chi_L \mathbf{v}'(t-h) + \sqrt{\text{TKE} (1 - \chi_L^2)} \hat{\alpha}. \quad (7.1)$$

Here, the time step is given by  $h$  and  $\hat{\alpha}$  is a random variable following the standard normal

---

<sup>1</sup> <https://github.com/pressel/pycles>

distribution. The correlation is described by  $\chi_L = \exp(-h \text{TKE}/D_{\text{mom}})$ , connected to the *turbulent kinetic energy* TKE and the momentum diffusion coefficient  $D_{\text{mom}}$ . In further development, local perturbations of the saturation were considered by assigning an additional variable  $S'$  to each simulation particle, which evolves according to  $\dot{S}' = a_S \mathbf{v}' - S'/\tau_S$  with coefficient  $a_S$  and relaxation time  $\tau_S$  [Grabowski19].

To be applicable in atmospheric use cases, our particle model should be extended to include several different soluble and insoluble species, occurring in the atmosphere. Firstly, solid residues will effect the dry size of evaporating particles and thereby the activation requirements. Secondly, the water activity is modified when a mixture of dissolved components is present. This can be modeled either by reformulating the number of effectively dissolved ions (3.8) in the Raoult term (3.7) to  $N_s = N_A \sum_s i_s m_s / M_s$ , where  $s$  runs over all soluble species or by applying numerically efficient single parameter descriptions like the  $\kappa$ -Köhler theory, proposed in [Petters07]. Additionally, droplets and ice crystals provide environments for liquid and solid phase chemistry as well as centers for the accretion of gaseous molecules. Oxidation reactions show considerable effects on the pH-level of droplets, which may lead to acid rain formation [Wang16], and can significantly influence the growth cycle by modifying the water activity [Faloona09]. A Lagrangian approach for modeling multi-component chemistry for each individual super-droplet was recently presented in [Jaruga18].

Modeling of ice containing clouds proves to entail serious challenges due to additional phase transitions, spontaneous break up and a variety of possible crystal shapes, structures and densities. In the following, we will address particle based approaches to treat complex ice micro-physics, which could be used to extend our presented program. In the approach of Söhlch and Kärcher [Söhlch10], particles are classified into several shape categories (*habits*), including spheres, hexagonal columns and bullet rosettes, based on field studies, evaluated in [Mitchell96] and [Heymsfield02]. Simulation particles are characterized by the attributes mass and habit, where each shape category has prescribed relations of mass, area and diameter. Agglomeration of two crystals is modeled by a stochastic description, depending on cross section, relative velocity and aggregation efficiency. Successful sticking events result in the formation of larger particles with more complex habits, further classified as *aggregates*. Another approach by Brdar and Seifert investigates the riming process in detail and characterizes ice particles by their ice crystal mass, rime mass, rime volume, and number of aggregated primary crystals. This emphasizes the capability of Lagrangian models to use more than two property arguments for the particle mass distribution, which is currently much more difficult to achieve in bin models [Grabowski19]. Although considerable progress in understanding and implementation of ice containing clouds has been achieved over the years, additional research is still necessary to build reliable models [Chen94, Morrison08, Morrison15, Milbrandt16, Jensen17].

We want to emphasize that Lagrangian schemes in first instance offer a numerical framework for a detailed description on the level of individual particles. One example of such an implementation is given by the presented model, which provides stable operation and plausible results, but can barely indicate all possible capabilities. The result quality of any implementation can however only be as good as the underlying physical model, which is restricted by applied assumptions and parametrizations of material properties and sub-grid effects. Many of the relevant processes are not fully understood or not sufficiently investigated by experimental measurements. This includes the interaction of particles and surrounding air by momentum, mass and heat exchange and further processes on the molecular level. To name one prominent example, the influence of hydrodynamic effects, turbulence, break-up and molecular sticking processes on the coalescence and aggregation efficiencies is poorly understood and the corresponding coefficients are most often set to quite arbitrary constants due to missing parametrizations. Similar limitations apply for the description of accommodation and condensation.

For reliable validation, we suggest to adapt the simulation models to available experimental setups, which can be conducted under controlled conditions. Especially for Lagrangian schemes, it would be worthwhile to initially analyze domains, containing such a small number of real particles, that a direct numerical representation is possible (i.e., setting all multiplicities to one). There are cloud chambers and wind tunnels<sup>2</sup>, where the atmospheric conditions as well as the CCN concentration and thus the number of cloud particles can be adjusted and subsequently closely observed. By comparing experiments with computer simulations of the very same setup, it might be possible to validate particular aspects of the applied models and further parametrize specific processes, which are on sub-grid scale for LES. In a consequent manner, the number of real particles could then be increased stepwise to compare experimental observations and results of SIP-models with larger multiplicities. This could lead to more meaningful analyses of numerical finite size effects and enable reasonable assessments for the required number of simulation particles per cell.

In consideration of their significant potential, it finally remains to say that we agree with the proposition of Grabowski *et al.* that Lagrangian schemes should and will play an increasing role in cloud modeling [Grabowski19] and expect major improvements in the quality of simulation results due to ongoing research and increasing computational capacities.

---

<sup>2</sup>For example LACIS and LACIS-T at the Leibniz Institute for Tropospheric Research [Hartmann11, Niedermeier17].

# APPENDIX

## A Material properties

Figure A.1 shows the water activity models for constant van't Hoff factor  $i_s = 2.0$  and the fitted curve with linearly dependent  $i_s(w_s)$ . It is notable that the basic model with constant van't Hoff factor describes the water activity accurately for  $w_s < 0.11$ . For the first two data points ( $w_s < 0.006$ ), the basic model is even more accurate than the fitted curve. To get an appropriate parametrization, the relevance for atmospheric processes should be considered. For a droplet of  $R_{\text{dry}} = 10 \text{ nm}$ , we find  $w_s < 0.003$  for a total droplet radius of  $R_p > 100 \text{ nm}$ . Thus, we are in the regime, where the basic case of constant van't Hoff is more accurate. The deviation of water activity from the basic Raoult-model is thus only applicable for very small droplets with large fractions of salt. Under this considerations, I chose to use the constant value  $i_s = 2$  for the region of  $w_s \leq w_s^{\text{cross}} = 0.0904$ , i.e., in the region before the constant model and linear fit model curves cross and the linear approximation  $i_s(w_s)$  for  $w_s > w_s^{\text{cross}}$  (see Fig. A.1).

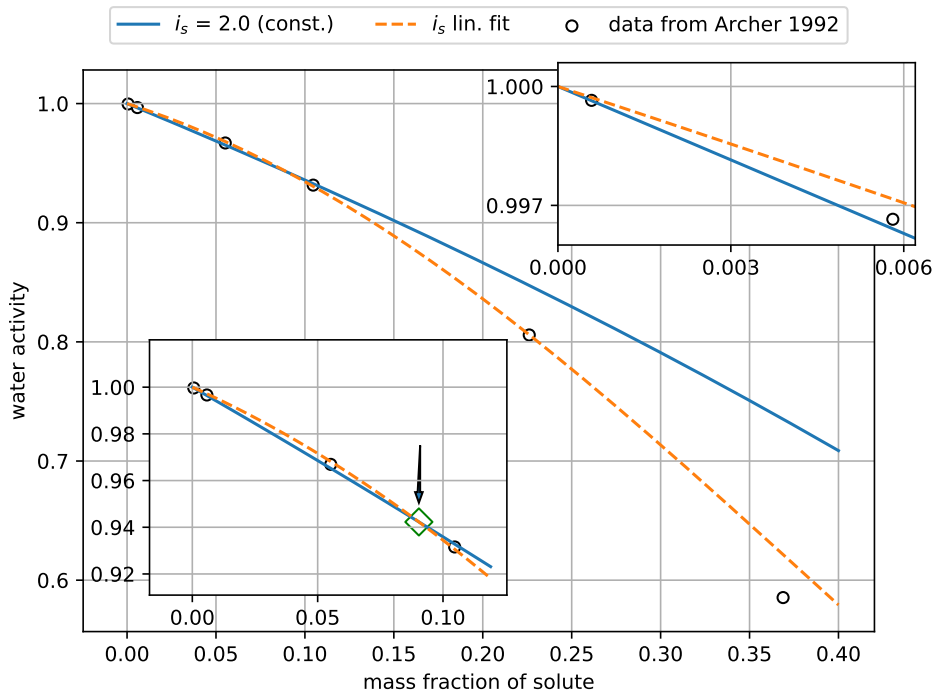


**Figure A.1:** The dependence of water activity on solute mass fraction  $w_s$  is calculated using Raoult's law. The blue solid line shows the curve for constant van't Hoff factor  $i_s$ . The dashed orange line shows the curve fitted to data from Archer, assuming a linearly dependent  $i_s$ . The insets magnify the regions of small  $w_s$  and indicate the crossing of the two model curves at the black arrow. The basic model with constant  $i_s$  is even more accurate for  $w_s < 0.006$ .

**Table A.1:** Material properties and basic physical relations

Quantity	Symbol	Formula/value	Source
Molar mass water	$M_w$	18.015 g/mol	Lide 2005 [Lide05]
Molar mass dry air	$M_{\text{dry}}$	28.9644 g/mol	ISO 1975 [ISO75]
Molar mass NaCl	$M_{\text{NaCl}}$	58.4428 g/mol	Lide 2005 [Lide05]
Partial mass density substance $j$	$\rho_j$	$\Delta m_j / \Delta V$	
... dry air	$\rho_{\text{dry}}$		
... water vapor, cloud & rain water	$\rho_v, \rho_c, \rho_r$	$\rho_c + \rho_r$	
... liquid water	$\rho_l$	$\sum_j \rho_j = \rho_{\text{dry}} + \rho_v + \rho_l + \rho_s$	NIST [Mohr16]
Total mass density	$\rho$	$8.3144598 \text{ J/(molK)}$	
Universal gas constant	$R^*$	$R^*/M_j$	
Specific gas constant substance $j$	$R_j$	$\rho_j R_j T$	ideal gas law
Partial pressure of ideal gas $j$	$p_j$	$\rho_{\text{dry}} + \rho_v$	ideal gas law
Mass density moist air	$\rho_m$	$= p_f / (R_m T_f)$ $(\rho_{\text{dry}} R_{\text{dry}} + \rho_v R_v) / \rho_m$ $\approx R_{\text{dry}} (1 + 0.608 r_v)$	
Specific gas constant moist air	$R_m$	$\rho_j / \rho_{\text{dry}}$	
Mass mixing ratio substance $j$	$r_j$	$\rho_v / \rho_m$	
Specific humidity	$q_v$	$m_s / (m_s + m_w)$	
Mass fraction of solute	$w_s$		
Dynamic viscosity dry air	$\mu_{\text{dry}}$	$1 \times 10^{-6} (18.56 + 0.0484(T - 300))$	Fit to data
Mass density liquid water	$\rho_w$	$T \text{ in K}, \mu \text{ in Pa s}$ $a_0 + a_1 (T - a_2)^2$ $T \text{ in K}, \rho_w \text{ in kg/m}^3$ $a_0 = 1.0001350 \times 10^3$ $a_1 = -4.68112708 \times 10^{-3}$ $a_2 = 2.72389977 \times 10^2$	from Kadoya 1985 [Kadoya85] Fit to data from Lide 2005 [Lide05]

Quantity	Symbol	Formula/value	Source
Mass density aq. NaCl solution	$\rho_{\text{sln}}$	$a_0 + a_1 w_s + a_2 T + a_3 w_s^2 + a_4 w_s T + a_5 T^2$ w <sub>s</sub> in kg/kg, T in K, $\rho_{\text{sln}}$ in kg/m <sup>3</sup>	Fit to data from Lide 2005 [Lide05]
		$a_0 = 7.6194440 \times 10^2, a_1 = 1.0212643 \times 10^3$	
		$a_2 = 1.8289702, a_3 = 2.4053521 \times 10^2$	
		$a_4 = -1.0805479, a_5 = -3.4928050 \times 10^{-3}$	
Mass density solution droplet	$\rho_p$	$\rho_w$ for $w_s < 0.001$ $\rho_{\text{sln}}$ for $w_s > 0.001$	
Surface tension of water	$\sigma_w$	$a_0 \tau^{1.256} (1 - a_1 \tau)$ $\tau = 1 - T/T_1, T$ in K, $\sigma_w$ in N/m	IAPWS 2014 [IAPWS14]
		$a_0 = 0.23558, a_1 = 0.625, T_1 = 647.096$	
Van't Hoff factor NaCl	$i_{\text{NaCl}}$	$2.0$ for $w_s < w_{\text{cross}}$	Lin. fit to data from Archer 1992 [Archer92]
		$a_0 + a_1 w_s$ for $w_s \geq w_{\text{cross}}$	
		$a_0 = 1.55199086, a_1 = 4.95679863$	
Solubility NaCl (mass fraction)	$w_{\text{NaCl}}^*$	$w_{\text{cross}} = 0.0903828$	Hargreaves 2010 [Hargreaves10]
Diffusion constant water vapor	$D_v$	$a_0 + a_1 T + a_2 T^2$ T in K	Fit to data from Lide 2005 [Lide05]
		$a_0 = 3.7725308 \times 10^{-1}$	
		$a_1 = -0.0008690$	
		$a_2 = 1.6470586 \times 10^{-6}$	
		$a_0 (T/T_0)^{1.94} (p_0/p)$	Pruppacher 1997 [Pruppacher97]
		$a_0 = 2.11 \times 10^{-5} \text{ m}^2/\text{s}$	
Isobaric heat capacity water (NTP)	$c_w$	$T_0 = 273.15 \text{ K}, p_0 = 101325 \text{ Pa}$	
Molar isobaric heat capacity dry air	$C_{\text{dry}}$	$4183.8 \text{ J}/(\text{kg K})$	Sabbah 1999 [Sabbah99]
Isobaric heat capacity dry air	$c_{\text{dry}}$	$7/2 R^* = 29.1006 \text{ J}/(\text{mol K})$	ideal gas w. 2 molec.
Thermal conductivity dry air	$K_{\text{dry}}$	$C_{\text{dry}}/M_{\text{dry}} = 1004.71 \text{ J}/(\text{kg K})$	
		$a_0 (5.69 + 0.017(T - T_0))$	Pruppacher 1997 [Pruppacher97]
Heat of vaporization	$L_v$	$a_0 = 4.1868 \times 10^{-3}, T_0 = 273.15 \text{ K}$	Dake 1972 [Dake72]
		$(a_0 + a_1 (T - T_0^*))1.0 \times 10^3$	
		T in K, $L_v$ in J/kg	
		$a_0 = 2500.82, a_1 = -2.358, T_0^* = 273.0$	

## B Advection test by solid body rotation

Following [Hundsdorfer95], the advection algorithm was tested simulating the transport of a solid cylinder in a circular velocity field

$$\mathbf{u} = (u, v)^\top = 2\pi \begin{pmatrix} y - \frac{1}{2} \\ -(x - \frac{1}{2}) \end{pmatrix}, \quad (\text{B.1})$$

shown in Fig. B.1.

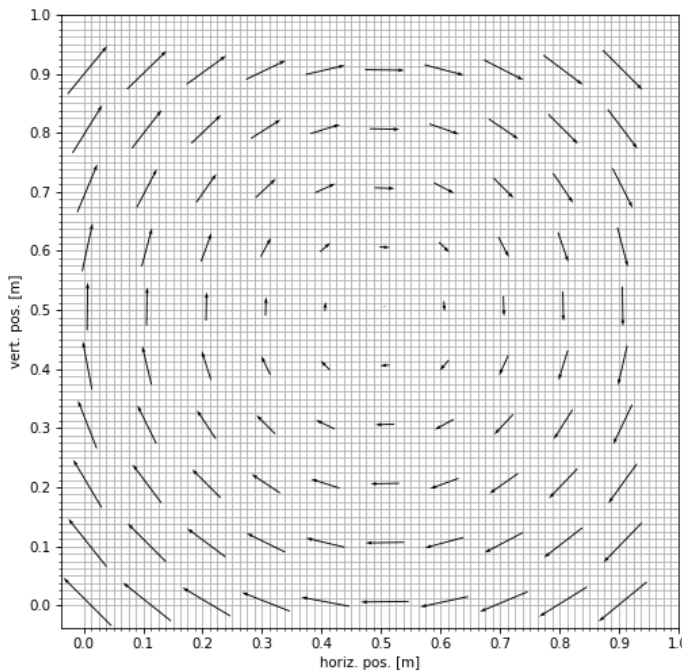


**Figure B.1:** Velocity field for the solid body advection test, given by Eq. (B.1)

The density function represents a solid cylinder of radius 0.1, centered at  $\mathbf{x}_0 = (1/2, 3/4)^\top$ :

$$\rho = \begin{cases} 1, & |\mathbf{x} - \mathbf{x}_0| < 0.1 \\ 0, & \text{else} \end{cases}, \quad \mathbf{x} = (x, y). \quad (\text{B.2})$$

In the given velocity field, the analytical solution at any time is  $\rho(x, y, t) = R(X(t), Y(t))$ , where

$$\begin{aligned} X &= \cos(2\pi t)(x - \frac{1}{2}) - \sin(2\pi t)(y - \frac{1}{2}) \\ Y &= \sin(2\pi t)(x - \frac{1}{2}) + \cos(2\pi t)(y - \frac{1}{2}), \end{aligned}$$

i.e., the initial profile rotates with period 1 around the center. For the numerical time integration, a 2nd order Runge-Kutta scheme is used with the effective divergence from Eq. (4.8) as right hand side. The time step is such that the maximum CFL number is  $\text{CFL}_{\max} = \Delta t \max(|u/\Delta x| + |v/\Delta y|) = 0.5$ . Results for  $t = 0 \dots 2$  are shown in Fig. B.2. After one rotation, the maximum value of the density is still  $> 0.9998$ , which indicates sufficiently low numerical diffusion.

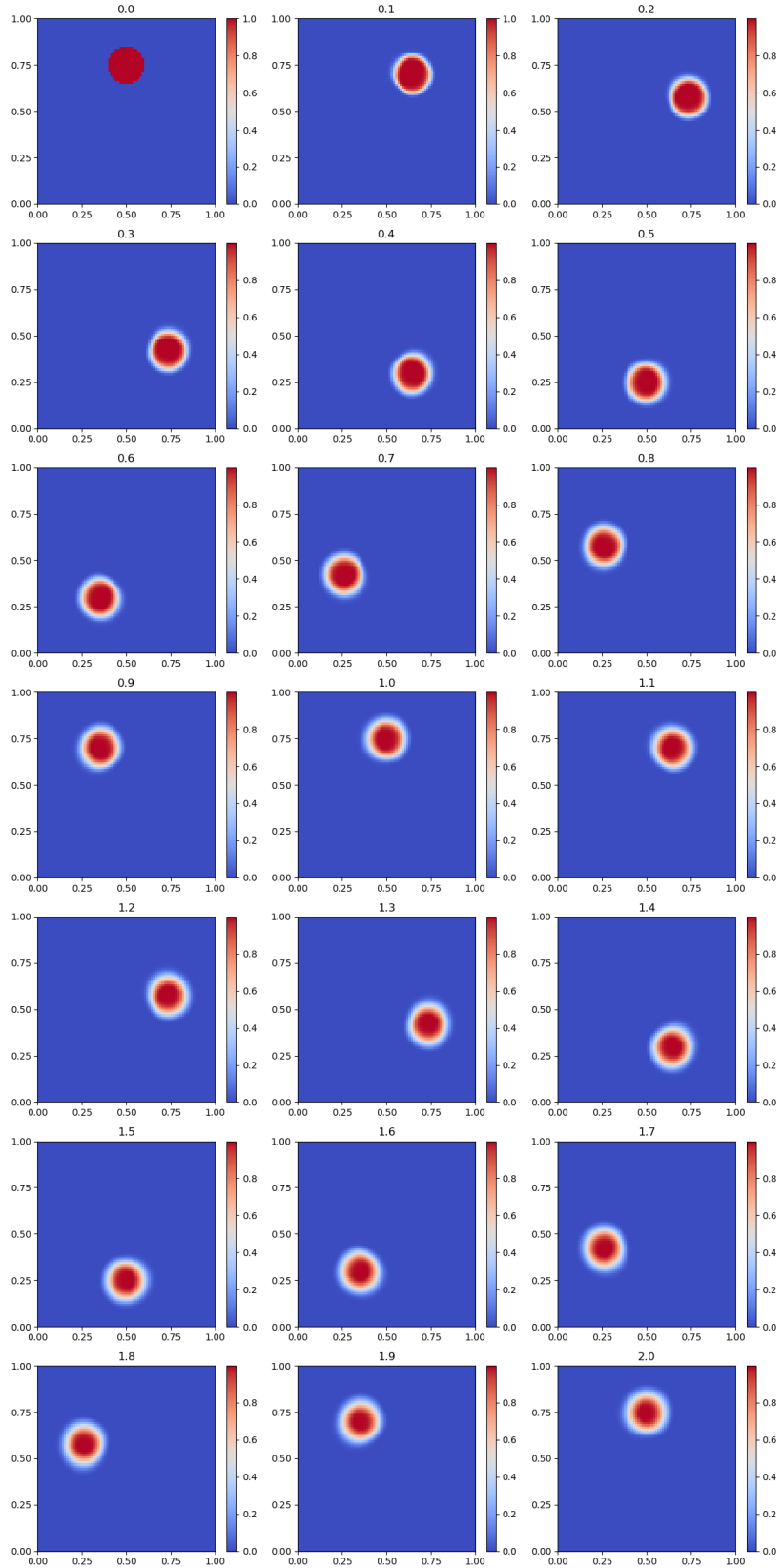


**Figure B.2:** Transport of a solid cylinder by the applied third order upwind advection scheme in a circular velocity field given by Eq. (B.1). The normalized time is shown at the top of each frame.

## C Derivations

### C.1 Integration of the hydrostatic equation for linear temperature profiles

Let the temperature be linear,  $T(z) = az + b$ , and assume  $r_v$  and  $r_t$  to be constant between  $z_j$  and  $z_{j+1}$ . From the hydrostatic equation (2.32) and the ideal gas equation (2.17), we obtain

$$\frac{dp}{dz} = -\rho_{\text{dry}}(1+r_t)g, \quad p = c_1 \rho_{\text{dry}} T, \quad c_1 = \tilde{R}_{\text{dry}}(1+r_v/\epsilon_v), \quad (\text{C.3})$$

and thus

$$\frac{dp}{p} = -c_2 \frac{dz}{T} \quad \text{with} \quad c_2 = \frac{(1+r_t)g}{c_1}. \quad (\text{C.4})$$

Integration of

$$\int_{p_j}^{p_{j+1}} \frac{dp}{p} = -c_2 \int_{z_j}^{z_{j+1}} \frac{dz}{az+b} \quad (\text{C.5})$$

yields

$$\ln\left(\frac{p_{j+1}}{p_j}\right) = -\frac{c_2}{a} \ln\left(\frac{T_{j+1}}{T_j}\right), \quad (\text{C.6})$$

and finally

$$\frac{p_{j+1}}{p_j} = \left(\frac{T_{j+1}}{T_j}\right)^{-c_2/a}, \quad (\text{C.7})$$

which is the form given in Sec. 6.1.2, when we consider  $a = (T_{j+1} - T_j)/\Delta z$ .

### C.2 Lognormal distribution

In the following, we will summarize the connection of normal and lognormal distribution and geometric and arithmetic expectation value and variance. Let  $Z$  be normal distributed ( $Z \sim N(\mu_z, \sigma_z^2)$ ) with PDF

$$f_Z(z) = \frac{1}{\sqrt{2\pi} \sigma_z} \exp\left[-\frac{1}{2} \left(\frac{z-\mu_z}{\sigma_z}\right)^2\right]. \quad (\text{C.1})$$

The probability of  $Z$  being smaller or equal than a value  $z$  is denoted by  $P(Z \leq z)$  and given by the cumulative distribution function

$$P(Z \leq z) = F_Z(z) = \int_{-\infty}^z dz' f_Z(z'), \quad (\text{C.2})$$

which is also defined by  $f_Z = \frac{dF_Z}{dz}$  and  $F_Z(-\infty) = 0$ .

Let  $Z = \ln X$  and  $z(x) = \ln x$ . Then the logarithm of  $X$  is normal distributed and  $X$  is said to be log-normal distributed. Since  $\ln(x)$  is a monotonic function, the probability  $P(X \leq x)$  must be the same as the probability  $P(Z \leq z(x))$ :

$$F_X(x) = F_Z(z(x)). \quad (\text{C.3})$$

For the PDF of  $X$  follows

$$f_X(x) = \frac{dF_X(x)}{dx} = \frac{dF_Z(z(x))}{dx} = \frac{dF_Z(z(x))}{dz} \frac{dz}{dx} = f_Z(\ln x) \frac{1}{x} \quad (\text{C.4})$$

$$= \frac{1}{\sqrt{2\pi} \sigma_z} \frac{1}{x} \exp \left[ -\frac{1}{2} \left( \frac{\ln x - \mu_z}{\sigma_z} \right)^2 \right] \quad (\text{C.5})$$

Defining now  $\mu^* := e^{\mu_z}$  and  $\sigma^* := e^{\sigma_z}$ , we can rewrite

$$f_X(x) = \frac{1}{\sqrt{2\pi} \ln(\sigma^*)} \frac{1}{x} \exp \left[ -\frac{1}{2} \left( \frac{\ln(x/\mu^*)}{\ln \sigma^*} \right)^2 \right]. \quad (\text{C.6})$$

This is the form of the log-normal distribution, which is often used for droplet dry size spectra in meteorology. The function is determined by the two parameters  $\mu^*$  and  $\sigma^*$ . Note however that  $\mu^*$  and  $(\sigma^*)^2$  are the *geometric* expectation value and variance, respectively, and not the *arithmetic* values, which are given by

$$\mu_x = E[X] = e^{\mu_z + \sigma_z^2/2} \quad (\text{C.7})$$

$$\sigma_x^2 = E[X^2] - \mu_x^2 = e^{2\mu_z + \sigma_z^2} (e^{\sigma_z^2} - 1). \quad (\text{C.8})$$

## D Collision box model

### D.1 Comparison to reference data

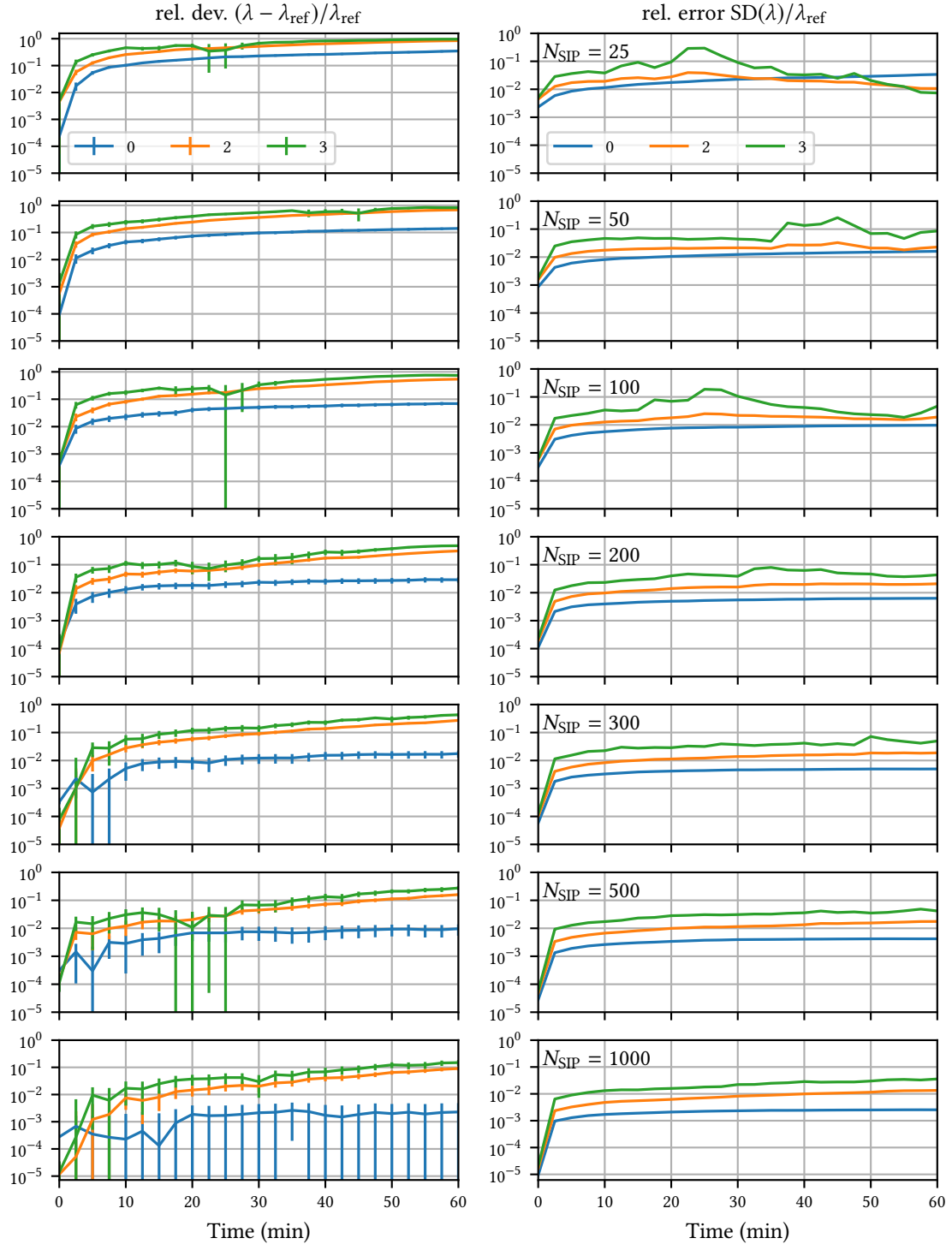


**Figure D.1:** Golovin kernel: Influence of the number of simulation particles per box  $N_{\text{SIP}}$  on the relative deviations and errors of the analyzed moments  $\lambda_k$  compared to the analytic reference solution. The color of the moment-order  $k$  is indicated in the legend.

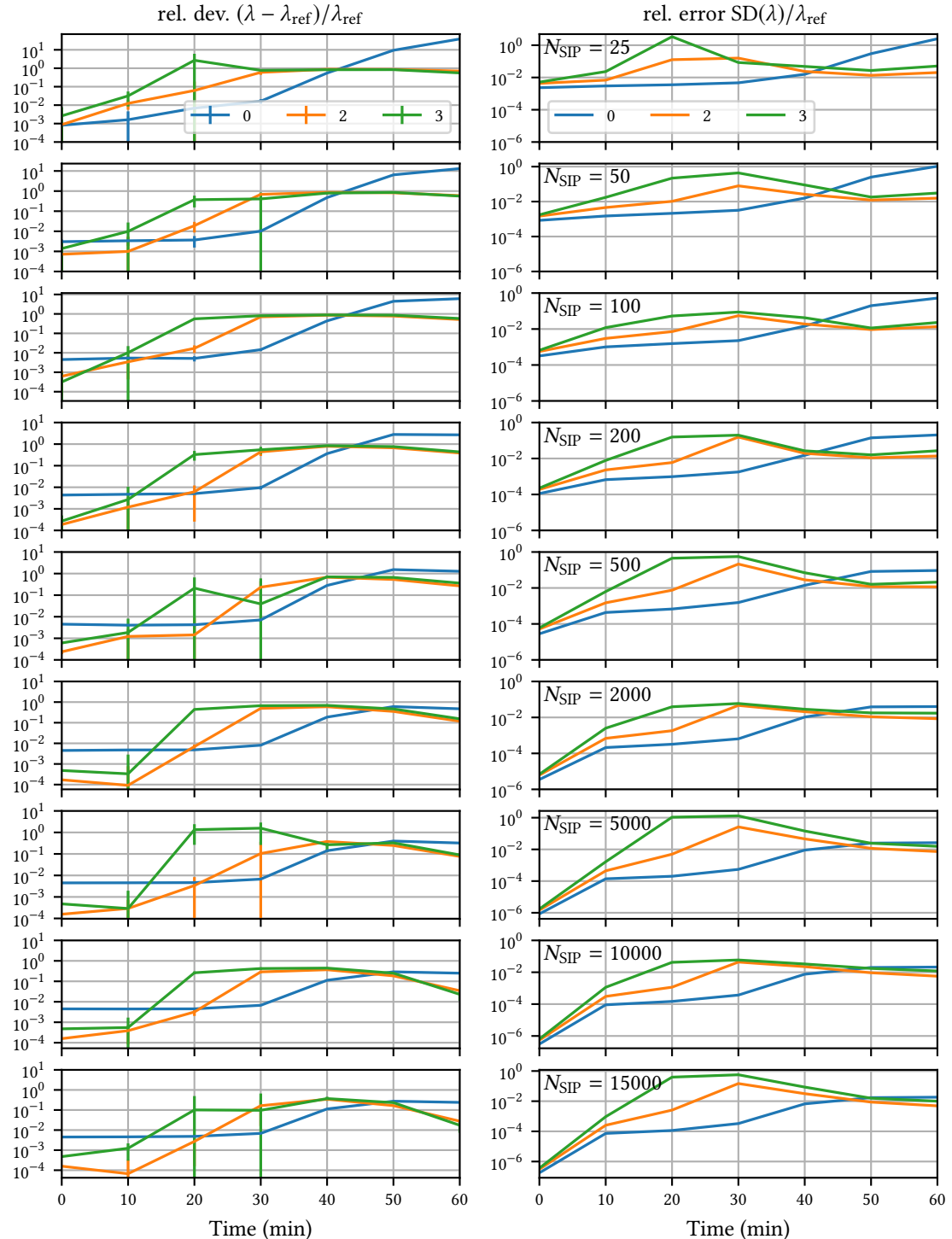


**Figure D.2:** Long kernel: Influence of the number of simulation particles per box  $N_{\text{SIP}}$  on the relative deviations and errors of the analyzed moments  $\lambda_k$  compared to the bin model reference solution by [Wang07]. The color of the moment-order  $k$  is indicated in the legend.

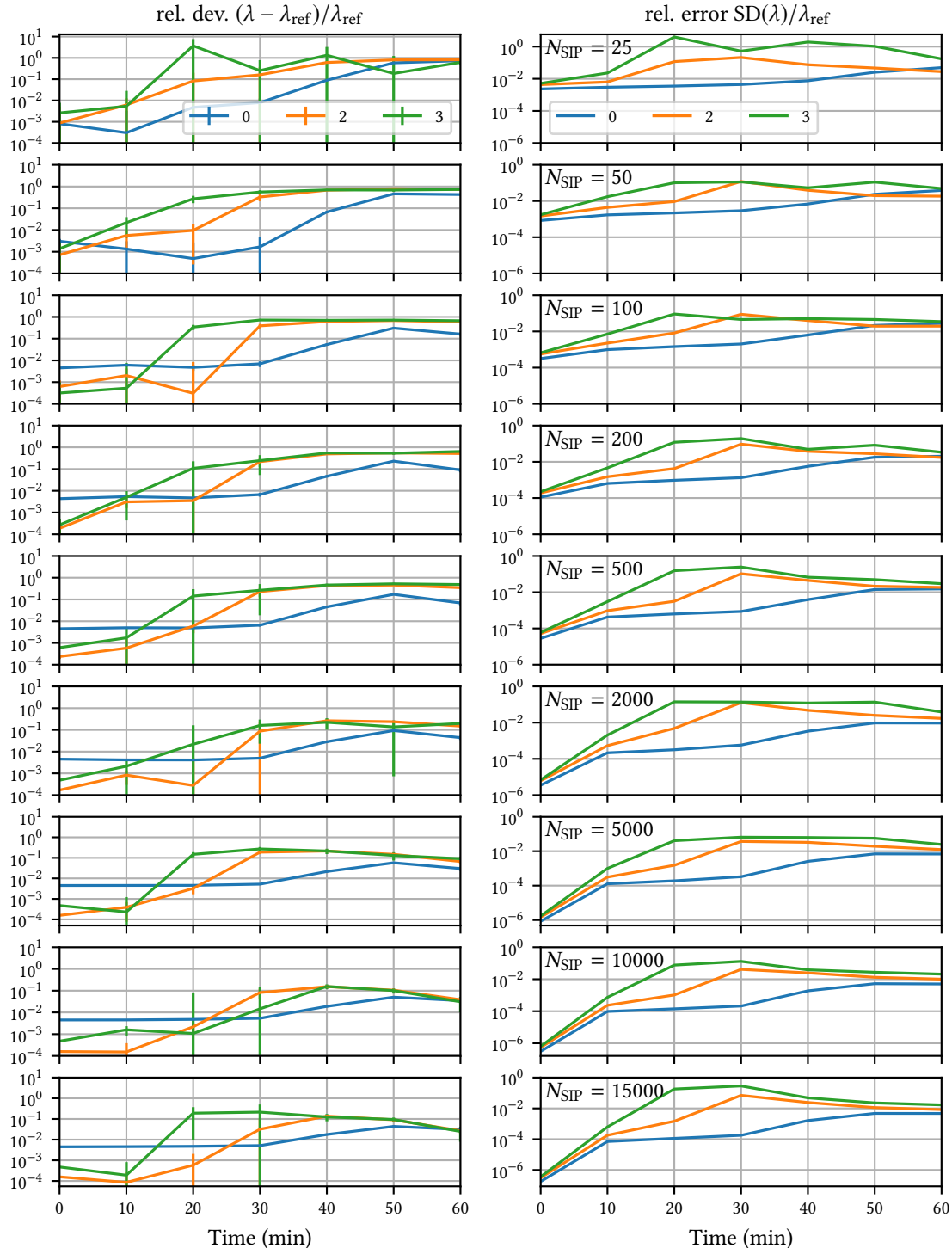


**Figure D.3:** Hall kernel: Influence of the number of simulation particles per box  $N_{\text{SIP}}$  on the relative deviations and errors of the analyzed moments  $\lambda_k$  compared to the bin model reference solution by [Wang07]. The color of the moment-order  $k$  is indicated in the legend.

## D.2 Convergence behavior when increasing the number of simulation particles

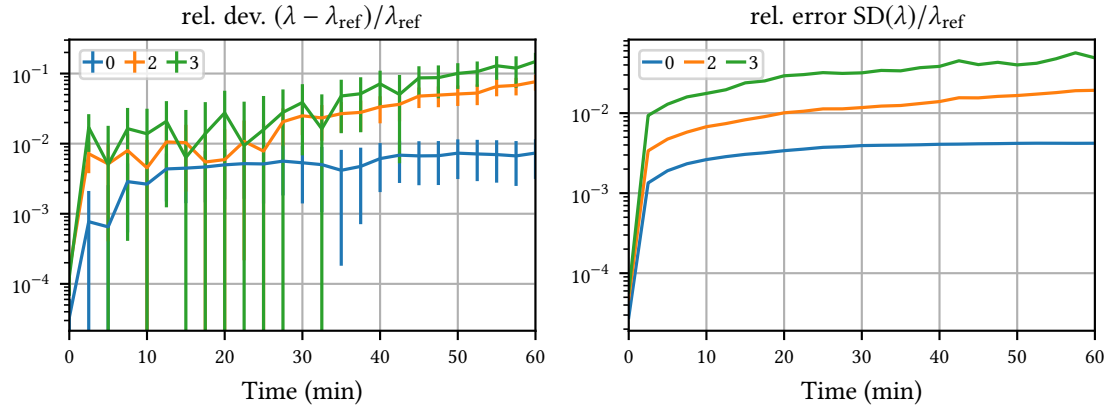


**Figure D.4:** Golovin kernel convergence: Relative deviations of the moments  $\lambda_k$  between simulations with  $N_{\text{SIP}} = 500$  and "reference"  $N_{\text{SIP}} = 1000$ . The color of the moment-order  $k$  is indicated in the legend.

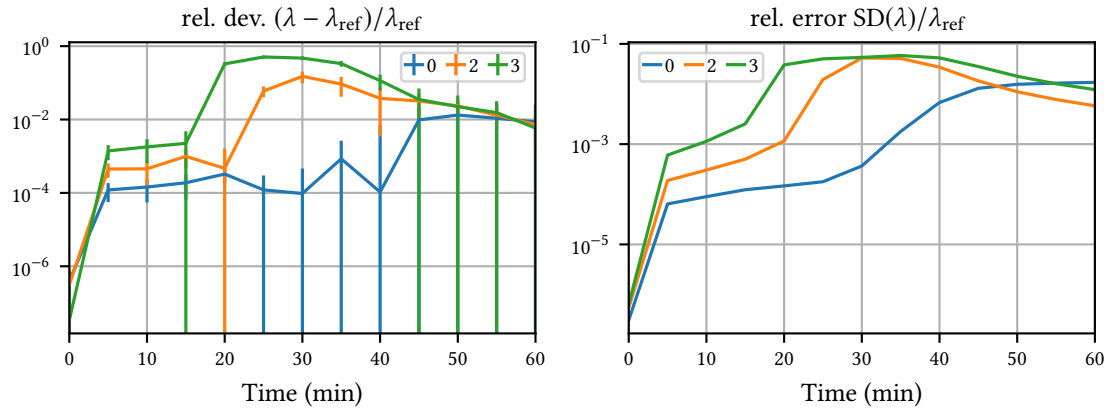


**Figure D.5:** Long kernel convergence: Relative deviations of the moments  $\lambda_k$  between simulations with  $N_{\text{SIP}} = 10\,000$  and "reference"  $N_{\text{SIP}} = 15\,000$ . The color of the moment-order  $k$  is indicated in the legend.

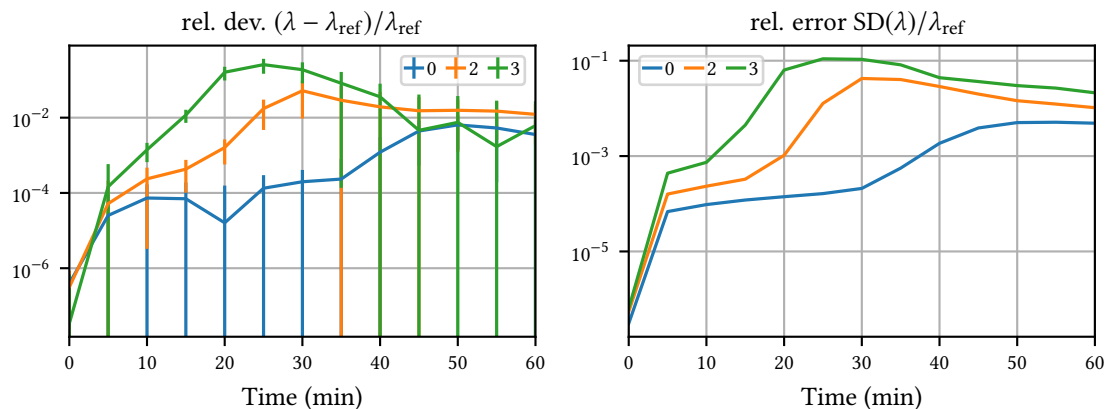


**Figure D.6:** Hall kernel convergence: Relative deviations of the moments  $\lambda_k$  between simulations with  $N_{\text{SIP}} = 10\,000$  and "reference"  $N_{\text{SIP}} = 15\,000$ . The color of the moment-order  $k$  is indicated in the legend.

## E Test case

### E.1 Simulation without collisions

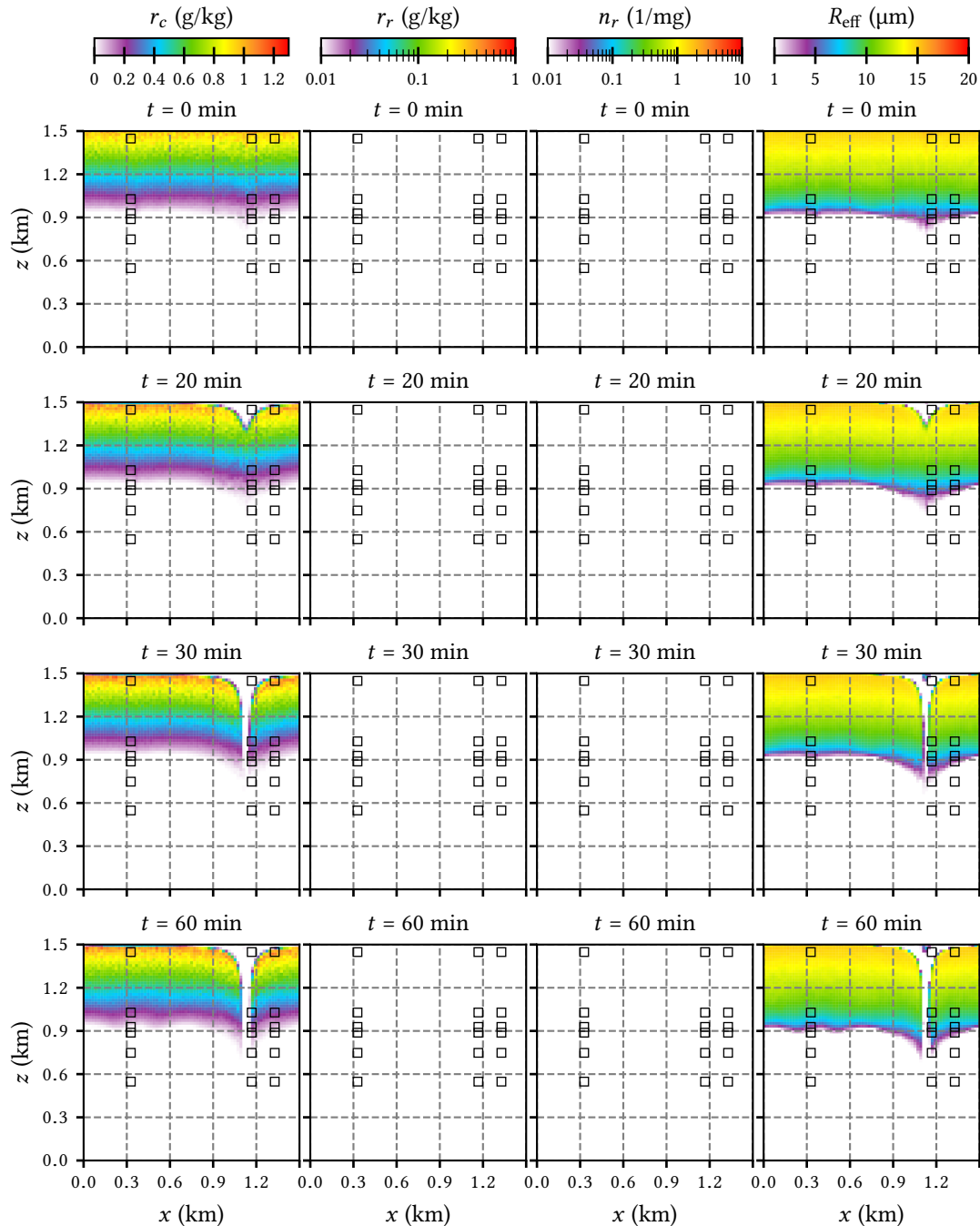


**Figure E.1:** Simulation results for the time evolution of cloud water and rain water mixing ratios, rain droplet number concentration and effective cloud droplet radius, when **switching of collisions entirely**. The presented values are averages over 50 independent simulations with  $N_{\text{SP}} = 64$ . The initial two hour spin-up period is not shown. Black boxes indicate regions where the particle size distribution is calculated in detail for the default case.

## E.2 Simulation of the default case

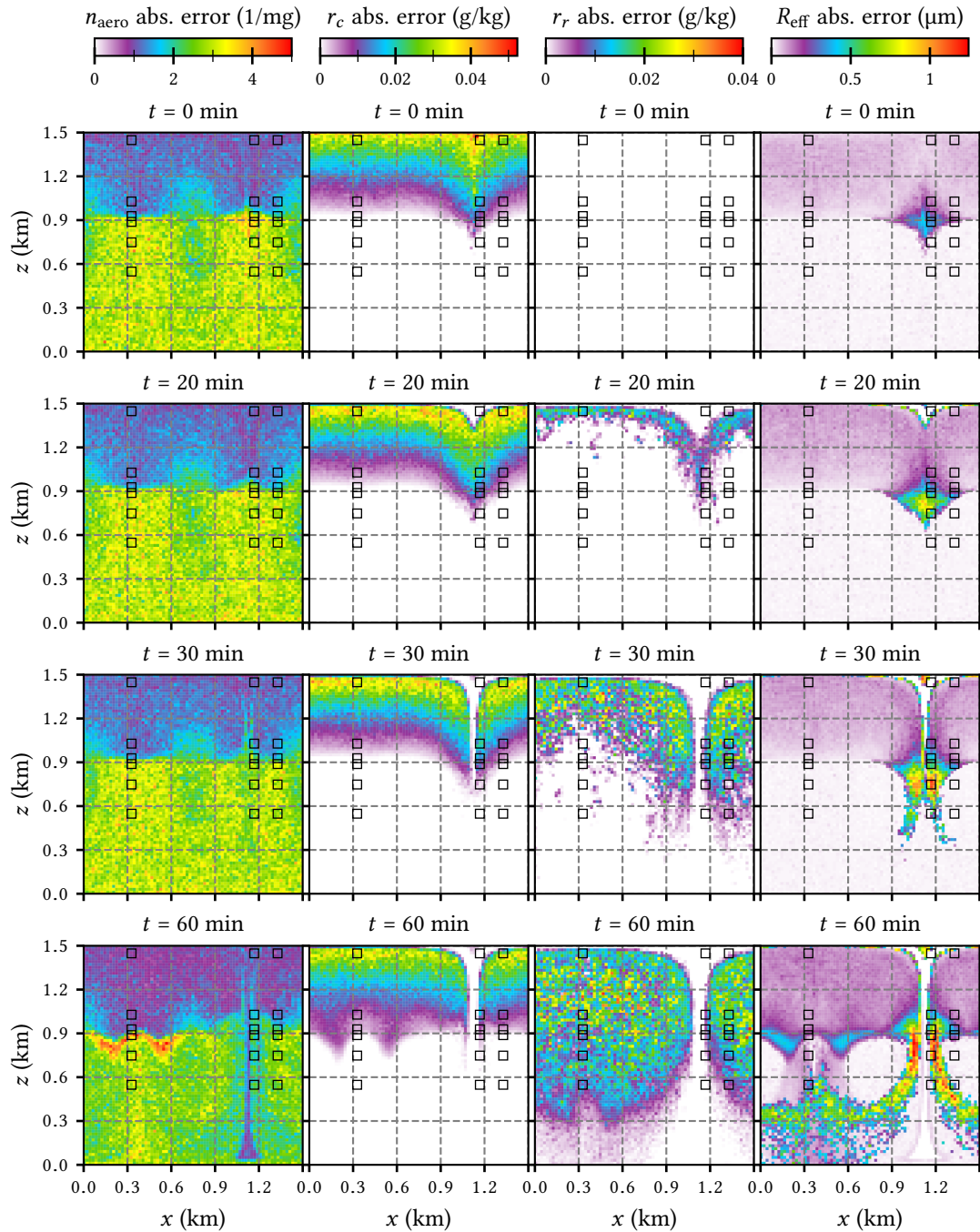


**Figure E.2:** Absolute errors for the aerosol number concentration (per dry air mass) and the mixing ratios of water vapor, cloud water and rain water, using the Long collision kernel with  $N_{\text{SIP}} = 64$  (**default case**). The absolute error of variable  $b$  is defined as estimated standard deviation of the average,  $\text{SD}(b_{\text{avg}})$ , when analyzing 50 independent simulations. The initial two hour spin-up period is not shown. Black boxes indicate regions where the particle size distribution is calculated in detail.

### E.3 Simulation with constant collision efficiency

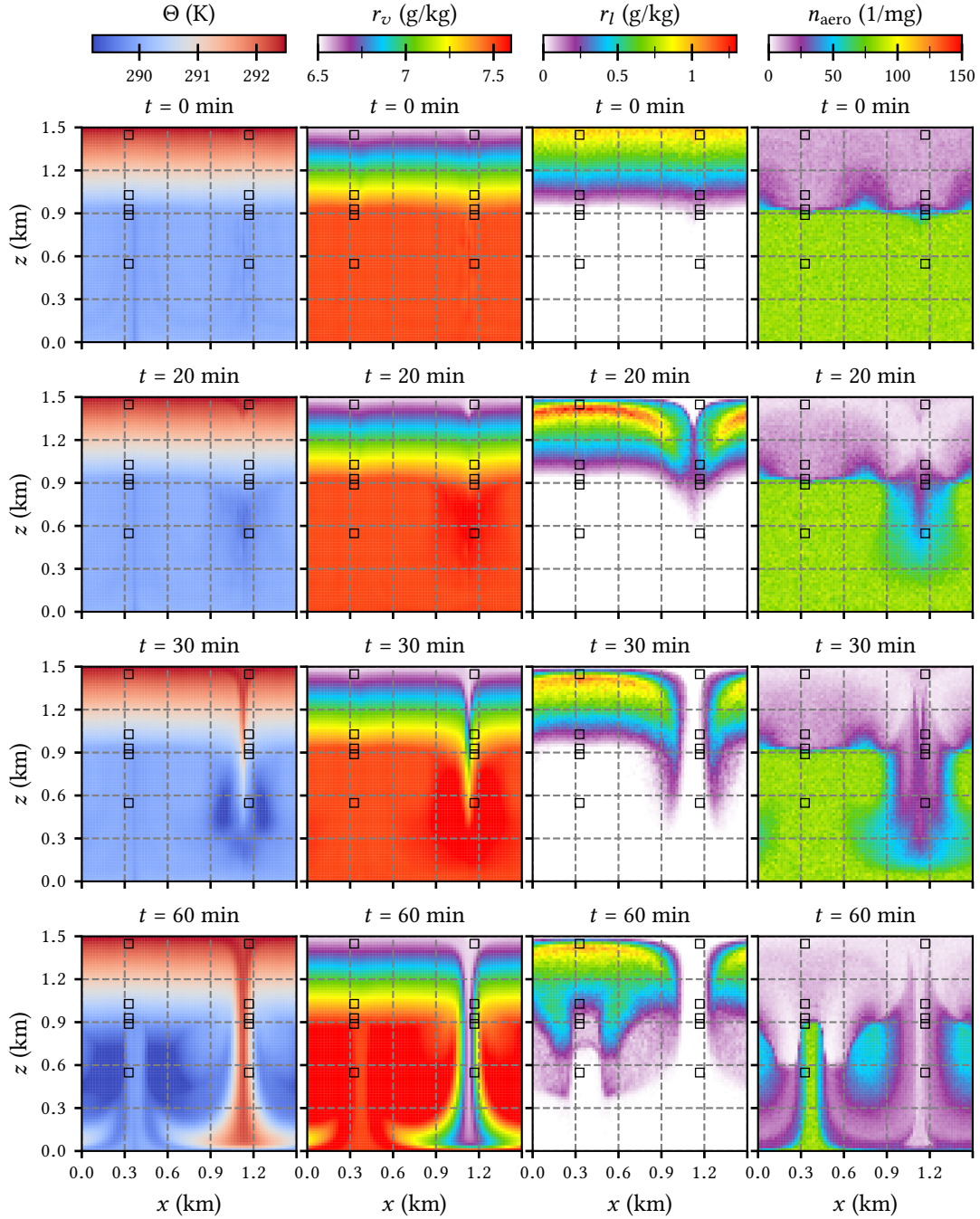


**Figure E.3:** Simulation results for the time evolution of moist potential temperature, water vapor and liquid water mixing ratios and aerosol number concentration (per dry air mass) for the hydrodynamic kernel with **constant collection efficiency**  $E_c = 0.5$ , corresponding to [Arabas15]. The presented values are averages over 50 independent simulations with  $N_{\text{SP}} = 64$ . The initial two hour spin-up period is not shown. Black boxes indicate regions where the particle size distribution is calculated in detail.

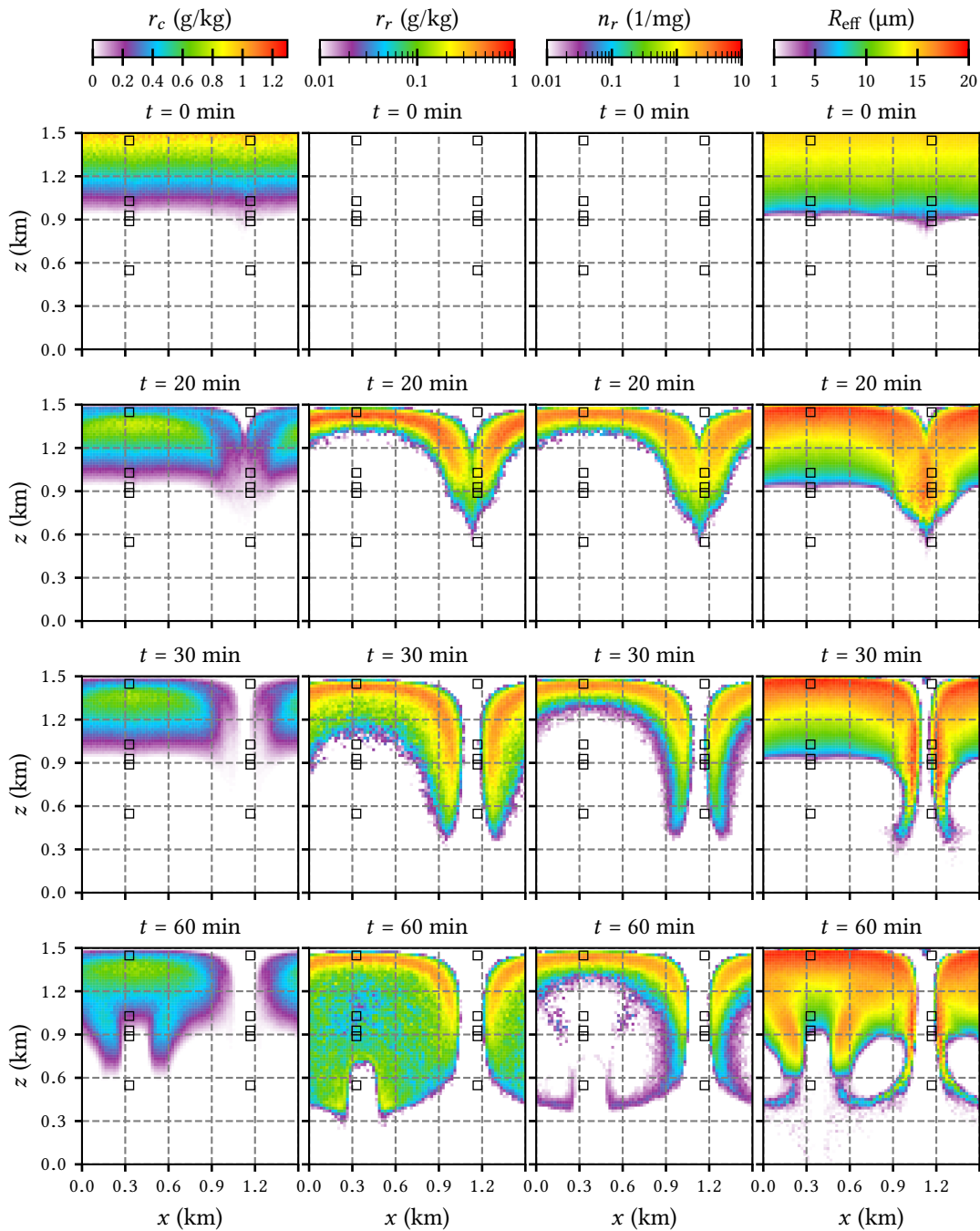


**Figure E.4:** Simulation results for the time evolution of cloud water and rain water mixing ratios, rain droplet number concentration (per dry air mass) and effective cloud droplet radius for the hydrodynamic kernel with **constant collection efficiency**  $E_c = 0.5$ , corresponding to [Arabas15]. The presented values are averages over 50 independent simulations with  $N_{\text{SIP}} = 64$ . The initial two hour spin-up period is not shown. Black boxes indicate regions where the particle size distribution is calculated in detail.

#### E.4 Variation of the collision time step

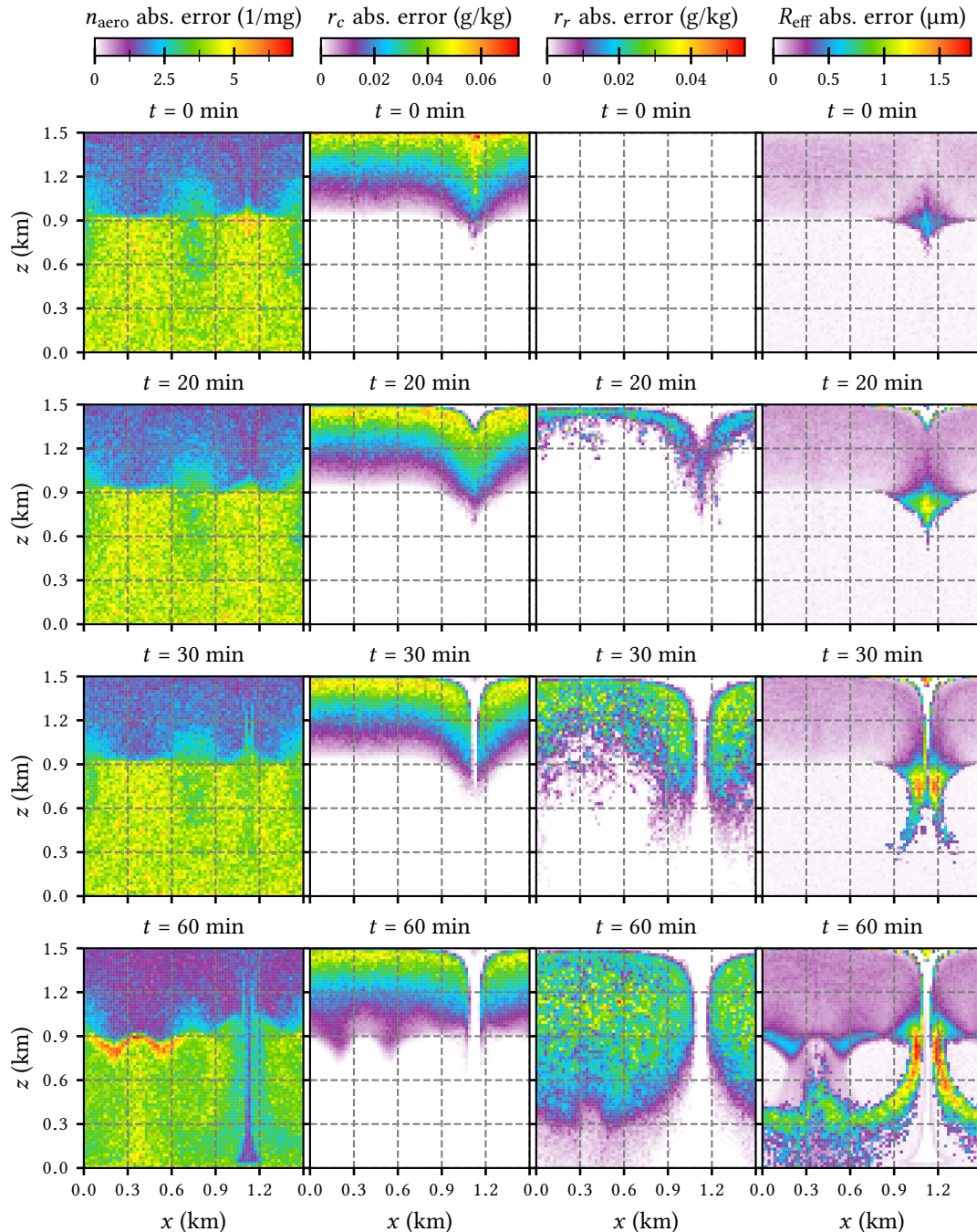


**Figure E.5:** Absolute errors for the deviation  $\Delta b = b_* - b_{\text{def}}$  between results of simulations with **collision time step**  $\Delta t_{\text{col}} = 0.1 \text{ s}$  ( $b_*$ ) and  $\Delta t_{\text{col}} = 0.5 \text{ s}$  ( $b_{\text{def}}$ ), where  $b_k$  is either the aerosol number concentration (per dry air mass), cloud water mixing ratio, rain water mixing ratio or effective cloud droplet radius. The errors of the difference are defined as  $\text{SD}(\Delta b_{\text{avg}}) = \sqrt{\text{SD}^2(b_{*,\text{avg}}) + \text{SD}^2(b_{\text{ref},\text{avg}})}$ , where  $\text{SD}(b_{\text{avg}})$  is the estimated standard deviation of the mean.

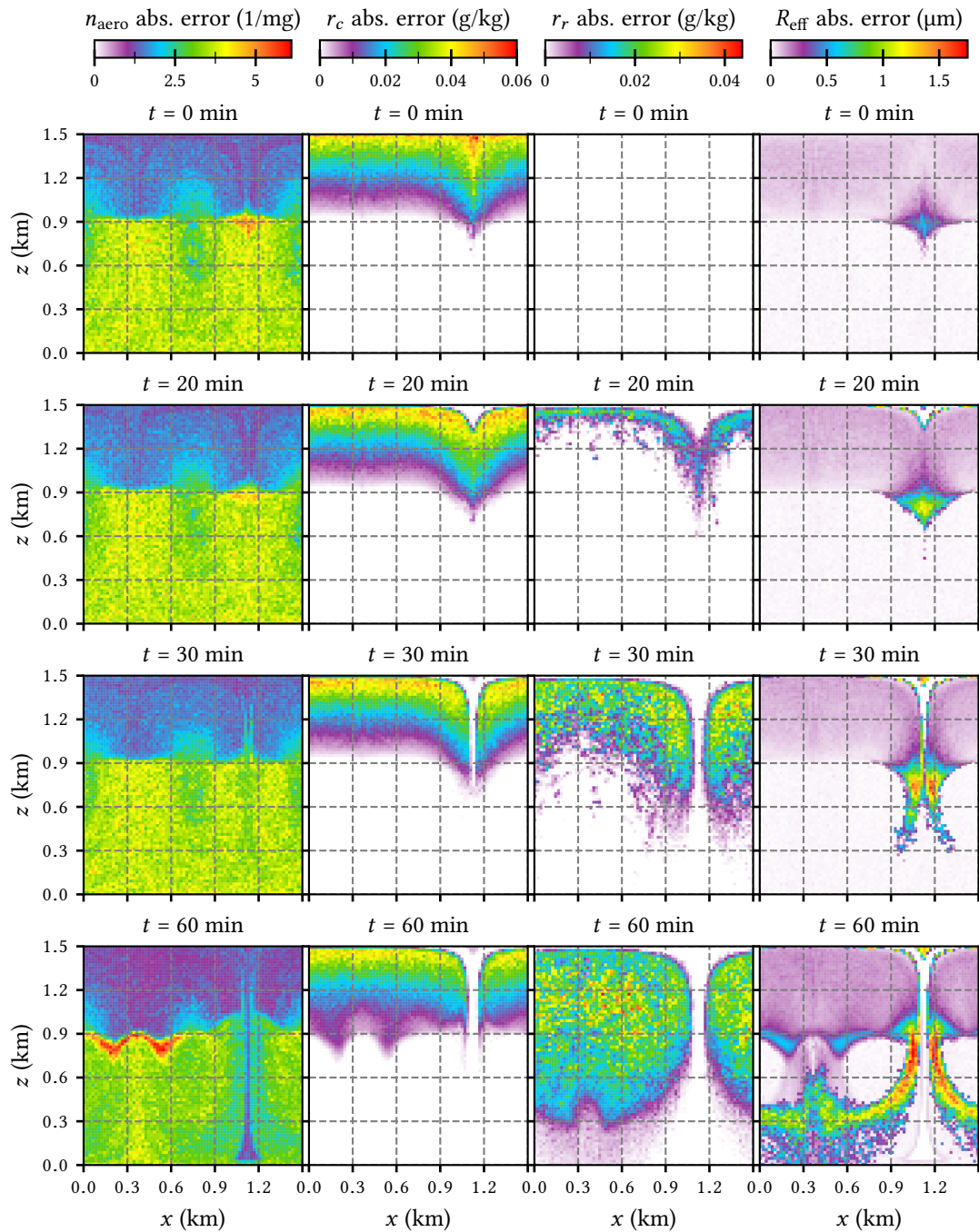


**Figure E.6:** Absolute errors for the deviation  $\Delta b = b_* - b_{\text{def}}$  between results of simulations with **numbers of simulation particles per cell**  $N_{\text{SIP}} = 128$  ( $b_*$ ) and  $N_{\text{SIP}} = 64$  ( $b_{\text{def}}$ ), where  $b_k$  is either the aerosol number concentration (per dry air mass), cloud water mixing ratio, rain water mixing ratio or effective cloud droplet radius. The errors of the difference are defined as  $\text{SD}(\Delta b_{\text{avg}}) = \sqrt{\text{SD}^2(b_{*,\text{avg}}) + \text{SD}^2(b_{\text{ref},\text{avg}})}$ , where  $\text{SD}(b_{\text{avg}})$  is the estimated standard deviation of the mean.



## BIBLIOGRAPHY

- [Abade18] Gustavo C. Abade, Wojciech W. Grabowski & Hanna Pawlowska, *Broadening of cloud droplet spectra through eddy hopping: Turbulent entraining parcel simulations*, Journal of the Atmospheric Sciences **75**, 3365 (2018).
- [Allen11] G. Allen, H. Coe, A. Clarke, C. Bretherton, R. Wood, S. J. Abel, P. Barrett, P. Brown, R. George, S. Freitag, C. McNaughton, S. Howell, L. Shank, V. Kapustin, V. Brekhovskikh, L. Kleinman, Y. N. Lee, S. Springston, T. Toniziano, R. Krejci, J. Fochesatto, G. Shaw, P. Krecl, B. Brooks, G. McMeeking, K. N. Bower, P. I. Williams, J. Crosier, I. Crawford, P. Connolly, J. D. Allan, D. Covert, A. R. Bandy, L. M. Russell, J. Trembath, M. Bart, J. B. McQuaid, J. Wang & D. Chand, *South East Pacific atmospheric composition and variability sampled along 20° S during VOCALS-REx*, Atmospheric Chemistry and Physics **11**, 5237 (2011).
- [Andrejczuk08] M. Andrejczuk, J. M. Reisner, B. Henson, M. K. Dubey & C. A. Jeffery, *The potential impacts of pollution on a nondrizzling stratus deck: Does aerosol number matter more than type?*, Journal of Geophysical Research Atmospheres **113**, 1 (2008).
- [Andrejczuk10] M. Andrejczuk, W. W. Grabowski, J. Reisner & A. Gadian, *Cloud-aerosol interactions for boundary layer stratocumulus in the Lagrangian Cloud Model*, Journal of Geophysical Research Atmospheres **115**, D22214 (2010).
- [Arabas13] Sylwester Arabas & Shin Ichiro Shima, *Large-eddy simulations of trade wind cumuli using particle-based microphysics with monte Carlo coalescence*, Journal of the Atmospheric Sciences **70**, 2768 (2013).
- [Arabas15] S. Arabas, A. Jaruga, H. Pawlowska & W. W. Grabowski, *Libcloudph++ 1.0: A single-moment bulk, double-moment bulk, and particle-based warm-rain microphysics library in C++*, Geoscientific Model Development **8**, 1677 (2015).
- [Archer92] Donald G. Archer, *Thermodynamic Properties of the NaCl+H<sub>2</sub>O System. II. Thermodynamic Properties of NaCl(aq), NaCl-2H<sub>2</sub>(cr), and Phase Equilibria*, Journal of Physical and Chemical Reference Data **21**, 793 (1992).
- [Aris62] Rutherford Aris, *Vectors, Tensors, and the Basic Equations of Fluid Mechanics*, Prentice-Hall, Englewood Cliffs, N. J. (1962).
- [Bayewitz74] Marvin H. Bayewitz, Joseph Yerushalmi, Stanley Katz & Reuel Shinnar, *The Extent of Correlations in a Stochastic Coalescence Process*, Journal of the Atmospheric Sciences **31**, 1604 (1974).
- [Beard76] K. V. Beard, *Terminal velocity and shape of cloud and precipitation drops aloft.*, Journal of the Atmospheric Sciences **33**, 851 (1976).

- [Berry67] E. X. Berry, *Cloud Droplet Growth by Collection*, Journal of the Atmospheric Sciences **24**, 688 (1967).
- [Berry74a] Edwin X. Berry & Richard L. Reinhardt, *An Analysis of Cloud Drop Growth by Collection: Part I. Double Distributions*, Journal of the Atmospheric Sciences **31**, 1814 (1974).
- [Berry74b] Edwin X. Berry & Richard L. Reinhardt, *An Analysis of Cloud Drop Growth by Collection Part II. Single Initial Distributions*, Journal of the Atmospheric Sciences **31**, 1825 (1974).
- [Berry74c] Edwin X. Berry & Richard L. Reinhardt, *An Analysis of Cloud Drop Growth by Collection: Part III. Accretion and Self-collection*, Journal of the Atmospheric Sciences **31**, 2118 (1974).
- [Betts73] A.K. Betts, *Non-precipitating cumulus convection and its parametrization*, Quarterly Journal of the Royal Meteorological Society **99**, 178 (1973).
- [Biskos06] G. Biskos, D. Paulsen, L. M. Russell, P. R. Buseck & S. T. Martin, *Prompt deliquescence and efflorescence of aerosol nanoparticles*, Atmospheric Chemistry and Physics **6**, 4633 (2006).
- [Bleck70] Rainer Bleck, *A Fast, Approximative Method for Integrating the Stochastic Coalescence Equation*, J. Geophys. Res. **75**, 5165 (1970).
- [Bott98] Andreas Bott, *A flux method for the numerical solution of the stochastic collection equation: Extension to two-dimensional particle distributions*, Journal of the Atmospheric Sciences **57**, 284 (1998).
- [Brdar18] S. Brdar & A. Seifert, *McSnow: A Monte-Carlo Particle Model for Riming and Aggregation of Ice Particles in a Multidimensional Microphysical Phase Space*, Journal of Advances in Modeling Earth Systems **10**, 187 (2018).
- [Bryan03] George H. Bryan, John C. Wyngaard & J. Michael Fritsch, *Resolution requirements for the simulation of deep moist convection*, Monthly Weather Review **131**, 2394 (2003).
- [Bryan08] George H. Bryan, *On the Computation of Pseudoadiabatic Entropy and Equivalent Potential Temperature*, Monthly Weather Review **136**, 5239 (2008).
- [Carpenter98] Richard L. Carpenter, Kelvin K. Droegemeier & Alan M. Blyth, *Entrainment and detrainment in numerically simulated cumulus congestus clouds. Part I: General results*, Journal of the Atmospheric Sciences **55**, 3417 (1998).
- [Chen94] Jen-Ping Chen & D. Lamb, *The theoretical basis for the parameterization of ice crystal habits: growth by vapor deposition*, Journal of the Atmospheric Sciences **51**, 1206 (1994).
- [Clark79] T. L. Clark, *Numerical simulations with a three-dimensional cloud model: lateral boundary condition experiments and multicellular severe storm simulations.*, Journal of the Atmospheric Sciences **36**, 2191 (1979).
- [Clift78] R. Clift, J. R. Grace & M. E. Weber, *Bubbles, Drops, and Particles*, Academic Press, New York (1978).

- [Cooper89] W. A. Cooper, *Effects of variable droplet growth histories on droplet size distributions. Part I: theory*, Journal of the Atmospheric Sciences **46**, 1301 (1989).
- [Croft09] B. Croft, U. Lohmann, R. V. Martin, P. Stier, S. Wurzler, J. Feichter, R. Posselt & S. Ferrachat, *Aerosol size-dependent below-cloud scavenging by rain and snow in the ECHAM5-HAM*, Atmospheric Chemistry and Physics **9**, 4653 (2009).
- [Crowe11] Clayton T. Crowe, John D. Schwarzkopf, Martin Sommerfeld & Yutaka Tsuji, *Multiphase Flows with Droplets and Particles*, CRC Press, 2nd Edition (2011).
- [Curry99] J. Curry & P. Webster, *Thermodynamics of Atmospheres and Oceans*, Academic Press (1999).
- [Dake72] Jonas M.K. Dake, *Evaporative cooling of a body of water*, Water Resources Research **8**, 1087 (1972).
- [Davis72] Milford H. Davis, *Collisions of Small Cloud Droplets: Gas Kinetic Effects*, Journal of the Atmospheric Sciences **29**, 911 (1972).
- [Dziekan19] Piotr Dziekan, Maciej Waruszewski & Hanna Pawłowska, *University of Warsaw Lagrangian cloud model (UWLCM) 1.0: A modern large-eddy simulation tool for warm cloud modeling with Lagrangian microphysics*, Geoscientific Model Development **12**, 2587 (2019).
- [Faloona09] Ian Faloona, *Sulfur processing in the marine atmospheric boundary layer: A review and critical assessment of modeling uncertainties*, Atmospheric Environment **43**, 2841 (2009).
- [Fukuta70] Norihiko Fukuta & L. A. Walter, *Kinetics of Hydrometeor Growth from a Vaper-Spherical Model*, Journal of the Atmospheric Sciences **27**, 1160 (1970).
- [Gillespie72] Daniel T. Gillespie, *The Stochastic Coalescence Model for Cloud Droplet Growth*, Journal of the Atmospheric Sciences **29**, 1496 (1972).
- [Golovin63] A. M. Golovin, *The solution of the coagulation equation for cloud droplets in a rising air current*, Izv. Geophys. Ser **5**, 482 (1963).
- [Grabowski93] W. W. Grabowski & T. L. Clark, *Cloud-environment interface instability. Part II: extension to three spatial dimensions*, Journal of the Atmospheric Sciences **50**, 555 (1993).
- [Grabowski96] Wojciech W. Grabowski & Piotr K. Smolarkiewicz, *Two-time-level semi-Lagrangian modeling of precipitating clouds*, Monthly Weather Review **124**, 487 (1996).
- [Grabowski98] Wojciech W. Grabowski, *Toward cloud resolving modeling of large-scale tropical circulations: A simple cloud microphysics parameterization*, Journal of the Atmospheric Sciences **55**, 3283 (1998).

- [Grabowski99] Wojciech W. Grabowski, *A parameterization of cloud microphysics for long-term cloud-resolving modeling of tropical convection*, Atmospheric Research **52**, 17 (1999).
- [Grabowski13] Wojciech W. Grabowski & Lian-Ping Wang, *Growth of Cloud Droplets in a Turbulent Environment*, Annual Review of Fluid Mechanics **45**, 293 (2013).
- [Grabowski17] Wojciech W. Grabowski & Gustavo C. Abade, *Broadening of cloud droplet spectra through eddy hopping: Turbulent entraining parcel simulations*, Journal of the Atmospheric Sciences **74**, 1485 (2017).
- [Grabowski19] Wojciech W. Grabowski, Hugh Morrison, Shin Ichiro Shima, Gustavo C. Abade, Piotr Dziekan & Hanna Pawlowska, *Modeling of cloud microphysics: Can we do better?*, Bulletin of the American Meteorological Society **100**, 655 (2019).
- [Haemeri00] Kaarle Haemeri, Minna Vaekevae, Hans Christen Hansson & Ari Laaksonen, *Hygroscopic growth of ultrafine ammonium sulphate aerosol measured using an ultrafine tandem differential mobility analyzer*, Journal of Geophysical Research Atmospheres **105**, 22231 (2000).
- [Hall80] William D. Hall, *A Detailed Microphysical Model Within a Two-Dimensional Dynamic Framework: Model Description and Preliminary Results*, Journal of the Atmospheric Sciences **37**, 2486 (1980).
- [Hamilton14] Douglas S. Hamilton, Lindsay A. Lee, Kirsty J. Pringle, Carly L. Reddington, Dominick V. Spracklen & Kenneth S. Carslaw, *Occurrence of pristine aerosol environments on a polluted planet*, Proceedings of the National Academy of Sciences of the United States of America **111**, 18466 (2014).
- [Hansen74] James E. Hansen & Larry D. Travis, *Light scattering in planetary atmospheres*, Space Science Reviews **16**, 527 (1974).
- [Hargreaves10] G. Hargreaves, N. O.A. Kwamena, Y. H. Zhang, J. R. Butler, S. Rushworth, S. L. Clegg & J. P. Reid, *Measurements of the equilibrium size of supersaturated aqueous sodium chloride droplets at low relative humidity using aerosol optical tweezers and an electrodynamic balance*, Journal of Physical Chemistry A **114**, 1806 (2010).
- [Harrington13] Jerry Y. Harrington, Kara Sulia & Hugh Morrison, *A method for adaptive habit prediction in bulk microphysical models. Part i: Theoretical development*, Journal of the Atmospheric Sciences **70**, 349 (2013).
- [Hartmann11] S. Hartmann, D. Niedermeier, J. Voigtländer, T. Clauss, R. A. Shaw, H. Wex, A. Kiselev & F. Stratmann, *Homogeneous and heterogeneous ice nucleation at LACIS: Operating principle and theoretical studies*, Atmospheric Chemistry and Physics **11**, 1753 (2011).
- [Heymsfield02] Andrew J. Heymsfield, Sharon Lewis, Aaron Bansemer, Jean Iaquinta, Larry M. Miloshevich, Masahiro Kajikawa, Cynthia Twohy & Michael R. Poellot, *A general approach for deriving the properties of cirrus and stratiform ice cloud particles*, Journal of the Atmospheric Sciences **59**, 3 (2002).

- [Hoffmann12] K. H. Hoffmann & N. D. Botkin, *Multiphase flows with phase transitions: Models and numerics*, JP Journal of Heat and Mass Transfer **6**, 73 (2012).
- [Hoffmann17] Fabian Hoffmann, Yign Noh & Siegfried Raasch, *The route to raindrop formation in a shallow cumulus cloud simulated by a Lagrangian cloud model*, Journal of the Atmospheric Sciences **74**, 2125 (2017).
- [Hoffmann19] Fabian Hoffmann, Takanobu Yamaguchi & Graham Feingold, *Inhomogeneous mixing in lagrangian cloud models: Effects on the production of precipitation embryos*, Journal of the Atmospheric Sciences **76**, 113 (2019).
- [Hundsdorfer95] W. Hundsdorfer, B. Koren, M. Van Loon & J. G. Verwer, *A positive finite-difference advection scheme*, Journal of Computational Physics **117**, 35 (1995).
- [IAPWS14] IAPWS, *IAPWS R1-76: Revised Release on Surface Tension of Ordinary Water Substance*, The International Association for the Properties of Water and Steam, Moscow, Russia (2014).
- [ISO75] ISO, *ISO 2533:1975 - Standard Atmosphere*, International Organization for Standardization, Geneva, Switzerland (1975).
- [Jaruga18] Anna Jaruga & Hanna Pawlowska, *Libcloudph++ 2.0: Aqueous-phase chemistry extension of the particle-based cloud microphysics scheme*, Geoscientific Model Development **11**, 3623 (2018).
- [Jensen17] Anders A. Jensen, Jerry Y. Harrington, Hugh Morrison & Jason A. Milbrandt, *Predicting ice shape evolution in a bulk microphysics model*, Journal of the Atmospheric Sciences **74**, 2081 (2017).
- [Jonas72] P. R. Jonas, *The collisions efficiency of small droplets*, Quarterly Journal of the Royal Meteorological Society **98**, 681 (1972).
- [Kadoya85] K. Kadoya, N. Matsunaga & A. Nagashima, *Viscosity and Thermal Conductivity of Dry Air in the Gaseous Phase*, Journal of Physical and Chemical Reference Data **14**, 947 (1985).
- [Kessler69] Edwin Kessler, *On the Distribution and Continuity of Water Substance in Atmospheric Circulations*, in *Meteorological Monographs*, vol 10., American Meteorological Society, Boston, MA (1969).
- [Khain15] A. P. Khain, K. D. Beheng, A. Heymsfield, A. Korolev, S. O. Krichak, Z. Levin, M. Pinsky, V. Phillips, T. Prabhakaran, A. Teller, S. C. Van Den Heever & J. I. Yano, *Representation of microphysical processes in cloud-resolving models: Spectral (bin) microphysics versus bulk parameterization*, Reviews of Geophysics **53**, 247 (2015).
- [Klemp78] Joseph B. Klemp & Robert B. Wilhelmson, *The simulation of three-dimensional convective storm dynamics*, Journal of the Atmospheric Sciences **35**, 1070 (1978).
- [Klett73] J. D. Klett & M. H. Davis, *Theoretical Collision Efficiencies of Cloud Droplets at Small Reynolds Numbers*, Journal of the Atmospheric Sciences **30**, 107 (1973).

- [Knoth98] Oswald Knoth & Ralf Wolke, *Implicit-explicit Runge-Kutta methods for computing atmospheric reactive flows*, Applied Numerical Mathematics **28**, 327 (1998).
- [Kogan91] Y. L. Kogan, *The simulation of a convective cloud in a 3-D model with explicit microphysics. Part I: model description and sensitivity experiments*, Journal of the Atmospheric Sciences **48**, 1160 (1991).
- [Kostinski05] Alexander B. Kostinski & Raymond A. Shaw, *Fluctuations and luck in droplet growth by coalescence*, Bulletin of the American Meteorological Society **86**, 235 (2005).
- [Lam15] Siu Kwan Lam, Antoine Pitrou & Stanley Seibert, *Numba: A LLVM-based python JIT compiler*, in *Proceedings of the Second Workshop on the LLVM Compiler Infrastructure in HPC - LLVM '15*, pages 1–6 (2015).
- [Lebo15] Z. J. Lebo & H. Morrison, *Effects of horizontal and vertical grid spacing on mixing in simulated squall lines and implications for convective strength and structure*, Monthly Weather Review **143**, 4355 (2015).
- [Lee15] Kok Foong Lee, Robert I.A. Patterson, Wolfgang Wagner & Markus Kraft, *Stochastic weighted particle methods for population balance equations with coagulation, fragmentation and spatial inhomogeneity*, Journal of Computational Physics **303**, 1 (2015).
- [Lide05] David R. Lide, *CRC Handbook of Chemistry and Physics, Internet Version 2005* (2005).
- [Lin75] C. L. Lin & S. C. Lee, *Collision Efficiency of Water Drops in the Atmosphere.*, Journal of the Atmospheric Sciences **32**, 1412 (1975).
- [Lin83] Y. L. Lin, R. D. Farley & H. D. Orville, *Bulk parameterization of the snow field in a cloud model.*, Journal of Climate & Applied Meteorology **22**, 1065 (1983).
- [Liu69] J. Y. Liu & H. D. Orville, *Numerical Modeling of Precipitation and Cloud Shadow Effects on Mountain-Induced Cumuli*, Journal of the Atmospheric Sciences **26**, 1283 (1969).
- [Lohmann16] Ulrike Lohmann, Felix Lüönd & Fabian Mahrt, *An introduction to clouds: From the microscale to climate*, Cambridge University Press (2016).
- [Long74] Alexis B. Long, *Solutions To the Droplet Collection Equation for Polynomial Kernels.*, Journal of the Atmospheric Sciences **31**, 1040 (1974).
- [Maronga19] Björn Maronga, Sabine Banzhaf, Cornelia Burmeister, Thomas Esch, Renate Forkel, Dominik Fröhlich, Vladimir Fuka, Katrin Frieda Gehrke, Jan Geletič, Sebastian Giersch, Tobias Gronemeier, Günter Groß, Wieke Heldens, Antti Hellsten, Fabian Hoffmann, Atsushi Inagaki, Eckhard Kadasch, Farah Kanani-Sühring, Klaus Ketelsen, Basit Ali Khan, Christoph Knigge, Helge Knoop, Pavel Krč, Mona Kurppa, Halim Mammari, Andreas Matzarakis, Matthias Mauder, Matthias Pallasch, Dirk Pavlik, Jens Pfafferott, Jaroslav Resler, Sascha Rissmann, Emmanuele

- Russo, Mohamed Salim, Michael Schrempf, Johannes Schwenkel, Gunther Seckmeyer, Sebastian Schubert, Matthias Sühring, Robert von Tils, Lukas Vollmer, Simon Ward, Björn Witha, Hauke Wurps, Julian Zeidler & Siegfried Raasch, *Overview of the PALM model system 6.0*, Geoscientific Model Development Discussions **in review**, 1 (2019).
- [Marowka18] Ami Marowka, *Python accelerators for high-performance computing*, Journal of Supercomputing **74**, 1449 (2018).
- [Milbrandt05] Jason A. Milbrandt & M. K. Yau, *A multimoment bulk microphysics parameterization. Part II: A proposed three-moment closure and scheme description*, Journal of the Atmospheric Sciences **62**, 3065 (2005).
- [Milbrandt16] J. A. Milbrandt & H. Morrison, *Parameterization of cloud microphysics based on the prediction of bulk ice particle properties. Part III: Introduction of multiple free categories*, Journal of the Atmospheric Sciences **73**, 975 (2016).
- [Mitchell96] David L. Mitchell, *Use of mass- and area-dimensional power laws for determining precipitation particle terminal velocities*, Journal of the Atmospheric Sciences **53**, 1710 (1996).
- [Mohr16] P.J. Mohr, D.B. Newell & B.N. Taylor, *The 2014 CODATA Recommended Values of the Fundamental Physical Constants (Web Version 7.2)*, National Institute of Standards and Technology, Gaithersburg, MD, US (2016).
- [Morrison07] Hugh Morrison & Wojciech W. Grabowski, *Comparison of bulk and bin warm-rain microphysics models using a kinematic framework*, Journal of the Atmospheric Sciences **64**, 2839 (2007).
- [Morrison08] Hugh Morrison & Wojciech W. Grabowski, *A novel approach for representing ice microphysics in models: Description and tests using a kinematic framework*, Journal of the Atmospheric Sciences **65**, 1528 (2008).
- [Morrison15] Hugh Morrison & Jason A. Milbrandt, *Parameterization of cloud microphysics based on the prediction of bulk ice particle properties. Part I: Scheme description and idealized tests*, Journal of the Atmospheric Sciences **72**, 287 (2015).
- [Morrison18] Hugh Morrison, Mikael Witte, George H. Bryan, Jerry Y. Harrington & Zachary J. Lebo, *Broadening of modeled cloud droplet spectra using bin microphysics in an eulerian spatial domain*, Journal of the Atmospheric Sciences **75**, 2437 (2018).
- [Muhlbauer13] Andreas Muhlbauer, Wojciech W. Grabowski, Szymon P. Malinowski, Thomas P. Ackerman, George H. Bryan, Zachary J. Lebo, Jason A. Milbrandt, Hugh Morrison, Mikhail Ovchinnikov, Sarah Tessendorf, Julie M. Theriault & Greg Thompson, *Reexamination of the state of the art of cloud modeling shows real improvements*, Bulletin of the American Meteorological Society **94**, 45 (2013).
- [Niedermeier17] D. Niedermeier, J. Voigtlander, H. Siebert, N. Desai, Raymond A. Shaw, K. Chang, S. Krueger, J. Schumacher & F. Stratmann, *LACIS-T - A moist air*

- wind tunnel for investigating the interactions between cloud microphysics and turbulence*, in *APS Meeting Abstracts*, page G15.002 (2017).
- [Patterson11] Robert I.A. Patterson, Wolfgang Wagner & Markus Kraft, *Stochastic weighted particle methods for population balance equations*, *Journal of Computational Physics* **230**, 7456 (2011).
- [Petters07] M.D. Petters & S.M. Kreidenweis, *A single parameter representation of hygroscopic growth and cloud condensation nucleus activity*, *Atmospheric Chemistry and Physics* **7**, 1961 (2007).
- [Pressel15] Kyle G. Pressel, Colleen M. Kaul, Tapio Schneider, Zhihong Tan & Siddhartha Mishra, *Large-eddy simulation in an anelastic framework with closed water and entropy balances*, *Journal of Advances in Modeling Earth Systems* **7**, 1425 (2015).
- [Pruppacher97] H. R. Pruppacher & J. D. Klett, *Microphysics of Clouds and Precipitation*, Kluwer Academic Publishers, Dordrecht (1997).
- [Rasinski11] Piotr Rasinski, Hanna Pawlowska & Wojciech W. Grabowski, *Observations and kinematic modeling of drizzling marine stratocumulus*, *Atmospheric Research* **102**, 120 (2011).
- [Rogers89] R. R. Rogers & M. K. Yau, *A Short Course in Cloud Physics*, Pergamon (1989).
- [Rutledge83] S. A. Rutledge & P. V. Hobbs, *The mesoscale and microscale structure and organization of clouds and precipitation in midlatitude cyclones. VIII: a model for the 'seeder-feeder' process in warm-frontal rainbands.*, *Journal of the Atmospheric Sciences* **41**, 2949 (1983).
- [Sabbah99] R. Sabbah, An Xu-wu, J.S. Chickos, M.L. Planas Leitão, M.V. Roux & L.A. Torres, *Reference materials for calorimetry and differential thermal analysis*, *Thermochimica Acta* **331**, 93 (1999).
- [Schoenberg Ferrier94] Brad Schoenberg Ferrier, *A Double-Moment Multiple-Phase Four-Class Bulk Ice Scheme. Part I: Description*, *Journal of the Atmospheric Sciences* **51**, 249 (1994).
- [Schwenkel18] Johannes Schwenkel, Fabian Hoffmann & Siegfried Raasch, *Improving collisional growth in Lagrangian cloud models: Development and verification of a new splitting algorithm*, *Geoscientific Model Development* **11**, 3929 (2018).
- [Scott68] William T. Scott, *Analytic Studies of Cloud Droplet Coalescence I*, *Journal of the Atmospheric Sciences* **25**, 54 (1968).
- [Sedunov74] Y.S. Sedunov, *Physics of the Drop Formation in the Atmosphere*, John Wiley and Sons, New York (1974).
- [Seeßelberg96] M. Seeßelberg, T. Trautmann & M. Thorn, *Stochastic simulations as a benchmark for mathematical methods solving the coalescence equation*, *Atmospheric Research* **40**, 33 (1996).

- [Shafrir71] Uri Shafrir & Tzvi Gal-Chen, *A Numerical Study of Collision Efficiencies and Coalescence Parameters for Droplet Pairs with Radii up to 300 Microns*, Journal of the Atmospheric Sciences **28**, 741 (1971).
- [Shima09] S. Shima, K. Kusano, A. Kawano, T. Sugiyama & S. Kawahara, *The super-droplet method for the numerical simulation of clouds and precipitation: A particle-based and probabilistic microphysics model coupled with a non-hydrostatic model*, Quarterly Journal of the Royal Meteorological Society **135**, 1307 (2009).
- [Smolík01] Jiří Smolík, Lucie Džumbová, Jaroslav Schwarz & Markku Kulmala, *Evaporation of ventilated water droplet: Connection between heat and mass transfer*, Journal of Aerosol Science **32**, 739 (2001).
- [Söhlch10] Ingo Söhlch & Bernd Kärcher, *A large-eddy model for cirrus clouds with explicit aerosol and ice microphysics and Lagrangian ice particle tracking*, Quarterly Journal of the Royal Meteorological Society **136**, 2074 (2010).
- [Sommerfeld08] Martin Sommerfeld, Berend van Wachem & Rene Oliemans, *Best Practice Guidelines: CFD of Dispersed Multiphase Flows*, European Research Community on Flow, Turbulence and Combustion (ERCOFTAC), 1. Edition (2008).
- [Sonntag03] R.E. Sonntag, C. Borgnakke & G.J. Van Wylen, *Fundamentals of Thermodynamics*, Wiley, 6 Edition (2003).
- [Stevens96] Bjorn Stevens, Graham Feingold, William R. Cotton & Robert L. Walko, *Elements of the microphysical structure of numerically simulated non-precipitating stratocumulus*, Journal of the Atmospheric Sciences **53**, 980 (1996).
- [Stevens98] Bjorn Stevens, William R. Cotton, Graham Feingold & Chin Hoh Moeng, *Large-eddy simulations of strongly precipitating, shallow, stratocumulus-topped boundary layers*, Journal of the Atmospheric Sciences **55**, 1616 (1998).
- [Stevens05] Bjorn Stevens, Chin Hoh Moeng, Andrew S. Ackerman, Christopher S. Bretherton, Andreas Chlond, Stephan de Roode, James Edwards, Jean Christophe Golaz, Hongli Jiang, Marat Khairoutdinov, Michael P. Kirkpatrick, David C. Lewellen, Adrian Lock, Frank Müller, David E. Stevens, Eoin Whelan & Ping Zhu, *Evaluation of large-eddy simulations via observations of nocturnal marine stratocumulus*, Monthly Weather Review **133**, 1443 (2005).
- [Szumowski98] Marcin J. Szumowski, Wojciech W. Grabowski & Harry T. Ochs, *Simple two-dimensional kinematic framework designed to test warm rain microphysical models*, Atmospheric Research **45**, 299 (1998).
- [Tang97] Ignatius N Tang, *Thermodynamic and optical properties of mixed-salt aerosols of atmospheric importance*, Journal of Geophysical Research **102**, 1883 (1997).
- [Thein18] Ferdinand Thein, *Results for Two Phase Flows with Phase Transition*, Dissertation, Ph.D. Thesis, University Magdeburg (2018).

- [Tzivion87] S. Tzivion, G. Feingold & Z. Levin, *An efficient numerical solution to the stochastic collection equation*, Journal of the Atmospheric Sciences **44**, 3139 (1987).
- [Unterstrasser14] S. Unterstrasser & I. Sölch, *Optimisation of the simulation particle number in a Lagrangian ice microphysical model*, Geoscientific Model Development **7**, 695 (2014).
- [Unterstrasser17] Simon Unterstrasser, Fabian Hoffmann & Marion Lerch, *Collection/aggregation algorithms in Lagrangian cloud microphysical models: Rigorous evaluation in box model simulations*, Geoscientific Model Development **10**, 1521 (2017).
- [Vaillancourt02] P. A. Vaillancourt, M. K. Yau, P. Bartello & W. W. Grabowski, *Microscopic approach to cloud droplet growth by condensation. Part II: Turbulence, clustering, and condensational growth*, Journal of the Atmospheric Sciences **59**, 3421 (2002).
- [Wang07] Lian Ping Wang, Yan Xue & Wojciech W. Grabowski, *A bin integral method for solving the kinetic collection equation*, Journal of Computational Physics **226**, 59 (2007).
- [Wang16] Gehui Wang, Renyi Zhang, Mario E. Gomez, Lingxiao Yang, Misti Levy Zamora, Min Hu, Yun Lin, Jianfei Peng, Song Guo, Jingjing Meng, Jianjun Li, Chunlei Cheng, Tafeng Hu, Yanqin Ren, Yuesi Wang, Jian Gao, Junji Cao, Zhisheng An, Weijian Zhou, Guohui Li, Jiayuan Wang, Pengfei Tian, Wilmarie Marrero-Ortiz, Jeremiah Secret, Zhuofei Du, Jing Zheng, Dongjie Shang, Limin Zeng, Min Shao, Weigang Wang, Yao Huang, Yuan Wang, Yujiao Zhu, Yixin Li, Jiaxi Hu, Bowen Pan, Li Cai, Yuting Cheng, Yuemeng Ji, Fang Zhang, Daniel Rosenfeld, Peter S. Liss, Robert A. Duce, Charles E. Kolb & Mario J. Molina, *Persistent sulfate formation from London Fog to Chinese haze*, Proceedings of the National Academy of Sciences of the United States of America **113**, 13630 (2016).
- [Wilkinson16] Michael Wilkinson, *Large Deviation Analysis of Rapid Onset of Rain Showers*, Physical Review Letters **116**, 018501 (2016).
- [Zein10] Ali Zein, *Numerical methods for multiphase mixture conservation laws with phase transition*, Dissertation, Ph.D. Thesis, University Magdeburg (2010).
- [Zhu07] H. P. Zhu, Z. Y. Zhou, R. Y. Yang & A. B. Yu, *Discrete particle simulation of particulate systems: Theoretical developments*, Chemical Engineering Science **62**, 3378 (2007).
- [Ziegler85] C. L. Ziegler, *Retrieval of thermal and microphysical variables in observed convective storms. Part 1: model development and preliminary testing*, Journal of the Atmospheric Sciences **42**, 1487 (1985).